



UNIVERSITAT DE
BARCELONA

Identification of the interaction networks of Mitofusin-1 and Mitofusin-2

Identificació de les xarxes d'interacció de Mitofusina-1 i Mitofusina-2

Isabel Gordaliza Alaguero

ADVERTIMENT. La consulta d'aquesta tesi queda condicionada a l'acceptació de les següents condicions d'ús: La difusió d'aquesta tesi per mitjà del servei TDX (www.tdx.cat) i a través del Dipòsit Digital de la UB (diposit.ub.edu) ha estat autoritzada pels titulars dels drets de propietat intel·lectual únicament per a usos privats emmarcats en activitats d'investigació i docència. No s'autoritza la seva reproducció amb finalitats de lucre ni la seva difusió i posada a disposició des d'un lloc aliè al servei TDX ni al Dipòsit Digital de la UB. No s'autoritza la presentació del seu contingut en una finestra o marc aliè a TDX o al Dipòsit Digital de la UB (framing). Aquesta reserva de drets afecta tant al resum de presentació de la tesi com als seus continguts. En la utilització o cita de parts de la tesi és obligat indicar el nom de la persona autora.

ADVERTENCIA. La consulta de esta tesis queda condicionada a la aceptación de las siguientes condiciones de uso: La difusión de esta tesis por medio del servicio TDR (www.tdx.cat) y a través del Repositorio Digital de la UB (diposit.ub.edu) ha sido autorizada por los titulares de los derechos de propiedad intelectual únicamente para usos privados enmarcados en actividades de investigación y docencia. No se autoriza su reproducción con finalidades de lucro ni su difusión y puesta a disposición desde un sitio ajeno al servicio TDR o al Repositorio Digital de la UB. No se autoriza la presentación de su contenido en una ventana o marco ajeno a TDR o al Repositorio Digital de la UB (framing). Esta reserva de derechos afecta tanto al resumen de presentación de la tesis como a sus contenidos. En la utilización o cita de partes de la tesis es obligado indicar el nombre de la persona autora.

WARNING. On having consulted this thesis you're accepting the following use conditions: Spreading this thesis by the TDX (www.tdx.cat) service and by the UB Digital Repository (diposit.ub.edu) has been authorized by the titular of the intellectual property rights only for private uses placed in investigation and teaching activities. Reproduction with lucrative aims is not authorized nor its spreading and availability from a site foreign to the TDX service or to the UB Digital Repository. Introducing its content in a window or frame foreign to the TDX service or to the UB Digital Repository is not authorized (framing). Those rights affect to the presentation summary of the thesis as well as to its contents. In the using or citation of parts of the thesis it's obliged to indicate the name of the author.

Identification of the interaction networks of Mitofusin-1 and Mitofusin-2.

Isabel Gordaliza Alaguero
Universitat de Barcelona



Barcelona, 2021

UNIVERSITAT DE BARCELONA

FACULTAT DE FARMÀCIA I CIÈNCIES DE L'ALIMENTACIÓ

INSTITUTE FOR RESEARCH IN BIOMEDICINE – IRB BARCELONA

PROGRAMA DE DOCTORAT EN BIOMEDICINA

**Identification of the interaction networks of
Mitofusin-1 and Mitofusin-2**

*Identificació de les xarxes d'interacció de
Mitofusina-1 i Mitofusina-2*

Isabel Gordaliza Alaguero

Barcelona, 2021



INSTITUT
DE RECERCA
BIOMÈDICA



UNIVERSITAT DE
BARCELONA

FACULTAT DE FARMÀCIA I CIÈNCIES DE L'ALIMENTACIÓ

INSTITUTE FOR RESEARCH IN BIOMEDICINE - IRB BARCELONA

PROGRAMA DE DOCTORAT EN BIOMEDICINA

Identification of the interaction networks of Mitofusin-1 and Mitofusin-2

*Identificació de les xarxes d'interacció
de Mitofusina-1 i Mitofusina-2*

Memòria presentada per Isabel Gordaliza Alaguero per optar al grau de doctora per la Universitat de Barcelona

GORDALIZA ALAGUERO
ISABEL - ***7271**
02/09/2021
Certificado emitido por
AC FNMT Usuarios

Digitally signed by Antonio
Zorzano
DN: cn=Antonio Zorzano,
o=IRB Barcelona, ou,
email=antonio.
zorzano@irbbarcelona.org,
c=ES
Date: 2021.09.02 17:02:07
+02'00'

A stylized, handwritten signature of Antonio Zorzano in red ink, overlapping the text.

Isabel Gordaliza Alaguero
Doctoranda

Antonio Zorzano Olarte
Director i tutor

Barcelona 2021

CONTENT

0. Abbreviations	27
1. Summary.....	43
1.1. Abstract.....	43
1.2. Introduction.....	44
1.3. Objectives and approach	45
1.4. Results	46
1.4.1. Generation of CRISPR-Cas9 MFN1-HA and MFN2-HA cell lines	46
1.4.2. Optimization of MFN1-HA and MFN2-HA immunoprecipitation	47
1.4.3. Identification of MFN1 and MFN2 binding partners by mass spectrometry	47
1.4.4. Validation of novel interaction partners of MFN1 and MFN2	48
1.4.5. Mitochondrial consequences of RAB5C absence	52
1.4.6. RNA binding proteins and mitochondria	53
1.4.7. SLC27A2 implications in autophagy	54
1.5. Discussion	58
1.5.1. CRISPR/Cas9 edited cellular models preserve mitochondrial and autophagic features of WT cells.....	58
1.5.2. MFN1 and MFN2 show decreased interaction candidates	

Content

upon starvation and RNA-binding protein enrichment in basal conditions.....	58
1.5.3. RAB5C is necessary for mitochondrial morphology maintenance and its ablation results in increased mitochondrial degradation	59
1.5.4. RNA-binding proteins interact with mitochondria.....	60
1.5.5. SLC27A2 interacts with proteins involved in phagophore expansion and its deficiency impairs autophagy	60
1.6. Conclusions	61
2. Introduction	67
2.1. Mitochondria.....	67
2.2. Mitochondrial dynamics.....	70
2.2.1. Mitochondrial fission.....	71
2.2.2. Mitochondrial fusion	72
2.3. Additional cellular functions of the mitofusins.....	75
2.3.1. Interorganelle communication.....	77
2.3.2. ER-stress and unfolded protein response	80
2.3.3. Macroautophagy	81
2.3.4. Mitochondrial quality control	82
2.3.5. Mitochondrial transport	83
2.3.6. Mitochondrial bioenergetics.....	83
2.3.7. Innate immune response	84

2.3.8. Cellular junctions.....	86
2.3.9. Cell cycle progression	87
2.3.10. Apoptosis	87
2.3.11. Cellular senescence	88
2.3.12. Cellular differentiation	89
2.4. Autophagosome formation.....	91
2.4.1. Autophagy initiation	92
2.4.2. Autophagosome nucleation.....	92
2.4.3. Phagophore expansion.....	93
2.4.4. Phagophore closure and cleavage	96
3. Objectives.....	101
4. Results.....	107
4.1. Generation of endogenous expressing MFN1-HA and MFN2-HA CRISPR/Cas9 cellular models	107
4.1.1. Design of a CRISPR/Cas9 strategy to tag endogenous MFN1 and MFN2.....	107
4.1.2. The designed CRISPR/Cas9 system efficiently drives Cas9 to its target sites in MFN1 and MFN2 and integrates the HA-tag sequenceb	112
4.1.3. Obtention of MFN1-HA and MFN2-HA HeLa clones after single cell sorting.....	114
4.1.4. HA-immunoprecipitation retrieves all the HA-tagged protein	

Content

from the lysate and reveals heterozygous insertion of the HA-tag	115
4.2. Validation of the MFN1-HA and MFN2-HA HeLa cell lines	117
4.2.1. C-terminal HA-tag insertion preserves mitochondrial fusogenic activity of MFN1 and MFN2.....	117
4.2.3. C-terminal HA-tagging of MFN1 and MFN2 results in normal induction of autophagy and mitochondrial elongation upon starvation treatment	121
4.3. Selection of the conditions of interest for finding MFN1-HA and MFN2-HA partners.....	126
4.4. Optimization of immunoprecipitation protocol.....	126
4.4.1. 1% Digitonin efficiently solubilizes MFN2-HA and preserves MFN1-MFN2 interaction	127
4.4.2. Magnetic beads improve the specificity of the HA-IP	128
4.4.3. Maximum binding of endogenous MFN2-HA to HA-beads is achieved with 6.25 mg of protein per 10 µl of beads	130
4.4.4. Immunoprecipitated MFN2-HA in basal and in starvation conditions is detectable by Coomassie staining	131
4.5. HA-IP coupled to MS identifies potential binding partners of MFN1-HA and MFN2-HA in basal and starvation conditions	132
4.5.1. Endogenous HA-IP of MFN1-HA and MFN2-HA provides insight into the composition of MFN1-MFN2 complexes.....	132
4.5.2. Mass spectrometry of HA-IP of MFN1-HA and MFN2-HA	

reveals different interactome landscapes in basal and starvation conditions.....	137
4.5.3. Mitochondrial proteins are identified among MS detected proteins	146
4.5.4. Mass spectrometry reveals possible interactions between MFN1 and MFN2 and proteins from other membranous compartments of the cell.....	147
4.5.5. Proteins that participate in post-translational modifications potentially interact with MFN1 and MFN2.....	149
4.5.6. Autophagy related proteins are enriched in basal and starvation conditions.....	151
4.5.7. RNA-binding proteins are highly enriched among basal binding candidates.....	152
4.6. Validation of some MFN1 and MFN2 binding candidates	158
4.6.1. NDFIP2 interacts with MFN1 and MFN2	158
4.6.2. RAB5C interacts with MFN1 and MFN2	159
4.6.3. S100A8 and S100A9 interact with MFN2.....	160
4.6.4. MFN2 interaction with RAB5C and S100A8 is affected by nutrient availability	162
4.6.5. SLC27A2 interacts with MFN2	164
4.6.6. AGO2 and FXR1 interact with MFN1 and MFN2.....	166
4.7. Further functional validation of some novel interactors of MFN1 and MFN2	167

Content

4.7.1. Mitochondrial effects of RAB5C ablation	167
4.7.1.1. RAB5C is necessary for MFN1 protein expression and mitochondrial morphology maintenance	167
4.7.1.2. RAB5C KO cells have less mitochondrial mass and mtDNA nucleoids	171
4.7.1.3. Bafilomycin treatment results in accumulation of mtDNA nucleoids	173
4.7.1.4. Genes implicated in mitochondrial clearance are upregulated in RAB5C KO cells.....	174
4.7.1.5. Bafilomycin treatment increases co-distribution of mtDNA and endosomes in RAB5C KO cells	175
4.7.2. Mitochondria locate in close proximity to AGO2 positive and G3BP1 positive structures.....	179
4.7.3 Consequences of SLC27A2 deficiency in autophagy	180
4.7.3.1. Deficiency of SLC27A2 or MFN2 decreases LC3B autophagic flux in starvation and autophagosome formation	180
4.7.3.2. SLC27A2 is degraded by autophagy during starvation	183
4.7.3.3. SLC27A2 deficiency modifies the autophagic fluxes of LC3B-II, P62 and GABARAP in basal and starvation conditions	184
4.7.3.4. SLC27A2 interacts with proteins involved in the	

expansion of the phagophore	186
4.7.3.5. LC3 and GABARAP puncta colocalize with SLC27A2	188
4.7.3.6. SLC27A2 contains evolutionarily conserved LIR domains	191
4.7.3.7. Absence of SLC27A2 impairs MFN2 targeting by autophagosomes	195
4.7.3.8. MFN2 interacts with SLC27A2 and ATG2A in basal and starvation conditions.....	197
5. Discussion	201
5.1. Endogenous IP coupled to MS is a physiological approach to identify MFN1 and MFN2 interactors.....	201
5.2. MFN1 and MFN2 interactomes are dependent on the nutrient availability of the cell.....	209
5.2.1. Nutrient availability determines MFN1- or MFN2-mediated mitochondrial tethering to other organelles.....	212
5.2.2. Post-translational modifications of MFN1 and MFN2 are dependent on nutrient availability.....	214
5.2.3. MFN2 potential interactors link its function to autophagy	217
5.3. RNA related structures interact with mitochondria in a MFN1/ MFN2-dependent manner	219
5.4. RAB5C interaction with MFN1 and MFN2 maintains mitochondrial morphology and prevents mitochondrial degradation.....	222

Content

5.5. SLC27A2 interacts with MFN2 to orchestrate phagophore expansion	225
6. Conclusions	239
7. Materials and methods.....	243
7.1. Cell culture procedures	247
7.1.1. Cell Maintenance	247
7.1.2. Freeze and Thaw cell aliquots	248
7.1.3. Cell treatments for autophagy assessment.....	249
7.1.4. CRISPR/Cas9 HA-tagged cell line generation.....	249
7.1.4.1. gRNA design and cloning	249
7.1.4.2. CRISPR/Cas9 HeLa cell clone generation.....	251
7.1.5. CRISPR/Cas9 Knockout cell line generation	252
7.1.6. Protein overexpression	253
7.1.7. Transient gene silencing	253
7.2. Molecular biology techniques	254
7.2.1. Total protein extraction	254
7.2.2. Western blot	255
7.2.3. Immunoprecipitation.....	257
5.2.3.1. Endogenous denaturing HA-IP in RIPA buffer to validate HA-tagging of MFN1 and MFN	257
5.2.3.2. Endogenous HA-IP coupled to mass spectrometry to identify MFN1 and MFN2 interactors	258

5.2.3.3. FLAG-IP of overexpressed proteins.....	262
7.2.4. Cell visualization by confocal microscopy.....	263
5.2.4.1. Immunostaining of fixed cells.....	263
5.2.4.2. Cell preparation for live imaging.....	264
5.2.4.3. Image acquisition.....	265
7.2.5. Gene expression measurement by quantitative real time PCR	265
5.2.5.1. RNA extraction.....	265
5.2.5.2. cDNA preparation.....	266
5.2.5.3. Quantitative real-time PCR.....	266
7.3. Statistics.....	267
8. References.....	271
9. Publications.....	297

FIGURES

Figure S-1. CRISPR/Cas9 edited MFN1-HA and MFN2-HA HeLa cell lines	46
Figure S-2. Validated interactors of MFN1 and MFN2	49
Figure S-3. Mitochondrial consequences of RAB5C ablation	52
Figure S-4. Contacts between mitochondria and RNA-related structures	54
Figure S-5. SLC27A2 implications in autophagy	55
Figure 1. Mitochondrial dynamics.....	71
Figure 2. BDLP tetramerization model adapted from Liu et al. 2018....	74
Figure 3. Functions of MFN1 and MFN2.....	76
Figure 4. Functions of MFN2 in which MFN1 does not participate	77
Figure 5. Contacts of mitochondria with other organelles that involve MFN1 and MFN2	78
Figure 6. First stages of autophagy.....	92
Figure 7. CRISPR/Cas9 approach.....	108
Figure 8. C-terminal HA-tagged MFN1 and MFN2	109
Figure 9. CRISPR/Cas9 strategy elements	110
Figure 10. CRISPR/Cas9 strategy to generate MFN1-HA and MFN2-HA cell lines.....	111
Figure 11. Assessment by PCR of HA-integration in MFN1 and MFN2	113

Figure 12. Generation of MFN1-HA and MFN2-HA clones115

Figure 13. Validation of HA-tagging of MFN1 and MFN2.....116

Figure 14. Mitochondrial morphology evaluation in MFN1-HA and MFN2-HA cells119

Figure 15. Assessment of mitochondrial protein levels of MFN1-HA clone 1120

Figure 16. Assessment of mitochondrial protein levels of MFN2-HA clone 12.....121

Figure 17. Assessment of starvation autophagic flux of LC3B-II in WT, MFN1-HA and MFN2-HA cells.....123

Figure 18. Mitochondrial elongation under starvation conditions in WT, MFN1-HA and MFN2-HA cells.....125

Figure 19. HA-IP performed with 1% Triton X-100, Brij99, CHAPS or Digitonin in lysis buffer128

Figure 20. HA-IP performed with agarose beads and magnetic beads129

Figure 21. Assessment of MFN2-HA binding to magnetic beads at different protein concentrations130

Figure 22. Coomassie staining of HA-IP in basal and starvation conditions132

Figure 23. HA-IP of WT, MFN1-HA cells and MFN2-HA cells in basal and starvation conditions133

Figure 24. Proportions of MFN1 or MFN2 that interact with MFN2 or

Content

MFN1 respectively	134
Figure 25. Absolute amount of MFN1 and MFN2 in MFN1-MFN2 complexes in 22.5 mg of total protein	137
Figure 26. Results of mass spectrometry of MFN1-HA and MFN2-HA HA-IP in basal and starvation conditions	138
Figure 27. Venn diagrams comparing the potential binding candidates identified by mass spectrometry after HA-IP of MFN1-HA and MFN2-HA under basal and starvation conditions	144
Figure 28. Venn diagram of all the mass spectrometry results of MFN1-HA and MFN2-HA HA-IP in basal and starvation conditions	145
Figure 29. Mitochondrial proteins found by mass spectrometry analysis of MFN1-HA and MFN2-HA HA-IP in basal and starvation conditions	147
Figure 30. Proteins of membranous compartments of the cell found by mass spectrometry analysis of MFN1-HA and MFN2-HA HA-IP in basal and starvation conditions	148
Figure 31. Protein modifiers found by mass spectrometry analysis of MFN1-HA and MFN2-HA HA-IP in basal and starvation conditions ...	150
Figure 32. Autophagy related candidates found by mass spectrometry analysis of MFN1-HA and MFN2-HA HA-IP in basal and starvation conditions	152
Figure 33. Reactome pathway analysis detects enrichment of RNA metabolism proteins among basal interactors	153

Figure 34. RNA related candidates found by mass spectrometry analysis of MFN1-HA and MFN2-HA HA-IP in basal and starvation conditions155

Figure 35. NDFIP2 interacts with MFN1 and MFN2159

Figure 36. RAB5C interacts with MFN1 and MFN2160

Figure 37. S100A8 and S100A9 interact with MFN2161

Figure 38. RAB5C and S100A8 interact with MFN2 differently in the presence or absence of amino acids163

Figure 39. SLC27A2 interacts with MFN2 under starvation conditions164

Figure 40. MFN2 interacts with overexpressed SLC27A2 under basal and starvation conditions165

Figure 41. AGO2 and FXR1 interact with MFN1 and MFN2167

Figure 42. RAB5C KO cells show decreased MFN1 levels as WT cells .168

Figure 43. RAB5C KO cells have equal MFN1 and MFN2 gene expression as WT cells169

Figure 44. RAB5C KO cells show have more fragmented mitochondria than WT cells170

Figure 45. TOM20 protein levels are decreased in RAB5C KO171

Figure 46. Mitochondrial mass is decreased in RAB5C KO cells172

Figure 47. RAB5C KO cells have less mtDNA nucleoids than WT cells.172

Figure 48. RAB5C KO cells accumulate mtDNA nucleoids upon

Content

baflomycin treatment.....	174
Figure 49. RAB5C KO cells have increased levels of mitophagy genes	175
Figure 50. LC3B and dsDNA co-distribute equally in RAB5C KO and WT cells (I).....	176
Figure 51. LC3B and dsDNA co-distribute equally in RAB5C KO and WT cells (II).....	177
Figure 52. EEA1 and dsDNA co-distribute more in RAB5C KO than in WT cells (I)	178
Figure 53. EEA1 and dsDNA co-distribute more in RAB5C KO than in WT cells (II).....	178
Figure 54. Mitochondria interact with AGO2 containing structures ...	179
Figure 55. Mitochondria interact with G3BP1 containing structures..	180
Figure 56. Silencing of MFN2 and SLC27A2 impairs LC3B-II autophagic flux.....	181
Figure 57. Decreased starvation induced autophagosome formation in MFN2 and SLC27A2 silenced cells (I).....	182
Figure 58. Decreased starvation induced autophagosome formation in MFN2 and SLC27A2 silenced cells (II).....	183
Figure 59. SLC27A2 is degraded with starvation induced autophagy	184
Figure 60. Silencing of SLC27A2 impairs starvation autophagic flux of LC3B-II more than basal autophagic flux	185
Figure 61. Silencing of SLC27A2 impairs basal and starvation autophagic	

fluxes of P62 and GABARAP186

Figure 62. SLC27A2 interacts with proteins involved in the expansion of the phagophore187

Figure 63. Some LC3 puncta and some GABARAP puncta co-localize with SLC27A2-FLAG.....189

Figure 64. Autophagosomal markers' signals correlate with SLC27A2-FLAG signal.....190

Figure 65. Human SLC27A2 contains 14 LIR motifs.....191

Figure 66. SLC27A2 LIR motifs are evolutionarily conserved.....194

Figure 67. Silencing of SLC27A2 results in impaired co-distribution of LC3B and MFN2196

Figure 68. MFN2-HA co-immunoprecipitates with SLC27A2 and ATG2A in basal and starvation conditions197

Figure 69. High confidence MFN2 interactors found in our study and their abundance in the screening performed by Antonicka et al.....207

Figure 70. High confidence interactors found by Antonicka et al. and their abundance in our screening.....208

Figure 71. Interaction network of MFN1 and MFN2 in basal conditions211

Figure 72. Interaction network of MFN1 and MFN2 in starvation conditions211

Figure 73. Proposed mechanisms of MFN1 and MFN2 post-translational modifications.....216

Content

Figure 74. Proposed model for MFN1 and MFN2 anchoring of RNA granules under basal and starvation conditions	221
Figure 75. Proposed model for selective mitochondrial degradation by MDVs in RAB5C KO cells	225
Figure 76. Proposed model for MFN2-SLC27A2 complex in autophagy	232
Figure 77. Proposed novel functions of MFN1 and MFN2.....	234

TABLES

Table 1. High confidence interactors of MFN1 and MFN2 under basal and starvation conditions	139
Table 2. MFN1 binding candidates localized in P-bodies and stress granules.....	156
Table 3. MFN2 binding candidates localized in P-bodies and stress granules.....	157
Table 4. MFN1 and MFN2 known interactors. Binding partners of MFN1 and MFN2 discovered by Co-IP.....	203
Table 5. Details of reagents	243
Table 6. Details of CRISPR/Cas9 and overexpression plasmids	244
Table 7. List of primary antibodies used in this thesis	245
Table 8. List of secondary antibodies used in several assays of this thesis	246
Table 9. Commercially available siRNAs used in this thesis.....	246
Table 10. Primers used in real time quantitative PCR to determine the expression of human genes.....	246
Table 11. Details of primers used in CRISPR/Cas9 strategy	247
Table 12. Sequences of ssODNs used in CRISPR/Cas9 strategy	247
Table 13. RIPA buffer composition	254
Table 14. Lysis and wash buffers used in endogenous HA-IP	258
Table 15. Lysis and wash buffers utilized in FLAG-IP.....	262

ABBREVIATIONS



0. ABBREVIATIONS

A

ACN: Acetonitrile

ACSBG1: Acyl-CoA synthetase bubblegum family member 1

ACSL: Long-chain acyl-CoA synthetase

acyl-CoA: Acyl coenzyme A

AFAP1: Actin filament-associated protein 1

AFAP1L1: Actin filament-associated protein 1-like 1

AGO2: Protein argonaute-2

Ale1: Lysophospholipid acyltransferase

ALPP: Alkaline phosphatase, placental type

ALS: Alsin

AMOTL1: Angiomotin-like protein 1

AMPK: 5'-AMP-activated protein kinase catalytic subunit alpha-2

ARP2/3: Actin related proteins 2 and 3

ASC: Activating signal cointegrator 1 complex subunit 2

ATF4: Cyclic AMP-dependent transcription factor ATF-4

ATF6: Cyclic AMP-dependent transcription factor ATF-6 alpha

ATG: Autophagy-related protein

ATG12: Autophagy-related protein 12

ATG14 : Autophagy-related protein 14

ATG16L1: Autophagy-related protein 16L

ATG2: Autophagy-related protein 2

ATG3: Autophagy-related protein 3

ATG5: Autophagy-related protein 5

ATG7: Autophagy-related protein 7

ATG8: Autophagy-related protein 8

ATG9: Autophagy-related protein 9

ATP: Adenosine triphosphate

AU: Arbitrary units

0 | Abbreviations

Axl2: Axial budding pattern protein 2

B

BAD: Bcl2-associated agonist of cell death

Baf A1: Bafilomycin A1

BAK: Bcl-2 homologous antagonist/killer

BAT: Brown adipose tissue

BAT3: HLA-B-associated transcript 3

BAX: Bcl-2-like protein 4

BCA: Bicinchoninic Acid Assay

BCL2: Apoptosis regulator Bcl-2

BDLP: Bacterial dynamin-like protein

BECN1:Beclin-1

BFDR: Bayesian false discovery rate

BioID: Proximity-dependent biotin identification

BirA: Biotin operon repressor protein

Brij99: 2-[(Z)-octadec-9-enoxy]ethanol

BSA: Bovine serum albumin

BYSL: Bystin

C

Ca⁺²: Calcium

CADH5: Cadherin-5

CALML5: Calmodulin-like protein 5

Cas9: CRISPR-associated endonuclease Cas9

CASP: Caspase-1

CCNB1: G2/mitotic-specific cyclin-B1

CDK1: Cyclin-dependent kinase 1

cDNA: Complementary deoxyribonucleic acid

CGN: Cingulin

CHAPS: 3-((3-cholamidopropyl) dimethylammonio)-1-propanesulfonate

CHMP2A: Charged multivesicular body protein 2a
CHOP: C/EBP-homologous protein
CLUH: Clustered mitochondria protein homolog
CO₂: Carbon dioxide
COP-II: Coat complex protein II
CORO2A: Coronin-2A
CPSF6: Cleavage and polyadenylation specificity factor subunit 6
CRISPR: Clustered regularly interspaced short palindromic repeats
CTNNB1: Catenin beta-1
CUL3: Cullin-3
Cx37: Connexin-37
Cx43: Connexin-43

D

DAPI: 4',6-diamidino-2-phenylindole
DDM: n-Dodecyl-B-D-Maltoside
DDX1: DEAD box protein 1
DDX17: DEAD box protein 17
DDX20: DEAD box protein 20
DHX30: DEAH box protein 30
DHX36: DEAH box protein 36
DHX9: DEAH box protein 9
DMEM: Dulbecco's Modified Eagle Medium
DMSO: Dimethyl sulfoxide
DNA: Deoxyribonucleic acid
DOHH: Deoxyhypusine hydroxylase
DRP1: Dynamin-related protein 1
DSB: Double strand break
DSC1: Desmocollin-1
DTT: Dithiothreitol

0 | Abbreviations

E

E3: E3 ubiquitin ligase

EBSS: Earle's balanced salts solution

ECL: Enhanced chemiluminescence

ECT1: Ethanolamine-phosphate cytidylyltransferase

EDTA: Ethylenediaminetetraacetic acid

EEA1: Early endosome antigen 1

eIF5A: Eukaryotic translation initiation factor 5A-1

ELAVL1: ELAV-like protein 1-A

EMD: Emerin

ER: Endoplasmic reticulum

ERK: Mitogen-activated protein kinase

ER-phagy: Reticulophagy

ESCRT: Endosomal sorting complexes required for transport

F

Faa1: Fatty acid activator 1

Faa4: Fatty acid activator 4

FACS: Fluorescence-activated cell sorting

FAF2: FAS-associated factor 2

FAM120A: Family with sequence similarity 120 member A

FAM98A: Family with sequence similarity 98 member A

Fat1: Very long-chain fatty acid transport protein

FBS: Fetal Bovine Serum

FC: Fold change

FDR: False discovery rate

FIS1: Mitochondrial fission 1 protein

FMR1: Fragile X mental retardation protein 1

FUNDC1: FUN14 domain-containing protein 1

FUS: RNA-binding protein FUS

FW: Forward

FXR1: Fragile X mental retardation syndrome-related protein 1

FXR2: Fragile X mental retardation syndrome-related protein 2

G

G1: Growth 1 phase of cell cycle

G2: Growth 2 phase of cell cycle

G3BP1: GAP SH3 domain-binding protein 1

G3BP2: GAP SH3 domain-binding protein 2

GABARAP: Gamma-aminobutyric acid receptor-associated protein

GABARAPL2: Gamma-aminobutyric acid receptor-associated protein-like 2

GAPDH: Glyceraldehyde-3-phosphate dehydrogenase

GASZ: Germ cell-specific ankyrin, SAM and basic leucine zipper domain-containing protein

GEMIN4: Gem-associated protein 4

GFP: Green fluorescence protein

GP78: Autocrine motility factor receptor

Gpt2: Glycerol-3-phosphate O-acyltransferase 2

gRNA: Guide RNA

GTP: Guanosine-5'-triphosphate

H

HA: Hemagglutinin

HDAC6: Histone deacetylase 6

HDR: Homologous directed repair

HECT: Homologous to the E6-AP carboxyl terminus

HNRNPA3: Heterogeneous nuclear ribonucleoprotein A3

HNRNPF: Heterogeneous nuclear ribonucleoprotein F

HNRNPH1: Heterogeneous nuclear ribonucleoprotein H

HNRNPUL1: Heterogeneous nuclear ribonucleoprotein U-like protein 1

HR: Homologous recombination

HUWE1: HECT, UBA and WWE domain-containing protein 1

0 | Abbreviations

I

IF: Immunofluorescence assay

IGF2BP3: Insulin-like growth factor 2 mRNA-binding protein 3

IL-18: Interleukin-18

IL-1 β : Interleukin-1 β

ILF2: Interleukin enhancer-binding factor 2

IMM: Inner mitochondrial membrane

IMS: Intermembrane space

INF2: Inverted formin-2

IP: Immunoprecipitation

IRE1 α : Serine/threonine-protein kinase/endoribonuclease IRE1

IRF3: Interferon regulatory factor 3

ITCH: E3 ubiquitin-protein ligase Itchy homolog

ITPR2: Inositol 1,4,5-trisphosphate receptor type 2

J

JMY: Junction-mediating and -regulatory protein

JNK: Mitogen-activated protein kinase 8

K

KLHL13: Kelch-like protein 13

KO: Knockout

L

LAMC1: Laminin subunit gamma-1

LARP1 : La-related protein 1

LB: Lysogeny Broth

LC3B: Microtubule-associated proteins 1A/1B light chain 3B

LD: Lipid droplet

LIR: LC3 interacting region

LRRFIP2: Leucine-rich repeat flightless-interacting protein 2

LUC7L2: Putative RNA-binding protein Luc7-like 2

M

M: Mitosis, cell division phase of cell cycle

MAM: Mitochondria-associated membranes

MARCHF5: Membrane-associated RING finger protein 5

MAVS: Mitochondrial antiviral signaling protein

MDVs: Mitochondria-derived vesicles

MEF: Mouse embryonic fibroblasts

MFF: Mitochondrial fission factor

MFN1: Mitofusin-1

MFN2: Mitofusin-2

MGRN1: Mahogunin RING finger protein 1

MID49: Mitochondrial dynamics protein of 49 kDa

MID51: Mitochondrial dynamics protein of 51 kDa

MIRO: Mitochondrial Rho GTPase

MIT: Massachusetts institute of technology

MNS1: Meiosis-specific nuclear structural protein 1

MOV10: Moloney leukemia virus 10 protein

MQ: Max Quant

mRNA: Messenger RNA

MS: Mass spectrometry

MTCH2: Mitochondrial carrier homolog 2

mtDNA: Mitochondrial DNA

mTORC1: Mammalian target of rapamycin complex 1

MUL1: Mitochondrial ubiquitin ligase activator of NFKB 1

MYH14: Myosin-14

MYL6: Myosin light polypeptide 6

MYO1F: Unconventional myosin-If

N

0 | Abbreviations

Na-DOC: Sodium deoxycholate

NCBP1: Nuclear cap-binding protein subunit 1

NDFIP2: NEDD4 family-interacting protein 2

NEDD4: Neural precursor cell expressed developmentally down-regulated protein 4

NEDD4L: HECT-type E3 ubiquitin transferase NED4L

NEK7: Serine/threonine-protein kinase Nek7

NFAT1: Nuclear factor of activated T-cells, cytoplasmic 2

NF- κ B: Nuclear factor NF-kappa-B

NHEJ: Non-homologous end joining

NIR: Near infrared fluorescence

NLRP3: NACHT, LRR and PYD domains-containing protein 3

NME3: Nucleoside diphosphate kinase 3

NONO: Non-POU domain-containing octamer-binding protein

NP-40: Nonyl phenoxyethoxyethanol

NSDHL: Sterol-4-alpha-carboxylate 3-dehydrogenase, decarboxylating

NUFIP2: Nuclear fragile X mental retardation-interacting protein 2

NUMB: Protein numb homolog

O

O₂: Oxygen

OMA1: Overlapping with the m-AAA protease 1 homolog

OMM: Outer mitochondrial membrane

OPA1: Optic atrophy protein 1

OXPPOS: Oxidative phosphorylation

P

P62: Phosphotyrosine-independent ligand for the Lck SH2 domain of 62 kDa

PABPC4: Polyadenylate-binding protein 4

PACS2: Phosphofurin acidic cluster sorting protein 2

PAM: Protospacer adjacent motif

PARK2: E3 ubiquitin-protein ligase parkin

P-body : Processing body
PBS: Phosphate buffered saline
PBST: Phosphate buffered saline with Tween-20
PC: Phosphatidylcholine
PCR: Polymerase chain reaction
PCT1: Choline-phosphate cytidyltransferase
PCYT1A: Choline-phosphate cytidyltransferase A
PD: Proteome Discoverer
PE: Phosphatidylethanolamine
PEI: Polyethylenimine
PERK: PRKR-like endoplasmic reticulum kinase
PFA: Paraformaldehyde
PHB: Prohibitin
PI: Phosphatidylinositol
PI3K: Phosphoinositide 3-kinase
PINK1: PTEN-induced putative kinase protein 1
PIP: Prolactin-inducible peptide
PIS: Phosphatidylinositol synthase
PKC: Protein kinase C
PLIN1: Perilipin-1
PNK: Polynuclotide kinase
POTEF: POTE ankyrin domain family member F
PRKAA1: 5'-AMP-activated protein kinase catalytic subunit alpha-1
PS: Phosphatidylserine
PS2: Presenilin-2
PSPC1: Paraspeckle component 1
PtdIns3P: Phosphatidylinositol-3-phosphate
PUF60: 60 kDa poly(U)-binding-splicing factor
PUM1: Pumilio homolog 1
PURA: Purine-rich single-stranded DNA-binding protein alpha
PVDF: Polyvinylidene fluoride

0 | Abbreviations

R

RAB2A: Ras-related protein Rab-2A

RAB5A: Ras-related protein Rab-5A

RAB5C: Ras-related protein Rab-5C

RAB7: Ras-related protein Rab-7

RABEX5: Rab5 GDP/GTP exchange factor

RAF1: RAF proto-oncogene serine/threonine-protein kinase

RAPH1: Ras-associated and pleckstrin homology domains-containing protein 1

RAS: GTPase Kras

RBM18: Probable RNA-binding protein 18

RHOT2: Mitochondrial Rho GTPase 2

RICTOR: Rapamycin-insensitive companion of mTOR

RIG-I: Antiviral innate immune response receptor RIG-I

RIN1: Ras and Rab interactor 1

RIPA buffer: Radioimmunoprecipitation assay buffer

RNA: Ribonucleic acid

ROS: Reactive oxygen species

RPA1: Replication factor A protein 1

RPL31: 60S ribosomal protein L31

RPS15 : 40S ribosomal protein S15

RPS5: 40S ribosomal protein S5

RSF1: Remodeling and spacing factor 1

RT: Room temperature

RT-PCR: Reverse transcription polymerase chain reaction

RTRAF: RNA transcription, translation and transport factor protein

RV: Reverse

S

S: Synthesis phase of cell cycle

S100A7: S100 calcium-binding protein A7

S100A8: S100 calcium-binding protein A8
S100A9: S100 calcium-binding protein A9
S1P: Sphingosine-1-phosphate
SAINT: Significance Analysis of INteractome
SCCPDH: Saccharopine dehydrogenase-like oxidoreductase
Sct1: Glycerol-3-phosphate O-acyltransferase 1
SDS: Sodium dodecyl sulfate
SDS-PAGE: Sodium dodecyl sulfate polyacrylamide gel electrophoresis
sec12: Guanine nucleotide-exchange factor SEC12
sec16: Guanine nucleotide-exchange factor SEC16
sec23: Guanine nucleotide-exchange factor SEC23
sec24: Guanine nucleotide-exchange factor SEC24
SFPQ: Splicing factor, proline- and glutamine-rich
SIPA1L1: Signal-induced proliferation-associated 1-like protein 1
siRNA: Small interference RNA
SIRT1: Sirtuin-1
SLC25A10: Solute carrier family 25 member 10
SLC25A24: Solute carrier family 25 member 24
SLC25A38: Solute carrier family 25 member 38
SLC27A2: Very long-chain acyl-CoA synthetase
SMAD2: Mothers against decapentaplegic homolog 2
SMURF2: E3 ubiquitin-protein ligase SMURF2
SN: Supernatant
SNX33: Sorting nexin-33
SRRT: Serrate RNA effector molecule homolog
ssODN: Single stranded oligodeoxynucleotide
STOML2: Stomatin-like protein 2, mitochondrial

T

TBP: TATA box-binding protein-like 1
TCHP: Trichoplein keratin filament-binding protein

0 | Abbreviations

TDP-43: TAR DNA-binding protein 43

TFCP2 : Alpha-globin transcription factor CP2

TIP60: Histone acetyltransferase KAT5

TM: Transmembrane

TMEM9: Proton-transporting V-type ATPase complex assembly regulator
TMEM9

TNF α : Tumor necrosis factor

TOM20: Mitochondrial 20 kDa outer membrane protein

TOM40: Mitochondrial 40 kDa outer membrane protein

U

UBA5: Ubiquitin-like modifier-activating enzyme 5

UBP1: Upstream-binding protein 1

ULK1: Unc-51-like kinase 1

UPF1: Up-frameshift suppressor 1 homolog

UPR: Unfolded protein response

USP10: Ubiquitin carboxyl-terminal hydrolase 10

USP30: Ubiquitin carboxyl-terminal hydrolase 30

UTR: Untranslated region

V

VAT1: Synaptic vesicle membrane protein VAT-1 homolog

VCP: Valosin-containing protein

VDAC1: Voltage-dependent anion-selective channel protein 1

VPS4: Vacuolar protein sorting-associated protein 4

W

WB: Western blot

WIPI: WD repeat domain phosphoinositide-interacting protein

WIPI2b: WD repeat domain phosphoinositide-interacting protein 2b

WT: Wild type

WWP1: WW domain-containing protein 1

WWP2: WW domain-containing protein 2

Y

YME1L: YME1-like protein 1

Z

ZNF185: Zinc finger protein 185

SUMMARY



1. SUMMARY

1.1. Abstract

Mitofusins (MFN1/2) have been demonstrated to play a role in several mitochondrial functions such as mitochondrial dynamics and bioenergetics, interorganelle communication, immune response, autophagy, cell cycle progression, cellular senescence and apoptosis. However, the role of MFN1/2 in the molecular mechanisms underlying these processes remains poorly understood. Here, we have studied MFN1/2 functions and regulation from an interactome perspective in order to gain insight into the accurate mechanisms by which they are involved in those cellular events. To this end, we have generated two HeLa cell lines expressing an HA-tag fused to the C-terminal domain of MFN1 and MFN2 applying CRISPR/Cas9 technology. This has facilitated MFN1/2 pulldown under endogenous expression levels in basal conditions and in conditions of nutrient deprivation. The fact that MFN1/2 expression levels remain endogenous is key since most of their binding partners known so far have been studied under overexpression conditions. Subsequently, we have performed mass spectrometry to identify interactors of MFN1 and MFN2 in basal or starvation conditions. We have observed that RNA-binding proteins are enriched in basal conditions among MFN1 and MFN2 binding candidates and that they are absent in starvation conditions. We have validated that FXR1, AGO2, RAB5C and NDFIP2 interact with MFN1 and MFN2, and that S100A8, S100A9 and SLC27A2 interact with MFN2. We have found that RAB5C

is necessary for mitochondrial morphology maintenance. Our data have also shown that SLC27A2 is a protein important for the process of autophagy.

1.2. Introduction

Mitochondria are dynamic organelles that constantly undergo processes of fusion and division. The adaptive changes in morphology are known as mitochondrial dynamics and are crucial for their function ¹. The main players in mitochondrial dynamics belong to the dynamin superfamily and they can promote either organelle membrane fusion or membrane fission ². Mitochondrial division is carried out mainly by DRP1 ³ that is recruited to the outer mitochondrial membrane. Mitochondrial fusion is performed by the outer mitochondrial membrane proteins MFN1 ⁴⁻⁶ and MFN2 ^{4,6,7} and the inner mitochondrial membrane protein OPA1 ⁸⁻¹⁰. Mitochondria are able to establish physical interactions with other membranous components of the cell and some of these contacts are mediated by MFN1 or MFN2 ^{11,12}. MFN1 mediates mitochondrial contacts with ER and the plasma membrane. MFN2 has been shown to participate in the apposition of mitochondria to ER, lysosomes, lipid droplets and melanosomes. Although classically known for their role in mitochondrial fusion, MFN1 and MFN2 are also implicated in many other cellular processes such as mitochondrial bioenergetics, immune response, autophagy, cell cycle progression, cellular senescence and apoptosis ¹³.

Nutrient availability has an impact on the functions of MFN1 and MFN2.

Upon nutrient starvation, MFN1 promotes mitochondrial hyperfusion presumably to protect healthy mitochondria from starvation induced autophagy ¹⁴. In contrast, under nutrient deprivation, MFN2 has been proposed to be implicated in autophagy. The lack of MFN2 in conditions of starvation results in an impairment of autophagosome formation at ER-mitochondria contact sites ¹⁵⁻¹⁸. Given the fact that MFN2 localizes at ER-mitochondria contact sites ¹⁹, it is likely that MFN2 is involved in the recruitment of early autophagy proteins to these sites.

1.3. Objectives and approach

The goal of this study has been to identify MFN1 and MFN2 novel binding partners in order to shed light into MFN1 and MFN2 functioning and regulation. Moreover, it is of our particular interest the identification of those interactors that participate in mitochondrial contacts with other organelles and those partners that could regulate the participation of MFN1 in starvation induced mitochondrial hyperfusion and the ones that could explain the implication of MFN2 in starvation induced autophagosome formation. To achieve these aims, we first used CRISPR/Cas9 technology to generate two HeLa cell lines expressing an HA-tag fused to the C-terminal domain of MFN1 and MFN2. We immunoprecipitated MFN1-HA and MFN2-HA from these cell lines using beads coupled to anti-HA antibodies in basal conditions and in starvation. Mass spectrometry was performed to unravel novel MFN1 and MFN2 binding candidates. We have validated some of these candidates and performed functional studies.

1.4. Results

1.4.1. Generation of CRISPR-Cas9 MFN1-HA and MFN2-HA cell lines

We used CRISPR/Cas9 technology to generate two HeLa cell lines expressing MFN1 and MFN2 fused to an HA-tag at the C-terminal (Figure S-1A). These cell lines preserve endogenous levels of expression of MFN1 and MFN2.

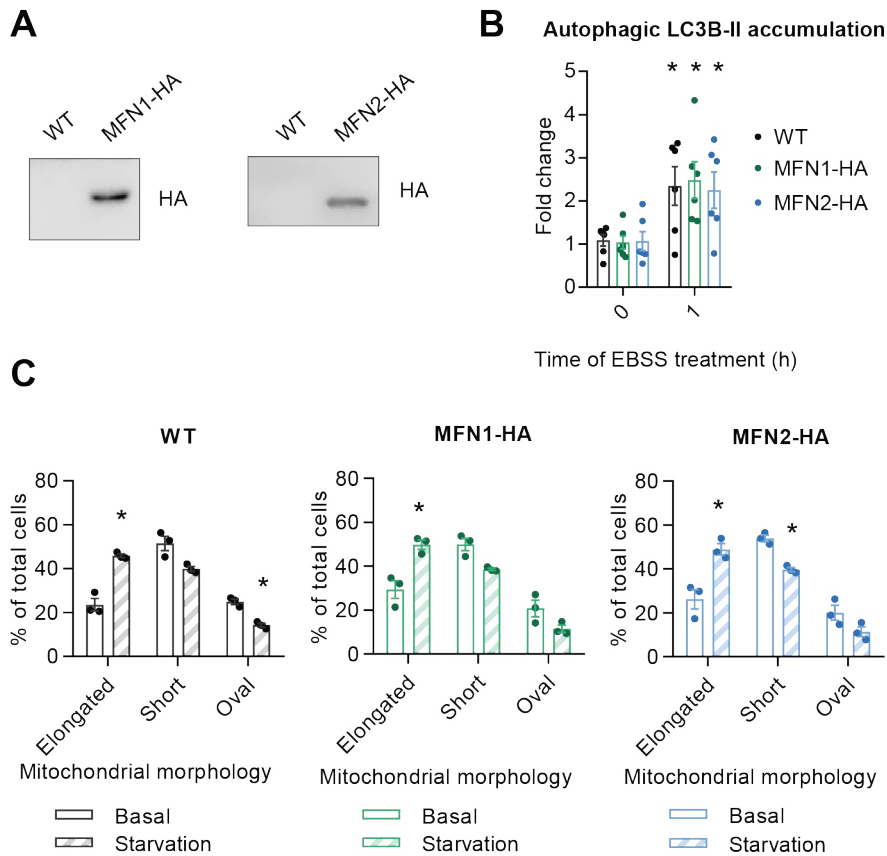


Figure S-1. CRISPR/Cas9 edited MFN1-HA and MFN2-HA HeLa cell lines.

(A) HA immunoblots of MFN1-HA and MFN2-HA HeLa cell lines. (B) Starvation

induced LC3 fold change in WT, MFN1-HA and MFN2-HA HeLa cells. * = p-value < 0.05. (C) Mitochondrial morphology in WT, MFN1-HA and MFN2-HA HeLa cells in basal and starvation conditions. * = p-value < 0.05.

We validated the suitability of these cell lines for our experiments by assessing mitochondrial morphology (Figure S-1C), and induction of autophagy (Figure S-1B) and mitochondrial hyperfusion after EBSS treatment (Figure S-1C).

1.4.2. Optimization of MFN1-HA and MFN2-HA immunoprecipitation

We improved several steps of the HA-immunoprecipitation (IP) protocol in order to preserve as many interactors as possible during the whole purification process until mass spectrometry was applied. After testing several detergents, we observed 1% digitonin works best to preserve the interaction between MFN1 and MFN2. Thus, we selected 1% digitonin to lyse the cells. Magnetic beads were chosen over agarose beads because a lower non-specific background was obtained with those. The quantity of protein per volume of beads was adjusted to minimize non-specific binding. We used 25 mg of protein in the lysate per 40 μ l of beads.

1.4.3. Identification of MFN1 and MFN2 binding partners by mass spectrometry

We performed three biological replicates of HA-IP of MFN1-HA cells and MFN2-HA cells in basal conditions and after 1 hour of nutrient deprivation. We identified the proteins recovered in these IPs by mass spectrometry and compared the results of all the biological replicates.

Under basal conditions we have obtained 44 potential binding partners for MFN1 and 51 for MFN2. In conditions of 1h of starvation we have identified 6 possible interaction partners for MFN1 and 16 for MFN2. Already known partners of MFN1 and MFN2 were identified: MFN2⁶ was detected between the candidates of MFN1, and MFN1⁶, MARCHF5²⁰ and RHOT2²¹ appeared between the potential partners of MFN2. Besides, we found several proteins that localize to other membranous components of the cell, proteins that modify other proteins and autophagy related proteins. At least one candidate from each of these groups was selected to be validated. Interestingly, an enrichment in RNA-binding proteins was observed under basal conditions and not under starvation conditions.

1.4.4. Validation of novel interaction partners of MFN1 and MFN2

Among the identified potential partners we found proteins from several membranous components of the cell: ER, endosomes, Golgi apparatus, lysosomes and the plasma membrane. These possible interactors could be involved in the contacts of mitochondria with other organelles. From these proteins, we focused on RAB5C, which was present among MFN1 possible interactors in basal conditions. RAB5C localizes in the membrane of early endosomes. RAB5C-FLAG was overexpressed and co-IP revealed that it interacts with MFN1 and MFN2 (Figure S-2A).

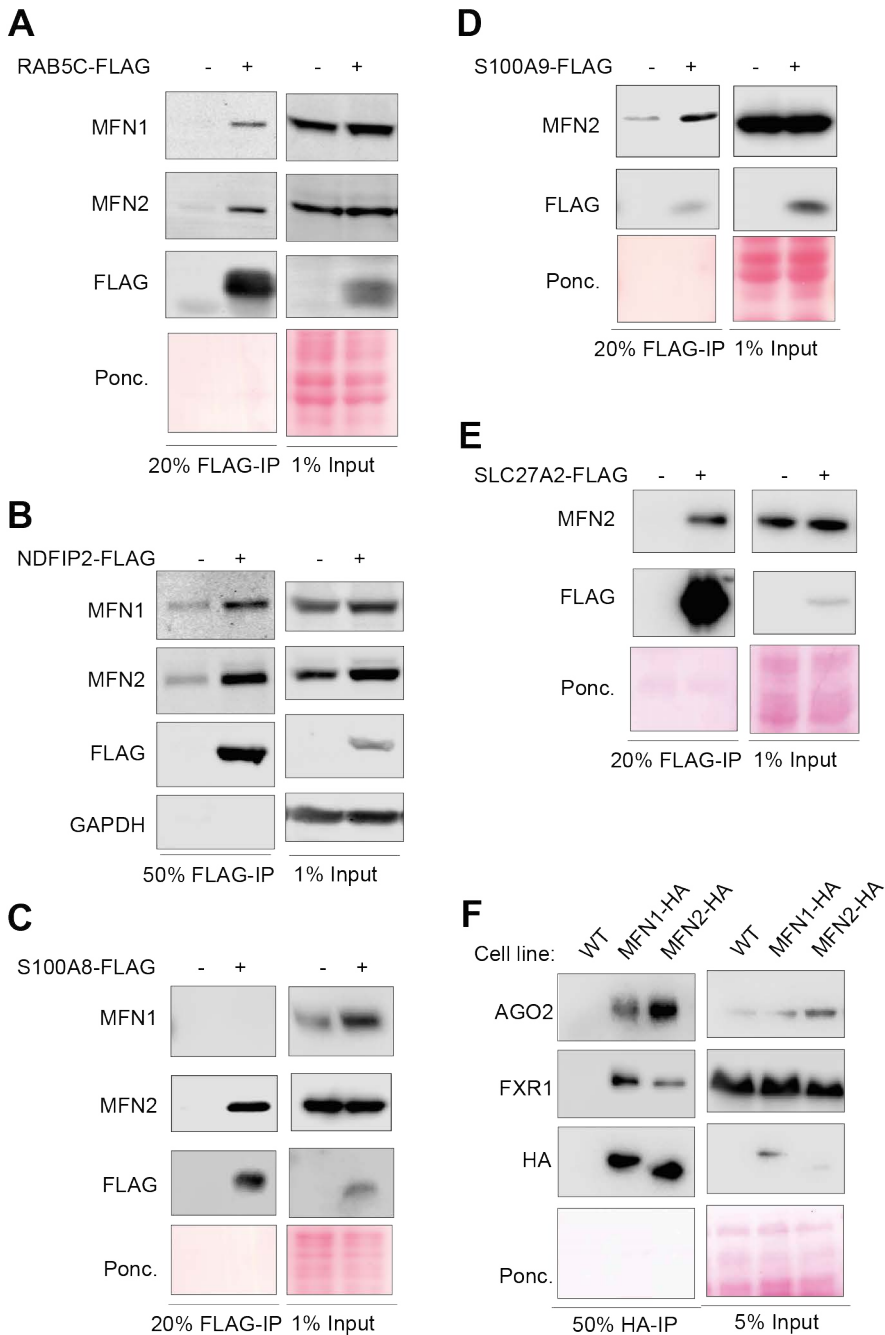


Figure S-2. Validated interactors of MFN1 and MFN2. (A) MFN1, MFN2 and FLAG immunoblots of input and IP fractions of FLAG-IP of RAB5C-FLAG. RAB5C-FLAG was overexpressed in WT HeLa cells. (B) MFN1, MFN2, FLAG

1 | Summary

and GAPDH immunoblots of input and IP fractions of FLAG-IP of NDFIP2-FLAG. NDFIP2-FLAG was overexpressed in WT HeLa cells. (C) MFN1, MFN2 and FLAG immunoblots of input and IP fractions of FLAG-IP of S100A8-FLAG. S100A8-FLAG was overexpressed in WT HeLa cells. (D) MFN1, MFN2 and FLAG immunoblots of input and IP fractions of FLAG-IP of S100A9-FLAG. S100A9-FLAG was overexpressed in WT HeLa cells. (E) MFN2 and FLAG immunoblots of input and IP fractions of FLAG-IP of SLC27A2-FLAG. SLC27A2-FLAG was overexpressed in WT HeLa cells. (F) AGO2, FXR1 and HA immunoblots of input and IP fractions of endogenous HA-IP of MFN1-HA and MFN2-HA.

Mass spectrometry data also revealed several proteins involved in protein posttranslational modifications as potential partners of MFN1 and MFN2. These proteins were involved in protein phosphorylation, ubiquitination, methylation and hypusination. NDFIP2 was selected to validate because it partially localizes to the mitochondria²² and activates E3 ubiquitin ligases²³. Mass spectrometry data showed significant enrichment of NDFIP2 among MFN1 potential binding partners under basal conditions. NDFIP2 was also detected among MFN2 possible interactors in basal conditions, but not in a significant manner. We overexpressed NDFIP2-FLAG and observed that it interacts with MFN1 and MFN2 (Figure S-2B).

Autophagy related proteins were identified in basal and starvation conditions potentially interacting with MFN1 and MFN2. Since we were interested in characterizing the partners that implicate MFN2 in starvation induced autophagy, we drew our attention to the autophagy proteins found in these conditions. Thus, we chose to validate S100A8 and S100A9. These two proteins were significant potential partners of MFN2 in starvation conditions and were not enriched in any case for

MFN1 or for MFN2 under basal conditions. S100A8 and S100A9 have been identified as autophagy inducers ²⁴, moreover S100A8 alone has also been reported to activate autophagy ²⁵. S100A8-FLAG was overexpressed and after co-IP we observed that it interacts with MFN2 and not with MFN1 (Figure S-2C). S100A9-FLAG was overexpressed and FLAG-IP was performed. We observed that S100A9 interacts with MFN2 (Figure S-2D). Another protein that could be implicated in autophagy and is identified among MFN2 binding candidates in starvation conditions is SLC27A2. This protein is the mammalian homologue of the yeast fatty acid transporter Faa1 that has been recently reported to participate in the expansion of the phagophore ²⁶. SLC27A2-FLAG was overexpressed and immunoprecipitated with FLAG-beads. We found that SLC27A2 interacts with MFN2 (Figure S-2E).

Reactome pathway analysis of the proteins identified by mass spectrometry revealed an unexpected enrichment in proteins implicated in the metabolism of RNA under basal conditions that was absent under starvation conditions. AGO2 and FXR1 were picked for validation by co-IP. We performed endogenous IP of MFN1-HA and MFN2-HA and found that AGO2 and FXR1 interact with both MFN1 and MFN2 (Figure S-2F).

1.4.5. Mitochondrial consequences of *RAB5C* absence

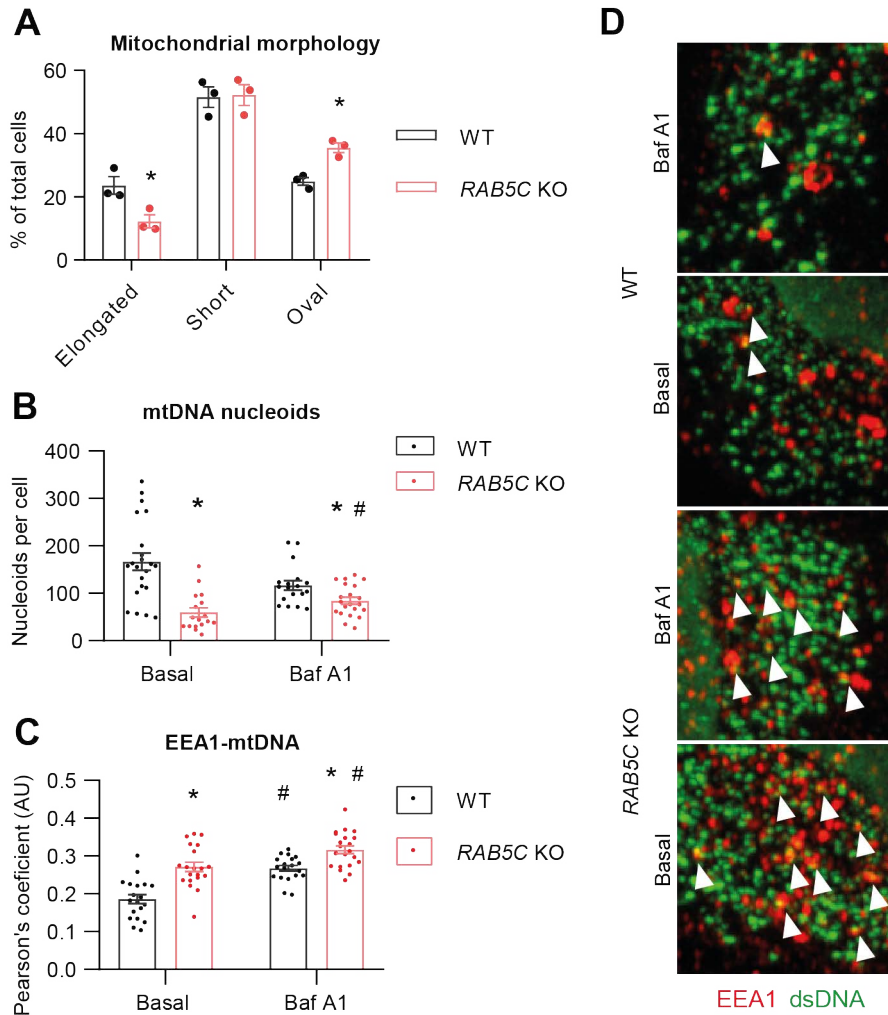


Figure S-3. Mitochondrial consequences of *RAB5C* ablation. (A) Quantification of mitochondrial morphology in *RAB5C* KO cells. * = p value < 0.05. (B) Quantification of mtDNA nucleoids in basal conditions and after 1h of bafilomycin 200 nM treatment. * = *RAB5C* KO vs WT p value < 0.05. # = Basal vs Baf A1 p value < 0.05. (C) Quantification of EEA1 dsDNA co-distribution. * = *RAB5C* KO vs WT p value < 0.05. # = Basal vs Baf A1 p value < 0.05. (D) Representative images of WT and *RAB5C* KO cells stained with antibodies

against EEA1 and dsDNA in basal conditions and treated with bafilomycin 200 nM for 1 hour. Arrows indicate dsDNA and EEA1 colocalization.

After validating RAB5C interaction with MFN1 and MFN2, we generated a CRISPR/Cas9 *RAB5C* KO HeLa cell line. We assessed mitochondrial morphology and observed increased fragmentation of the mitochondrial network in *RAB5C* KO cells (Figure S-3A). Moreover MFN1 and TOM20 protein levels, mitochondrial mass, and mtDNA nucleoids were decreased in KO cells. These results suggested that mitochondrial degradation in *RAB5C* KO cells could be more active. *PINK1* and *PARK2* gene expression and PINK1 protein expression were upregulated in *RAB5C* KO cells. Bafilomycin treatment promoted mtDNA accumulation in KO cells (Figure S-3B), which confirmed increased mitochondrial degradation in *RAB5C* KO cells. LC3-mtDNA co-localization was the same in WT and *RAB5C* KO cells under basal conditions and after bafilomycin treatment. However, mtDNA co-distribution with endosomes was increased in *RAB5C* KO cells both in basal conditions and after bafilomycin treatment (Figure S-3C and D). This result could indicate that mitochondria are degraded in endosomal compartments in upon *RAB5C* ablation.

1.4.6. RNA binding proteins and mitochondria

It is known that AGO2, FXR1 and many other proteins that we identified among the potential interactors are core components of RNA-related structures^{27,28}. AGO2 participates in P-bodies and FXR1 appears in stress granules. After validating that AGO2 and FXR1 interact with MFN1 and MFN2, we wanted to assess if RNA-related structures to which they belong establish contacts with mitochondria. We overexpressed the

P-body protein AGO2 and the stress granule and CLUH-granule protein G3BP1 fused to GFP. We overexpressed G3BP1 since we had also found it in our mass spectrometry data. We analyzed by confocal microscopy the juxtaposition of these structures and mitochondria. Both, AGO2-GFP positive structures and G3BP1-GFP positive structures were found in close proximity with the mitochondrial network (Figure S-4).

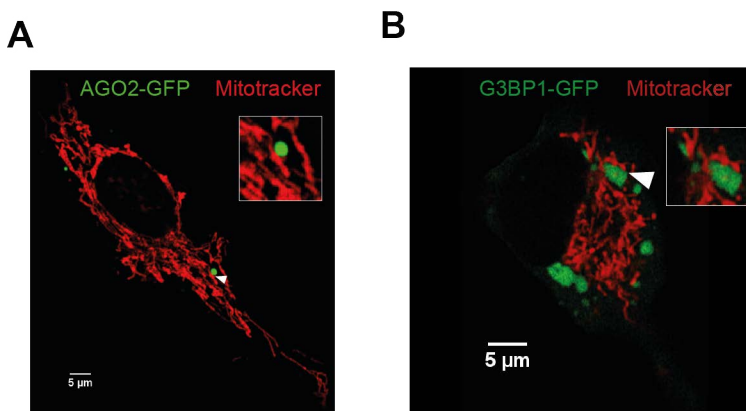


Figure S-4. Contacts between mitochondria and RNA-related structures.

(A) Representative image of a WT cell overexpressing AGO2-GFP stained with Mitotracker Deepred 100nM for 30 min. Scale bar = 5 µm. (B) Representative image of a WT cell overexpressing G3BP1-GFP stained with Mitotracker Deepred 100nM for 30 min. Scale bar = 5 µm.

1.4.7. *SLC27A2* implications in autophagy

Subsequent to the validation of the interaction of MFN2 with SLC27A2, we wanted to know if SLC27A2 was implicated in the process of autophagy and, if so, how it could involve MFN2 in this process.

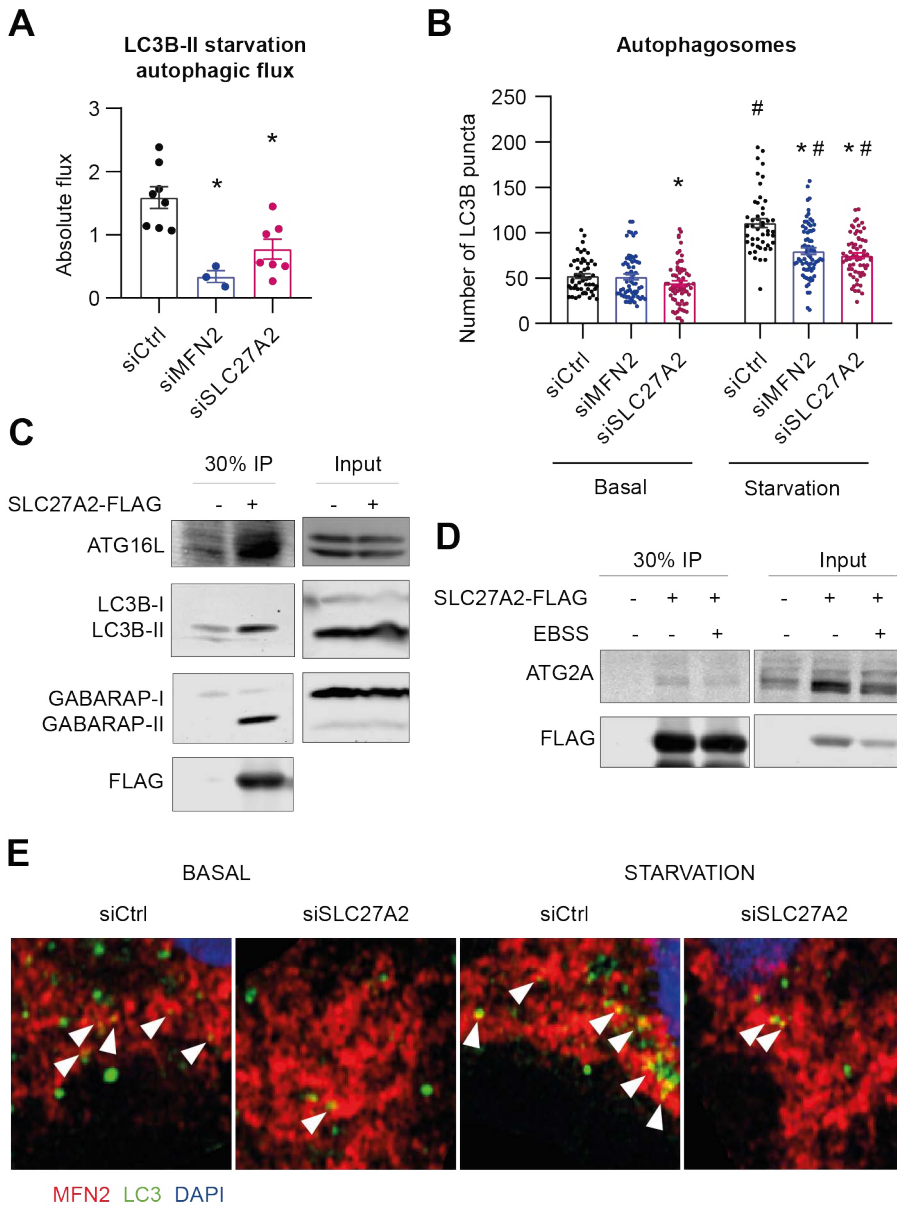


Figure S-5. SLC27A2 implications in autophagy. (A) One hour LC3B-II starvation autophagic flux in cells treated with siRNAs against *MFN2* and *SLC27A2*. * = p value < 0.05 (B) Number of autophagosomal structures after 1 hour of starvation treatment with EBSS in cells treated with siRNAs against *MFN2* and *SLC27A2*. * = p value < 0.05. (C) ATG16L, LC3B, GABARAP and FLAG

1 | Summary

immunoblots of input and IP fractions of FLAG-IP of SLC27A2-FLAG. (D) ATG2A and FLAG immunoblots of input and IP fractions of FLAG-IP of SLC27A2-FLAG in cells that were subjected or not to 1 hour of starvation treatment with EBSS. (E) Representative images of *SLC27A2* silenced and control cells in basal conditions or after 1 hour of starvation treatment with EBSS. Cells stained with antibodies against MFN2 and LC3B and treated with DAPI. Arrows indicate MFN2 and LC3B colocalization.

It has been previously shown and we have validated in our model that, upon 1h of nutrient deprivation, HeLa cells deficient in MFN2 show reduced LC3B-II autophagic flux and decreased autophagosome formation (Figure S-5A S-5B). We transiently silenced *SLC27A2* in HeLa cells and assessed the autophagic flux of autophagosome markers. We observed that LC3B-II flux under starvation conditions was decreased in the silenced cells (Figure S-5A). Moreover, p62 and GABARAP autophagic fluxes under starvation conditions were completely abrogated after *SLC27A2* silencing. In the control cells we observed that SLC27A2 accumulates when cells are starved and treated with bafilomycin. Subsequently, autophagosome formation upon nutrient deprivation in *SLC27A2* silenced cells was assessed by confocal microscopy. We observed less LC3B puncta in silenced cells than in control cells both in basal and in starvation conditions (Figure S-5B).

Given these observations and taking into account the role of Faa1 in phagophore expansion, we wondered whether SLC27A2 could also be involved in autophagosome formation. Thus, we overexpressed SLC27A2-FLAG and performed FLAG-IP in order to know if SLC27A2 interacts with proteins related to this process. Co-immunoprecipitation

revealed that SLC27A2 interacts with ATG2A, ATG16L, LC3B-II and GABARAP (Figure S-5C and S-5D), which are proteins that contribute to the expansion of the phagophore. ATG2A incorporates phospholipids into the phagophore and ATG16L participates in the activation of ATG8 proteins. LC3 and GABARAP belong to the ATG8 family of proteins and cover the autophagosome membrane when activated. Moreover we noticed the presence of LC3 interacting regions in SLC27A2, although we did not functionally characterize them. Since we found that SLC27A2 is an interactor of MFN2, we wanted to know if MFN2 could also interact with phagophore expansion proteins. Thus, we immunoprecipitated endogenous MFN2-HA and observed that ATG2A co-immunoprecipitated with MFN2-HA.

Next, confocal microscopy was used to determine whether there was a considerable co-localization of LC3B and GABARAP with SLC27A2. We found a positive correlation between SLC27A2 signal and autophagosomal markers signals in basal and starvation conditions.

Eventually, we investigated whether the deficiency of SLC27A2 could affect the targeting of MFN2 by autophagosomes. Thus we analyzed the co-distribution of MFN2 and LC3B puncta in basal and starvation conditions and found that there was less co-distribution when cells lacked SLC27A2 (Figure S-5E).

1.5. Discussion

1.5.1. CRISPR/Cas9 edited cellular models preserve mitochondrial and autophagic features of WT cells

We edited HeLa cells with CRISPR/Cas9 technology to generate MFN1 and MFN2 HA-tagged cell lines with endogenous expression levels of MFN1 and MFN2. Since MFN1 and MFN2 overexpression results in apoptosis induction, it is important that expression levels remain endogenous. Therefore, this approach was chosen instead of overexpression.

1.5.2. MFN1 and MFN2 show decreased interaction candidates upon starvation and RNA-binding protein enrichment in basal conditions

After performing mass spectrometry of MFN1-HA and MFN2-HA HA-IP, we identified proteins from other membranous compartments of the cell such as the ER, endosomes, Golgi apparatus, lysosomes and the plasma membrane. We validated the interaction of the endosomal protein RAB5C with MFN1 and MFN2. This interaction could be important for maintaining the tethering of endosomes to mitochondria. Moreover, proteins involved in modification of other proteins that could shed light into MFN1 and MFN2 regulation were found. NDFIP2 interaction with MFN1 and MFN2 was validated. This interaction could be responsible of the regulation by ubiquitination of MFN1 and MFN2. Proteins that have been implicated in autophagy were detected as well. We demonstrated that the autophagy related proteins S100A8 and S100A9 interact with MFN2. We also showed that SLC27A2 interacts with MFN2.

More proteins were identified by mass spectrometry under basal conditions than under starvation conditions. This observation could be a consequence of a more specialized function of MFN1 and MFN2 in conditions of nutrient deprivation. MFN1 would be more actively participating in mitochondrial elongation and MFN2 would exert its role predominantly in autophagy.

RNA-binding proteins were identified more enriched upon basal conditions and absent in starvation conditions both for MFN1 and MFN2. A previous study has shown that RNA-binding proteins that belong in the nuage in mouse sperm cells interact with MFN2 ²⁹. Some of the RNA-binding proteins that we have identified appear in membraneless structures composed of RNA and proteins such as P-bodies ²⁸, stress granules ²⁷ and CLUH granules ³⁰. P-bodies have already been shown to appear in close proximity to mitochondria ³¹. We demonstrated that MFN1 and MFN2 interact with the RNA-binding proteins FXR1 and AGO2, which probably mediate the contacts of mitochondria with RNA related membraneless organelles.

1.5.3. RAB5C is necessary for mitochondrial morphology maintenance and its ablation results in increased mitochondrial degradation

RAB5C KO cells have a more fragmented mitochondrial network. The absence of *RAB5C* also results in increased mitochondrial degradation that does not happen through autophagosomes. Increased co-distribution of endosomes and mitochondria is observed in *RAB5C* deficient cells. This suggests that an endosomal pathway is probably in charge of

clearing these mitochondria. Given the fact that RAB5C interacts with MFN1 and MFN2, it is likely that this interaction happens at contacts between mitochondria and endosomes. Those contacts could be crucial for mitochondrial homeostasis maintenance.

1.5.4. RNA-binding proteins interact with mitochondria

We found that AGO2-GFP positive structures, probably P-bodies, and G3BP1-GFP positive structures, likely stress granules or CLUH-granules, establish physical contacts with mitochondria. Taking into account the interaction of MFN1 and MFN2 with AGO2 and FXR1 that we have shown, we hypothesize that these interactions happen at the interface between mitochondria and these structures. Moreover, P-bodies, stress granules and CLUH granules play a role in the regulation of mRNA translation^{30,32,33}. We propose that the interactions between mitochondria and these structures through MFN1 and MFN2 could serve to regulate the translation of mitochondrial proteins, as previously shown by Pla-Martín et al.³⁰. On the other hand it could be that mitochondria also regulate the function of these organelles as it has been previously shown by Huang et al.³¹.

1.5.5. SLC27A2 interacts with proteins involved in phagophore expansion and its deficiency impairs autophagy

SLC27A2 silencing impairs autophagic flux and autophagosome formation. Besides interacting with MFN2, *SLC27A2* interacts with proteins involved in the expansion of the phagophore such as ATG2A, LC3B, GABARAP and ATG16L and some LC3 and GABARAP puncta

co-localize with SLC27A2. These findings are in line with previous observations in yeast that implicate SLC27A2 yeast homologue, Faa1, in the elongation of the phagophore by participating in the synthesis de novo of phospholipids to be included in the autophagosome membrane²⁶. Thus, SLC27A2 could be supplying fatty acids to the elongation of the phagophore. MFN2 interacts with ATG2A and we believe that it could belong to the same complex with ATG2A and SLC27A2. We observe these interactions both under basal and starvation conditions, meaning that under conditions of starvation there must be a stimuli that favors the cooperation of these proteins with the autophagosome formation machinery. Importantly, the absence of SLC27A2 uncouples autophagosomes from MFN2. Previously published studies have shown that the absence of MFN2 results in impaired autophagosome formation at ER-mitochondria contact sites^{16,17}. Thus, we propose that ER-mitochondria tethering complexes of MFN2 associated with SLC27A2 and ATG2A serve as a platform to recruit other proteins involved in the expansion of the phagophore such as GABARAP or LC3 upon induction of autophagy. Nevertheless, more experiments need to be performed to confirm this hypothesis.

1.6. Conclusions

1. MFN1 and MFN2 present different interaction networks depending on nutrient availability of the cell.
2. MFN1 and MFN2 interact with RNA-binding proteins.
3. RAB5C interacts with MFN1 and MFN2 and it is crucial to maintain mitochondrial morphology.

1 | Summary

4. SLC27A2 interacts with MFN2 and it is necessary for the correct functioning of autophagy.

1. ABBREVIATIONS

A

ACN: Acetonitrile

ACSBG1: Acyl-CoA synthetase bubblegum family member 1

ACSL: Long-chain acyl-CoA synthetase

acyl-CoA: Acyl coenzyme A

AFAP1: Actin filament-associated protein 1

AFAP1L1: Actin filament-associated protein 1-like 1

AGO2: Protein argonaute-2

Ale1: Lysophospholipid acyltransferase

ALPP: Alkaline phosphatase, placental type

ALS: Alsin

AMOTL1: Angiomotin-like protein 1

AMPK: 5'-AMP-activated protein kinase catalytic subunit alpha-2

ARP2/3: Actin related proteins 2 and 3

ASC: Activating signal cointegrator 1 complex subunit 2

ATF4: Cyclic AMP-dependent transcription factor ATF-4

ATF6: Cyclic AMP-dependent transcription factor ATF-6 alpha

ATG: Autophagy-related protein

ATG12: Autophagy-related protein 12

ATG14 : Autophagy-related protein 14

ATG16L1: Autophagy-related protein 16L

ATG2: Autophagy-related protein 2

ATG3: Autophagy-related protein 3

ATG5: Autophagy-related protein 5

ATG7: Autophagy-related protein 7

ATG8: Autophagy-related protein 8

ATG9: Autophagy-related protein 9

ATP: Adenosine triphosphate

AU: Arbitrary units

Axl2: Axial budding pattern protein 2

B

BAD: Bcl2-associated agonist of cell death

Baf A1: Bafilomycin A1

BAK: Bcl-2 homologous antagonist/killer

BAT: Brown adipose tissue

BAT3: HLA-B-associated transcript 3

BAX: Bcl-2-like protein 4

BCA: Bicinchoninic Acid Assay

BCL2: Apoptosis regulator Bcl-2

BDLP: Bacterial dynamin-like protein

BECN1:Beclin-1

BFDR: Bayesian false discovery rate

BioID: Proximity-dependent biotin identification

BirA: Biotin operon repressor protein

Brij99: 2-[(Z)-octadec-9-enoxy]ethanol

BSA: Bovine serum albumin

BYSL: Bystin

C

Ca²⁺: Calcium

CADH5: Cadherin-5

CALML5: Calmodulin-like protein 5

Cas9: CRISPR-associated endonuclease Cas9

CASP: Caspase-1

CCNB1: G2/mitotic-specific cyclin-B1

CDK1: Cyclin-dependent kinase 1

2. INTRODUCTION

2.1. Mitochondria

Mitochondria appeared two billion years ago as the result of the engulfment of an α -proteobacterium by another prokaryotic cell³⁴. This bacterium remained functional inside the host cell with several peculiar features: being surrounded by two lipid bilayers, harboring its own genome, and synthesizing proteins with its own ribosomes.

In 1857, Albert Kölliker noticed mitochondria for the first time. He observed that human striated muscle cells contained granules³⁵. Later on, in 1888 he isolated these granules from insect muscle cells and demonstrated that they were surrounded by a membrane³⁶. In 1898 the term “mitochondria” was used for the first time by Carl Brenda in his publication about animal spermatogenesis³⁷. In the mid-twentieth century more key features of mitochondrial biology were discovered. Albert Claude found that cytochrome oxidase and other enzymes responsible for the respiratory chain were isolated inside the mitochondria³⁸. Eugene Kennedy and Albert Lehninger identified mitochondria as the site of oxidative phosphorylation in eukaryotes³⁹. Margit and Sylvan Nass discovered mitochondrial DNA⁴⁰. In 1967, Lynn Margulis proposed the endosymbiotic hypothesis on the origin of mitochondria⁴¹. This theory suggested a prokaryotic origin for mitochondria, given the common features that had been observed between bacteria and mitochondria such as protein synthesis, mitochondrial DNA and aerobic metabolism.

Mitochondria are composed of two lipid bilayers (outer and inner membranes) that delimit the area of the intermembrane space, and a matrix, the central region surrounded by the inner membrane. The outer mitochondrial membrane (OMM) surrounds the whole mitochondrion. It has a protein-to-phospholipid ratio similar to that of the plasma membrane. Many of the integral membrane proteins inserted in this membrane are porins, which form aqueous channels through the lipid bilayer. The OMM is permeable for molecules that are 5000 Daltons or less such as metabolites, ions or small proteins. The outer membrane also contains enzymes, for instance those in charge of mitochondrial lipid synthesis, and proteins involved in membrane dynamics. Disruption of the outer membrane permits proteins in the intermembrane space to leak into the cytosol, leading to cell death. The mitochondrial outer membrane can associate with other membranous compartments of the cell.

The area between the outer membrane and the inner membrane is the intermembrane space. Given the permeability of the OMM to small molecules, such as ions and sugars, the concentrations of these in the intermembrane space are the same as in the cytosol. However, large proteins must have a specific signaling sequence to be transported across the outer membrane. Hence, the protein composition of this space is different from the protein composition of the cytosol. Enzymes that use ATP transported from the matrix to phosphorylate other nucleotides are present in the IMS.

The inner mitochondrial membrane (IMM) surrounds the central part of

the mitochondria, the matrix. It contains a high proportion of cardiolipin, which is responsible of its low permeability. Molecules that enter and leave the mitochondrial matrix need specific transport proteins in the IMM. This membrane has a very high protein-to-phospholipid ratio. The proteins located in this membrane are: proteins related to oxidative phosphorylation, metabolite and protein transporters, mitochondrial dynamics proteins and ATP synthases.

The IMM contains several infoldings called cristae, which expand the surface area of the inner mitochondrial membrane. This expansion of the IMM surface results in enhanced ability to produce ATP. The proteins that generate ATP, ATP synthases, are inserted in the cristae. The number of cristae is variable among cells. Mitochondria from cells that have a great demand for ATP contain an elevated number of cristae. Mitochondria within the same cell can have different amounts of cristae.

The matrix is the space enclosed by the IMM. It contains a high proportion of enzymes for metabolic processes such as pyruvate and fatty acid oxidation. The matrix is important in the production of ATP with the aid of the ATP synthases located at the IMM. Besides its enzymatic content, the matrix harbors mitochondrial ribosomes, tRNA, and mitochondrial DNA (mtDNA) packaged into nucleoids. Human mtDNA encodes: 22 tRNA, 2 rRNA, and 13 peptide genes. The 13 proteins codified in the mtDNA are components of the mitochondrion. The rest of the mitochondrial proteins are encoded by the nuclear genome.

The functions carried out by mitochondria are numerous and unique within the cell. Mitochondria have become a signaling hub and a cellular

fitness center. Mitochondria initiate apoptotic signaling, manage the bioenergetics of the cell, maintain cellular proteostasis, participate in inflammatory response, regulate redox homeostasis, determine stem cell fate, allow cell cycle progression, contribute to autophagosome formation, produce heat, synthesize hormones, participate in heme biosynthesis and regulate the dynamics of other organelles.

2.2. Mitochondrial dynamics

The dynamism of mitochondria is crucial for their function. Mitochondria undergo processes of fusion and division in order to satisfy the needs of the cell. These adaptive changes in morphology are known as mitochondrial dynamics. The main players in mitochondrial dynamics (MFN1, MFN2, OPA1 and DRP1) belong to the dynamin superfamily, a family of proteins involved in organelle membrane dynamics (Figure 1) ². Dynamin superfamily proteins possess a structurally conserved core composed of a GTPase domain and a helix bundle that confers oligomerization capacity to these proteins ². There are dynamin related proteins that promote organelle membrane fusion and other members of this family that cooperate for membrane fission. Mitochondrial division is carried out mainly by DRP1 ³ and fusion is performed by MFN1 ⁴⁻⁶, MFN2 ^{4,6,7} and OPA1 ⁸⁻¹⁰. Mitochondrial dynamics are regulated by protein post-translational modifications such as phosphorylation, ubiquitination or proteolytic cleavage ⁴² and by contacts with other organelles such as the endoplasmic reticulum (ER) or lysosomes ^{43,44}.

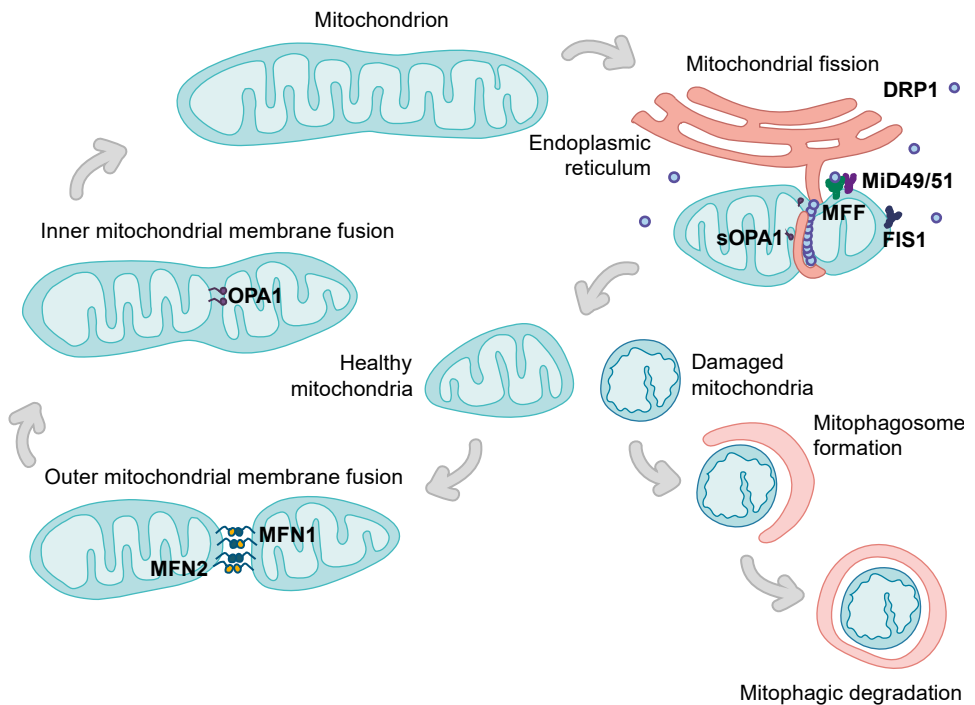


Figure 1. Mitochondrial dynamics. For mitochondrial fission to take place, DRP1 needs to be recruited from the cytosol to the OMM by one of its receptors in this surface (MFF, FIS1, MiD49 or MiD51) in order to form a ring to which the ER will bind. The ER constricts the mitochondrion until it is split into two mitochondria. Short isoforms of OPA1 (sOPA1) help in the process of IMM fission. If the resulting mitochondrial pieces are damaged they will undergo mitophagic degradation. If those pieces are healthy they will be able to fuse with other healthy mitochondria to maximize energy production in the cell. Fusion of the OMM is achieved by oligomerization of MFN1 and MFN2 and takes place before IMM fusion. Eventually, OPA1 in the IMM brings together the inner membranes of the mitochondria that are being fused.

2.2.1. Mitochondrial fission

Mitochondrial division occurs when cytosolic DRP1 is recruited to mitochondria by its receptors FIS1, MFF, MID49 and MID51 on the OMM

⁴⁵⁻⁴⁷. DRP1 shows a punctate pattern which marks sites of scission ³. ER tubules surround and constrict mitochondria at these sites ⁴⁸. Constriction is mediated by actin filaments that accumulate between mitochondria and the ER and that are polymerized at the ER membrane by INF2 ⁴⁹. INF2-mediated actin polymerization leads to an accumulation of myosin type II ⁵⁰, an increase in mitochondria-ER contacts, and the subsequent stimulation of mitochondrial Ca²⁺ uptake before constriction of the IMM and mitochondrial division ⁵¹. Regions of mitochondrial scission are sites for mtDNA synthesis where the nascent mtDNA stays in the daughter mitochondria after fission ⁵². Mitochondrial fission is coupled to mitochondrial removal by the protein FUNDC1. FUNDC1 localizes at mitochondria-ER contact sites where it interacts with DRP1 on the mitochondrial surface to promote both autophagosome recruitment and mitochondrial fission ⁵³. After mitochondrial fission, two different mitochondria are generated: one with increased membrane potential that likely will undergo mitochondrial fusion and another one with decreased membrane potential and reduced levels of OPA1, therefore with less probability of mitochondrial fusion ⁵⁴.

2.2.2. Mitochondrial fusion

Mitochondrial fusion is mediated by MFN1 ⁴⁻⁶ and MFN2 ^{4,6,7} on the OMM and OPA1 ⁸⁻¹⁰ in the IMM. Mitofusins present in adjacent mitochondria interact with each other to fuse the OMMs by forming homo-oligomers or hetero-oligomers. Oligomerization is dependent on GTP hydrolysis and mediated by a heptad repeat region in the C-terminal region ^{55,56}. After OMM fusion, OPA1 on one mitochondria interacts with a cardiolipin

rich domain in the IMM of the other mitochondria and IMMs fuse⁵⁷. It is still not clear how many MFN1, MFN2 and OPA1 molecules oligomerize to carry out this function. Dimeric and tetrameric interaction models have been proposed⁵⁸⁻⁶⁰. One of the short isoforms of OPA1 is associated with mitochondrial fission rather than fusion⁶¹.

Structural studies have been performed to gain insight into MFN1/2 mediated membrane fusion. For many years, bacterial dynamin-like proteins (BDLP) have been used as a model to understand the structure and oligomerization of the proteins from the dynamin superfamily^{62,63}. BDLPs have been shown to form tetramers that bind lipid bilayers independently of GTP hydrolysis (Figure 2)⁶⁰. In these tetramers there is a core composed of two BDLPs bound by their GTPase domains. Each of these two subunits harbor an N-terminal α -helix that interacts with the so called “assembly domain” of one of the remaining BDLP subunits of the complex. This tetramerization had already been reported from *in silico* predictions⁶⁴. Given these findings, dynamin superfamily proteins have been suggested to form tetrameric structures.

In 2017, crystal structures of a short version of human MFN1 containing the GTPase domain and a helical domain were resolved⁶⁵. It was observed that binding to GTP induces conformational changes and favors GTPase domain dimerization⁶⁵. When the GTPase domain dimerization is disrupted, fusogenic activity of MFN1 is lost⁶⁵. In 2019, a structural study of a truncated version of MFN2 containing the GTPase domain was published⁶⁶. The authors found that MFN2 GTPase domain is able to dimerize also after GTP hydrolysis⁶⁶. MFN2 GTPase domain has a

low GTP hydrolyzation capacity, whereas MFN1 can more efficiently hydrolyze GTP ⁶⁶. Heterodimerization of MFN1 and MFN2 GTPase domains is GTP dependent ⁶⁶. These MFN1 and MFN2 GTPase domain dimers could be compatible with a tetramer oligomerization model, as described for BDLPs, although complete forms of MFN1 and MFN2 have not been crystalized to date.

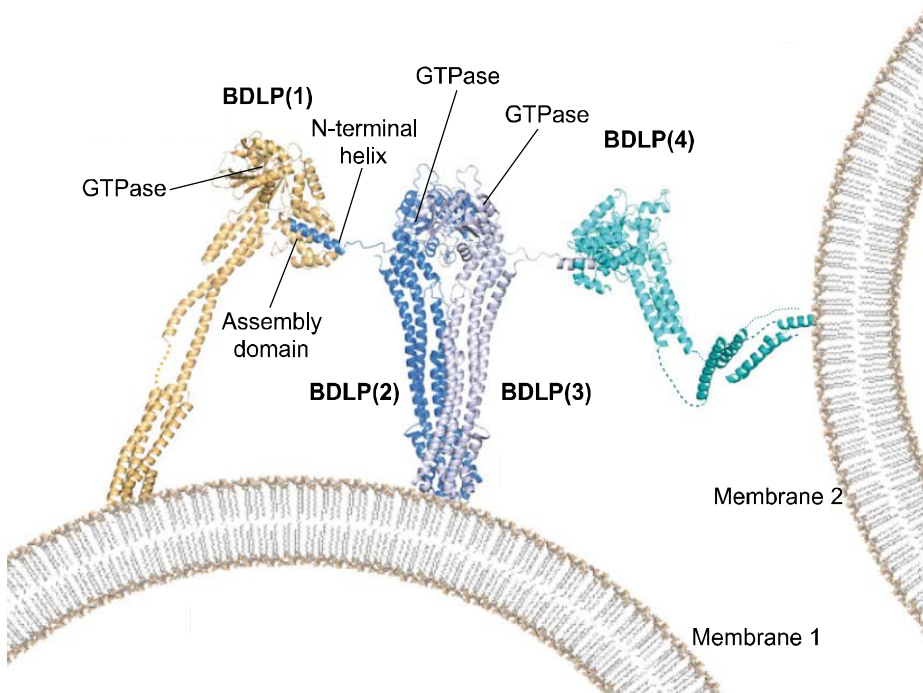


Figure 2. BDLP tetramerization model adapted from Liu et al. 2018. BDLP subunits of the tetramer are named BDLP(1), (2), (3) and (4). Membrane 1 and membrane 2 are the tethered membranes or membranes to be fused.

Mitochondrial fusion can be regulated through post-translational modifications of its main effectors. Ubiquitination of both MFN1 and MFN2 by PARK2 results in increased mitochondrial fission ^{67,68}. A similar

effect is achieved upon MFN2 ubiquitination by HUWE1⁶⁹. MARCHF5 can also ubiquitinate MFN1 and MFN2 although its impact in mitochondrial dynamics regulation is still under debate. Overexpressed MARCHF5 interacts with MFN1 and has been shown to induce mitochondrial fragmentation⁷⁰. However, a different study showed that *MARCHF5* overexpression leads to mitochondrial elongation and that MARCHF5 interacts with MFN2⁷¹. MARCHF5 ubiquitination of MFN2 was proposed to promote MFN2 oligomerization and ER-mitochondria contacts formation⁷². Inhibition of mitochondrial fusion is also achieved by PKC or JNK dependent phosphorylation of MFN1⁷³ and MFN2 respectively⁶⁹. Moreover, acetylation of MFN1 reduces mitochondrial fusion⁷⁴. This effect is reversed by HDAC6, which deacetylates MFN1⁷⁴. OPA1 activity is mainly regulated through proteolytic cleavage. YME1L cleavage of OPA1 is necessary for mitochondrial fusion⁷⁵. OMA1 cleavage of OPA1 inhibits mitochondrial fusion⁷⁶. Protein interactions can also regulate mitochondrial fusion. FIS1 interacts with MFN1, MFN2 and OPA1 in order to inhibit their fusogenic activity⁷⁷.

2.3. Additional cellular functions of the mitofusins

Besides their role in mitochondrial dynamics, MFN1 and MFN2 take part in several other cellular processes namely: mitochondrial bioenergetics, mitochondrial transport, interorganelle communication, inflammatory signaling, autophagy or mitophagy, apoptosis, cellular senescence, cell cycle progression, cellular differentiation, and ER-stress (Figure 3 and Figure 4).

Functions of MFN1 and MFN2

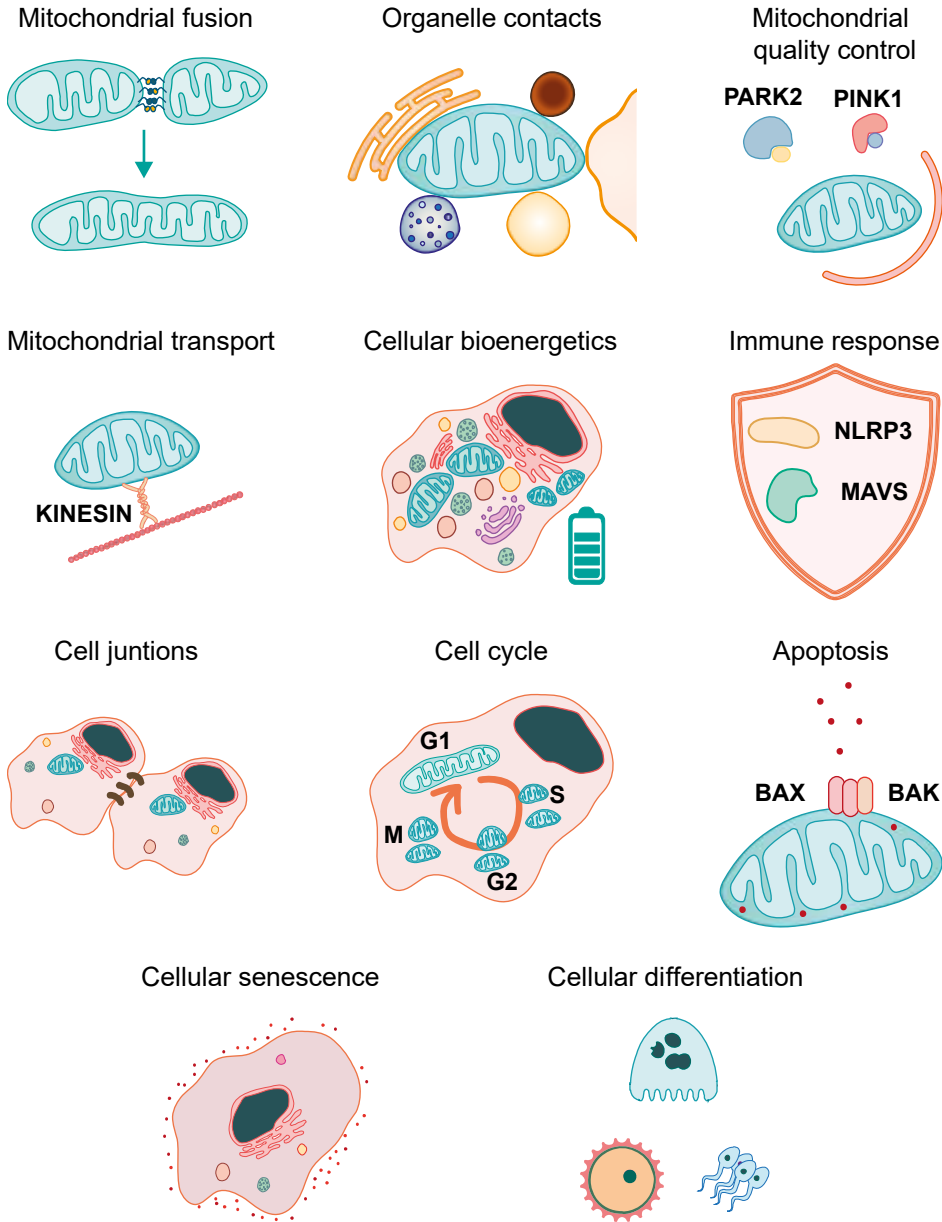


Figure 3. Functions of MFN1 and MFN2. MFN1 and MFN2 are involved in mitochondrial fusion; contacts with mitochondria and other organelles; mitochondrial quality control through interaction with PARK2 and PINK1; mitochondrial transport through microtubules by attaching mitochondria to

kinesins; cellular bioenergetics; immune response by interacting with NLRP3 and MAVS; cellular junctions; cell cycle progression which needs different mitochondrial morphologies; apoptosis in which they bind BAX and BAK; cellular senescence; and cellular differentiation.

Functions of MFN2

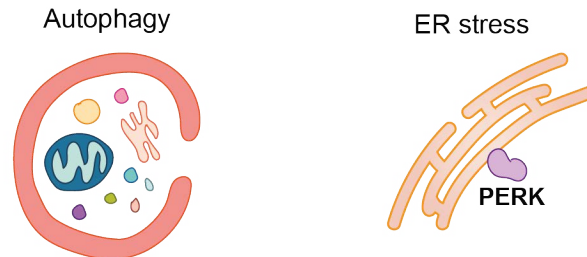


Figure 4. Functions of MFN2 in which MFN1 does not participate. MFN2 is involved in autophagy and ER-stress inhibition. MFN1 is not involved in these processes.

2.3.1. Interorganelle communication

Mitochondria are social organelles. They maintain active contacts with other membranous compartments of the cell. Mitochondria communicate with the endoplasmic reticulum (ER), lipid droplets (LDs), Golgi apparatus, endosomes, lysosomes, melanosomes and peroxisomes by establishing physical contacts ¹¹. Fluorescent labeling of organelles *in vivo* has revealed cellular regions where three or more organelles physically interact ⁷⁸. MFN1 and MFN2 are key in several organelle apposition sites (Figure 5).

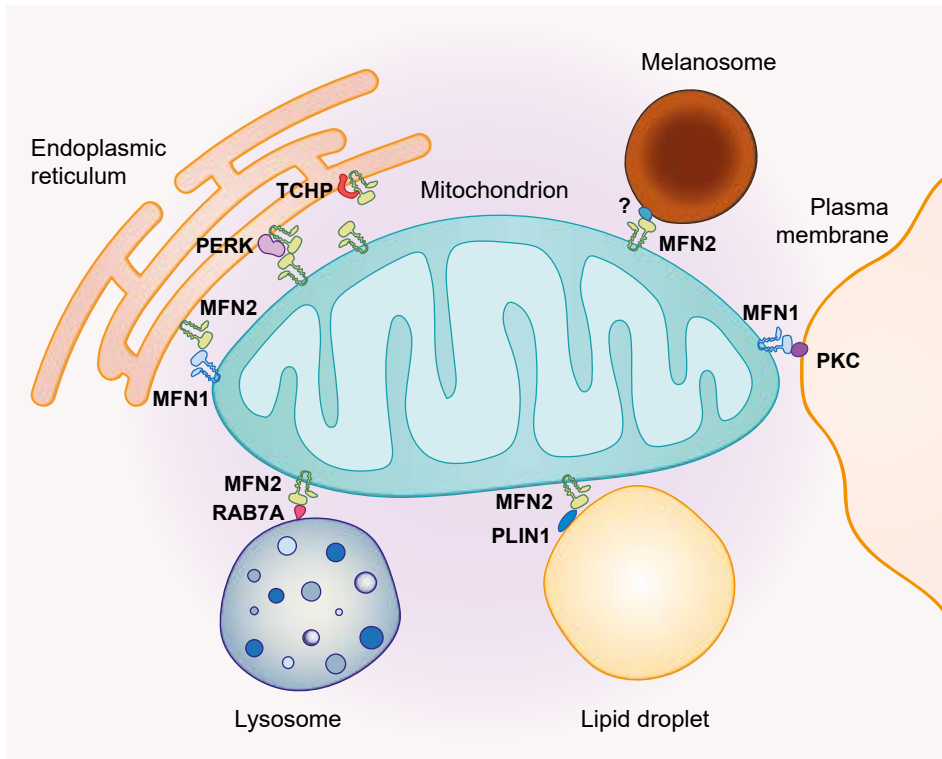


Figure 5. Contacts of mitochondria with other organelles that involve MFN1 and MFN2.

Mitochondria-ER contacts are established by several proteins in the OMM that interact with proteins located in the ER surface. MFN2 is localized both in the mitochondria and in the ER, and is able to homo-oligomerize and to hetero-oligomerize with MFN1 to tether both organelles ^{79–83}. Although several studies performed in our laboratory and by other research groups have confirmed the role of MFN2 as a tether of ER and mitochondria ^{19,81}, there are other studies that argue that MFN2 is an organelle spacer, rather than a tether ^{84,85}. MFN2 tethering role is regulated by the ER protein TCHP ⁴³. TCHP prevents mitochondria-ER tethering and favors mitochondrial elongation when it is bound to

MFN2⁴³.

Mitochondria-ER contact sites harbor several functions that are perturbed when their architecture is disrupted. Particularly, the ablation of MFN2 results in the suppression of autophagosome formation^{16,17}, which is explained more into detail in the following sections of this thesis. Moreover, the absence of MFN2 in mouse livers disrupts phospholipid trafficking between ER and mitochondria by impeding phosphatidylserine (PS) transference from the ER membrane to the OMM⁸⁶. *Mfn2* depletion also affects calcium homeostasis^{18,87}. MFN2 interacts with the unfolded protein response (UPR) protein PERK which localizes in the ER and represses its activity¹⁸. MFN2 loss-of-function in MEF cells dysregulates the three branches of the UPR by enhancing the PERK-eIF2 α -ATF4-CHOP pathway¹⁸. The implication of MFN2 in ER stress and UPR is further explained in the next epigraph.

Mitochondria and LDs are in active communication in highly metabolic tissues such as BAT, skeletal muscle and heart⁸⁸⁻⁹¹. The contacts between mitochondria and LD functionally support triacylglyceride synthesis⁹² and they are sustained by the interaction between MFN2 and PLIN1⁸⁹. Mice that lack *Mfn2* specifically in brown adipose tissue show impaired thermogenic function⁸⁹. Nevertheless, *Mfn1* deficiency in brown adipose tissue does not have the same effect⁸⁹. Interestingly, perturbing mitochondrial dynamics by modifying the expression of *Mfn1* in MEF cells affects the size of LDs⁹³. *Mfn1* ablation results in greater accumulation of fatty acids in LDs⁹³.

The interface between mitochondria and lysosomes could play a role in

autophagy. It is known that MFN2 interacts with RAB7 in mouse hearts⁹⁴. This interaction increases upon autophagy induction by starvation and has been proposed to be involved in autophagosome-lysosome fusion⁹⁴. Melanosomes, which are lysosome-related organelles that store pigments, also interact with mitochondria⁹⁵. These contact sites are associated with the process of melanogenesis⁹⁵. MFN2 has been found at these areas of juxtaposition and its knockdown reduces these interorganelle connections⁹⁵. However, the melanosomal component of these junctions remains unknown.

Mitochondria-plasma membrane contacts are poorly studied in mammalian cells. Nevertheless, it has been shown that mitochondria can be tethered to the plasma membrane by the binding of MFN1 to plasma membrane-associated PKC isoform- ζ and NUMB in human MCF12A epithelial cells⁹⁶. Fused mitochondria are anchored to the plasma membrane during cellular division and mitochondria are differentially distributed among daughter cells. This allows a stem cell and a differentiated cell to arise from the same cellular division. The stem cell keeps the fused mitochondria that were anchored to the membrane and the differentiated cell keeps the fragmented ones⁹⁶. Lack of *MFN1* results in symmetric cell division and impaired differentiation⁹⁶.

2.3.2. ER-stress and unfolded protein response

Stress conditions such as nutrient deprivation, hypoxia, loss of Ca²⁺ homeostasis, and free fatty acids disturb protein folding efficiency at the ER⁹⁷⁻¹⁰². The accumulation of large amounts of these misfolded

proteins activates the Unfolded Protein Response (UPR) in order to restore protein homeostasis or to induce apoptosis^{103,104}. The UPR has three main branches, PERK, ATF6 and IRE1 α , named after their signal transducers in the ER¹⁰⁵. These branches are interconnected downstream of ER transducers stimulation¹⁰⁵. PERK activation induces eIF2 α phosphorylation¹⁰⁶. Phosphorylated eIF2 α inhibits global protein translation and activates ATF4, which translocates to the nucleus to induce the expression of survival genes¹⁰⁷. Prolonged UPR activation induces apoptosis through the activation of CHOP by ATF4¹⁰⁸. UPR mission is to restore cellular homeostasis by correcting protein folding and recovering damaged ER environment¹⁰⁶. As long as protein folding efficiency is not resolved UPR is activated¹⁰⁶. ER stress results in increased mitochondria coupling to ER which increases ATP production, oxygen consumption and mitochondrial Ca²⁺ uptake¹⁰⁹. Chronic UPR signaling initiates a signaling cascade in mitochondria-ER contact sites that eventually leads to apoptosis¹⁰⁶. MFN2 interacts with PERK and inhibits its transducing activity¹⁸. The ablation of *Mfn2* results in increased ER-stress signaling^{18,110} although it reduces ER-stress associated apoptosis¹⁸. Nevertheless, ablation of *Mfn1* does not generate a similar ER-stress phenotype¹¹⁰ and this is probably due to MFN2 tethering properties.

2.3.3. Macroautophagy

In order to preserve cellular homeostasis, damaged or unnecessary components of the cell must be degraded or recycled. This process is achieved by autophagy, that will be discussed in the following section. In brief, autophagosomes engulf damaged or needless cellular components

and can originate from mitochondria-ER contact sites ^{16,17}. At the ER side of this contact sites, proteins related to autophagosome formation start to accumulate and form a structure known as the isolation membrane. This structure protrudes from the ER and finally closes around the cellular components to be eliminated, forming a vesicle named the autophagosome ¹¹¹. The absence of MFN2 at mitochondria-ER contact sites results in impaired autophagosome formation ^{16,17}, nevertheless the role or mechanism of action of MFN2 in this process has not been described yet. It has not been studied whether MFN1 ablation disturbs autophagosome formation. However, it has been demonstrated that under autophagy induction conditions, MFN1 is a key player on mitochondrial hyperfusion to protect mitochondria from autophagic degradation ¹⁴.

2.3.4. Mitochondrial quality control

Damaged mitochondria are removed by mitochondrial selective autophagy or mitophagy ¹¹². Defective clearance of impaired mitochondria results in inflammatory signaling and tissue damage ^{113,114}. Fragmentation of the mitochondrial network facilitates mitophagic removal and in this context occurs independently of DRP1 ¹¹⁵. PINK1 and PARK2 target damaged mitochondria for degradation ¹¹⁶⁻¹¹⁹. PINK1 phosphorylates MFN2, which is recognized by PARK2 for ubiquitination ¹⁸. PARK2 ubiquitinates MFN1 and MFN2 for proteasomal degradation and inhibition of mitochondrial fusion at the early stage of mitophagy ¹²⁰⁻¹²². Although rapidly degraded upon mitophagy induction, *Mfn1* and *Mfn2* simultaneous ablation provokes decreased mitophagy, resulting in

the accumulation of damaged mitochondria ¹²³. Hence, MFN1 and MFN2 are probably needed during early mitophagic signaling.

2.3.5. Mitochondrial transport

Different energetic needs within the cell are satisfied by mitochondria that migrate to the cellular regions where they are necessary. How mitochondria move along the cell has been studied mainly on neuronal models. Mitochondria are transported through the microtubule network by kinesin-1 which is recruited by the adaptor proteins MILTON1 and MILTON2 ¹²⁴. MILTON1 and MILTON2 form a complex with the mitochondrial proteins MIRO1 and MIRO2 ^{21,124}. Both, MFN1 and MFN2 interact with MIRO and MILTON proteins ²¹. Depletion of *Mfn2* in mammalian and fly models results in deficient mitochondrial transport such as *Miro2* silencing ^{21,125,126}. Deficient mitochondrial migration can be corrected by overexpression of *Mfn1* and *Mfn2* ^{21,125}.

2.3.6. Mitochondrial bioenergetics

Mitochondria are hubs for respiration and metabolite oxidation. The simultaneous ablation of *Mfn1* and *Mfn2* results in decreased mitochondrial respiration, accompanied by an increase in mitochondrial mass and respiratory complex II activity ¹²⁷. When *Mfn2* is ablated alone in cellular models a decrease is observed in mitochondrial membrane potential, cellular oxygen consumption, mitochondrial proton leak, and mitochondrial co-enzyme Q level, as well as decreased oxidation of glucose, pyruvate, and fatty acids ^{4,7,128,129}. As a compensatory effect of *Mfn2* depletion, glucose uptake by the cell is increased, glycogen

synthesis is decreased and anaerobic glycolysis is enhanced to generate ATP¹²⁸. Although metabolic adaptations occur, mitochondrial mass remains unchanged^{7,128}. Another consequence of MFN2 loss is the repression of the expression of some of the complexes involved in oxidative phosphorylation (OXPHOS), namely complexes I, II, III and V¹²⁸. These complexes are upregulated upon overexpression of *MFN2*¹²⁸. The mechanism by which MFN2 regulates the expression of OXPHOS complexes subunits and therefore the OXPHOS process has not been deciphered yet. Studies on metabolic effects of *MFN1* ablation alone have not been performed to date.

2.3.7. Innate immune response

Mitochondria are hubs for innate immune signaling¹³⁰. One of the pathways that is activated against RNA viruses and involves mitochondria is the RIG-I-like receptor pathway¹³¹. RIG-I detects invading viral RNA and, through the OMM protein MAVS¹³², initiates a downstream cascade to activate the transcription factors NF- κ B and IRF3¹³¹. MFN1 and MFN2 interact with MAVS¹³³. MFN1 is necessary for the activation of the downstream cascade of RIG-I¹³³, nevertheless MFN2 plays the opposite role and inhibits mitochondrial antiviral signaling¹³⁴. MAVS degradation, a step in RIG-I-like signaling cascade, promotes mitochondrial elongation, likely by release of MFN1¹³⁵.

In addition to RIG-I-like receptor signaling pathway, mitochondria operate as a platform for the activation of the NLRP3 inflammasome^{136,137}. The NLRP3 inflammasome is a complex formed by the oligomerization of

NLRP3, CASP1, NEK7 and ASC, whose formation leads to the activation of the pro-inflammatory cytokines IL-1 β and IL-18 for secretion and in last term leads to cell death ¹³⁸. Activation of the NLRP3 inflammasome occurs in response to a variety of threats that cause cellular stress such as infectious agents, endogenous signals or environmental irritating compounds ¹³⁸. Upon mitochondrial exacerbated production of reactive oxygen species (ROS), the NLRP3 inflammasome is activated ¹³⁷. Both MFN1 and MFN2 interact with NLRP3 ¹³⁹. The absence of MFN2 impairs NLRP3 signaling ¹³⁹. MFN2 is necessary for NLRP3 inflammasome components association ¹³⁹. MAVS interacts with the NLRP3 and promotes the NLRP3 inflammasome-mediated IL-1 β secretion ¹⁴⁰. MFN2 enhances NLRP3 and MAVS interaction ¹³⁹. Full activation of NLRP3 inflammasome needs a fused mitochondrial network and intact mitochondrial membrane potential ¹³⁹.

Moreover, a role of MFN2 in the adaptation of mitochondrial respiration and ROS production has been described in macrophages ¹⁴¹. *Mfn2* deficient macrophages show lack of ROS production ¹⁴¹. This leads to impaired ERK and p38 signaling, which reduces pro-inflammatory cytokines and nitric oxide production ¹⁴¹. Moreover, the absence of MFN2 in macrophages causes defective antigen processing ¹⁴¹. Nonetheless, none of these phenotypes are observed upon *Mfn1* ablation in macrophages ¹⁴¹. Therefore, these effects are not a consequence of reduced mitochondrial fusion.

2.3.8. Cellular junctions

Mitofusins have been found to participate in different types of cellular junctions. The role of MFN2 at the plasma membrane has been studied in endothelial cells, where it stabilizes adherens junctions and blocks inflammatory signaling in response to TNF α stimuli. Overexpressed MFN2 interacts with the adherens junction proteins VE-cadherin and β -catenin and co-localizes with VE-cadherin in the plasma membrane of human lung endothelial cells independently of TOM20¹⁴². Inflammatory stimulation with TNF α , which dissociates adherens junctions, promotes MFN2 interaction with β -catenin, but not with VE-cadherin¹⁴². MFN2 suppresses the transcriptional activity of β -catenin¹⁴². Silencing of *Mfn2* in endothelial cells results in increased plasma membrane permeability that is rescued upon *Mfn2* overexpression¹⁴². Conversely, specific *Mfn2* deletion in lung endothelium of mice also leads to increased lung permeability¹⁴².

Targeted deletion of *Mfn1* in mouse oocytes results in disruption of adherens and gap junctions between oocytes and granulosa cells and results in defective oocyte maturation and female infertility¹⁴³. Oocytes from *Mfn1* KO mice display downregulated adherens junction related genes and proteins, such as E-cadherin and N-cadherin¹⁴³. Gap junctions are also affected by the lack of *Mfn1*: expression of the gap junction related genes *Cx37* and *Cx43* is significantly decreased in *Mfn1* ablated oocytes and granulosa cells¹⁴³. *Mfn1* KO mice secondary follicles show defective contact between oocyte and granulosa cells and decreased gap junctions¹⁴³.

2.3.9. Cell cycle progression

During the cell cycle, there are phases characterized by different energy demands or which require different organelle architectures. Mitochondria change their morphology as an adaptation to the different cell cycle stages: during G1 mitochondria elongate and mitochondrial fission machinery is inhibited; during S phase and G2 phase, mitochondria are fragmented upon activation of DRP1 and inactivation of MFN1; and during M phase fragmented mitochondria segregate into the two daughter cells ¹⁴⁴. During G2/M phases MFN1 interacts with CDK1/CCNB1 complex ¹⁴⁵ and it is more ubiquitinated by MARCHF5 ¹⁴⁵. ERK activation through RAS-RAF1 signaling cascade is mandatory for G1 to S phase transition ¹⁴⁶. MFN2 blocks cellular proliferation by inhibiting de RAS-RAF1-ERK signaling pathway ¹⁴⁷. MFN2 interacts with RAS and RAF1 and impedes phosphorylation and activation of RAF1 and ERK ¹⁴⁷.

2.3.10. Apoptosis

During programmed cell death mitofusins participate in the needed mitochondrial morphology changes and in apoptotic signaling. During apoptotic signaling mitochondria become fragmented. Mitochondrial fusion machinery needs to be inhibited in these circumstances ^{148,149}. MFN1 is phosphorylated by ERK to inhibit mitochondrial fusion ¹⁵⁰. This phosphorylation favors mitochondrial permeabilization and apoptosis ¹⁵⁰. MFN2 is phosphorylated by JNK in response to stress which results in MFN2 proteasomal degradation, mitochondrial fragmentation and apoptosis ⁶⁹. Although MFN2 is degraded during apoptosis induction,

MFN2 deficient cells show impaired activation of apoptosis during ER stress ¹⁸.

Regarding apoptotic signaling, at the early stages of programmed cell death BCL2-family proteins BAX and BAK oligomerize at the OMM for their activation ^{151,152}. BAX translocates from the cytosol to the OMM, where BAK locates constitutively. Although not yet demonstrated, it is believed that cytochrome c exits mitochondria from the pores formed by these oligomers ¹⁵³. After cytochrome c release, an apoptotic protease cascade is initiated ¹⁵⁴. BAX and BAK interact with MFN1, MFN2 and DRP1 ^{155,156}. BAX translocates to specific sites on the mitochondrial surface that subsequently become mitochondrial fission sites ¹⁵⁵. BAX has been suggested to play a dual role: promotes mitochondrial fusion via its interaction with MFN2 ¹⁵⁷ and promotes apoptosis when it dissociates from MFN2 and associates with MFN1 ¹⁵⁶. *Bak* or *Bax* ablation inhibits mitochondrial fragmentation in response to apoptotic stimulus and reduces cytochrome c release from mitochondria and apoptosis ¹⁵⁶. Simultaneous depletion of *Bax* and *Bak* results in total blockage of cytochrome c release and apoptosis ¹⁵⁶. Cytosolic BAX is not able to target fragmented mitochondria from *Mfn1* knockout cells, which suggests that BAX needs a minimum size of mitochondria in order to adapt its conformation and attach to the OMM ¹⁵⁸.

2.3.11. Cellular senescence

During senescence cells stop dividing, however they remain metabolically active ¹⁵⁹. Elongation of the mitochondrial network is

associated with cellular senescence ^{160,161}. Since proliferation arrest during senescence is accompanied by a decrease in mitochondrial biogenesis ¹⁶², it has been suggested that this elongation could suppose an adaptation to reduced mitochondrial biogenesis ¹³. On the other hand, exacerbated mitochondrial elongation can induce premature senescence ¹⁶¹. MARCHF5 has been suggested to regulate senescence through mitochondrial dynamics. Reduced MARCHF5 levels increase MFN1 expression and result in mitochondrial elongation and induction of cellular senescence ⁷⁰. Moreover, during senescence, the levels of FIS1, which binds and inhibits MFN1 and MFN2 fusogenic activity ⁷⁷, are reduced and as a consequence mitochondria elongate ¹⁵⁹.

2.3.12. Cellular differentiation

Mitofusins play a role in several processes of embryonic and adult stem cell differentiation, namely gamete differentiation, stemness maintenance, cardiac differentiation, osteoclastogenesis, and lymphoid potential maintenance.

Female and male gamete generation require the action of mitofusins. In mouse oocytes, MFN2 is required for meiotic maturation ¹⁶³. MFN2 associates spatially with microtubules and the meiotic spindle during maturation of mouse oocytes ¹⁶³. MFN2 deficiency results in arrested meiosis and spindle defects ¹⁶³. Spermatogonial differentiation requires MFN1 and MFN2 ¹⁶⁴. If *Mfn1* and *Mfn2* are depleted in the germline cells of male mice, spermatogenesis is arrested ¹⁶⁴. GASZ, a protein that is necessary for spermatogenesis and essential for male fertility, interacts

with MFN1 and MFN2 and promotes mitochondrial fusion ¹⁶⁵. In the fly testis the depletion of MFN1/2 homologous protein Marf results in the loss of germ stem cells ¹⁶⁶.

Mitofusins also take part in the exit of pluripotency. Mitochondrial elongation promoted by MTCH2 drives the exit from naïve pluripotency ¹⁶⁷. In *Mtch2* deficient embryonic stem cells, mitochondria fail to elongate and maintain higher levels of naïve pluripotency markers ¹⁶⁷. Moreover, the overexpression of *Mfn2* in *Mtch2* ablated cells results in pluripotency leave ¹⁶⁷. When *Mfn1* or *Mfn2* are depleted in somatic cells, these enter into a pluripotent state ¹⁶⁸. This reprogramming occurs through activation of RAS-RAF1 pathway ¹⁶⁸.

Distribution of mitochondria among the daughter cells after a stem cell divides is crucial for differentiation and preservation of stemness. During stem cell differentiation, MFN1 is essential for asymmetric cell division in epithelial to mesenchymal transition ⁹⁶. MFN1 interacts with PKC in the plasma membrane and tethers mitochondria to the cortical part of the cell ⁹⁶. Depletion of *Mfn1* causes equal distribution of mitochondria in epithelial cells and symmetric cell division ⁹⁶.

Heart development needs MFN1 and MFN2. Mice embryos defective in *Mfn1* and *Mfn2* show defects in heart formation ¹⁶⁹. Depletion of *Mfn2* in embryonic stem cells leads to impaired differentiation into cardiomyocytes ¹⁶⁹. These cells show increased calcium entry in the cell and calcineurin activity ¹⁶⁹. Moreover, aberrant localization of mitochondria is observed: higher proportion of mitochondria localize close to the plasma membrane in *Mfn2* deficient embryonic stem cells

¹⁶⁹. The authors of the study propose that defective heart development is due to compromised mitochondrial fusion.

Differentiation of osteoclasts is also dependent on the presence of MFN2. On the one hand, during osteoclast differentiation from bone marrow derived macrophages, MFN2 is necessary to positively regulate the NFAT1 axis ¹⁷⁰. Lack of MFN2 decreases osteoclastogenesis ¹⁷⁰. On the other hand, MFN2 is necessary to maintain hematopoietic stem cell lymphoid potential through NFAT1 axis inhibition ¹⁷¹. *Mfn2* depletion decreases hematopoietic stem cell differentiation potential ¹⁷¹.

2.4. Autophagosome formation

Autophagy is the process by which intracellular components are degraded into molecules that the cell can re-utilize. There are several stimuli that provoke autophagosome emergence such as nutrient starvation, stress, organelle damage, immune response or microbial infection. During autophagosome formation, a membrane structure known as ‘phagophore’ or ‘isolation membrane’ starts arising in the cytoplasm from the ER, elongates, is closed and is cleaved. The first stages of autophagosome formation that are described in this section are illustrated in Figure 6.

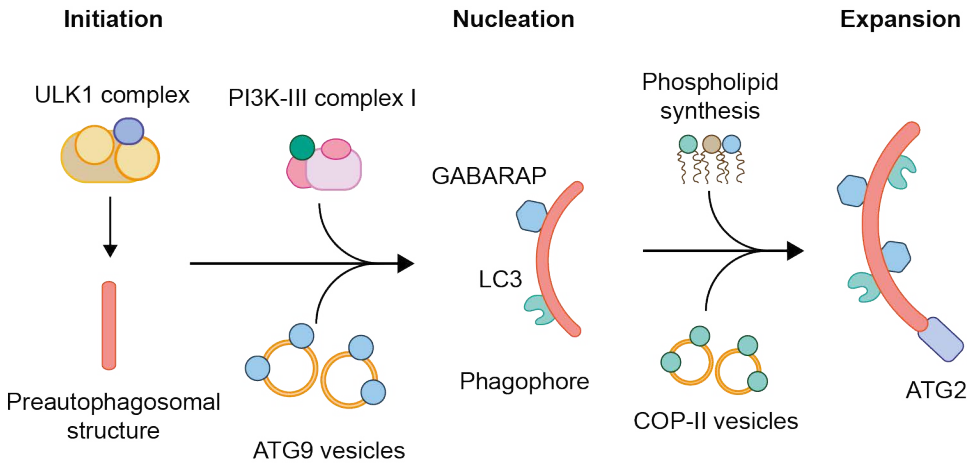


Figure 6. First stages of autophagy.

2.4.1. Autophagy initiation

The signals that induce non-selective autophagy are transmitted through different pathways that generally converge on mTORC1 and inhibit its activity ¹⁷². When mTORC1 is active it phosphorylates ULK1 complex subunits to block autophagosome biogenesis ¹⁷³. Low glucose levels can induce autophagy by inhibiting mTORC1 and by activating AMPK which directly activates ULK1 by phosphorylation ¹⁷³. For selective autophagy initiation, autophagy targets are the source of the signals that induce autophagosome formation ¹⁷⁴. Autophagy receptors facilitate the assembly of ULK1 complexes on these targets.

2.4.2. Autophagosome nucleation

Autophagosome formation occurs at the ER membrane, mostly in sites of interaction between ER and mitochondria ¹⁶. After autophagy induction, ULK complexes are recruited to these ER regions, which are

enriched in phosphatidylinositol synthase (PIS), and form a scaffold to recruit other ATG proteins ^{175,176}. Next, ATG9 vesicles are attracted to the autophagosome formation sites ^{177,178}. It is still not known whether these vesicles are derived from the trans-Golgi network or from the plasma membrane. In yeast it has been described that Atg9 vesicles serve as a seed to form the autophagosome precursor ¹⁷⁹. However, this fact has not been proved in mammalian cells.

Next, PI3K complex I is directed to the autophagosome formation sites ¹⁸⁰. PI3K complex I and PtdIns3P binding proteins are necessary for the formation of the autophagosome precursor ^{180,181}. Then, ATG16L1 complex coupled to WIPI2b is recruited to the autophagosome formation sites by WIPI2b binding to PtdIns3P ¹⁸². ATG16L complex interacts with ATG3 to favor the lipidation of Atg8-family proteins ^{183,184}. Lipidated Atg8-proteins play different roles during autophagosome formation that will be discussed in the next epigraph.

The ATG2-WIPI complex localizes to PtdIns3 positive autophagosome precursor membranes ¹⁸⁵. ATG2 interacts with ATG9 for the correct formation of autophagosomes ¹⁸⁶. The ATG2-WIPI complex serves as a tether of the isolation membrane to the ER and promotes its growth from the ER ¹⁸⁷.

2.4.3. Phagophore expansion

Atg8-family proteins are localized in the whole surface of the isolation membrane. These proteins interact with each other and tether membranes together when conjugated to phosphatidylethanolamine

2 | Introduction

(PE)¹⁸⁸. There are two subfamilies of Atg8-family proteins in mammals, the LC3 isoforms and GABARAP like proteins. These proteins play different roles in the process of autophagosome biogenesis. It has been proposed that LC3 isoforms are involved in membrane expansion, whereas GABARAPs act later, during membrane closure¹⁸⁹. Atg8-family proteins recruit other proteins for the expansion of the phagophore. The recruited proteins harbor an LC3-interacting region (LIR)¹⁹⁰.

There are several models and hypotheses on how autophagosome membranes and lipids originate. The contact sites between ER and mitochondria have been proposed as sources of autophagosome membranes¹⁶. Moreover, it has also been suggested that lipids can be directly transferred from specific subdomains in the ER (omegasomes) to the isolation membrane¹⁹¹. Another source of membranes would be COP-II vesicles¹⁹².

Mitochondria-ER contacts are key sites in autophagosome formation. It has been demonstrated that mitochondria supply lipids to the expansion of the phagophore¹⁷. More specifically, ER synthesized PS is transferred to mitochondria where it is converted into PE, which has been shown to be transferred to the phagophore. Moreover, autophagy protein complexes occur at the interface between mitochondria and the ER¹⁶. The ablation of MFN2 or PACS2, which are involved in the tethering of mitochondria to the ER, results in impaired autophagosome formation^{16,17}.

Several studies point towards direct lipid transfer from the ER to the autophagosome precursor membrane. Lipid transfer would occur at

the region of tethering between the ER and the autophagosome, the omegasome. This transport may involve ATG2 as it has the ability to transfer lipids between membranes enhanced by WIPI proteins^{185,193} and the capacity to tether ER membranes to isolation membranes in cooperation with WIPI proteins¹⁹⁴.

COP-II vesicles originate in the ER and they transport lipids and proteins to the Golgi apparatus. In yeast, mutant strains in the coatomer proteins of COP-II vesicles *sec12*, *sec16*, *sec23*, and *sec24* are not able to form autophagosomes¹⁹⁵. Another study showed that COP-II vesicles are able to transfer Axl2, an ER transmembrane protein, to the isolation membrane¹⁹². All these data suggest that COP-II vesicles are a source for autophagosome membrane expansion, but it is still unclear if they are a major source of proteins and lipids or they just load specific proteins and lipids into the autophagosomes.

Recently, the yeast acyl-CoA synthetase Faa1 has been revealed to participate in fatty acid incorporation in autophagosome membranes at contact sites with the ER²⁶. This has opened the door to speculate on the participation of *de novo* lipid synthesis in autophagosome biogenesis. Absence of Faa1 in yeast can be recovered by human ACSL4v1 protein expression²⁶. Double null mutants of *faa1* and *faa4* are recovered by the expression of the human proteins ACSBG1, ACSL1/3/4/5/6, or SLC27A2/4, although their role in phagophore expansion in mammals has not been investigated yet¹⁹⁶. From those proteins, ACSL3 has been suggested to play a role in ER-phagy¹⁹⁷.

2.4.4. Phagophore closure and cleavage

During its expansion, the phagophore acquires a spherical shape. At the end of the expansion, a small pore remains, which will close to finish autophagosome formation and its separation from the ER. The ESCRT complex machinery, which mediates membrane fission events, has been pointed as the main actor in autophagosome closure. The ESCRT-III complex proteins CHMP2A and VPS4 are essential in this process ¹⁹⁸.

OBJECTIVES



3. OBJECTIVES

Given the gaps underlying MFN1 and MFN2 molecular mechanisms in basal conditions and in conditions of nutrient deprivation, the objectives of this thesis are:

1. To identify MFN1 and MFN2 interaction partners in basal conditions. The mechanisms behind MFN1 and MFN2 functions, such as regulation of mitochondrial bioenergetics, interorganelle contacts or innate immune response, are poorly understood. Therefore, the identification of new binding partners will shed light into how MFN1 and MFN2 operate in these processes.
2. To identify MFN1 partners that contribute to amino acid starvation induced mitochondrial hyperfusion. The lack of MFN1 impedes mitochondrial elongation to protect mitochondria from being degraded during starvation-induced autophagy. The detection of the proteins that interact with MFN1 when amino acids are depleted from the medium will clarify how MFN1 is activated for mitochondrial hyperfusion.
3. To identify MFN2 partners in amino acid starvation induced autophagy and to elucidate the role of MFN2 in autophagosome biogenesis. The absence of MFN2 prevents autophagosome formation at mitochondria-ER contact sites. Thus, MFN2 must have a function in autophagosome biogenesis. To elucidate this function it is crucial to know which proteins interact with MFN2 during starvation-induced autophagy.

3 | Objectives

In this study, endogenous MFN1 and MFN2 have been immunoprecipitated under basal and amino acid starvation conditions and mass spectrometry has been performed to elucidate which proteins interact with the mitofusins and clarify which are the mechanisms behind their functions.

RESULTS



4. RESULTS

4.1. Generation of endogenous expressing MFN1-HA and MFN2-HA CRISPR/Cas9 cellular models

Protein overexpression may result in aberrant protein localization inside the cell, compensation of cellular changes by upregulation or downregulation of other proteins, organelle clumping, or erroneous protein complex formation. Particularly, MFN1 overexpression affects mitochondrial function and motility ¹⁹⁹ and overexpression of MFN2 results in mitochondrial clustering around the nucleus and cell death ²⁰⁰. Therefore, to study MFN1 and MFN2 functions it is desirable to keep their expression at endogenous levels.

4.1.1. Design of a CRISPR/Cas9 strategy to tag endogenous MFN1 and MFN2

The prokaryotic adaptive immune system CRISPR/Cas is capable of facilitating RNA-guided site-specific DNA cleavage ²⁰¹. This system has been modified and adapted in such a way that Cas9 nucleases can be directed by short RNAs to induce precise cleavage at endogenous genomic loci in several cell types, including mouse cells ^{202–204}. These short RNAs are known as guide RNAs (gRNAs) and they are complementary to a 20 nucleotide sequence in the DNA that is contiguous to a protospacer adjacent motif (PAM) (Figure 7A). The PAM sequence consists of three nucleotides and contains two guanines in the 3' end. The cleavage induced by Cas9 in the DNA is a double-strand break (DSB) that localizes

3 nucleotides upstream of the PAM sequence. The induced DSB can then be repaired by non-homologous end joining (NHEJ) if there is not any template DNA sequence or by homologous recombination (HR) if there is a template DNA sequence that can recombine with the cleaved DNA molecule²⁰⁵ as it is shown in Figure 7B. A single-stranded oligonucleotide that contains regions of homology shorter than 100bp can be used as a template sequence to generate insertions in the genome^{206,207}.

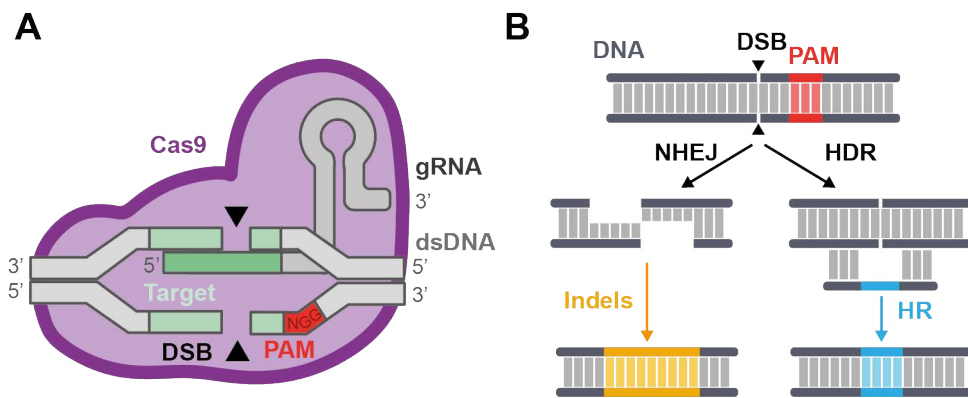


Figure 7. CRISPR/Cas9 approach. (A) Scheme of Cas9 induction of DSB. Cas9 is guided through the genome with a gRNA until it reaches its target site to induce a double strand break 3 nt upstream of the PAM sequence. (B) Illustration of DSB possible reparations after Cas9 cut. NHEJ results in indels and HDR results in nt insertion by HR.

CRISPR/Cas9 technology was used to insert an HA tag in the genome sequences of MFN1 and MFN2 for subsequent molecular biology studies (Figure 8). The application of a CRISPR/Cas9 strategy to tag MFN1 and MFN2 enabled the maintenance of endogenous expression levels of these proteins.

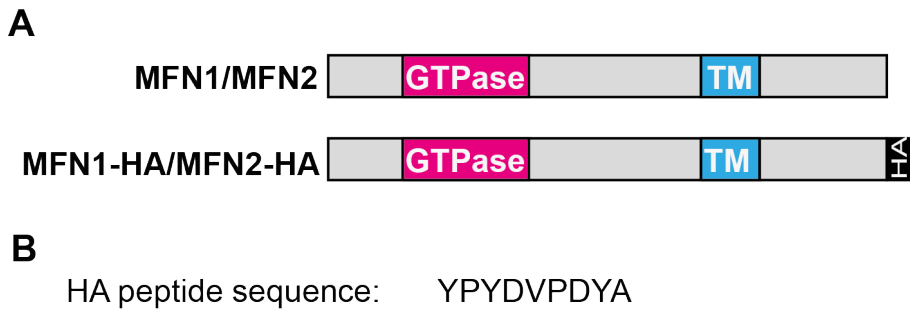


Figure 8. C-terminal HA-tagged MFN1 and MFN2. (A) Schematic representation of MFN1 and MFN2 GTPase and transmembrane (TM) domains before and after and HA-tag insertion. (B) Sequence of HA-tag.

By using CRISPR/Cas9 technology, two different HeLa cell lines were generated, one cell line expressing MFN1-HA and another cell line expressing MFN2-HA. HA-tag was selected among other tags typically used for immunoprecipitation due to its short length, the existence of good antibodies for its detection, and the existence of reliable beads coupled to antibodies for its optimal immunoprecipitation. The GTPase domain of MFN1 and MFN2 is situated near the N-terminal region. Thus, the CRISPR/Cas9 strategy was designed to target the C-terminal region for the insertion of the HA-tag, so that there was no interference with the folding or functionality of this region. Moreover C-terminal insertion of the HA-tag does not affect the transmembrane domain (TM) of MFN1 or MFN2.

For each gene, *MFN1* and *MFN2*, in order to achieve CRISPR/Cas9 mediated HA-tag insertion, the tools used were a plasmid and a single stranded oligodeoxynucleotide (ssODN) of 110 nt (Figure 9). The plasmid (pSpCas9(BB)-2A-GFP (PX458)) encoded the sequences of the Cas9

nuclease and the gRNA. The ssODN was composed of the sequence of the HA-tag flanked by two sequences of 40 nt homologous to the area around the stop codon of *MFN1* or *MFN2*.

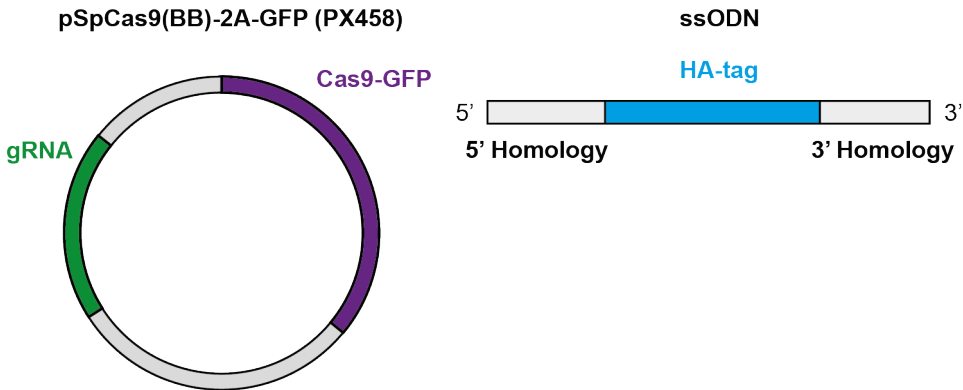


Figure 9. CRISPR/Cas9 strategy elements. CRISPR/Cas9 edited HeLa cells were transfected with a plasmid containing the gRNA sequence and the Cas9 sequence fused to GFP and with an ssODN containing an HA-sequence flanked by two regions of homology.

For gRNA identification, a sequence of 100 nt around the stop codon of either *MFN1* or *MFN2* was analyzed with the CRISPR MIT tool to identify PAMs and score their corresponding gRNAs in terms of specificity for *MFN1* or *MFN2* in the human genome. The gRNAs returned by the CRISPR MIT tool with the less predicted off-target effects were selected and are displayed in Figure 10. To integrate an HA tag by homologous recombination, the long ssODN was designed for each gene as depicted in Figure 10. The 5' end of the ssODN consisted of the 40 nt upstream of the stop codon of each gene, then the nucleotide sequence of the HA tag and on the 3' end 40 nt downstream of the stop codon. The way in which this system works is as follows: Cas9 is guided across the genome by the

gRNA to the area around *Mfn1* or *Mfn2* stop codon; Cas9 induces a DSB in the DNA that can be repaired by HR or NHEJ; the ssODN containing the sequence of the HA-tag serves as a template for DSB reparation by HR; as a result HA-tag is integrated in the genome.

Legend:

gRNA

PAM

STOP codon

Cleavage site ▲

HA-tag

MFN1 coding sequence 3' end

```
5'
AATTTTACTAAGCAGTTTCTACCTTCAAGCAATGAAGAATCCTTAAACAATAGA
GATTGCTTTGGTGTACCATGATAGGAGGAAAC 3'
```

ssODN sequence containing HA and *MFN1* homology regions

```
5'
AATTTTACTAAGCAGTTTCTACCTTCAAGCAATGAAGAATCCTTACCCATACG
ATGTTCCAGATTACGCTTAAACAATAGAGATTGCTTTGGTGTACCATGATAGGA
GAAAC 3'
```

MFN2 coding sequence 3' end

```
5'
AGCTCAACATGTTCACACACCAGTACCTGCAGCCAGCAGATAGTGGGCA
CCTGAGGCGGAGTCTGCGTGGAGAGGGGCGG 3'
```

ssODN sequence containing HA and *MFN2* homology regions

```
5'
AGCTCAACATGTTCACACACCAGTACCTGCAGCCAGCAGATACCCATACG
ATGTTCCAGATTACGCTTAGTGGGCACCTGAGGCGGAGTCTGCGTGGAGA
GGGGCGGTG 3'
```

Figure 10. CRISPR/Cas9 strategy to generate MFN1-HA and MFN2-HA cell lines. MFN1 and MFN2 genomic sequences and designed ssODNs for HA

insertion are shown.

4.1.2. The designed CRISPR/Cas9 system efficiently drives Cas9 to its target sites in MFN1 and MFN2 and integrates the HA-tag sequence

As a first approach to know whether HA-tag could be integrated in the desired sites of the genome, HeLa cells were transfected using the designed CRISPR/Cas9 tools for *MFN1* and for *MFN2*. Genomic DNA was isolated from these cells (Figure 11A) and two rounds of PCR were performed. In the first PCR round, a region of about 300 bp around the stop codon was amplified (Figure 11B). In the second round of PCR, a fragment of 200 bp was amplified using the FW primer from the previous reaction and a RV primer mapping the HA-tag sequence (Figure 11C). DNA from cells that were transfected with the plasmid, but not with the ssODN, was used as a negative control. PCR products were detected at the expected size (200 bp) for the cells transfected with the Cas9 plasmid and the ssODN, and no product was detected in the negative controls, meaning successful integration of HA-sequence in the genome (Figure 11C).

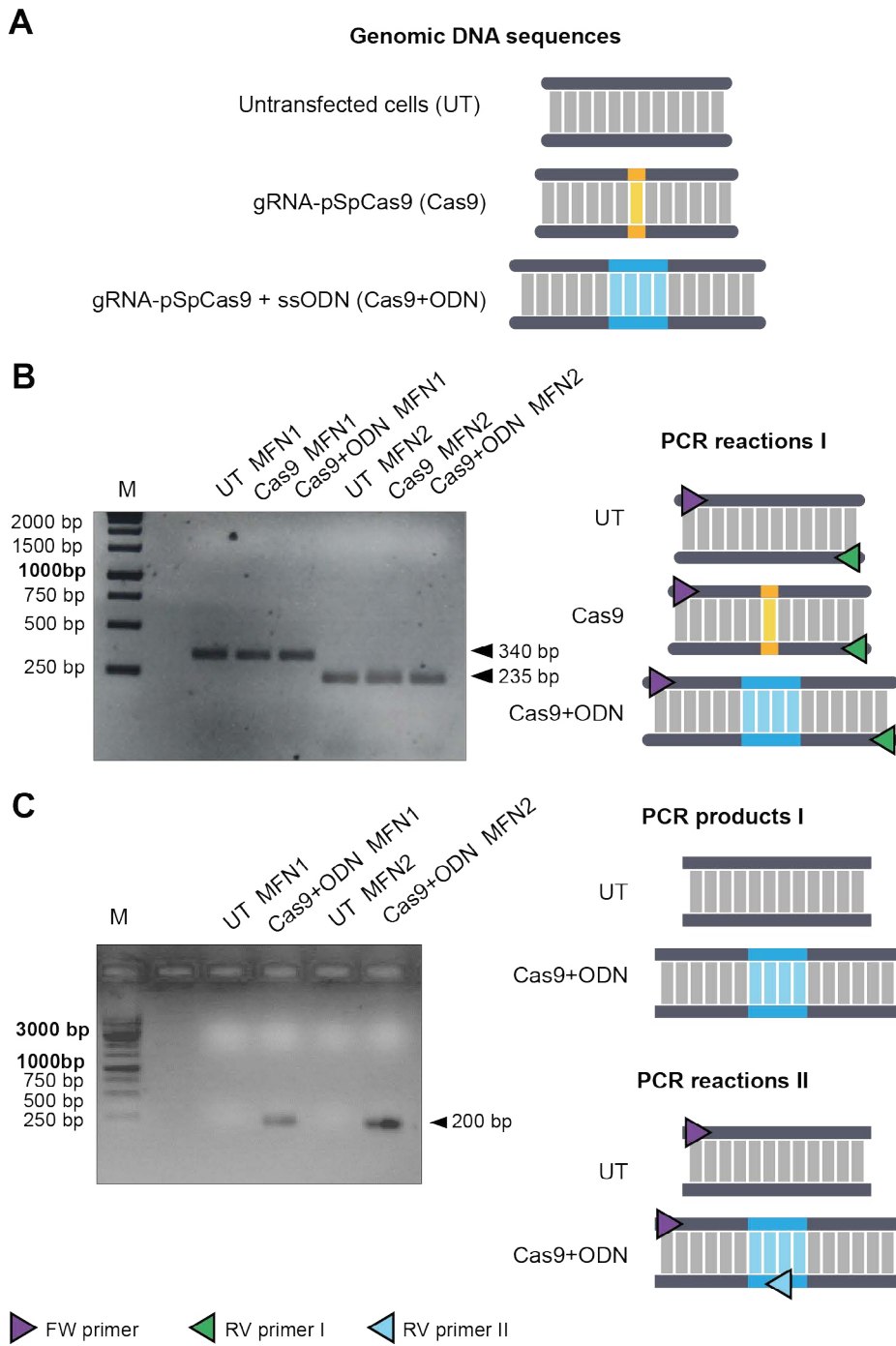


Figure 11. Assessment by PCR of HA-integration in MFN1 and MFN2. (A) Legend of DNA sequences. (B) PCR of the regions around the stop codon of MFN1

and MFN2 performed in genomic DNA of untransfected cells, cells transfected with the gRNA-pSpCas9 plasmid and cells transfected with the plasmid and ssODN. (C) PCR performed in the PCR products from B of untransfected cells and cells transfected with the gRNA-pSpCas9 plasmid and the ssODN using a primer that maps in the HA-insert.

4.1.3. Obtention of MFN1-HA and MFN2-HA HeLa clones after single cell sorting

Next, knowing that the designed CRISPR/Cas9 system effectively delivers the sequence of the HA-tag to the loci of interest, monoclonal HeLa cell lines with HA-tagged MFN1 and MFN2 were generated. HeLa cells were transfected with pSpCas9(BB)-2A-GFP (PX458) plasmid containing either the gRNA of MFN1 or the gRNA of MFN2 and the ssODN for each gene and subsequently selected based on GFP expression by fluorescence activated cell sorting (FACS) (Figure 12A). GFP positive cells were seeded individually and expanded until the number of cells of each clone was enough for protein extraction. Each clone was analyzed for the presence of HA by western blot (Figure 12B). The size expected for the HA band was 83 kDa for MFN1 and 87 kDa for MFN2. Among the 96 cells that were individually seeded for each gene, over 20 clones were able to grow. From these, two clones were positive for MFN1 and one clone was HA-positive for MFN2 as shown in Figure 12B.

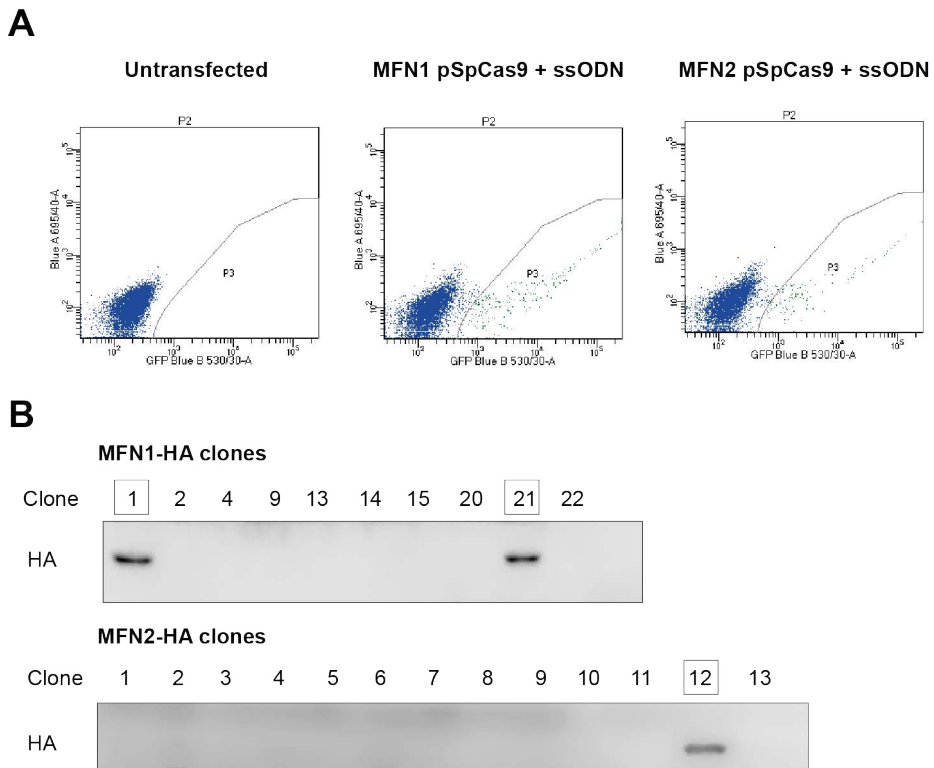


Figure 12. Generation of MFN1-HA and MFN2-HA clones. (A) Flow cytometry separation of GFP positive cells in untransfected cells and cells transfected with gRNA-pSpCas9 plasmid and ssODN to target MFN1 or MFN2. The graphs show the selected viable and non-aggregated cells, among which blue dots GFP free cells and green dots contained in the P3 sections represent GFP expressing cells. The cells in the P3 section were isolated and seeded in a 96 well plate. The X axis displays green fluorescence measurement in arbitrary units. The Y axis shows blue fluorescence measurement in arbitrary units. (B) HA-immunoblots of expanded GFP positive clones.

4.1.4. HA-immunoprecipitation retrieves all the HA-tagged protein from the lysate and reveals heterozygous insertion of the HA-tag

After obtaining HA-positive clones, the next step was to know whether it

was possible to immunoprecipitate endogenously expressed HA-tagged MFN1 and MFN2 and if the integration of the HA-tag sequence had been homozygous or heterozygous.

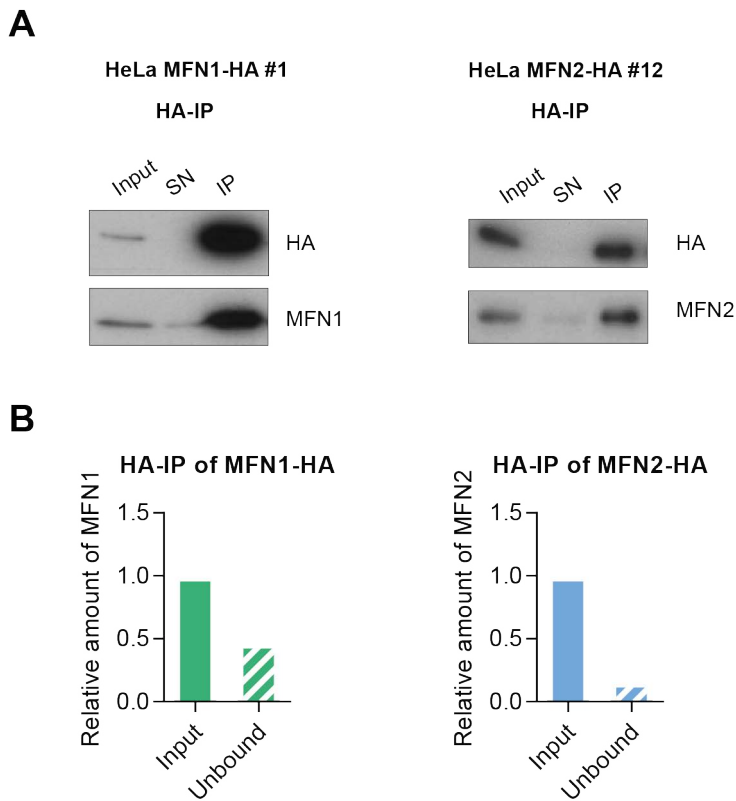


Figure 13. Validation of HA-tagging of MFN1 and MFN2. (A) HA, MFN1 and MFN2 western blots of input, supernatant (SN) and eluate (IP) fractions of HA-immunoprecipitation of MFN1-HA clone 1 and MFN2-HA clone 12. (B) Quantification of MFN1 and MFN2 that are not tagged.

Thus, HA-IP was performed in total cell lysates of the MFN1-HA and MFN2-HA HeLa cell lines using beads coupled to antibodies against HA (Figure 13A). The different fractions collected during the IP (input, supernatant and eluate) were analyzed by western blot using HA

antibodies. All the HA-tagged protein present in the input was absent in the supernatant fraction and appeared in the eluate fraction. Thus, all the HA-tagged protein in the lysate had been successfully bound to the beads and therefore immunoprecipitated. When using antibodies against MFN1 or MFN2, there was still a small fraction of MFN1 and MFN2 remaining in the supernatant, meaning that the HA-tag insertion had been heterozygous. HA-tagged MFN1 represented 50% of the whole amount of MFN1 in HeLa cells, whereas HA-tagged MFN2 was around 80% of the total quantity of MFN2 (Figure 13B). Since this fact would not affect considerably the subsequent experiments, we decided to continue using these cell lines throughout the next phases of the project.

4.2. Validation of the MFN1-HA and MFN2-HA HeLa cell lines

As the objective of this study is to identify functional partners of MFN1 and MFN2 in basal conditions and in conditions of induced autophagy and induced mitochondrial elongation by nutrient deprivation, we needed to verify that the insertion of an HA-tag does not affect the functioning of MFN1 and MFN2 under these conditions. Thus, mitochondrial morphology, mitochondrial protein expression, autophagy induction and starvation induced mitochondrial elongation were assessed.

4.2.1. C-terminal HA-tag insertion preserves mitochondrial fusogenic activity of MFN1 and MFN2

Mitochondrial morphology of MFN1-HA and MFN2-HA cell lines was

4 | Results

assessed by confocal microscopy. Cells were fixed and stained with an antibody against TOM20. Cells were classified in three categories according to the predominant morphology of their mitochondria: elongated, short or oval. The three categories were equally represented in MFN1-HA and MFN2-HA cells compared to WT HeLa cells (Figure 14).

Protein expression of mitochondrial proteins was examined by western blot in total protein lysates of MFN1-HA and MFN2-HA cell lines. Mitochondrial fusion machinery proteins levels were assessed to verify the correct functioning of the mitochondrial fusion process. The expression of porin (VDAC1) was also analyzed as a marker for mitochondrial mass. The levels of MFN1, MFN2, OPA1 and VDAC1 remained the same as in the WT in both MFN1-HA (Figure 15) and MFN2-HA (Figure 16). These results together with the mitochondrial morphology analysis indicate that the insertion of an HA-tag does not affect the fusogenic properties of MFN1 and MFN2.

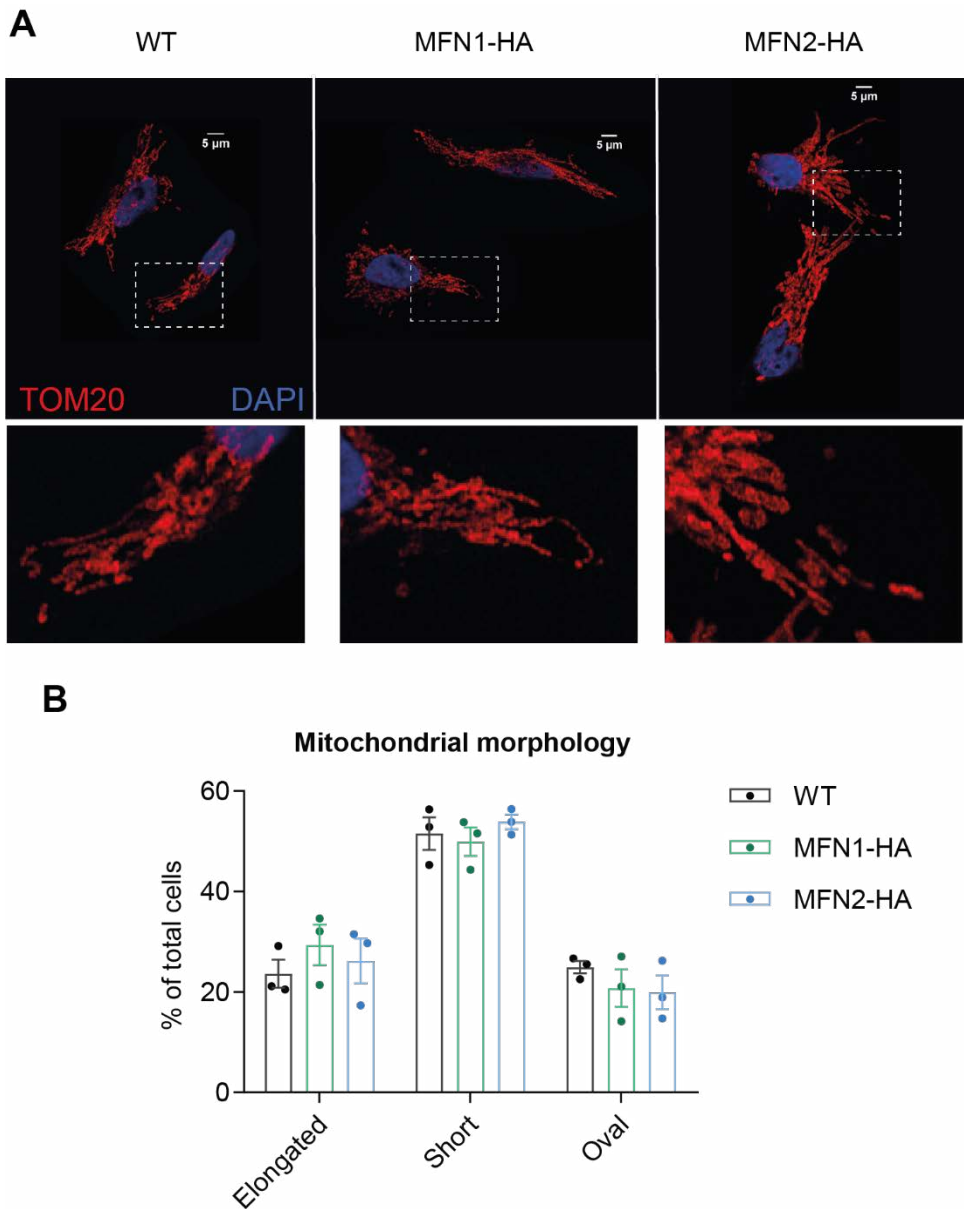


Figure 14. Mitochondrial morphology evaluation in MFN1-HA and MFN2-HA cells. (A) Representative images of fixed WT, MFN1-HA and MFN2-HA cells stained with an antibody against TOM20 and DAPI. Scale bar: 5 μ m. (B) Quantification of mitochondrial morphology in WT, MFN1-HA and MFN2-HA HeLa cells. Percentages of each category of cells (elongated, short, oval)

4 | Results

per experiment are represented in the bar graph. Three experiments were performed and >120 cells were counted per cell line per experiment. Data passed Saphiro-Wilk normality test. Results of MFN1-HA and MFN2-HA were compared with the results of the WT using T-test.

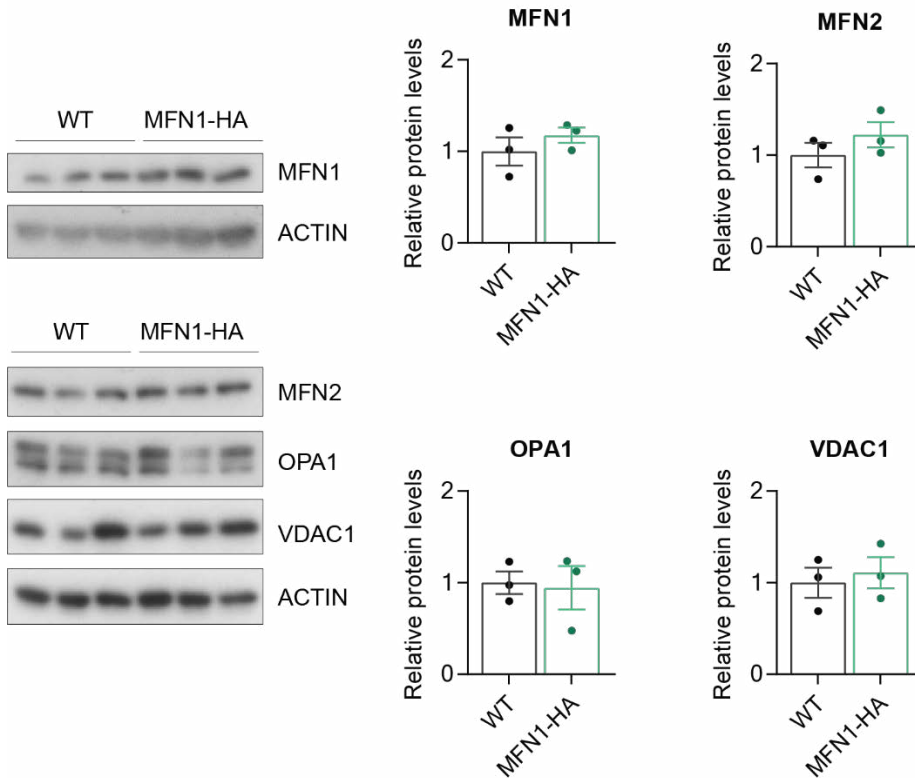


Figure 15. Assessment of mitochondrial protein levels of MFN1-HA clone 1. Western blots of MFN1, MFN2, OPA1 and VDAC1 from total protein homogenates of WT cells and MFN1-HA cells and quantifications of protein levels. N=3. Saphiro-Wilk test was performed and protein expression levels were found to follow a Gaussian distribution. Levels of expression of the mentioned proteins in WT and MFN1-HA cells were compared using paired T-test.

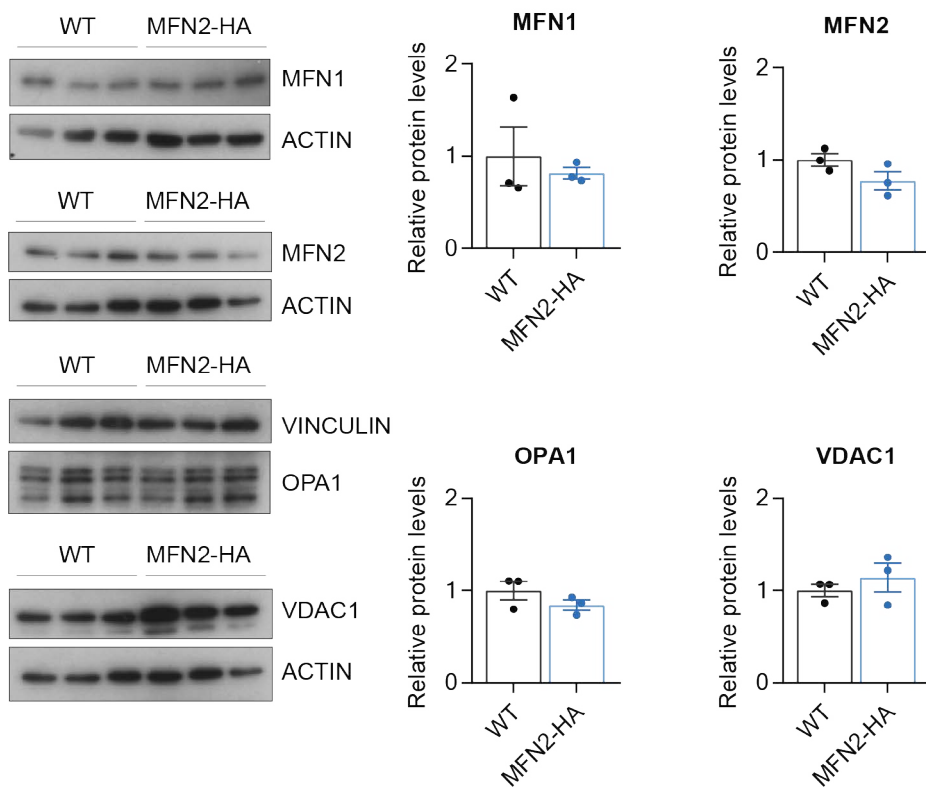


Figure 16. Assessment of mitochondrial protein levels of MFN2-HA clone 12. Western blots of MFN1, MFN2, OPA1 and VDAC1 from total protein homogenates of WT cells and MFN2-HA cells and quantifications of protein levels. N=3. Saphiro-Wilk test was performed and protein expression levels were found to follow a Gaussian distribution. Levels of expression of the mentioned proteins in WT and MFN2-HA cells were compared using paired T-test.

4.2.3. C-terminal HA-tagging of MFN1 and MFN2 results in normal induction of autophagy and mitochondrial elongation upon starvation treatment

Before studying how nutrient deprivation affects the functioning of

4 | Results

MFN1 and MFN2 in mitochondrial elongation or autophagy, it was necessary to evaluate these processes in the CRISPR/Cas9 generated cell lines. Previous studies have used EBSS treatment (5 mM KCl, 26 mM NaHCO₃, 117 mM NaCl, 1mM NaH₂PO₄-H₂O, 5 mM D-Glucose) to generate an environment of serum and nutrient deprivation and promote autophagosome formation¹⁶ and mitochondrial hyperfusion¹⁴.

In order to know whether autophagy occurred in the correct way upon starvation stimulus in the HA-tagged cell lines, cells were treated with EBSS medium or EBSS and Bafilomycin A1 (Baf A1) for different time durations: 0, 0.5, 1, 1.5 and 2 h. By treating the cells with EBSS, the formation of autophagosomes is induced. Baf A1 blocks autophagosome fusion with lysosomes and lysosomal degradation. Therefore, by adding Baf A1 to EBSS medium, the formation of autophagosomes is promoted and their degradation is blocked. To quantify autophagosome accumulation, protein levels of the autophagosomal marker LC3B-II were measured and compared in WT cells and HA-tagged cells (Figure 17A). The fold change of LC3B-II upon addition of Baf A1 to EBSS medium was calculated for every timepoint (Figure 17B) in order to quantify the magnitude of autophagosome accumulation. After 1h of starvation treatment we observed that LC3B-II started to accumulate in all the cell lines and this accumulation was enhanced in later timepoints. The rise in the accumulation of LC3B-II started to be statistically significant after 1 h of treatment in all the cell lines. There was a 2-fold increase in LC3B-II protein accumulation in WT, MFN1-HA and MFN2-HA cells after 1 h of EBSS treatment combined with Baf A1 (Figure 17B and 17C). Thus,

HA-insertion does not affect autophagosome formation upon starvation treatment.

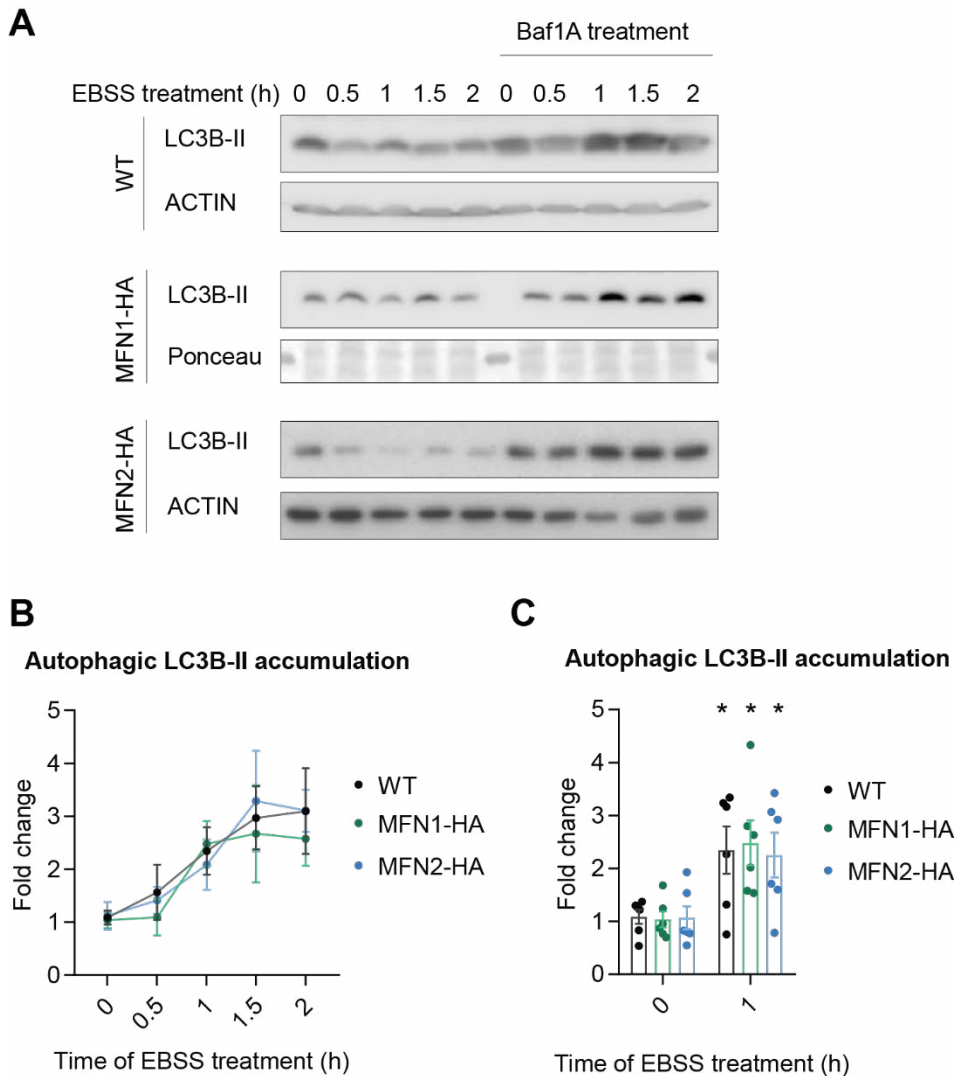


Figure 17. Assessment of starvation autophagic flux of LC3B-II in WT, MFN1-HA and MFN2-HA cells. (A) Immunoblots of LC3B-II after starvation or starvation and Bafilomycin A1 treatments for the indicated durations in WT, MFN1-HA and MFN2-HA cells. (B) Fold change in LC3B-II accumulation after starvation treatments of different durations in WT, MFN1-HA and MFN2-HA cells

4 | Results

normalized to 0h of treatment. N=6. (C) Fold change in LC3B-II accumulation after 1 hour of starvation treatment normalized to 0h of treatment. N=6. Data passed normality Saphiro-Wilk test. MFN1-HA and MFN2-HA results were compared with WT results using unpaired T-test. * represents p-values ≤ 0.05 .

It is also known that mitochondria elongate during starvation in a MFN1 and OPA1 dependent manner¹⁴. To evaluate whether nutrient deprivation could promote mitochondrial elongation in the CRISPR/Cas9 generated cell lines, mitochondrial morphology after 1 h of EBSS treatment was assessed. Cells were treated with EBSS for 1 h and then fixed for fluorescent labeling with antibodies against TOM20 in order to visualize mitochondria (Figure 18A). In the three cell lines analyzed, mitochondria became more elongated to the same extent after 1 h of EBSS treatment (Figure 18B). Hence, HA-tag insertion did not have any detrimental effects for starvation induced mitochondrial elongation.

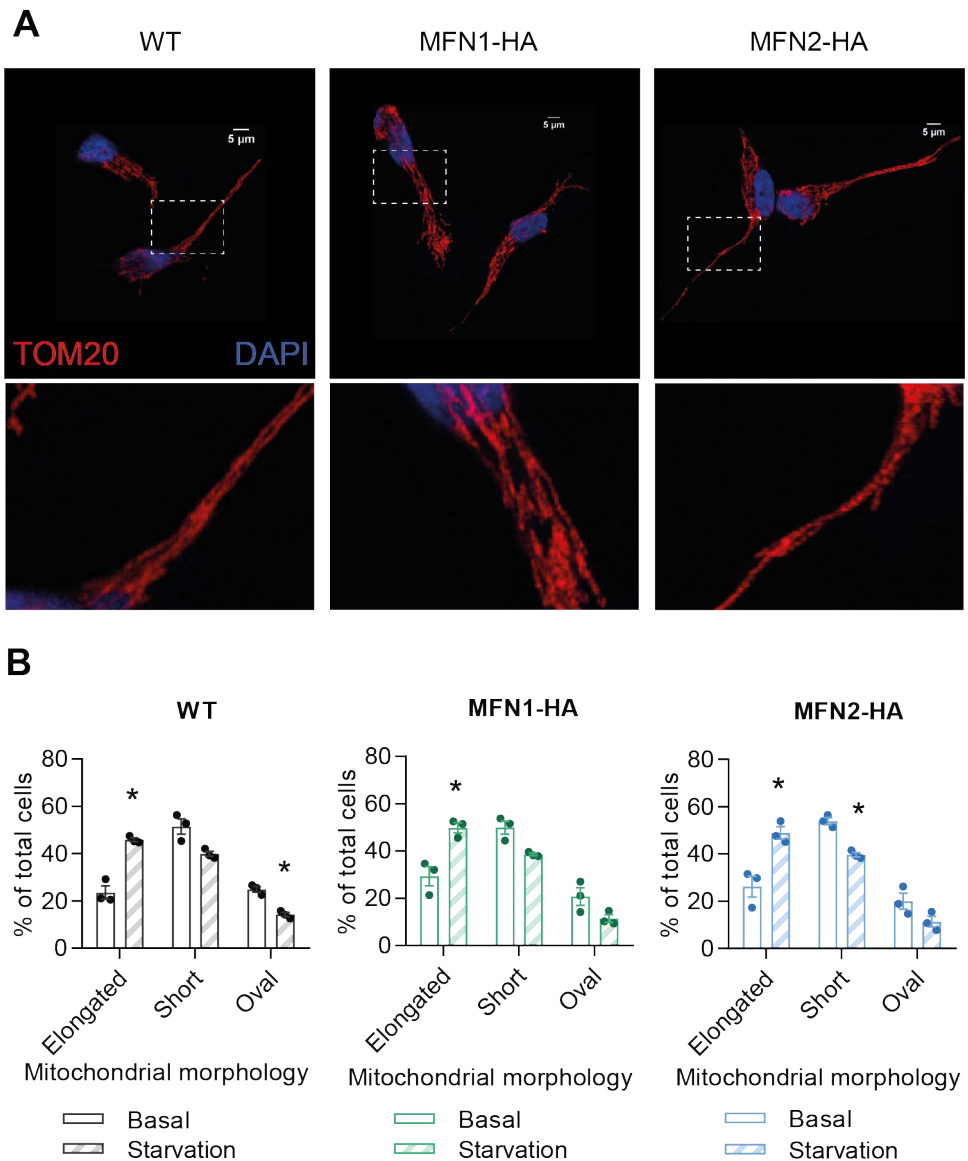


Figure 18. Mitochondrial elongation under starvation conditions in WT, MFN1-HA and MFN2-HA cells. Representative images of cells treated with DMEM or EBSS starvation medium for 1h that were fixed and stained with an antibody against TOM20 and with DAPI. Scale bar: 5 μ m. Percentages of each category of cells (elongated, short, oval) per experiment are represented in the bar graphs. Three experiments were performed and >120 cells were counted

per cell line per experiment. Data passed Saphiro-Wilk normality test. Results of starvation conditions were compared with the results of basal conditions using T-test. * represents p-values ≤ 0.05 .

4.3. Selection of the conditions of interest for finding MFN1-HA and MFN2-HA partners

The goal of this study was to identify novel interactors of MFN1 and MFN2 and to better characterize the participation of MFN2 in autophagosome formation and the role of MFN1 in mitochondrial elongation conditions of restricted nutrient availability. Since 1 h of EBSS treatment boosts autophagosome formation (Figure 17) and induces mitochondrial elongation (Figure 18), we chose this condition to identify MFN1 and MFN2 binding partners contributing to mitochondrial elongation and autophagy. In summary, we chose to work under basal conditions and in conditions of 1 h of treatment with EBSS.

4.4. Optimization of immunoprecipitation protocol

The next step was to optimize the protocol to immunoprecipitate MFN1-HA and MFN2-HA. Previously used protocols were taken into account and modified to find the best IP settings. Since MFN1 and MFN2 have a high degree of similarity, are both present in the OMM and are transmembrane proteins, we assumed that an optimal IP protocol would be the same for both proteins. Therefore, the optimization process was performed only with MFN2-HA cells.

4.4.1. 1% Digitonin efficiently solubilizes MFN2-HA and preserves MFN1-MFN2 interaction

MFN1 and MFN2 are transmembrane proteins which probably will participate in membrane protein complexes. This fact is critical for choosing the right detergent to solubilize MFN1 and MFN2 in such a way that their interactions are preserved. For this reason, the suitability of four mild detergents for immunoprecipitation of MFN1 and MFN2 was assessed. Triton X-100, Brij99, CHAPS and digitonin were tested for MFN2 solubilization and MFN1-MFN2 interaction preservation. Triton X-100 is widely used for protein IP and has been preferentially used to study MFN2 protein interactions ^{18,21,43}. Brij99 is used to preserve hydrophobic interactions between proteins ^{208,209}. CHAPS is a mild detergent that has been used to solubilize OMM proteins ²¹⁰. Digitonin is preferentially used to co-immunoprecipitate mitochondrial membrane complexes ^{211,212}. After literature reviewing, the concentration used for cell lysis and protein binding to the beads was 1% for all the detergents and it was decreased to 0.1% for the washing steps.

After Dounce homogenization in lysis buffer containing 1% Triton X-100, Brij99, CHAPS and digitonin and 30 minutes of incubation of the HeLa cells at 4°C, we were able to solubilize MFN2. Moreover, HA-immunoprecipitation was performed successfully with all these detergents (Figure 19). Nevertheless, the interaction between MFN1 and MFN2 was better preserved when using CHAPS, and even better with digitonin (Figure 19). The interaction was lost when lysis buffer was prepared with Triton X-100 or Brij99 (Figure 19). Several studies

have shown that CHAPS is not fully efficient for protein complex solubilization and that digitonin should be preferentially chosen over CHAPS ^{213,214}. Therefore, digitonin was selected for endogenous HA-immunoprecipitation of MFN1-HA and MFN2-HA.

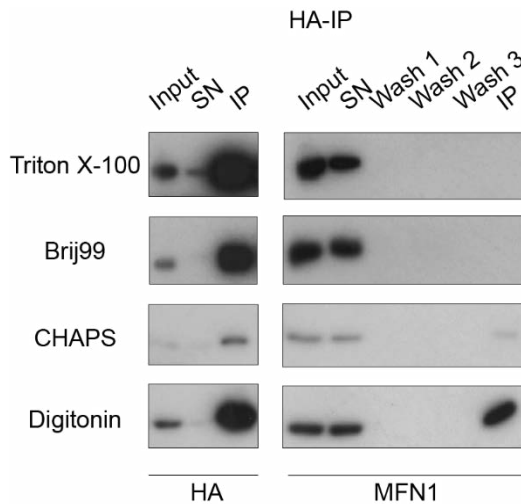


Figure 19. HA-IP performed with 1% Triton X-100, Brij99, CHAPS or Digitonin in lysis buffer. HA immunoblots of input, supernatant (SN) and eluate (IP) fractions are shown. MFN1 immunoblots of input, SN, washing steps 1, 2 and 3, and IP are displayed. MFN2-HA HeLa cells were mechanically disrupted in lysis buffer with a Dounce homogenizer and incubated at 4°C for 30 minutes. Lysis buffer contained 1% Triton X-100, Brij99, CHAPS or Digitonin. Beads were washed 5 times with wash buffer containing 0.1% of the detergent used for lysis.

4.4.2. Magnetic beads improve the specificity of the HA-IP

In order to minimize non-specific binding of proteins to the HA-beads that would interfere with the detection of true interactors, non-specific binding was compared in agarose beads and dynabeads (magnetic

beads). MFN2-HA IP was performed in parallel in agarose beads and in dynabeads. Digitonin was used to lyse the cells and in the washing steps as described in the previous section. Eluates were run on a polyacrylamide gel and subjected to silver staining to examine the total protein content and analyzed by western blot.

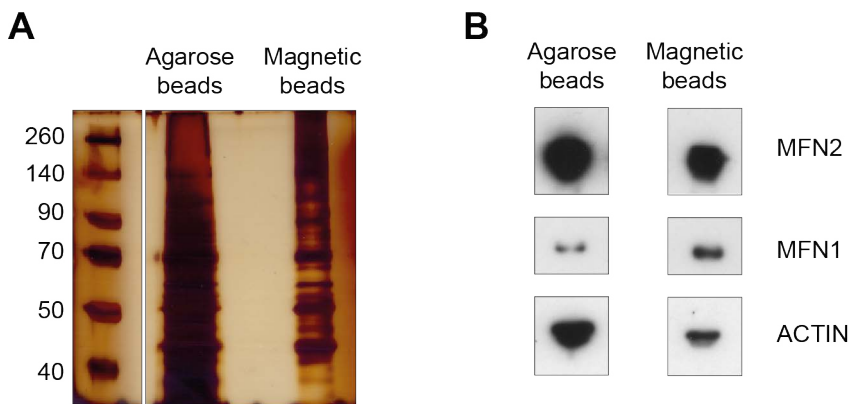


Figure 20. HA-IP performed with agarose beads and magnetic beads. (A) Silver staining of IP fractions of two experiments of HA-IP of MFN2-HA cells where agarose beads or magnetic beads were used. (B) MFN2, MFN1 and ACTIN immunoblots of IP fractions obtained from HA-IP of MFN2-HA cells performed with agarose beads and magnetic beads.

Higher content of background was observed in agarose beads compared to dynabeads (Figure 20A). Moreover, immunoblots of IP fractions revealed higher yield of MFN1 after HA-IP of MFN2-HA when using magnetic beads and lower non-specific binding of actin (Figure 20B). Altogether, these results indicated that magnetic beads improved the specificity of the HA-IP. Hence, we decided to use HA-dynabeads for immunoprecipitation of MFN1-HA and MFN2-HA.

4.4.3. Maximum binding of endogenous MFN2-HA to HA-beads is achieved with 6.25 mg of protein per 10 μ l of beads

In order to maximize the binding of MFN1-HA and MFN2-HA to the beads, different ratios of protein to beads were examined. Five different quantities of protein extracted from MFN2-HA cells (5 mg, 6.25 mg, 7.5 mg, 8.75 mg and 10 mg) were immunoprecipitated with 10 μ l of HA-dynabeads (Figure 21). The binding capacity of these beads is around 300 pmol per μ l of beads. Therefore, 10 μ l of HA-dynabeads could bind to 3 nmol of HA-protein.

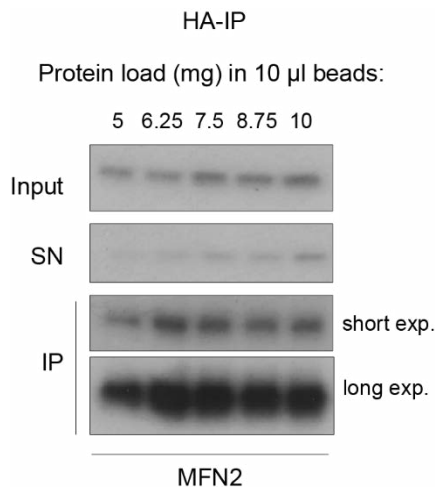


Figure 21. Assessment of MFN2-HA binding to magnetic beads at different protein concentrations. HA-IP of MFN2-HA cells using different protein amounts (5, 6.25, 7.5, 8.75 and 10 mg) per 10 μ l of beads. MFN2 western blots of input, supernatant (SN) and eluate (IP) fractions are shown.

Binding capacity of the beads with MFN2-HA was saturated when 6.25 mg of protein were added to 10 μ l of beads and higher quantities of protein did not yield a bigger amount of MFN2. Therefore, we chose the

ratio of 6.25 mg of protein to 10 μ l of beads to perform the HA-IP for the MS analysis. For MS detection of novel binding candidates of MFN1 and MFN2, the amount of protein and beads used for IP were escalated to a level that was sufficient for protein identification by MS. Twenty five mg of protein and 40 μ l of beads were used for HA-IP. These 40 μ l of HA-dynabeads could bind to 12 nmol of HA-protein.

4.4.4. Immunoprecipitated MFN2-HA in basal and in starvation conditions is detectable by Coomassie staining

Next, to assess the enrichment of MFN2-HA in the HA-beads eluate, HA-IP of MFN2-HA was performed in basal and starvation conditions. The optimized protocol was applied to pull down MFN2-HA. The eluate was ran on a polyacrylamide gel which was stained with InstantBlue Coomassie. MFN2 was detectable in the both IP experiments, the one performed in basal conditions and the one done under starvation conditions (Figure 22). Bands corresponding to potential interactors that did not appear in the WT control were observed. More bands were appreciated in basal conditions than in starvation, which could mean that MFN2 interacts with more proteins in basal conditions than after EBSS treatment.

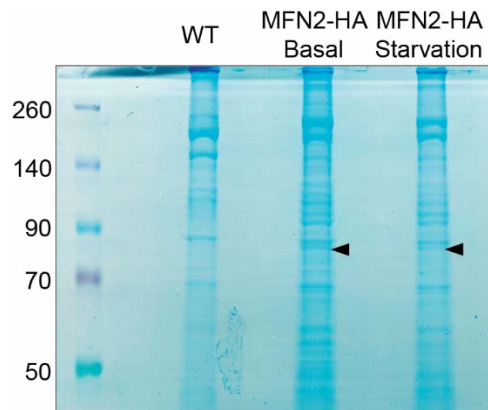


Figure 22. Coomassie staining of HA-IP in basal and starvation conditions. IP fractions of HA-IP performed in MFN2-HA cells in basal and starvation conditions and WT cells as a negative control. Arrows indicate MFN2-HA band.

4.5. HA-IP coupled to MS identifies potential binding partners of MFN1-HA and MFN2-HA in basal and starvation conditions

4.5.1. Endogenous HA-IP of MFN1-HA and MFN2-HA provides insight into the composition of MFN1-MFN2 complexes

We performed endogenous HA-IP in WT, MFN1-HA and MFN2-HA HeLa cells under basal and under starvation conditions (Figure 23). HA-IP performed in WT cells was used as a negative control in subsequent mass spectrometry analysis to determine which proteins were bound in a non-specific manner to the beads after MFN1-HA and MFN2-HA immunoprecipitation. Three biological replicates of this HA-IP were performed. We observed that after MFN2-HA IP a considerable amount of MFN1 was co-immunoprecipitated, however when pulling down MFN1-

HA, the quantity of MFN2 that was recovered was lower. Moreover, when MFN1 was immunoprecipitated after one hour of starvation more MFN2 was observed in the eluate in basal conditions than in starvation conditions. However, when MFN2 was immunoprecipitated, more MFN1 was observed in the eluate under starvation conditions than in a basal state.

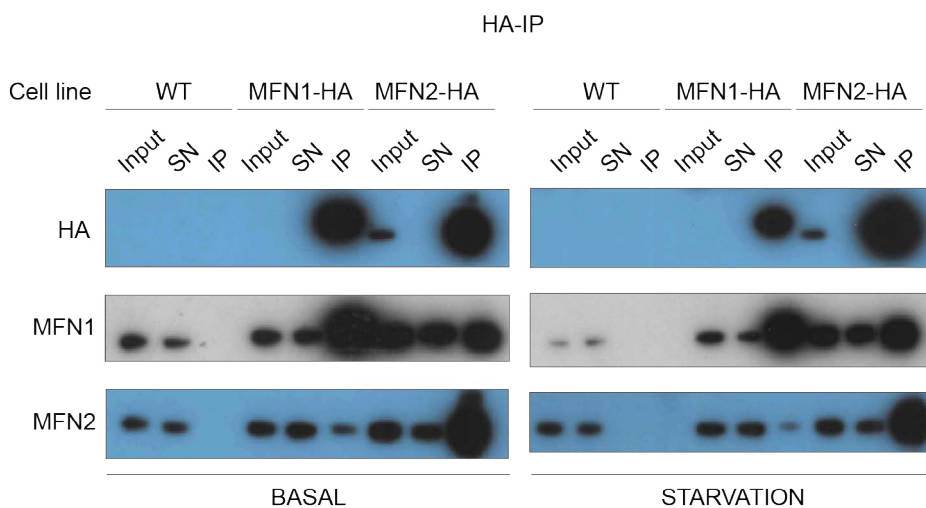


Figure 23. HA-IP of WT, MFN1-HA cells and MFN2-HA cells in basal and starvation conditions. HA, MFN1 and MFN2 immunoblots of input, supernatant (SN) and eluate (IP) fractions of HA-IP of WT, MFN1-HA and MFN2-HA cells in basal conditions and after 1 hour of EBSS treatment. Input = 0.5%, SN = 0.5%, IP = 5%. N=3.

In order to assess more precisely the amount of MFN1 and MFN2 that is present in MFN1-MFN2 complexes, we quantified the proportion of total MFN1 that interacted with MFN2 and the proportion of total MFN2 that interacted with MFN1 (Figure 24).

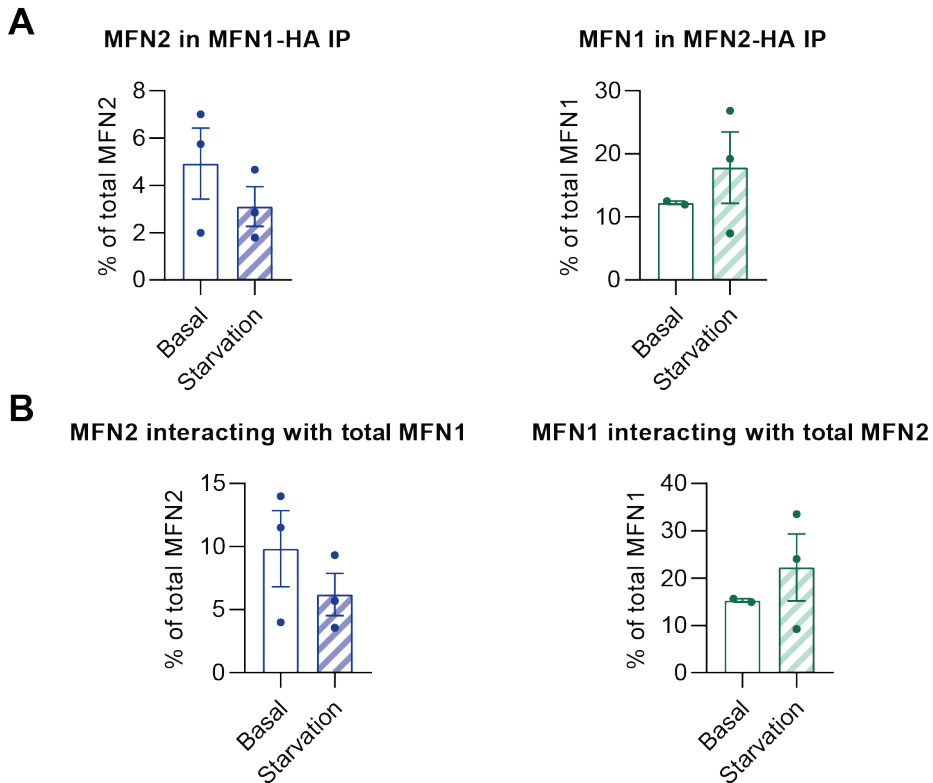


Figure 24. Proportions of MFN1 or MFN2 that interact with MFN2 or MFN1 respectively. (A) Quantity of MFN2 present in MFN1-HA IP and MFN1 present in MFN2-HA IP. N=3. (B) Quantity of MFN2 that interacts with all the MFN1 present in the cell (with and without HA-tag) and quantity of MFN1 that interacts with all the MFN2 in the cell (with and without HA-tag).

First, the amount of MFN1 that immunoprecipitated with MFN2-HA and the quantity of MFN2 that immunoprecipitated with MFN1-HA were calculated. MFN1 and MFN2 signal was quantified in HA-IP immunoblots of each replicate. Next, the signal was normalized by the western blot load. Input signals quantified corresponded to 0.5% of total lysate used and IP signals represented 5% of the eluate. IP normalized values were divided by input normalized values to obtain how much of

MFN2 interacted with MFN1 and how much of MFN1 interacted with MFN2. These calculations retrieved the proportion of MFN1 or MFN2 that were present in MFN2-HA or MFN1-HA IPs. These proportions are shown in Figure 24A. Subsequently, knowing that HA-tagged MFN1 represents 50% of the whole amount of MFN1 in HeLa cells and MFN2-HA represents 80% of the total MFN2, we extrapolated the percentage of the total MFN1 or MFN2 in the cell that interacts with MFN2 or MFN1 respectively (Figure 24B).

Under basal conditions, 10% of total MFN2 interacts with MFN1, and under starvation conditions this percentage drops down to 6%. Besides, in basal conditions, 15% of total MFN1 interacts with MFN2 and under starvation conditions this percentage is increased to 22%. These differences that we observed were not statistically significant, although the trends observed were in line with the preliminary assumptions that we had made: 1) From the total pool of MFN2, more MFN2 interacts with MFN1 under basal conditions than under starvation conditions; 2) From the total MFN1 in the cell, more MFN1 interacts with MFN2 under starvation conditions than under basal conditions.

Subsequently, we estimated the total amount in terms of moles of MFN1 and MFN2 that form MFN1-MFN2 complexes in the samples that we had immunoprecipitated under basal and starvation conditions. The cellular lysates used for HA-IP contained 22.5 mg of total protein. We assumed that all the MFN1-MFN2 complexes had the same composition.

Knowing that the maximum amount of HA-protein recovered by one μ l of beads was 300 pmol, we calculated that the HA-protein bound by

4 | Results

40 μ l of beads was 12 nmol. Next, we calculated the amount in nmol recovered of MFN2 after MFN1-HA IP and of MFN1 after MFN2-HA IP. Since we observed under basal conditions that the same amount of HA-MFN1 and HA-MFN2 was recovered, we considered that MFN1-HA IP had yielded 12 nmol of MFN1 and that MFN2-HA IP had yielded 12 nmol of MFN2. However, under starvation conditions, HA-immunoblot revealed a higher amount of MFN2 immunoprecipitated after MFN2-HA IP than MFN1 immunoprecipitated after MFN1-HA IP. Therefore we considered that MFN2-HA IP had yielded 12 nmol of MFN2 and we estimated the nmol of MFN1 in MFN1-HA IP taking into account the signal of the HA-antibody compared to MFN2-HA IP. The average estimated amount of immunoprecipitated MFN1-HA under starvation conditions was 4.5 nmol. We obtained the absolute quantities of MFN1 and MFN2 that form complexes in 22.5 mg of a cell lysate (Figure 25).

In basal conditions, 0.27 nmol of MFN1 interact with 0.15 nmol of MFN2 in a cellular lysate containing 22.5 mg of total protein. Depriving the cells from amino acids supposes a decrease in the amount of MFN1-MFN2 complexes since 0.15 nmol of MFN1 interact with 0.06 nmol MFN2 in a cellular lysate containing 22.5 mg of total protein. Although these changes were not statistically significant, the trends that we could observe were coherent with the appreciation that we had previously made: MFN1-MFN2 heterooligomers are composed of more MFN1 subunits than MFN2 subunits.

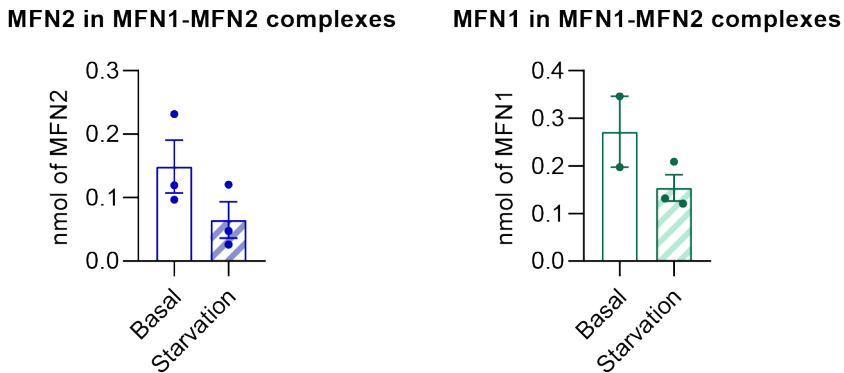


Figure 25. Absolute amount of MFN1 and MFN2 in MFN1-MFN2 complexes in 22.5 mg of total protein. MFN1 and MFN2 nmol that participate in MFN1-MFN2 complexes under basal and starvation conditions in a cellular lysate that contains 22.5 mg of total protein.

4.5.2. Mass spectrometry of HA-IP of MFN1-HA and MFN2-HA reveals different interactome landscapes in basal and starvation conditions

The eluates from the three biological replicates of endogenous HA-IP of MFN1-HA and MFN2-HA in basal and starvation conditions were processed for subsequent MS analysis. Briefly, samples were digested with trypsin and injected in an Orbitrap mass spectrometer for peptide detection. The peptides identified from MFN1-HA and MFN2-HA samples were compared with the peptides from WT samples to identify those peptides that were significantly enriched.

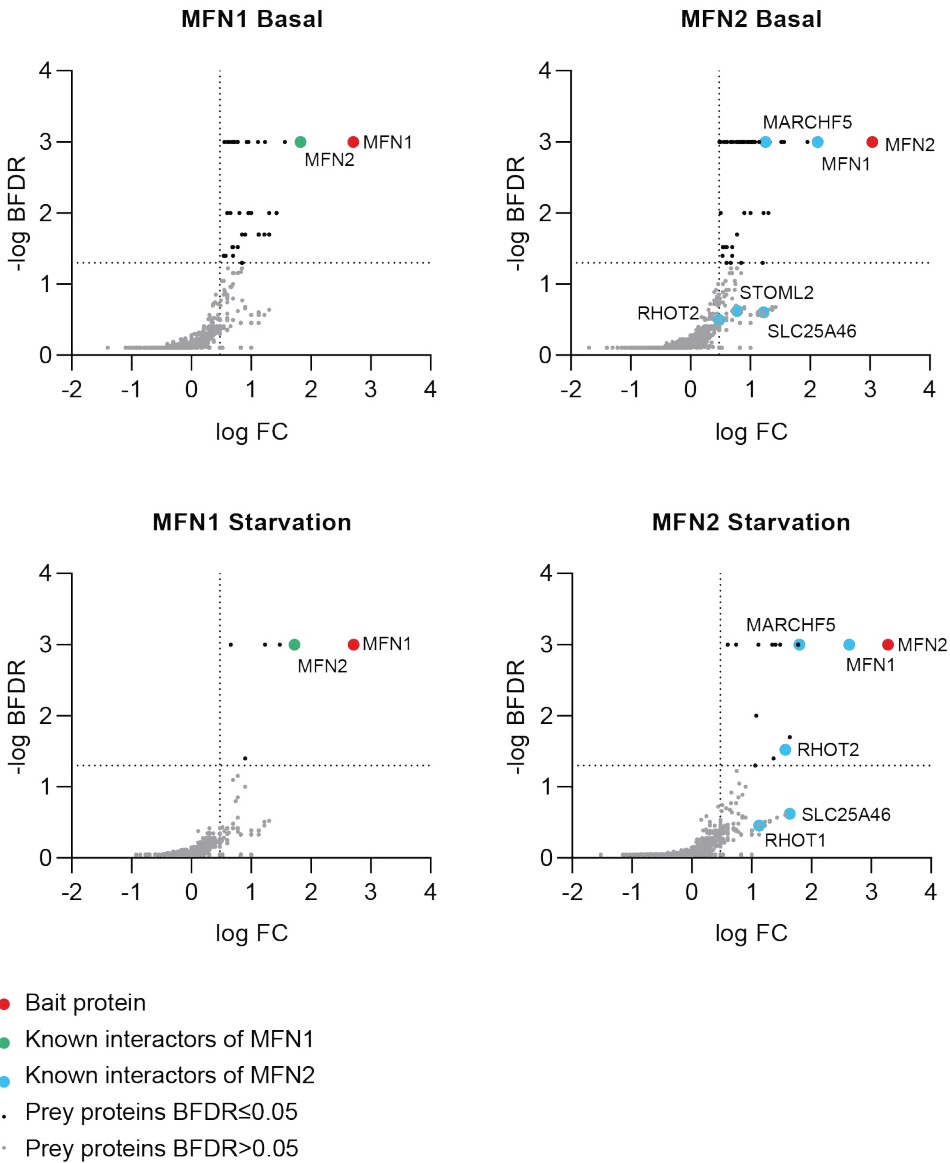


Figure 26. Results of mass spectrometry of MFN1-HA and MFN2-HA HA-IP in basal and starvation conditions. Dot plot diagrams of mass spectrometry results after applying SAINT express algorithm. Bait proteins are shown in red. Known interactors of MFN1 and MFN2 found enriched after SAINT express analysis are shown in green or in blue respectively. Binding candidates showing BFDR equal or lower than 0.05 are displayed in black. Proteins with BFDR

higher than 0.05 appear in grey. Dotted lines inside the diagram represent the thresholds of $-\log$ BFDR and \log FC to consider a protein as a high confidence interactor.

Fold changes (FC) and Bayesian false discovery rates (BFDR) in the number of unique peptides identified for each protein were calculated in MFN1-HA and MFN2-HA samples taking WT samples as a negative control. Thresholds applied to consider any of the identified proteins as a potential binding partner were a BFDR lower or equal to 0.05 and a FC higher or equal to 3. In order to plot the identified proteins, the logarithms of the FC and BFDR were calculated, and each protein was assigned an X value (\log FC) and a Y value ($-\log$ BFDR). These values were plotted in the graphs that are shown in Figure 26. We present all the high confidence interactors discovered together with the number of unique peptides identified, FC and BFDR in Table 1. Already known binding partners of MFN1 and MFN2 that were identified are shown in the plots in green for MFN1 or in blue for MFN2. MFN2⁶ was detected with statistical significance among the candidates of MFN1, and MFN1⁶, MARCHF5²⁰ and RHOT2²¹ appeared significantly enriched among the potential partners of MFN2.

Table 1. High confidence interactors of MFN1 and MFN2 under basal and starvation conditions. Bait value is MFN1-B for the interactors of MFN1 under basal conditions, MFN1-S for MFN1 partners under starvation conditions, MFN2-B for the binding candidates of MFN2 under basal conditions and MFN2-S for MFN2 interactors under starvation conditions. PreyGene refers to the prey proteins identified by MS. Spec is the number of unique peptides for each prey per replicate. AvgSpec is the average of unique peptides in the three replicates. Ctrl is the number of unique peptides identified in the negative control. FC

4 | Results

(Fold change) is the enrichment of the prey compared to the negative control.

BFDR is the Bayesian false discovery rate.

Bait	PreyGene	Spec	AvgSpec	Ctrl	FC	BFDR
MFN1-B	MFN1-HA	48 63 42	51	0 0 0	510	0
MFN1-B	MFN2	6 9 5	6.67	0 0 0	66.67	0
MFN1-B	PSPC1	7 4 0	3.67	0 0 0	36.67	0
MFN1-B	ZNF185	8 6 3	5.67	0 1 0	17	0
MFN1-B	AMOTL1	1 8 4	4.33	0 0 1	13	0
MFN1-B	ITPR2	10 7 1	6	0 1 1	9	0
MFN1-B	NDFIP2	0 8 9	5.67	0 1 1	8.5	0
MFN1-B	FMR1	9 8 1	6	1 1 1	6	0
MFN1-B	UPF1	27 14 0	13.67	3 3 1	5.86	0
MFN1-B	NONO	94 58 11	54.33	6 23 2	5.26	0
MFN1-B	FXR2	14 11 1	8.67	2 2 1	5.2	0
MFN1-B	DHX30	18 12 1	10.33	3 2 1	5.17	0
MFN1-B	NUFIP2	15 19 2	12	2 4 1	5.14	0
MFN1-B	FUS	15 29 14	19.33	3 4 5	4.83	0
MFN1-B	G3BP2	16 17 2	11.67	2 4 2	4.38	0
MFN1-B	SFPQ	83 76 22	60.33	5 28 12	4.02	0
MFN1-B	G3BP1	48 25 6	26.33	7 5 10	3.59	0
MFN1-B	RSF1	1 2 5	2.67	0 0 0	26.67	0.01
MFN1-B	DOHH	2 4 2	2.67	0 0 0	26.67	0.01
MFN1-B	FAM98A	4 2 0	2	0 0 0	20	0.01
MFN1-B	AFAP1	5 2 3	3.33	0 1 0	10	0.01
MFN1-B	MYO1F	1 3 5	3	1 0 0	9	0.01
MFN1-B	AFAP1L1	0 3 6	3	0 0 1	9	0.01
MFN1-B	CGN	12 12 8	10.67	1 4 0	6.4	0.01
MFN1-B	FXR1	19 10 7	12	3 4 1	4.5	0.01
MFN1-B	LRRFIP2	4 8 8	6.67	1 2 2	4	0.01
MFN1-B	BYSL	2 2 2	2	0 0 0	20	0.02
MFN1-B	TMEM9	2 2 2	2	0 0 0	20	0.02
MFN1-B	RAPH1	2 1 2	1.67	0 0 0	16.67	0.02
MFN1-B	RPL31	2 2 0	1.33	0 0 0	13.33	0.02
MFN1-B	KLHL13	2 2 0	1.33	0 0 0	13.33	0.02
MFN1-B	PUF60	2 2 0	1.33	0 0 0	13.33	0.02
MFN1-B	RAB5C	0 2 2	1.33	0 0 0	13.33	0.02
MFN1-B	RBM18	0 2 2	1.33	0 0 0	13.33	0.02

MFN1-B	SIPA1L1	6 2 8	5.33	2 0 0	8	0.02
MFN1-B	UBP1	1 3 3	2.33	0 1 0	7	0.02
MFN1-B	SLC25A24	1 7 4	4	0 1 1	6	0.03
MFN1-B	RPS15	3 7 5	5	1 1 1	5	0.03
MFN1-B	ALPP	11 7 16	11.33	1 1 5	4.86	0.03
MFN1-B	ELAVL1	5 4 1	3.33	0 1 1	5	0.04
MFN1-B	LUC7L2	5 8 2	5	1 2 1	3.75	0.04
MFN1-B	POTEF	3 6 5	4.67	0 2 2	3.5	0.04
MFN1-B	AGO2	5 2 0	2.33	0 1 0	7	0.05
MFN1-B	RTRAF	5 2 0	2.33	1 0 0	7	0.05
MFN1-S	MFN1-HA	44 56 55	51.67	0 0 0	516.67	0
MFN1-S	MFN2	11 0 5	5.33	0 0 0	53.33	0
MFN1-S	SLC25A10	0 4 5	3	0 0 0	30	0
MFN1-S	PHB	0 9 8	5.67	0 0 1	17	0
MFN1-S	RPS5	27 41 37	35	11 7 5	4.57	0
MFN1-S	RAB2A	3 1 4	2.67	0 0 1	8	0.04
MFN2-B	MFN2-HA	73 152 104	109.67	0 0 0	1096.67	0
MFN2-B	MFN1	12 12 16	13.33	0 0 0	133.33	0
MFN2-B	DHX36	15 12 0	9	0 0 0	90	0
MFN2-B	NCBP1	8 3 0	3.67	0 0 0	36.67	0
MFN2-B	PUM1	7 3 0	3.33	0 0 0	33.33	0
MFN2-B	FAM98A	6 4 0	3.33	0 0 0	33.33	0
MFN2-B	USP10	15 6 0	7	1 0 0	21	0
MFN2-B	MARCHF5	5 7 6	6	0 0 1	18	0
MFN2-B	DHX30	42 42 0	28	3 2 1	14	0
MFN2-B	FAM120A	22 14 0	12	2 1 0	12	0
MFN2-B	UPF1	43 39 0	27.33	3 3 1	11.71	0
MFN2-B	AGO2	6 5 0	3.67	0 1 0	11	0
MFN2-B	ELAVL1	11 9 1	7	0 1 1	10.5	0
MFN2-B	MOV10	43 36 5	28	4 2 2	10.5	0
MFN2-B	HNRNPUL1	43 13 2	19.33	3 1 2	9.67	0
MFN2-B	FMR1	16 12 0	9.33	1 1 1	9.33	0
MFN2-B	FXR2	26 14 4	14.67	2 2 1	8.8	0
MFN2-B	HNRNPA3	7 6 3	5.33	1 0 1	8	0
MFN2-B	NONO	136 93 10	79.67	6 23 2	7.71	0

4 | Results

MFN2-B	RPS5	32 66 13	37	4 5 6	7.4	0
MFN2-B	NUFIP2	19 30 1	16.67	2 4 1	7.14	0
MFN2-B	LARP1	33 20 0	17.67	5 2 1	6.63	0
MFN2-B	FXR1	28 15 7	16.67	3 4 1	6.25	0
MFN2-B	MYL6	6 25 10	13.67	2 1 4	5.86	0
MFN2-B	RPA1	20 25 7	17.33	2 2 6	5.2	0
MFN2-B	CAPRIN1	62 39 3	34.67	16 4 2	4.73	0
MFN2-B	HNRNPH1	12 15 6	11	1 4 2	4.71	0
MFN2-B	DDX1	22 30 1	17.67	7 1 5	4.08	0
MFN2-B	DHX9	67 55 12	44.67	14 10 10	3.94	0
MFN2-B	G3BP2	14 14 1	9.67	2 4 2	3.62	0
MFN2-B	IGF2BP3	20 14 4	12.67	4 4 4	3.17	0
MFN2-B	PABPC4	20 17 1	12.67	3 4 5	3.17	0
MFN2-B	G3BP1	45 22 0	22.33	7 5 10	3.05	0
MFN2-B	BSYL	3 2 1	2	0 0 0	20	0.01
MFN2-B	TMEM9	2 0 3	1.67	0 0 0	16.67	0.01
MFN2-B	PURA	7 3 0	3.33	1 0 0	10	0.01
MFN2-B	SRRT	5 3 0	2.67	0 0 1	8	0.01
MFN2-B	RTRAF	5 3 0	2.67	1 0 0	8	0.01
MFN2-B	CORO2A	18 12 28	19.33	5 4 9	3.22	0.01
MFN2-B	CPSF6	3 3 0	2	1 0 0	6	0.02
MFN2-B	TFCP2	0 22 13	11.67	0 7 0	5	0.03
MFN2-B	SNX33	8 23 26	19	0 11 3	4.07	0.03
MFN2-B	EMD	2 10 11	7.67	0 4 2	3.83	0.03
MFN2-B	HNRNPF	11 17 7	11.67	4 4 2	3.5	0.03
MFN2-B	DDX17	13 12 3	9.33	5 3 0	3.5	0.03
MFN2-B	JMY	4 1 5	3.33	1 0 1	5	0.04
MFN2-B	ILF2	16 12 10	12.67	4 1 6	3.45	0.04
MFN2-B	UBP1	0 14 2	5.33	0 1 0	16	0.05
MFN2-B	SLC25A10	2 0 5	2.33	0 0 1	7	0.05
MFN2-B	NSDHL	6 0 8	4.67	0 0 3	4.67	0.05
MFN2-B	MYH14	5 5 2	4	1 0 2	4	0.05
MFN2-S	MFN2-HA	107 135 332	191.33	0 0 0	1913.33	0
MFN2-S	MFN1	21 19 89	43	0 0 0	430	0
MFN2-S	MARCHF5	4 1 14	6.33	0 0 0	63.33	0
MFN2-S	S100A8	12 0 6	6	0 0 0	60	0

MFN2-S	DSC1	4 0 5	3	0 0 0	30	0
MFN2-S	S100A9	18 1 6	8.33	0 1 0	25	0
MFN2-S	UBP1	0 5 17	7.33	0 0 1	22	0
MFN2-S	SLC27A2	7 4 2	4.33	0 0 1	13	0
MFN2-S	FAF2	12 2 8	7.33	2 0 2	5.5	0
MFN2-S	SCCPDH	10 4 14	9.33	3 2 2	4	0
MFN2-S	DDX20	0 9 3	4	0 0 1	12	0.01
MFN2-S	S100A7	11 0 2	4.33	0 0 0	43.33	0.02
MFN2-S	PIP	2 1 8	3.67	0 0 0	36.67	0.03
MFN2-S	RHOT2	2 1 8	3.67	0 0 0	36.67	0.03
MFN2-S	LAMC1	2 4 1	2.33	0 0 0	23.33	0.04
MFN2-S	CALML5	4 2 17	7.67	0 1 1	11.5	0.05

A total number of 44 binding candidates were identified for MFN1 in basal conditions. For MFN1 under starvation conditions 6 potential interactors were found. MFN2 possible partners in basal conditions detected were 51. In conditions of nutrient deprivation, 16 binding candidates were identified. Interestingly, the number of high confidence candidates found after one hour of starvation treatment is considerably smaller than the amount of candidates in basal conditions. We next wondered whether there were common interactors between MFN1 and MFN2 or between basal and starvation conditions. The results of this analysis are plotted in Figure 27.

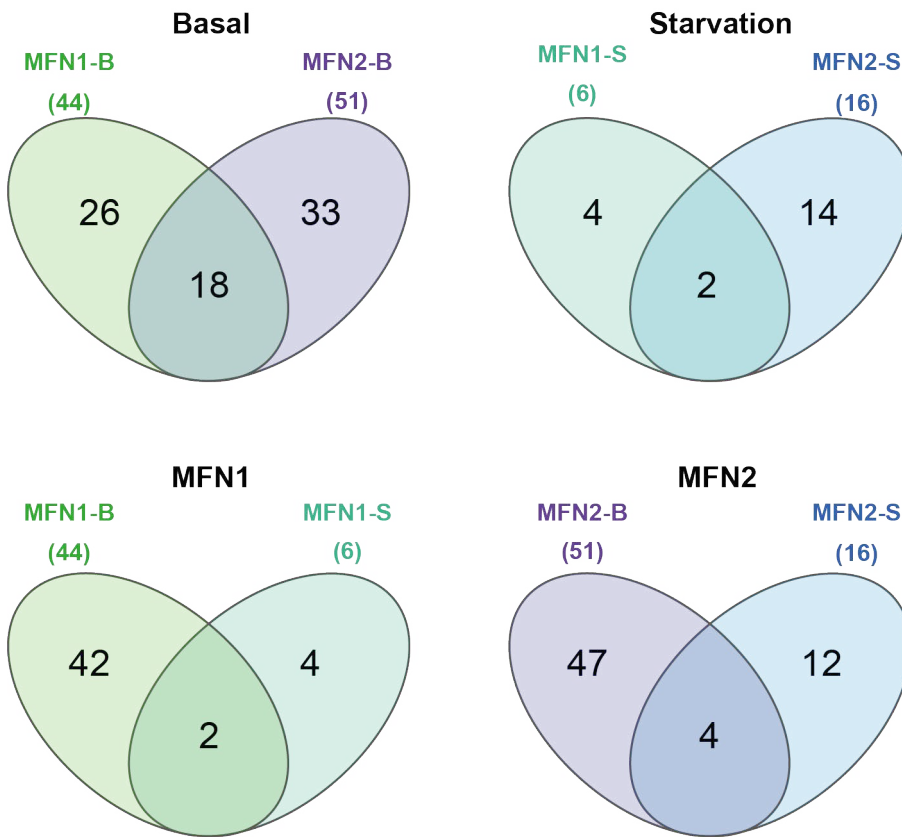


Figure 27. Venn diagrams comparing the potential binding candidates identified by mass spectrometry after HA-IP of MFN1-HA and MFN2-HA under basal and starvation conditions. Basal diagram shows the results found for MFN1 under basal conditions (MFN1-B) compared to MFN2 in the same conditions (MFN2-B). Starvation figure displays the proteins identified under starvation conditions for MFN1 (MFN1-S) and MFN2 (MFN2-S). MFN1 chart includes the binding candidates of MFN1 under basal (MFN1-B) and starvation conditions (MFN1-S). MFN2 graph contains the comparison of MFN2 results under basal (MFN2-B) and starvation conditions (MFN2-S).

We found that under basal conditions, MFN1 and MFN2 shared 18 binding candidates, namely: MFN1, MFN2, FMR1, UPF1, NONO, FXR2, DHX30, NUFIP2, G3BP2, G3BP1, FXR1, FAM98A, UBP1, BYSL, TMEM9,

ELAVL1, AGO2, RTRAF. Under starvation conditions, the only proteins found in common among the interactors of MFN1 and MFN2 were MFN1 and MFN2. The common interactors of MFN1 during basal and starvation conditions were as well MFN1 and MFN2. In the case of MFN2, basal and starvation conditions shared the following potential partners: MFN1, MFN2, MARCHF5 and UBP1.

We next analyzed the common proteins between all the experimental groups (MFN1 basal, MFN1 starvation, MFN2 basal and MFN2 starvation). These results are plotted in Figure 28.

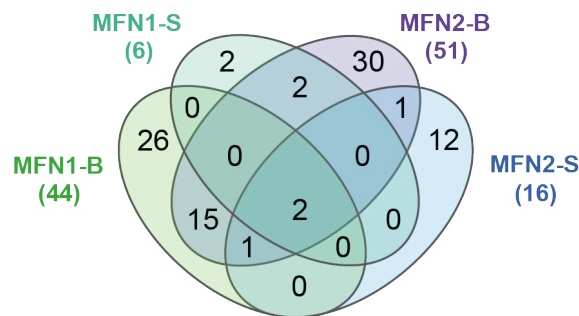


Figure 28. Venn diagram of all the mass spectrometry results of MFN1-HA and MFN2-HA HA-IP in basal and starvation conditions. Overlaps of MFN1 and MFN2 significant binding candidates in basal (MFN1-B, MFN2-B) and starvation (MFN1-S, MFN2-S) conditions are shown in a Venn diagram. Numbers between parentheses represent the total numbers of high confidence interactors. Numbers within the chart show the amount of significant candidates that overlap or not between the different categories.

Besides what we had already observed, we noticed 1 interactor shared between MFN1 in basal conditions and MFN2 both in basal and starvation conditions (UBP1) and 2 possible interactors shared between MFN1 in starvation conditions and MFN2 in basal conditions (SLC25A10

and RPS5).

4.5.3. Mitochondrial proteins are identified among MS detected proteins

Mitochondrial proteins were detected as potential interactors of MFN1 and MFN2 under basal and starvation conditions. This finding is coherent with the fact that MFN1 and MFN2 are outer mitochondrial membrane proteins. Mitochondrial preys that we detected and that had been already notified as interactors of MFN1 or MFN2 are MFN2 for MFN1 and MFN1, MARCHF5, RHOT2 for MFN2. Proteins that have been found in mitochondria and identified by mass spectrometry in this study are shown in the dot plot of Figure 29. Dot color represents the absolute abundance in peptides of each prey protein in each experiment, the size of the dots represents the relative abundance of the preys across all the experiments, and the color of the edge of each dot stands for the BFDR. We observed that under basal conditions MFN1 and MFN2 both interact with DHX30. The only mitochondrial interactor of MFN1 in basal conditions maintained under starvation conditions is MFN2. The interactions of MFN2 with MARCHF5 and MFN1 occur in basal and starvation conditions. Interestingly, from the 6 MFN1 potential binding candidates found statistically significant under starvation conditions, 4 are mitochondrial.

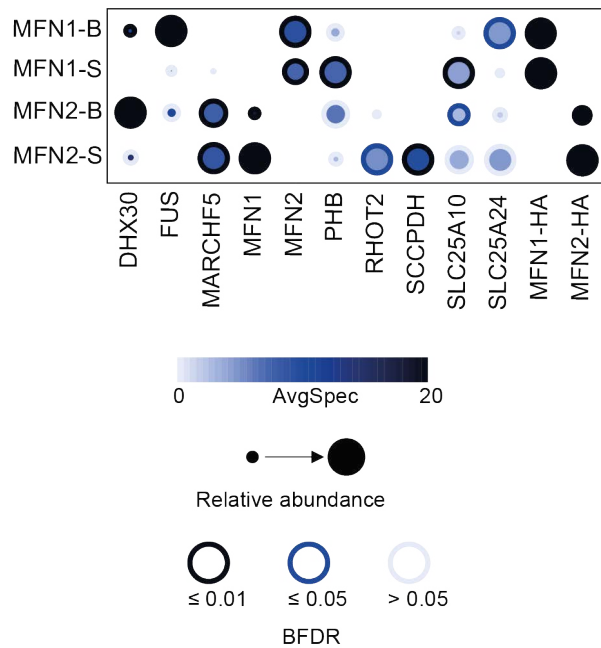


Figure 29. Mitochondrial proteins found by mass spectrometry analysis of MFN1-HA and MFN2-HA HA-IP in basal and starvation conditions. Dot plot generated with ProHits visualization tool of all the significant mitochondrial proteins. Dot color intensity refers to the average number of unique peptides of a protein found in the 3 biological replicates of the experiment. Dot size represents the relative abundance of each interactor across all the HA-IPs. Line color stands for the statistical significance with which each protein was found.

4.5.4. Mass spectrometry reveals possible interactions between MFN1 and MFN2 and proteins from other membranous compartments of the cell

The possible interactors of MFN1 and MFN2 under basal and starvation conditions were classified into the membranous compartment of the cell in which they localize. We identified proteins from the ER, endosomes, and the plasma membrane, as it is shown in Figure 30.

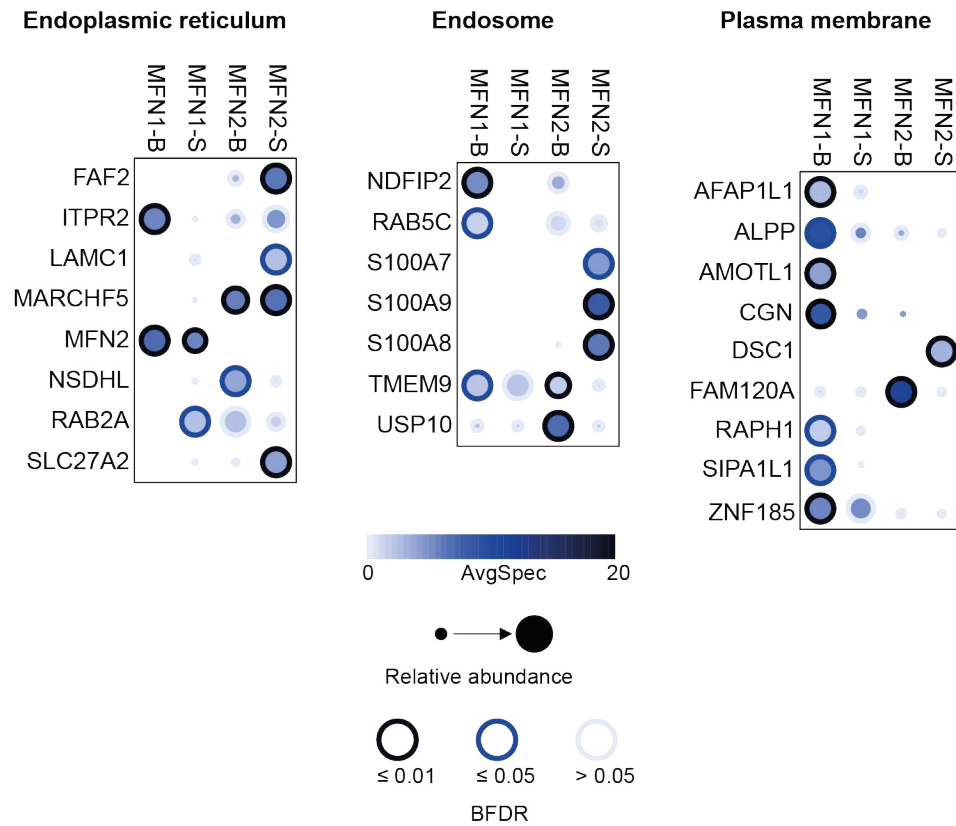


Figure 30. Proteins of membranous compartments of the cell found by mass spectrometry analysis of MFN1-HA and MFN2-HA HA-IP in basal and starvation conditions. Dot plots generated with ProHits visualization tool of all the significant proteins localized in endoplasmic reticulum, endosome and plasma membrane. Dot color intensity refers to the average number of unique peptides of a protein found in the 3 biological replicates of the experiment. Dot size represents the relative abundance of each interactor across all the HA-IPs. Line color stands for the statistical significance with which each protein was found.

Among ER proteins identified, most of them were binding candidates of MFN2 and they were increased in starvation. Under basal conditions MFN2 potential interactors were MARCHF5 and NSDHL. Starvation

preserved the interaction between MFN2 and MARCHF5 and favored the interactions with other ER proteins: FAF2, LAMC1 and SLC27A2. We appreciated that MFN1 interacted with ITPR2 and MFN2 in basal conditions and in starvation conditions its potential partners were MFN2 and RAB2A.

We observed that MFN1 interacted with proteins present in the endosomal membrane under basal conditions (NDFIP2, RAB5C and TMEM9), but no endosomal partners were found under starvation conditions. Endosomal binding candidates of MFN2 were different in basal and starvation conditions: TMEM9 and USP10 were found under basal conditions and S100A7, S100A8 and S100A9 under basal conditions.

Proteins that localize in the plasma membrane were notably enriched among MFN1 basal candidates (AFAP1L1, ALPP, AMOTL1, CGN, RAPH1, SIPA1L1 and ZNF185). However, these were lost under starvation conditions. MFN2 plasma membrane potential interactors were FAM120A under basal conditions and DSC1 under conditions of nutrient deprivation.

4.5.5. Proteins that participate in post-translational modifications potentially interact with MFN1 and MFN2

Proteins that are involved in post-translational modification of other proteins were identified among binding candidates of MFN1 and MFN2 mostly under basal conditions and their abundance and statistical significance among the experimental groups are plotted in Figure 31.

4 | Results

Proteins found were related to dephosphorylation (ALPP), hypusination (DOHH), ubiquitination (KLHL13, MARCHF5, AMOTL1, NDFIP2) and deubiquitination (USP10).

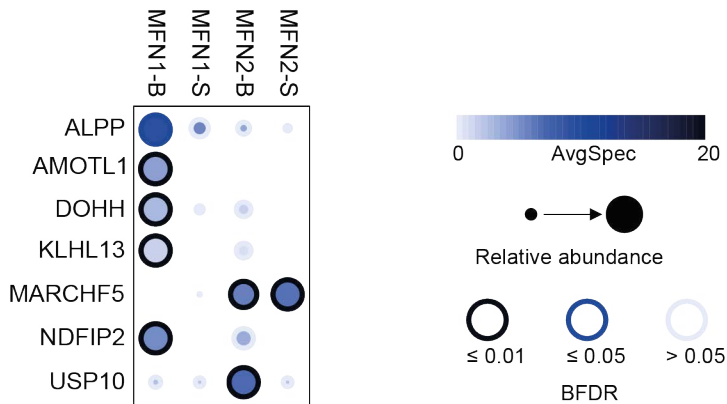


Figure 31. Protein modifiers found by mass spectrometry analysis of MFN1-HA and MFN2-HA HA-IP in basal and starvation conditions. Dot plot generated with ProHits visualization tool of all the significant protein modifiers. Dot color intensity refers to the average number of unique peptides of a protein found in the 3 biological replicates of the experiment. Dot size represents the relative abundance of each interactor across all the HA-IPs. Line color stands for the statistical significance with which each protein was found.

We observed that MFN1 under basal conditions interacted with 5 proteins involved in post-translational modification (ALPP, AMOTL1, DOHH, KLHL13 and NDFIP2). Under starvation conditions, no protein modifiers were observed among MFN1 potential interactors. MFN2 under basal conditions interacted with the ubiquitin ligase MARCHF5 and the de-ubiquitinase USP10. Under starvation conditions, MFN2 interacted with MARCHF5, but no other protein modifiers were found among its possible binding partners.

4.5.6. Autophagy related proteins are enriched in basal and starvation conditions

Literature research was performed to determine if the possible interactors of MFN1 and MFN2 in basal and starvation conditions were related to autophagy or not. Homologues of proteins that had been related to autophagy in yeast were also considered. The identified autophagy related proteins are plotted together with their enrichment and statistical reliability in Figure 32. In absolute numbers, more autophagy related proteins were identified for MFN2 than for MFN1. MFN1 was found to interact with the mitophagy proteins RAB5C in basal conditions and PHB when amino acids were removed from the medium. Moreover under starvation conditions RAB2A was also found to interact with MFN1. Under basal and starvation conditions MFN2 interacted with MARCHF5, which has been described to regulate mitophagy. Regarding macroautophagy, MFN2 potential binding partners in basal conditions were JMY and USP10. Moreover, under starvation conditions the possible interactors of MFN2 related to macroautophagy were S100A8, S100A9 and SLC27A2.

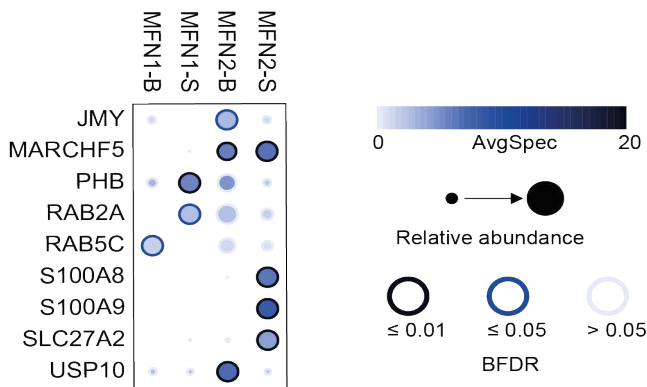


Figure 32. Autophagy related candidates found by mass spectrometry analysis of MFN1-HA and MFN2-HA HA-IP in basal and starvation conditions. Dot plot generated with ProHits visualization tool of all the significant proteins involved in autophagy. Dot color intensity refers to the average number of unique peptides of a protein found in the 3 biological replicates of the experiment. Dot size represents the relative abundance of each interactor across all the HA-IPs. Line color stands for the statistical significance with which each protein was found.

4.5.7. RNA-binding proteins are highly enriched among basal binding candidates

In order to have a global vision of the differences between the interactomes of MFN1 and MFN2 under basal and starvation conditions, Reactome Pathway Analysis was performed. Interestingly we discovered that the pathways with more enrichment under basal conditions, both for MFN1 and MFN2 binding candidates, were those related to RNA metabolism (Figure 33). This enrichment was not observed under starvation conditions.

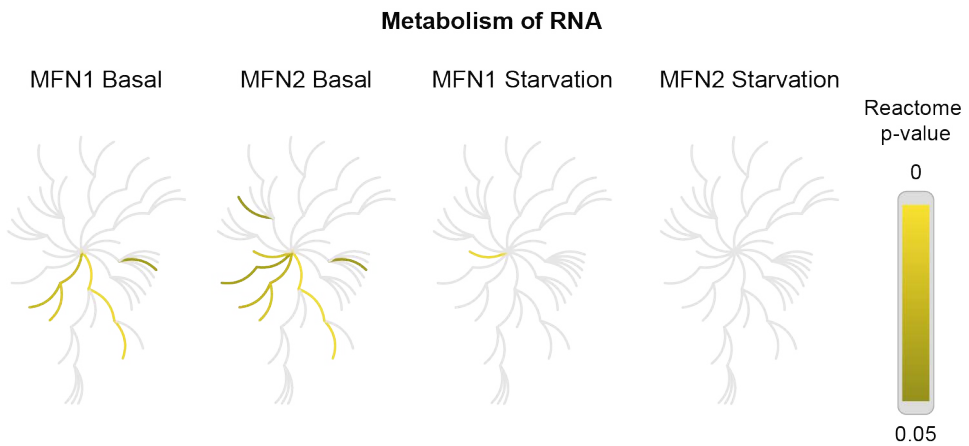


Figure 33. Reactome pathway analysis detects enrichment of RNA metabolism proteins among basal interactors. Plots obtained with Reactome pathway analysis tool applied to mass spectrometry results. Each branch of these charts represents a pathway of RNA metabolism. Proteins considered for the analysis had a BFDR lower or equal to 0.1. Only the proteins related with the metabolism of RNA are shown.

More specifically, MFN1 binding candidates related to RNA metabolism were implicated in mRNA splicing (PUF60, FUS, ELAVL1), nonsense-mediated decay (RPL31, RPS15, UPF1), regulation of mRNA stability (ELAVL1), RNA processing (RPL31, RPS15, BYSL) and tRNA processing (RTRAF). MFN2 binding candidates that played a role in RNA metabolism were involved in processing of capped pre-mRNA (NCBP1, CPSF6, HNRNPH1, DHX9, HNRNPUL1, SRRT, HNRNPF, CPSF6, HNRNPA3, ELAVL1), tRNA processing (DDX1, RTRAF), nonsense-mediated decay (NCBP1, RPS5, UPF1), RNA binding by insulin-like growth factor-2 mRNA binding proteins (IGF2BP3), RNA processing (RPS5, BYSL), mRNA capping (RTRAF) and metabolism of non-coding RNA (NCBP1).

Besides this analysis, we performed bibliographic search and identified

all the potential interactors of MFN1 and MFN2 that were RNA-binding proteins. These proteins are plotted in Figure 34. As observed when Reactome Pathway Analysis was applied, MFN1 and MFN2 interact with RNA-binding proteins under basal conditions and not under starvation conditions. Furthermore, more RNA-binding proteins seemed to interact with MFN2 than with MFN1.

Subsequently, we wondered whether RNA membraneless structures were represented among the proteins identified by mass spectrometry. We compared our results with the RNA granule database contained in <http://rnagranuledb.lunenfeld.ca/>. We observed that under basal conditions the proteomes of MFN1 and MFN2 were enriched in proteins that constitute processing bodies (P-bodies) and stress granules (Table 2 and Table 3).

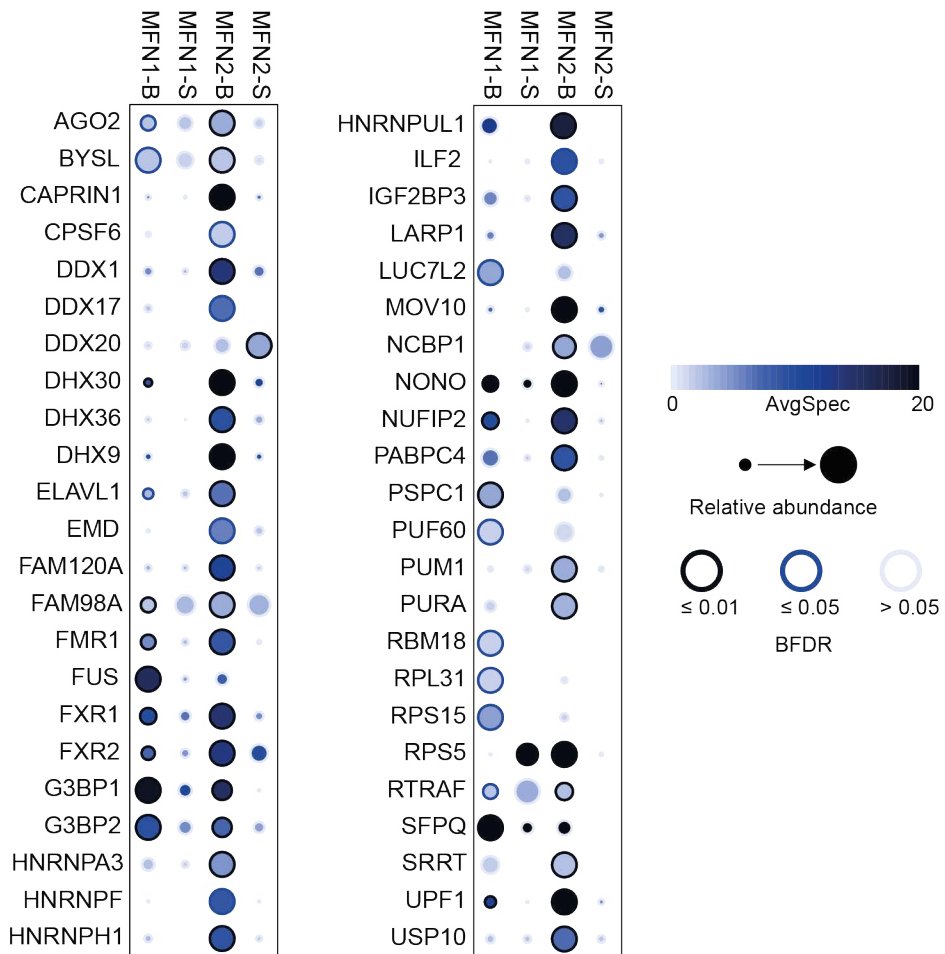


Figure 34. RNA related candidates found by mass spectrometry analysis of MFN1-HA and MFN2-HA HA-IP in basal and starvation conditions. (B)

Dot plot generated with ProHits visualization tool of all the significant RNA-binding proteins. Dot color intensity refers to the average number of unique peptides of a protein found in the 3 biological replicates of the experiment. Dot size represents the relative abundance of each interactor across all the HA-IPs. Line color stands for the statistical significance with which each protein was found.

Table 2. MFN1 binding candidates localized in P-bodies and stress granules.

MFN1 binding candidates	P-bodies	Stress granules
AGO2	X	X
DHX30	X	X
ELAVL1	X	X
FAM98A		X
FMR1		X
FXR1		X
FXR2		X
G3BP1		X
G3BP2		X
NUFIP2		X
PUF60	X	X
SIPA1L1		X
UPF1	X	X

Table 3. MFN2 binding candidates localized in P-bodies and stress granules.

MFN2 binding candidates	P-bodies	Stress granules
AGO2	X	X
CALML5		X
CAPRIN1		X
CPSF6		X
DDX1		X
DHX30	X	X
DHX9	X	
DSC1	X	
ELAVL1	X	X
FAM120A	X	X
FAM98A		X
FMR1		X
FXR1		X
FXR2		X
G3BP1		X
G3BP2		X
HNRNPA3		X
HNRNPUL1		X
IGF2BP3	X	X
ILF2	X	
LARP1		X
MOV10	X	X
NCBP1	X	
NUFIP2		X
PABPC4		X
PIP	X	
PUM1	X	X
PURA		X
RTRAF		X
SRRT		X
UPF1	X	X
USP10		X

4.6. Validation of some MFN1 and MFN2 binding candidates

From the list of potential binding partners of MFN1 and MFN2, some of them related to organelle contacts, post-translational modifications and autophagy were validated by IP.

4.6.1. *NDFIP2 interacts with MFN1 and MFN2*

From the proteins that participate in the modification of other proteins, NDFIP2 was considered as an interesting candidate to validate because it partially localizes with endosomes ²¹⁵ and it activates E3 ubiquitin ligases like NEDD4, NEDD4L, SMURF2, WWP1 and WWP2 through physical interaction ²³. Moreover, NDFIP2 participates in multivesicular bodies trafficking ²¹⁶. Mass spectrometry data showed significant enrichment of NDFIP2 among MFN1 potential binding partners under basal conditions (Figure 35A). NDFIP2 was also detected among MFN2 possible interactors in basal conditions, but not in a significant manner. To validate whether NDFIP2 interacts with MFN1 and MFN2, NDFIP2-FLAG was overexpressed in HeLa cells and FLAG-IP was performed. Both MFN1 and MFN2 co-immunoprecipitated with NDFIP2 (Figure 35B). These results were obtained under basal conditions. FLAG-IP was not performed under starvation conditions.

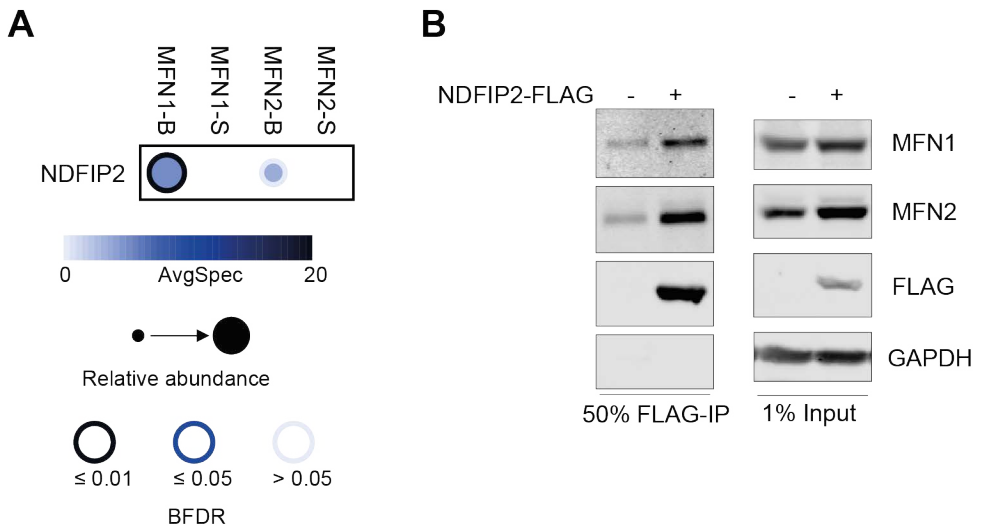


Figure 35. NDFIP2 interacts with MFN1 and MFN2. (A) Dot plot generated with ProHits visualization tool of NDFIP2 results. Dot color intensity refers to the average number of unique peptides of a protein found in the 3 biological replicates of the experiment. Dot size represents the relative abundance of each interactor across all the HA-IPs. Line color stands for the statistical significance with which each protein was found. (B) FLAG-IP of overexpressed NDFIP2-FLAG in HeLa cells. FLAG, MFN1 and MFN2 immunoblots of input and eluate (IP) fractions are shown. N=2.

4.6.2. RAB5C interacts with MFN1 and MFN2

Regarding the contacts of mitochondria with other organelles, RAB5C was selected for validation, since it had been previously identified in the interface between mitochondria and endosomes²¹⁷ and it plays a role in mitochondrial removal by autophagy²¹⁸. RAB5C appeared significantly enriched for MFN1 in basal conditions and enriched but not significantly for MFN2 both in basal and starvation conditions (Figure 36A). RAB5C-FLAG was overexpressed in HeLa cells and immunoprecipitated using

beads coupled to antibodies against FLAG-tag (Figure 36B). Western blot was performed to detect MFN1 and MFN2 in the eluate. MFN1 and MFN2 were both found to co-immunoprecipitate with RAB5C. These results were obtained under basal conditions.

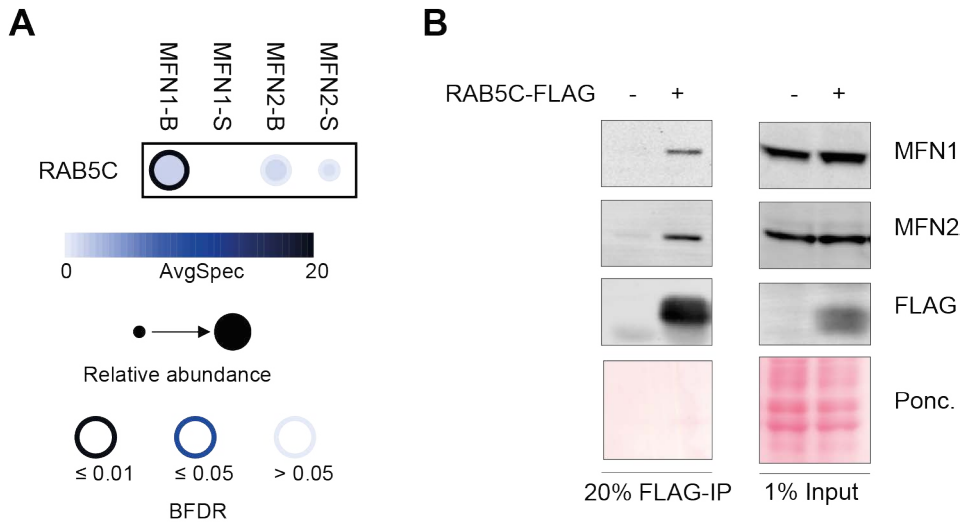


Figure 36. RAB5C interacts with MFN1 and MFN2. (A) Dot plot generated with ProHits visualization tool of RAB5C results. Dot color intensity refers to the average number of unique peptides of a protein found in the 3 biological replicates of the experiment. Dot size represents the relative abundance of each interactor across all the HA-IPs. Line color stands for the statistical significance with which each protein was found. (B) FLAG-IP of overexpressed RAB5C-FLAG in HeLa cells. FLAG, MFN1 and MFN2 immunoblots of input and eluate (IP) fractions are shown. N=6.

4.6.3. S100A8 and S100A9 interact with MFN2

Since one of the aims of this study was to shed light into the role of MFN2 in starvation-induced autophagy, S100A8 and S100A9 were selected among potential partners of MFN2 in starvation based on previously

reported data that relate S100A8 and S100A9 with autophagy activation^{24,219,220}. These proteins form a complex called calprotectin that is important during inflammatory signaling²²¹. S100A8 and S100A9 were significantly enriched only for MFN2 in starvation conditions (Figure 37A).

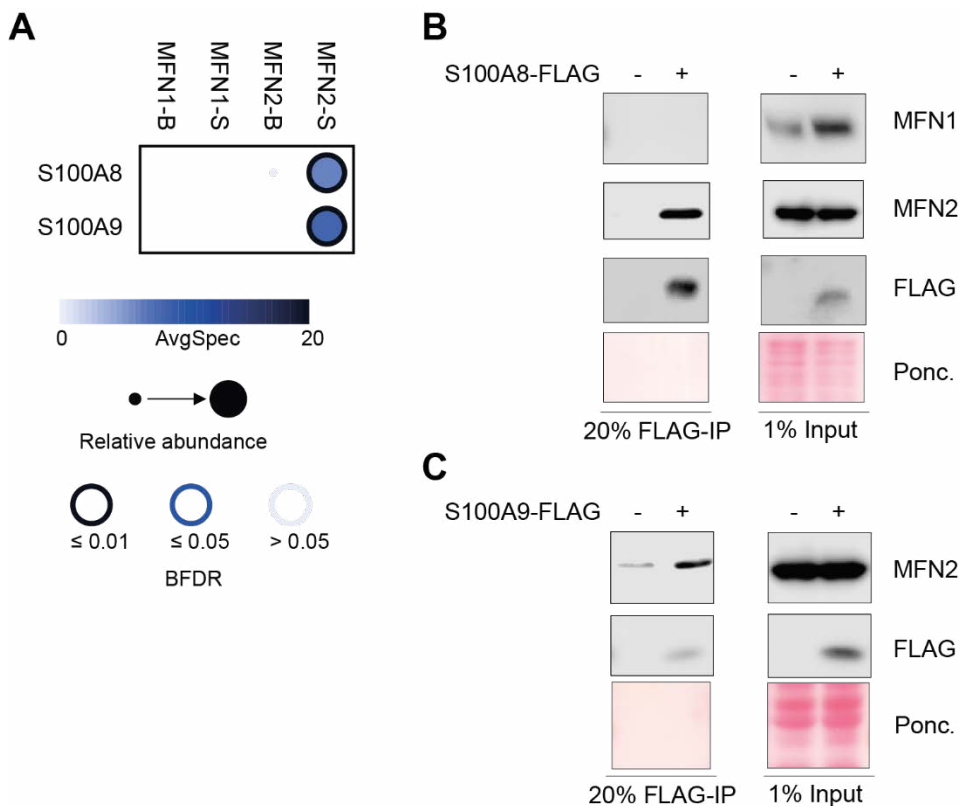


Figure 37. S100A8 and S100A9 interact with MFN2. (A) Dot plot generated with ProHits visualization tool of S100A8 and S100A9 results. Dot color intensity refers to the average number of unique peptides of a protein found in the 3 biological replicates of the experiment. Dot size represents the relative abundance of each interactor across all the HA-IPs. Line color stands for the statistical significance with which each protein was found. (B) FLAG-IP of overexpressed S100A8-FLAG. FLAG, MFN1 and MFN2 immunoblots of input

4 | Results

and eluate (IP) fractions are shown. N=4. (C) FLAG-IP of overexpressed S100A9-FLAG. FLAG and MFN2 immunoblots of input and eluate (IP) fractions are shown. N=1.

S100A8-FLAG was overexpressed in HeLa cells and immunoprecipitated with FLAG-beads. MFN2 was found to co-immunoprecipitate with S100A8, but MFN1 did not co-immunoprecipitate with S100A8 (Figure 37B). Then, S100A9-FLAG was overexpressed in HeLa cells and immunoprecipitated with beads coupled to antibodies against FLAG. MFN2 co-immunoprecipitated with S100A9 (Figure 37C). We did not assess whether MFN1 interacts or not with S100A9. These results were obtained under basal conditions. S100A8 and S100A9 overexpression is probably enhancing MFN2 interaction with these proteins under basal conditions.

4.6.4. MFN2 interaction with RAB5C and S100A8 is affected by nutrient availability

Since we found by mass spectrometry that the interactions of MFN1 and MFN2 are different in basal and starvation conditions, we assessed whether the interaction of MFN2 with RAB5C and S100A8 was affected by nutrient deprivation. RAB5C-FLAG and S100A8-FLAG were overexpressed and then cells were treated or not treated with EBSS medium for 1 hour. FLAG-IP was performed and MFN2 presence in the eluate was analyzed (Figure 38). We found that MFN2 interacted more with RAB5C in basal conditions, which is in line with MS data from Figure 36A, although RAB5C was not a significant binding candidate of MFN2. Moreover, the interaction between MFN2 and S100A8 was enhanced by

EBSS treatment, as we had observed in our MS data (Figure 37A).

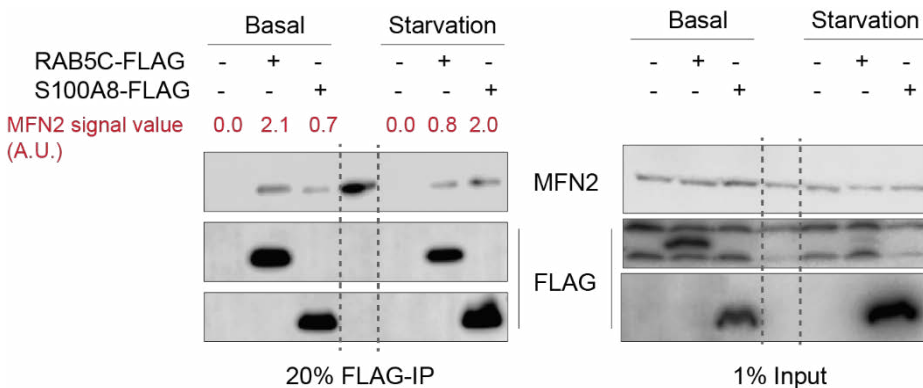


Figure 38. RAB5C and S100A8 interact with MFN2 differently in the presence or absence of amino acids. FLAG-IP of overexpressed RAB5C-FLAG and S100A8-FLAG under basal and starvation conditions achieved by 1 hour of EBSS treatment. FLAG and MFN2 immunoblots of input and eluate (IP) fractions are shown. The values of MFN2 antibody signal were quantified for the IP fractions. Data between the discontinuous gray lines should not be considered. N=1.

The fact that we observe interaction between MFN2 and S100A8 under basal conditions could be an artefact of S100A8 overexpression. Moreover, FLAG immunoblots revealed that overexpressed RAB5C is more abundant under basal conditions than under starvation conditions. Contrarily, overexpressed S100A8 is more abundant under starvation conditions than under basal conditions. These differences in the protein levels of RAB5C-FLAG and S100A8-FLAG induced by the absence of amino acids in the medium could explain the changes observed in the interactions. We did not assess how MFN1 interactions are affected by changes in nutrient availability and neither if these changes occur as reflected by MS data.

4.6.5. *SLC27A2* interacts with *MFN2*

Another protein that could play a role in autophagy and could be key to the understanding of the function of *MFN2* in autophagy is *SLC27A2*. Recently, a study published in yeast revealed that *Faa1*, a yeast homologue of *SLC27A2*¹⁹⁶, is necessary for fatty acid supply to de novo phospholipid synthesis during phagophore expansion²⁶. *SLC27A2* potentially interacted with *MFN2* and not with *MFN1*, and was enriched upon starvation treatment and not in basal conditions (Figure 39A).

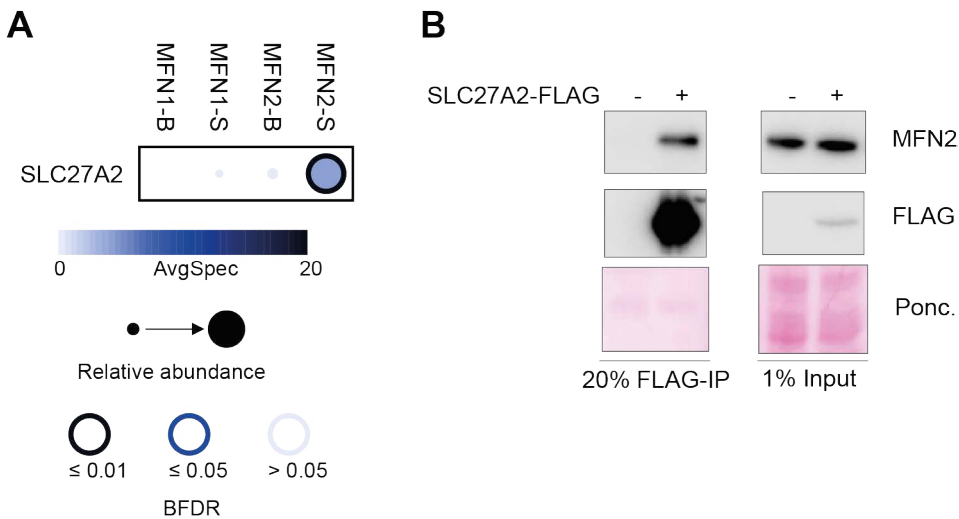


Figure 39. *SLC27A2* interacts with *MFN2* under starvation conditions.

(A) Dot plot generated with ProHits visualization tool of *SLC27A2* results. Dot color intensity refers to the average number of unique peptides of a protein found in the 3 biological replicates of the experiment. Dot size represents the relative abundance of each interactor across all the HA-IPs. Line color stands for the statistical significance with which each protein was found. (B) FLAG-IP of overexpressed *SLC27A2*-FLAG in HeLa cells under starvation conditions. FLAG, *MFN1* and *MFN2* immunoblots of input and eluate (IP) fractions are shown. N=6.

SLC27A2-FLAG was overexpressed in HeLa cells and FLAG-IP was carried out after one hour of EBSS treatment. MFN2 was observed to immunoprecipitate with SLC27A2 (Figure 39B). We did not assess whether MFN1 interacts with SLC27A2.

We also analyzed whether there were differences in the interaction between MFN2 and SLC27A2 when cells were grown for 1 hour in the absence of amino acids and serum. SLC27A2-FLAG was overexpressed and then cells were treated or not with EBSS medium for 1 hour. FLAG-IP was performed and the presence of MFN2 in the eluate was analyzed (Figure 40). We observed that MFN2 was able to interact with SLC27A2 under basal and starvation conditions. The signal of MFN2 in the eluate fraction was similar in basal and starvation conditions. Nevertheless, the levels of SLC27A2-FLAG were decreased upon nutrient deprivation. This could implicate increased interaction of MFN2 and SLC27A2-FLAG under starvation conditions.

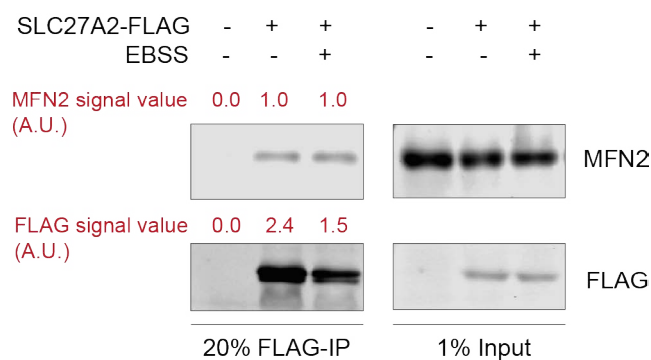


Figure 40. MFN2 interacts with overexpressed SLC27A2 under basal and starvation conditions. FLAG-IP of overexpressed SLC27A2-FLAG under basal

and starvation conditions achieved by 1 hour of EBSS treatment. FLAG and MFN2 immunoblots of input and eluate (IP) fractions are shown. The values of MFN2 antibody signal were quantified for the IP fractions and FLAG signal was quantified in the input fraction. N=2.

4.6.6. AGO2 and FXR1 interact with MFN1 and MFN2

As mass spectrometry data showed that RNA-binding proteins were an important part of the potential interactors of MFN1 and MFN2, two of these proteins, AGO2 and FXR1 (Figure 41A), were chosen for validation by co-immunoprecipitation. AGO2 is a protein that is present in P-bodies, which are membraneless structures composed of RNA and proteins. P-bodies can appear juxtaposed to mitochondria ³¹. When mitochondrial function is impaired, AGO2 fails to localize in P-bodies ³¹. FXR1 is part of stress granules ²⁷, which are cytosolic membraneless structures integrated by RNA and proteins. From cells endogenously expressing MFN1-HA and MFN2-HA, MFN1 and MFN2 were respectively immunoprecipitated using HA-beads. AGO2 and FXR1 were detected with specific antibodies. We observed that endogenous AGO2 and FXR1 co-immunoprecipitated with MFN1 and MFN2 (Figure 41B). We did not perform these experiments under starvation conditions.

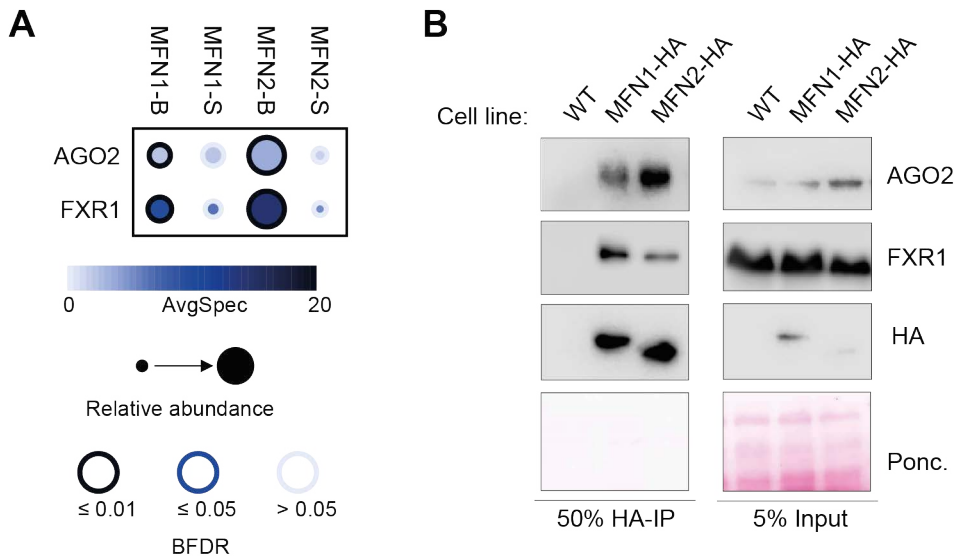


Figure 41. AGO2 and FXR1 interact with MFN1 and MFN2. (A) Dot plot generated with ProHits visualization tool of AGO2 and FXR1 results. Dot color intensity refers to the average number of unique peptides of a protein found in the 3 biological replicates of the experiment. Dot size represents the relative abundance of each interactor across all the HA-IPs. Line color stands for the statistical significance with which each protein was found. (B) HA-IP of MFN1-HA and MFN2-HA cells. HA, AGO2 and FXR1 immunoblots of input and eluate (IP) fractions and Ponceau staining of input fractions are shown. N=1.

4.7. Further functional validation of some novel interactors of MFN1 and MFN2

4.7.1. Mitochondrial effects of RAB5C ablation

4.7.1.1. RAB5C is necessary for MFN1 protein expression and mitochondrial morphology maintenance

By using a commercially available CRISPR/Cas9 system, RAB5C was depleted from HeLa cells (Figure 42A). In this cellular model, the levels

4 | Results

of expression of MFN1 and MFN2 were assessed (Figure 42B). A 50% decrease of MFN1 was observed in *RAB5C* KO cells. Nevertheless, the levels of MFN2 in *RAB5C* KO cells were not significantly changed.

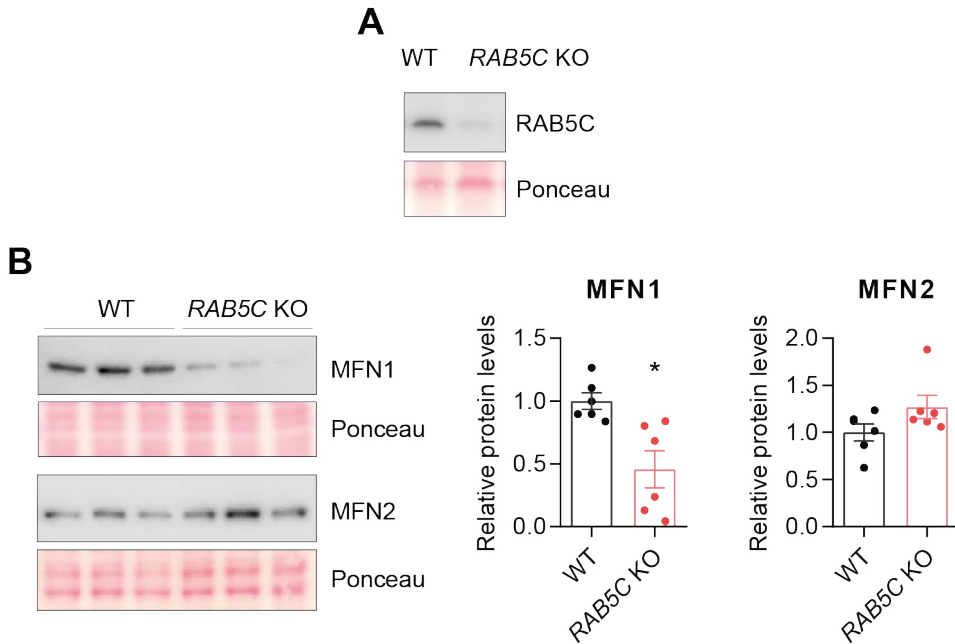


Figure 42. *RAB5C* KO cells show decreased MFN1 levels as WT cells.

(A) Western blot of RAB5C in WT HeLa cells and in *RAB5C* KO HeLa cells. (B) Representative western blot and quantification of MFN1 and MFN2 protein levels in *RAB5C* KO cells and WT cells. N=6. MFN1 data passed Saphiro-Wilk normality test and data were compared using T-student paired test. MFN2 data did not pass Saphiro-Wilk normality test and Wilcoxon test was applied to determine statistical significant differences. * represents p-values ≤ 0.05 .

To know whether the changes observed occurred at the protein level or were a consequence of differential gene expression, gene expression of *MFN1* and *MFN2* was analyzed (Figure 43). No significant differences between *RAB5C* KO cells and WT cells were detected.

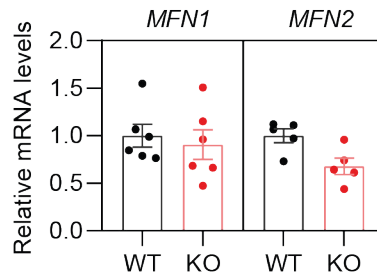
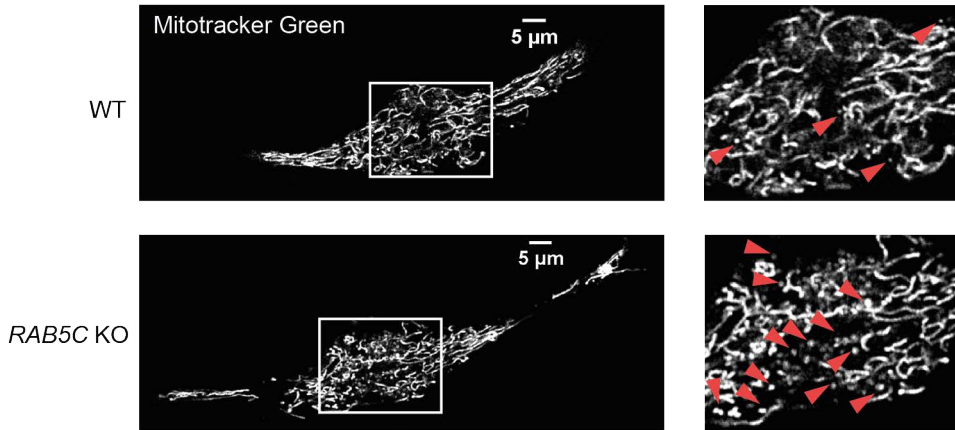


Figure 43. *RAB5C* KO cells have equal *MFN1* and *MFN2* gene expression as WT cells. Relative mRNA levels of *MFN1* and *MFN2* in WT and *RAB5C* KO cells. *MFN1* data passed Saphiro-Wilk normality test and data were compared using T-student paired test. *MFN2* data did not pass Saphiro-Wilk normality test and Wilcoxon test was applied to determine statistical significant differences.

Given the drop in *MFN1* protein levels, the next step was to analyze mitochondrial morphology. By staining mitochondria with the specific probe Mitotracker green, we observed a more fragmented mitochondrial network in *RAB5C* KO cells than in WT cells (Figure 44A). *RAB5C* KO cells were fixed and stained with an antibody against TOM20. Mitochondrial morphology was assessed by classifying the cells in three categories according to the predominant morphology of their mitochondria: elongated, short or oval. *RAB5C* ablated cells showed a decreased amount of cells with elongated mitochondria and an increase in the quantity of cells with predominantly oval mitochondria (Figure 44B).

A



B

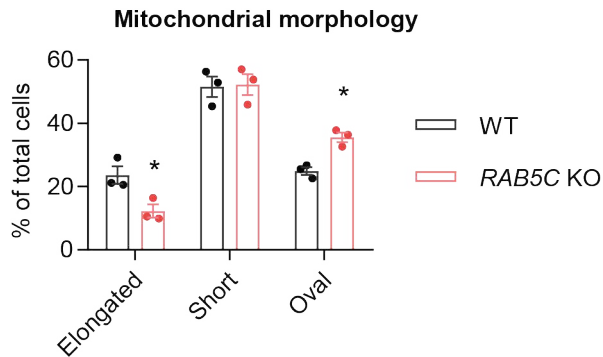


Figure 44. *RAB5C* KO cells show have more fragmented mitochondria than WT cells. (A) Representative images of live WT and *RAB5C* KO cells. Mitochondria were labeled during 30 minutes with 100 μM MitoTracker Green. Red arrows indicate fragmented mitochondria. Scale bar = 5μm. (B) Quantification of mitochondrial morphology in fixed cells stained with an antibody against TOM20. Scale bar: 5 μm. Percentages of each category of cells (elongated, short, oval) per experiment are represented in the bar chart. Three experiments were performed and >120 cells were counted per cell line per experiment. Data passed Saphiro-Wilk normality test. Results of *RAB5C* KO cells were compared with the results of WT cells using unpaired T-test. * represents p-values ≤ 0.05.

4.7.1.2. *RAB5C* KO cells have less mitochondrial mass and mtDNA nucleoids

To further assess the mitochondrial phenotype of *RAB5C* KO cells, TOM20 levels, mitochondrial mass and mtDNA nucleoids number were measured. We found that the levels of TOM20 were decreased by a 50% in *RAB5C* KO cells compared to WT cells.

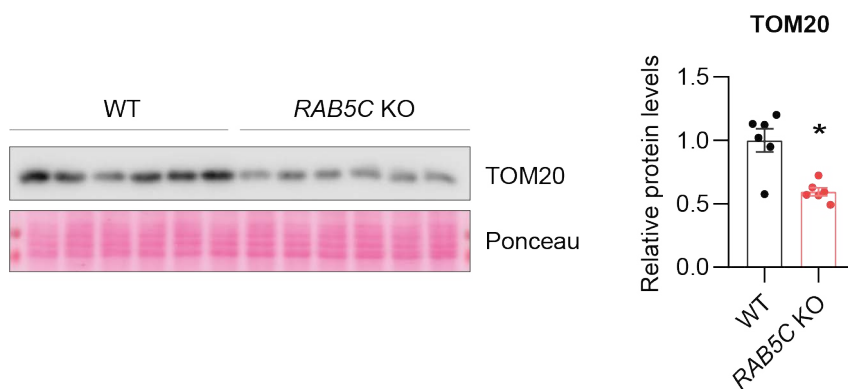


Figure 45. TOM20 protein levels are decreased in *RAB5C* KO. TOM20 western blot of total protein homogenates from WT and *RAB5C* KO cells and protein levels quantification. N=6. Data passed Saphiro-Wilk normality test and paired T-test was applied to compare WT and *RAB5C* KO results.

Mitochondrial mass was determined in living WT and *RAB5C* KO cells after labeling mitochondria with Mitotracker green and using flow cytometry to measure fluorescence. *RAB5C* KO cells showed a slight decrease (5%) of mitochondrial mass (Figure 46).

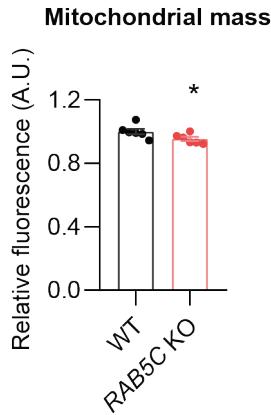


Figure 46. Mitochondrial mass is decreased in *RAB5C* KO cells. Detected fluorescence after 30 minutes treatment with 100 μ M MitoTracker Green staining of mitochondria and FACS analysis. N=6. Data passed normality Saphiro-Wilk test and T-test was performed.

The number of mtDNA nucleoids was determined in fixed cells after staining cellular double stranded DNA with a specific antibody and counting 3D objects stained with this antibody outside the nucleus. Mitochondrial DNA nucleoids were decreased by a 65% in *RAB5C* KO cells compared to WT cells (Figure 47).

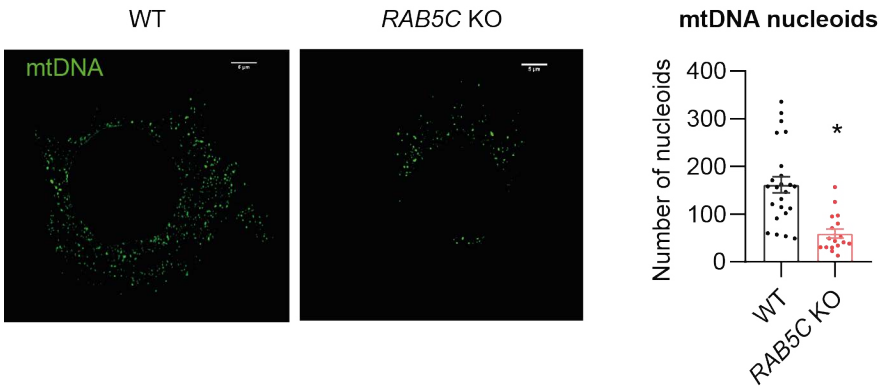


Figure 47. *RAB5C* KO cells have less mtDNA nucleoids than WT cells. Representative images of mtDNA nucleoids in WT and *RAB5C* KO cells and

quantification. WT N=24 cells and RAB5C KO N=17 cells. Data did not pass Shapiro-Wilk test and Mann-Whitney analysis was performed to compare the data. * represents p-values ≤ 0.05 .

4.7.1.3. Bafilomycin treatment results in accumulation of mtDNA nucleoids

Next, we wondered whether the changes observed in mitochondrial mass and mtDNA nucleoids were due to a process of mitochondrial degradation that was increased in *RAB5C* KO cells. To confirm whether mitochondrial degradation was more active in *RAB5C* KO cells, mtDNA nucleoids were measured after 1 hour of Baf A1 treatment (Figure 48). In WT cells, no significant changes were observed after bafilomycin treatment. Nevertheless, in *RAB5C* KO cells the number of nucleoids was increased after the treatment.

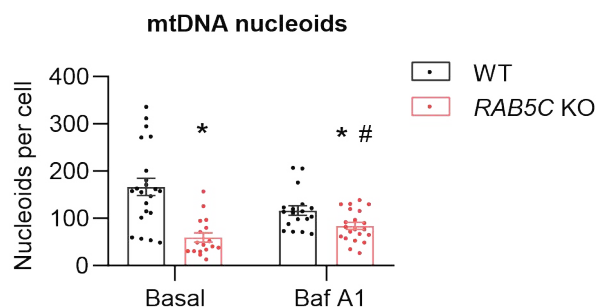
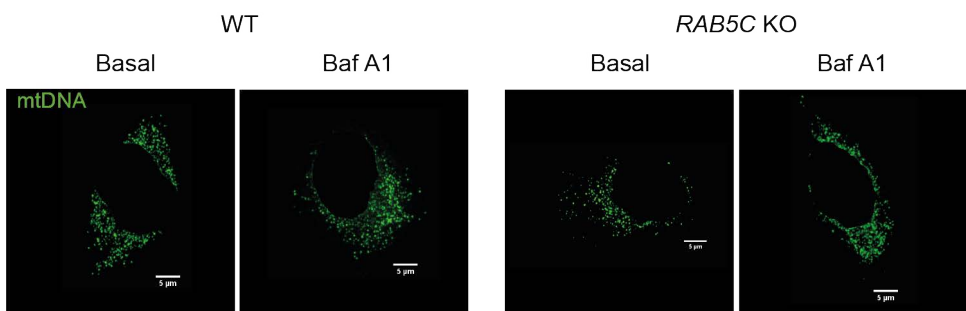


Figure 48. *RAB5C* KO cells accumulate mtDNA nucleoids upon bafilomycin treatment. Representative images of mtDNA nucleoids staining in WT and *RAB5C* KO HeLa cells in basal and after 1 hour of treatment with 200 nM bafilomycin (Baf A1) and quantification of the number of nucleoids. Scale bar: 5 μ m. WT basal N=22 cells, WT Baf A1 N=20 cells, *RAB5C* KO basal N=17 cells, *RAB5C* KO Baf A1 N=22 cells. Outlier test was performed and outliers were removed. Data did not pass Shapiro-Wilk normality test and Mann-Whitney test was used to compare WT and *RAB5C* KO data. * and # represent p-values \leq 0.05. * is used for WT vs. *RAB5C* KO. # is used for basal vs. Baf A1.

4.7.1.4. Genes implicated in mitochondrial clearance are upregulated in *RAB5C* KO cells

After observing that mtDNA nucleoids were accumulated with bafilomycin treatment in *RAB5C* KO cells, we wondered whether mitochondria could be undergoing a process of mitophagy. The expression of the mitophagy related genes *PINK1* and *PARK2* was analyzed (Figure 49A) as well as *PINK1* protein levels (Figure 49B). *PINK1* and *PARK2* were upregulated in *RAB5C* KO cells. *PINK1* protein levels were also increased in these cells.

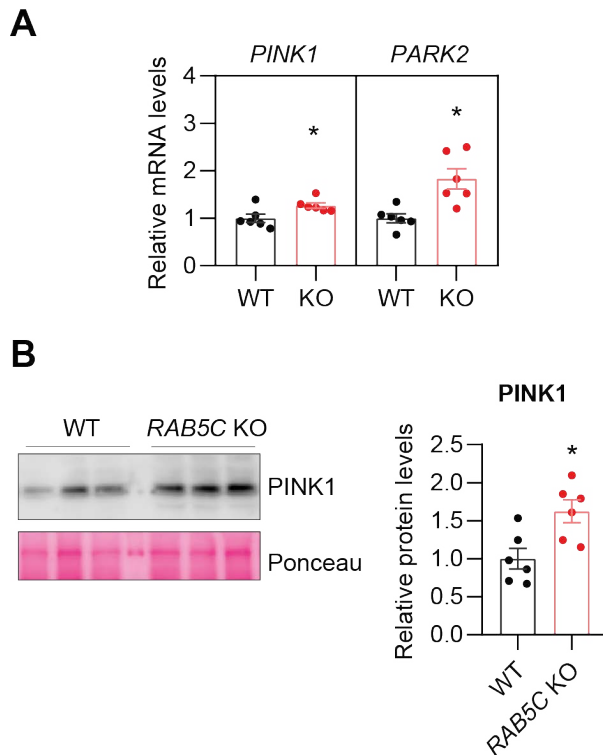


Figure 49. *RAB5C* KO cells have increased levels of mitophagy genes. (A) qPCR assessment of *PINK1* and *PARK2* expression levels in WT and *RAB5C* KO cells. N=6. Data passed Saphiro-Wilk normality test and paired T-test was used to compare WT and *RAB5C* KO results. (B) *PINK1* immunoblot of total protein homogenates of WT and *RAB5C* KO cells and quantification of protein levels. N=6. Data passed Saphiro-Wilk normality test and paired T-test was used to compare WT and *RAB5C* KO results. * represents p-values ≤ 0.05 .

4.7.1.5. Bafilomycin treatment increases co-distribution of mtDNA and endosomes in *RAB5C* KO cells

To further determine through which cellular compartment mitochondria of *RAB5C* KO cells were eliminated, co-localization of mtDNA with autophagosomes was analyzed (Figure 50 and Figure 51).

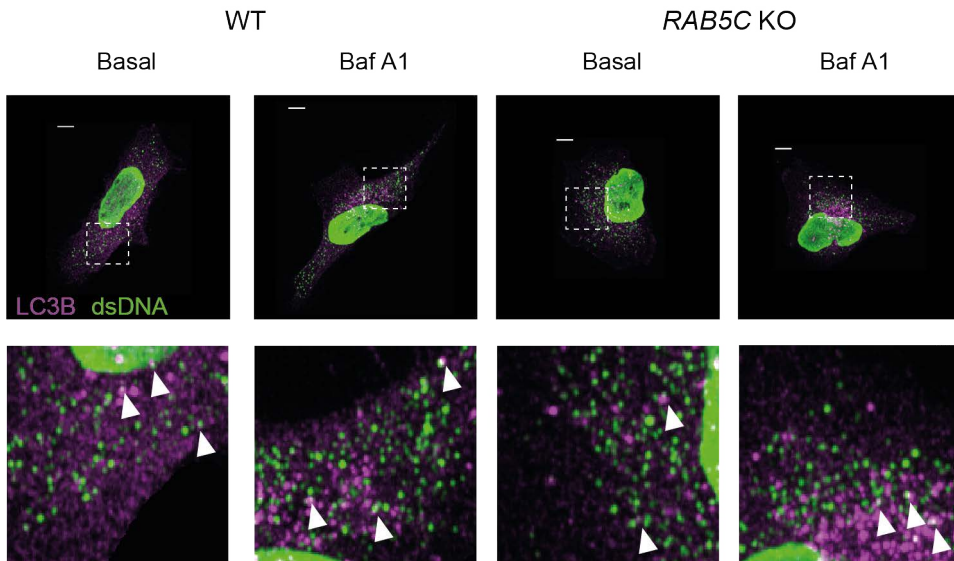


Figure 50. LC3B and dsDNA co-distribute equally in *RAB5C* KO and WT cells (I). Representative images of WT and *RAB5C* KO cells in basal conditions and treated with 200 nM bafilomycin (Baf A1) for 1 hour. Cells were fixed after treatment and stained with antibodies against dsDNA and LC3B.

Pearson’s coefficient was used to determine the differences between WT cells and *RAB5C* KO cells in co-distribution levels of mtDNA and LC3 (Figure 51). The co-distribution of mtDNA and autophagosomes was the same in *RAB5C* KO cells as in WT cells both under basal and bafilomycin treatment conditions.

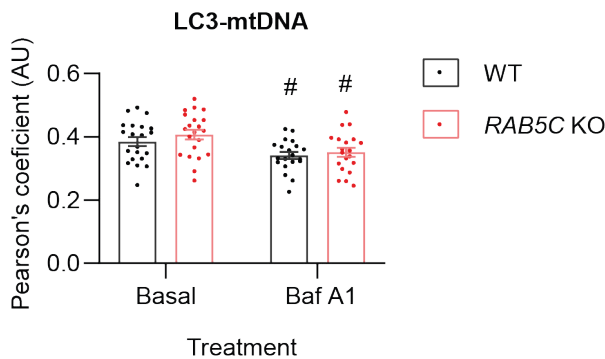


Figure 51. LC3B and dsDNA co-distribute equally in *RAB5C* KO and WT cells (II). Quantification of LC3B and dsDNA co-distribution in WT and *RAB5C* KO cells. Pearson's coefficient was calculated for each image of a single cell. WT basal N=21 cells, WT Baf A1 N=20 cells, *RAB5C* KO basal N=21 cells, *RAB5C* KO Baf A1 N=20 cells. Outlier test was performed and outliers were removed. Data passed Shapiro-Wilk normality test and unpaired T-test was used to compare results. # represents p-values ≤ 0.05 . # is used for basal vs. Baf A1.

Since no changes in LC3 and mtDNA co-distribution were detected neither in basal conditions nor after bafilomycin treatment between *RAB5C* KO cells and WT cells, we considered the possibility of mitochondrial degradation through a different compartment. Thus, the co-localization of mtDNA with early endosomes was analyzed (Figure 52 and Figure 53). Pearson's coefficient of mtDNA-EEA1 co-distribution was obtained in WT and *RAB5C* KO cells in basal and bafilomycin treatment conditions. We observed increased co-distribution of EEA1 with mtDNA in *RAB5C* KO cells both in basal conditions and after bafilomycin treatment. This could indicate that mitochondrial degradation associated to the lack of *RAB5C* occurs through endosomes.

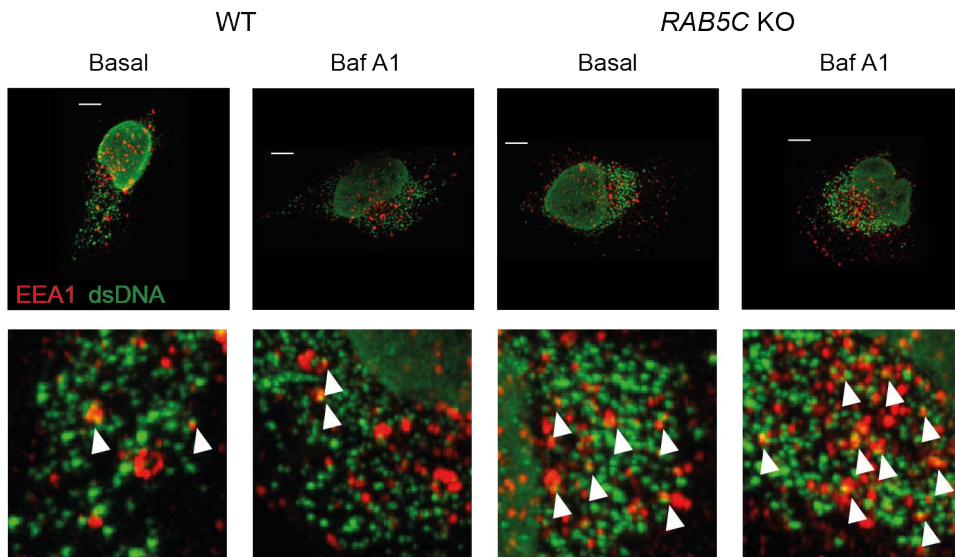


Figure 52. EEA1 and dsDNA co-distribute more in *RAB5C* KO than in WT cells (I). Representative images of WT and *RAB5C* KO cells in basal conditions and treated with 200 nM bafilomycin (Baf A1) for 1 hour. Cells were fixed after treatment and stained with antibodies against dsDNA and EEA1.

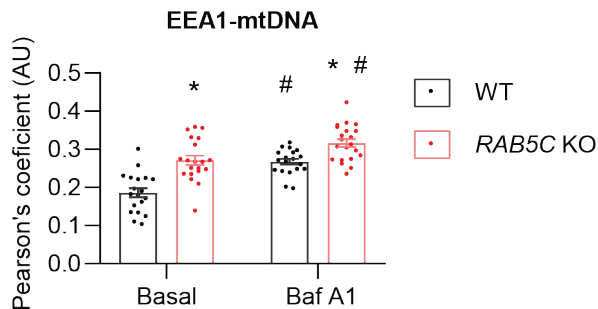


Figure 53. EEA1 and dsDNA co-distribute more in *RAB5C* KO than in WT cells (II). Quantification of EEA1 and dsDNA co-distribution in WT and *RAB5C* KO cells. Pearson's coefficient was calculated for each image of a single cell. WT basal N=19 cells, WT Baf A1 N=20 cells, *RAB5C* KO basal N=20 cells, *RAB5C* KO Baf A1 N=21 cells. Outlier test was performed and outliers were removed. Data passed Saphiro-Wilk normality test and unpaired T-test was used to compare results. * and # represent p-values ≤ 0.05 . * is used for WT vs. *RAB5C* KO. # is

used for basal vs. Baf A1.

4.7.2. Mitochondria locate in close proximity to AGO2 positive and G3BP1 positive structures

After validating the interaction of MFN1 and MFN2 with FXR1 and AGO2, we wondered whether it could be possible that this is part of an interaction between mitochondria and RNA related structures. AGO2 is frequently associated with processing bodies (P-bodies) and FXR1 often appears in stress granules. In order to determine if mitochondria are in close proximity with RNA-related structures, AGO2-GFP or G3BP1-GFP were overexpressed and mitochondria were labeled with Mitotracker Deep Red. G3BP1 is a protein that is found in stress granules²⁷ and CLUH granules³⁰ and that we identified in the mass spectrometry analysis (Figure 34).

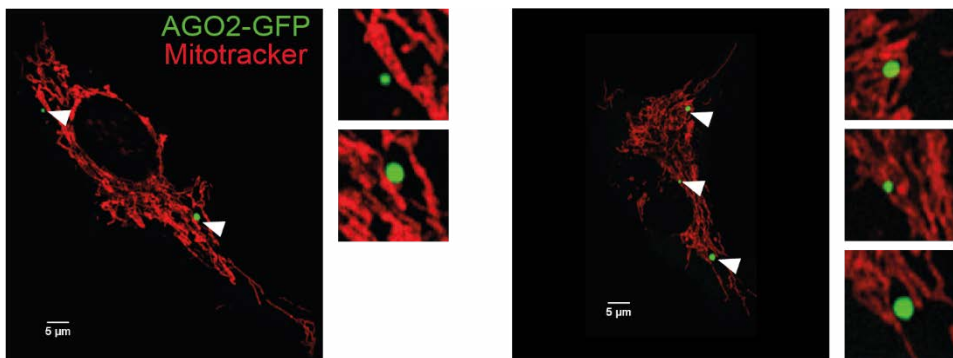


Figure 54. Mitochondria interact with AGO2 containing structures.

Representative images of mitochondria and AGO2-GFP. AGO2-GFP was overexpressed. Mitochondria were stained for 30 minutes with 100 nM MitoTracker deep red. Scale bar = 5 µm.

Some of the AGO2-GFP bodies, presumably P-bodies, appeared in close

proximity with mitochondria (Figure 54). Moreover, a part of the G3BP1-GFP positive structures were juxtaposed to mitochondria (Figure 55).

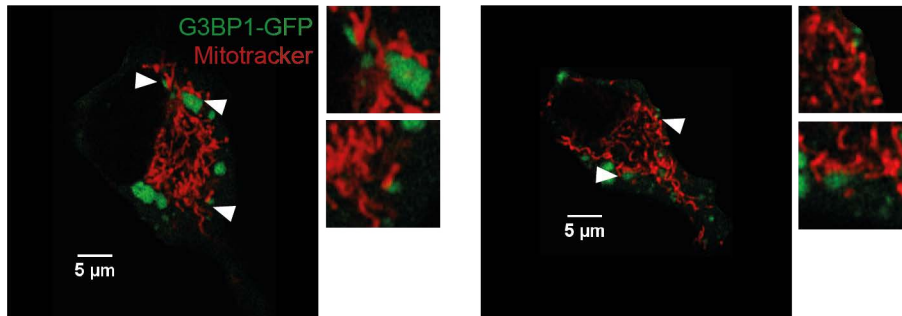


Figure 55. Mitochondria interact with G3BP1 containing structures.

Representative images of mitochondria and G3BP1-GFP. *G3BP1-GFP* was overexpressed. Mitochondria were stained for 30 minutes with 100 nM MitoTracker deep red. Scale bar = 5 µm.

4.7.3 Consequences of *SLC27A2* deficiency in autophagy

4.7.3.1. Deficiency of *SLC27A2* or *MFN2* decreases LC3B autophagic flux in starvation and autophagosome formation

SLC27A2 is a membrane fatty acid transporter and an acyl-CoA synthetase of very long chain and long chain fatty acids. It is localized in the ER, the plasma membrane and peroxisomes. *SLC27A2* is a mammalian homologue of the yeast fatty acid transporter *Faa1*¹⁹⁶ that activates fatty acids for phospholipid synthesis to be incorporated in the phagophore²⁶. We wondered whether the lack of *SLC27A2* would have an impact on amino acid starvation induced autophagic flux similar to that of *MFN2* deficiency. We transiently silenced *MFN2* and *SLC27A2* (Figure 56A) and treated the silenced cells for 1 hour with starvation medium or with starvation medium and Bafilomycin (Figure 56B). The levels of LC3B-II

were assessed and the starvation autophagic flux was determined.

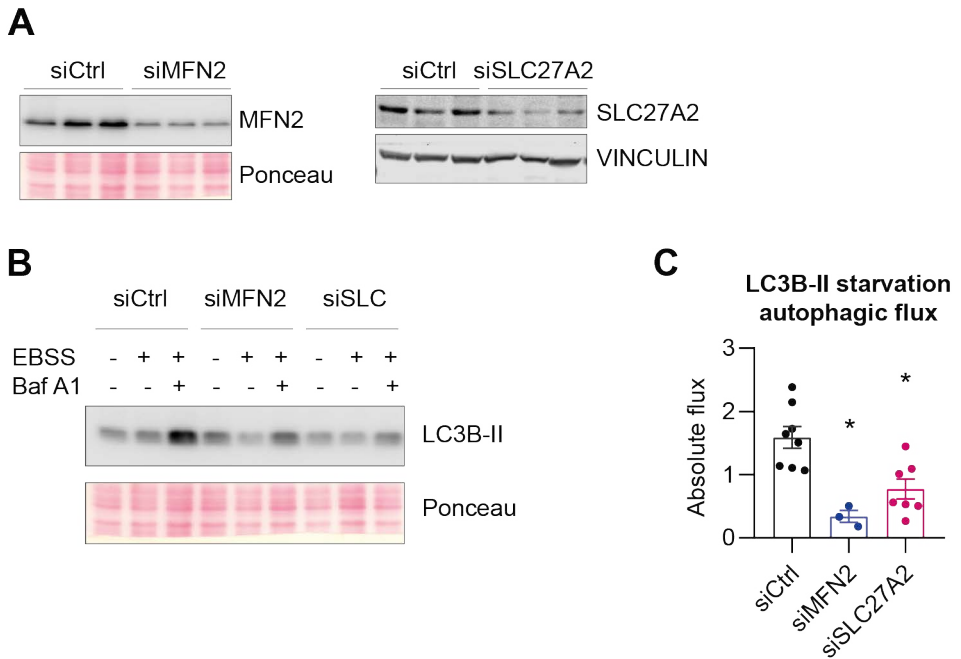


Figure 56. Silencing of *MFN2* and *SLC27A2* impairs LC3B-II autophagic flux. (A) Immunoblots of siRNA mediated silencing of *MFN2* and *SLC27A2*. (B) LC3B-II immunoblot in basal conditions, after 1 hour of starvation treatment and after 1 hour of starvation treatment and 200 nM bafilomycin (Baf A1) of cells in which *MFN2* or *SLC27A2* were silenced. (C) LC3B-II starvation autophagic flux of siCtrl, siMFN2 and siSLC27A2 (siSLC) treated cells. siCtrl N=8, siMFN2 N=3, siSLC27A2 N=7. Outlier test was performed and outliers were removed. Data passed Saphiro-Wilk test and T-test was performed to compare results. * represents p-values ≤ 0.05 .

LC3B-II starvation autophagic flux was decreased in the absence of *MFN2* and *SLC27A2*. *MFN2* silencing had a bigger impact in autophagic flux impairment than *SLC27A2* silencing.

Next, the capacity of *MFN2* and *SLC27A2* deficient cells to form

autophagosomes during nutrient deprivation was analyzed. Cells were starved for 1 hour, then fixed and stained with an antibody against LC3B (Figure 57).

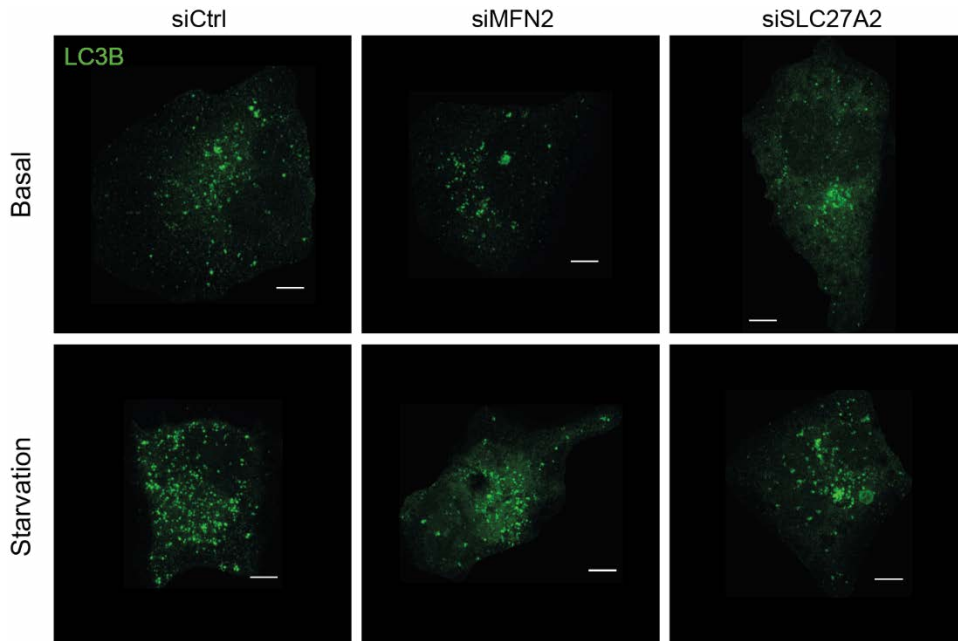


Figure 57. Decreased starvation induced autophagosome formation in *MFN2* and *SLC27A2* silenced cells (I). Representative images of LC3B staining in siCtrl, siMFN2 and siSLC27A2 treated cells in basal conditions and starved for 1 hour with EBSS. $N \geq 50$ cells per experimental condition.

Confocal microscopy revealed that the deficiency of MFN2 and SLC27A2 results in impaired autophagosome formation although cells are still able to respond to starvation stimulus to form autophagosomes (Figure 58).

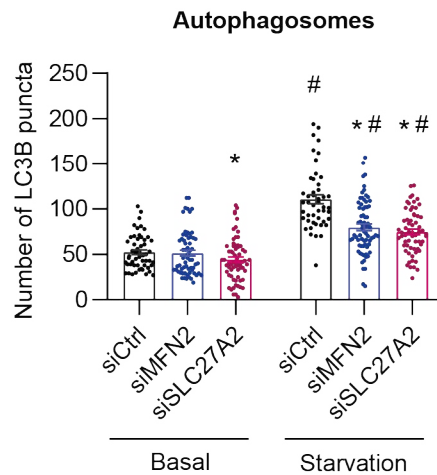


Figure 58. Decreased starvation induced autophagosome formation in *MFN2* and *SLC27A2* silenced cells (II). Quantification of the number of LC3B puncta in basal and starvation conditions. Data did not pass normality test and Mann-Whitney was used to compare the results. * and # represent p-values ≤ 0.05 . * is used for siCtrl vs. siMFN2 or siSLC27A2. # is used for basal vs. starvation.

4.7.3.2. SLC27A2 is degraded by autophagy during starvation

Knowing that SLC27A2 could contribute to autophagosome formation, next step was to determine whether SLC27A2 was removed by autophagy. HeLa cells were subjected to autophagy induction by starvation treatment in combination or not with blockage of autophagosome degradation with bafilomycin (Figure 59). We observed that, upon starvation in combination with bafilomycin treatment, SLC27A2 was accumulated. Moreover, although not statistically significant, we observed a trend towards a decrease of SLC27A2 upon nutrient deprivation.

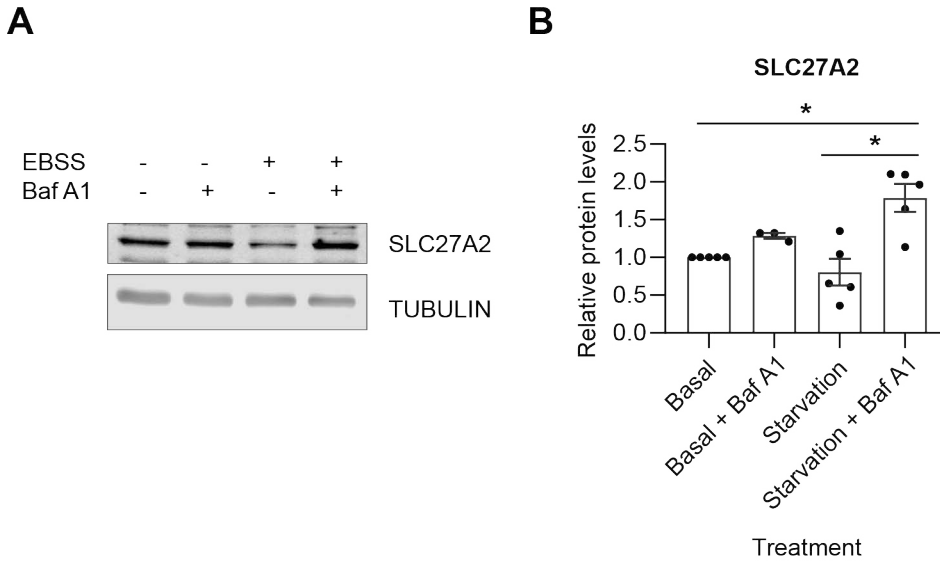


Figure 59. SLC27A2 is degraded with starvation induced autophagy. (A) SLC27A2 immunoblot of cells untreated, treated with bafilomycin (Baf A1), with 1 hour of starvation (EBSS) and with 1 hour of starvation and EBSS. (B) Quantification of SLC27A2 protein levels in these conditions. N=5. Data were subjected to Saphiro-Wilk test to assess normality and compared to basal control using T-test or Wilcoxon test depending on their normality. Basal and Basal + Baf A1 were compared with Wilcoxon test. Basal and Starvation + Baf A1 were compared using T-test. Starvation and Starvation + Baf A1 were compared with T-test. * represents p-values ≤ 0.05 .

4.7.3.3. SLC27A2 deficiency modifies the autophagic fluxes of LC3B-II, P62 and GABARAP in basal and starvation conditions

After observing that SLC27A2 deficiency impairs starvation LC3B-II autophagic flux, basal LC3B-II flux of *SLC27A2* silenced cells was analyzed (Figure 60).

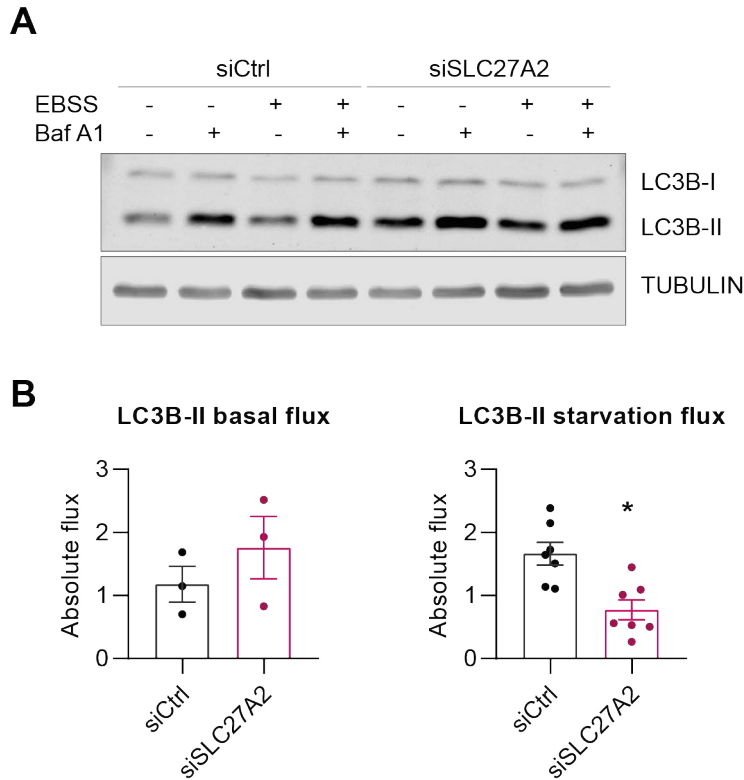


Figure 60. Silencing of *SLC27A2* impairs starvation autophagic flux of LC3B-II more than basal autophagic flux. (A) LC3B western blot of siCtrl and siSLC27A2 treated cells in basal conditions and starved for 1 hour with and without bafilomycin (Baf A1). (B) Quantification of LC3B-II basal and starvation autophagic fluxes. Basal flux N=3, starvation flux N=7. Normality of the data was determined with Saphiro-Wilk test and T-test was used to compare siCtrl and siSLC27A2 autophagic fluxes. * and # represent p-values ≤ 0.05 . * is used for siCtrl vs. siSLC27A2. # is used for basal vs. starvation.

While starvation autophagic flux of LC3B-II was decreased in silenced cells, we observed a trend towards an increase in basal autophagic flux of LC3B-II in silenced cells, although this difference was not statistically significant.

To further determine how autophagy was influenced by the absence of SLC27A2, autophagic fluxes of GABARAP and P62 were analyzed (Figure 61). We observed that basal and starvation autophagic fluxes were abrogated upon *SLC27A2* ablation, nevertheless the number of experiments was not sufficient to perform any statistical test.

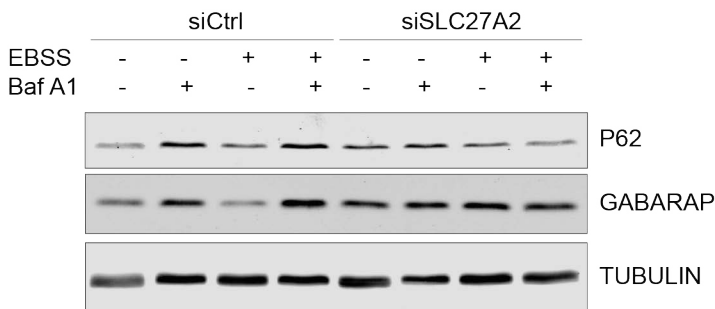


Figure 61. Silencing of *SLC27A2* impairs basal and starvation autophagic fluxes of P62 and GABARAP. P62 and GABARAP immunoblots of siCtrl and siSLC27A2 treated cells in basal conditions and starved for 1 hour with and without bafilomycin (Baf A1). N=2.

Since SLC27A2 is localized in the ER, its absence could result in ER damage and degradation by ER-phagy independent of p62 and GABARAP under basal conditions. Nevertheless, we have not further investigated this hypothesis.

4.7.3.4. SLC27A2 interacts with proteins involved in the expansion of the phagophore

Subsequently, taking into account that Faa1 plays a role in phagophore expansion, we assessed if SLC27A2 could interact with autophagy related proteins and more specifically with proteins involved in the initial steps of autophagy (Figure 62A).

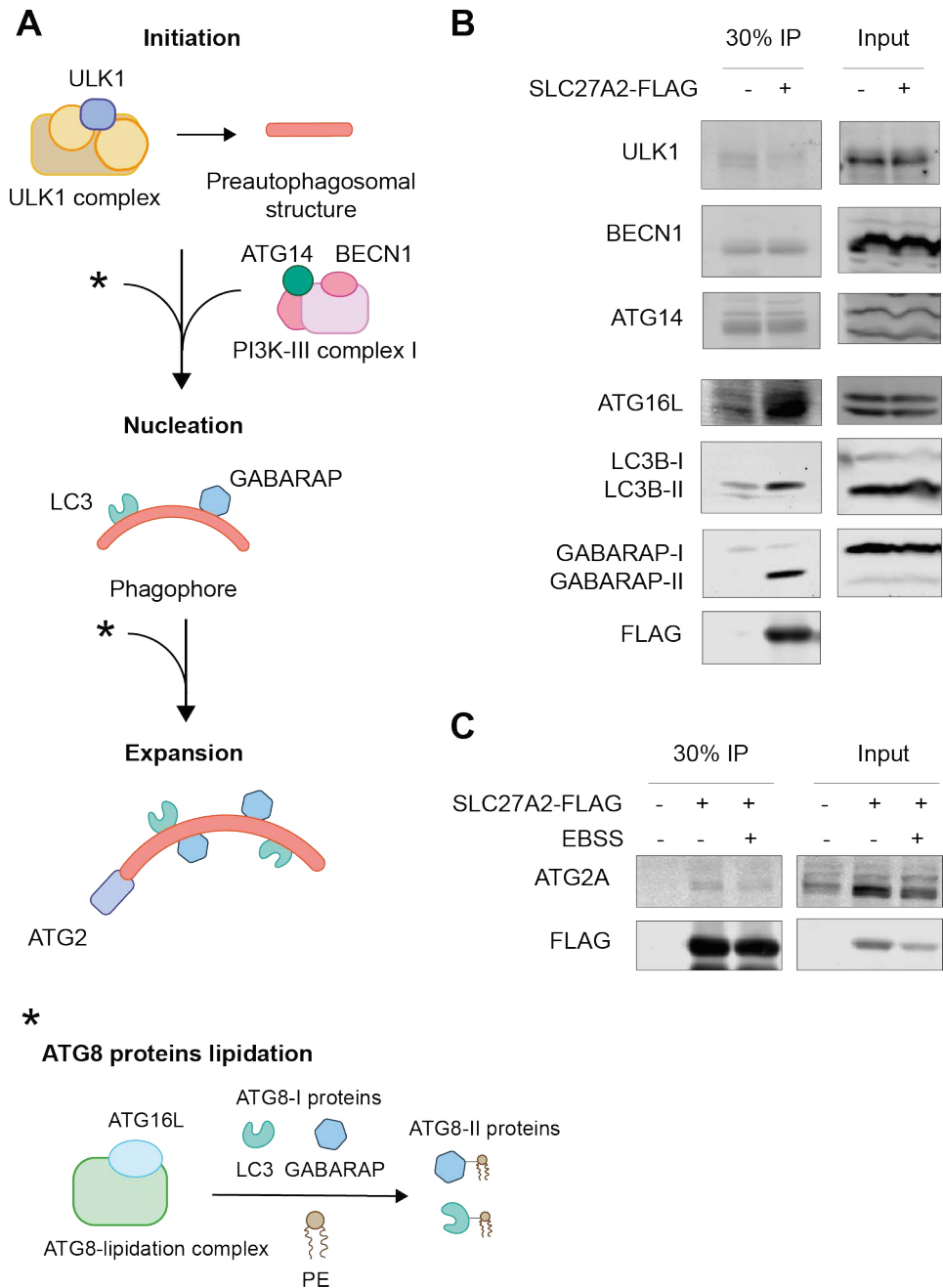


Figure 62. SLC27A2 interacts with proteins involved in the expansion of the phagophore. (A) Schematic view of early stages of autophagosome formation. (B) FLAG-IP of overexpressed SLC27A2-FLAG in HeLa cells. ULK1,

4 | Results

BECN1, ATG14, ATG16L1, LC3B, GABARAP and FLAG immunoblots of eluate (IP) and input fractions are shown. N=1. (C) FLAG-IP of overexpressed SLC27A2-FLAG in HeLa cells. ATG2A and FLAG immunoblots of eluate (IP) and input fractions are shown. N=4.

SLC27A2-FLAG was overexpressed in HeLa cells, cells were starved for one hour and immunoprecipitation using beads coupled to an antibody against FLAG was performed. In the eluate, we searched for the presence of ULK1, BECN1 and ATG14, which are related to autophagy initiation, and for ATG16L1, LC3B and GABARAP, which participate in the elongation of the phagophore (Figure 62B). SLC27A2 interacted with proteins necessary during phagophore expansion (ATG16L1, LC3B and GABARAP) and not with the selected proteins from previous stages of autophagy. Interestingly, SLC27A2 interacted with the lipidated forms of LC3B and GABARAP and not with the non-lipidated versions. Moreover, since one of the proteins that transfer phospholipids into the forming autophagosome membrane is ATG2A, we explored whether SLC27A2 was able to interact with ATG2A under basal and starvation conditions (Figure 62C). In both cases, SLC27A2-FLAG co-immunoprecipitated with ATG2A, which could mean that this interaction does not depend on the nutrient availability of the cell.

4.7.3.5. LC3 and GABARAP puncta colocalize with SLC27A2

To further validate the interaction of SLC27A2 with LC3 and GABARAP, the co-distribution of these markers with SLC27A2 was analyzed. SLC27A2-FLAG was overexpressed and cells were fixed and immunostained with antibodies against FLAG and LC3 or GABARAP. Cells were visualized by

confocal microscopy (Figure 63A and B) and Mander's coefficients of LC3 or GABARAP puncta were calculated for each cell. We observed that around 40% of the LC3 (Figure 63C) and GABARAP (Figure 63D) puncta co-localized with SLC27A2-FLAG under basal conditions.

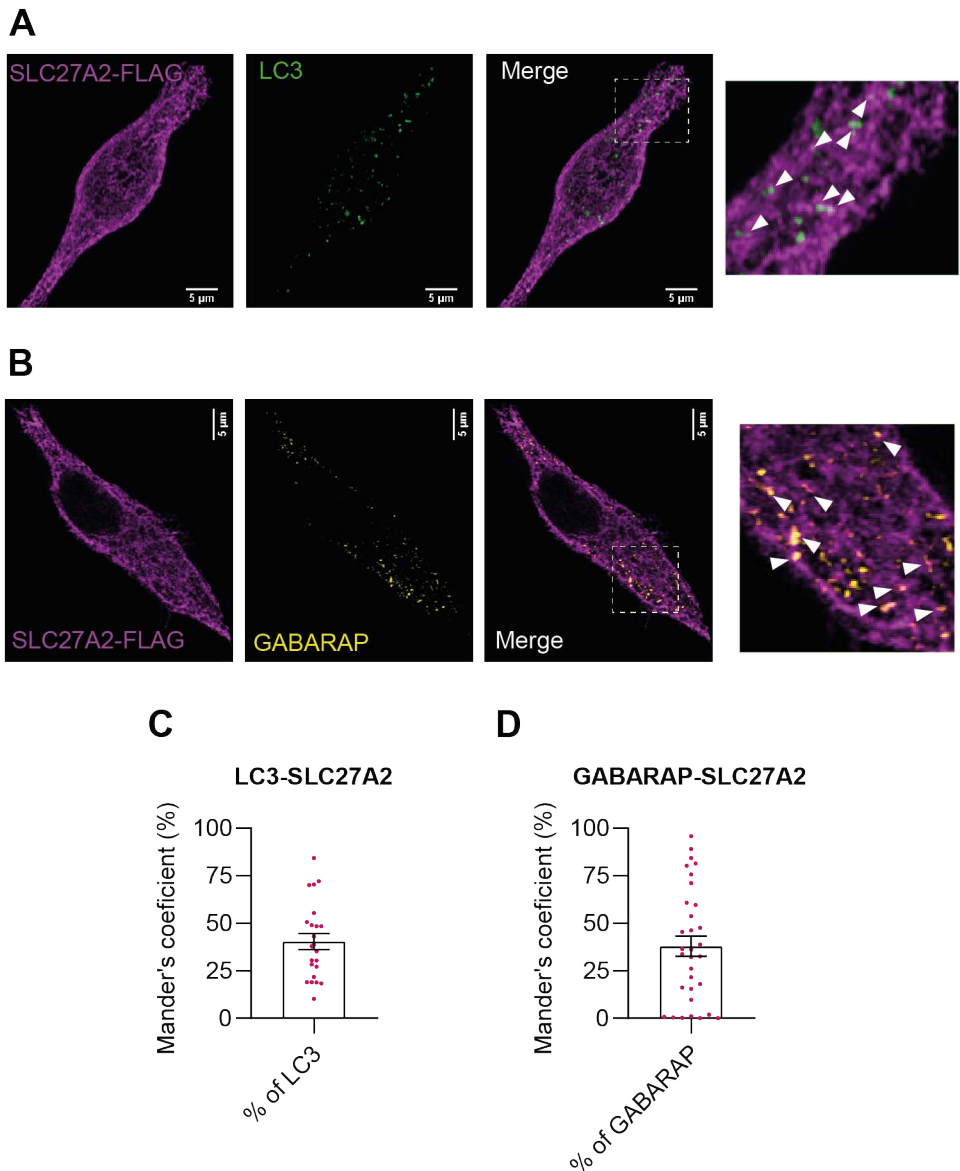


Figure 63. Some LC3 puncta and some GABARAP puncta co-localize with

4 | Results

SLC27A2-FLAG. (A) Representative images of a cell overexpressing FLAG-SLC27A2 stained with FLAG and LC3B antibodies. A threshold of 2000 AU was applied to LC3B signal to only show LC3B puncta. Scale bar: 5 μm . (B) Representative images of a cell overexpressing FLAG-SLC27A2 stained with FLAG and GABARAP antibodies. A threshold of 4000 AU was applied to LC3B signal to only show GABARAP puncta. Scale bar: 5 μm . (C) Quantification of LC3B co-distribution with SLC27A2-FLAG. N=23 cells. (D) Quantification of GABARAP co-distribution with SLC27A2-FLAG. N=29 cells.

Moreover, Pearson's correlation coefficients were calculated to determine to which extent the signals of FLAG and LC3B or GABARAP co-distribute (Figure 64). A correlation of around 0.8 out of 1 was observed for LC3 and GABARAP with FLAG, which indicates a good co-distribution of these signals.

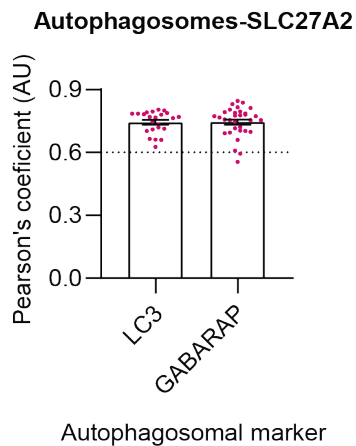


Figure 64. Autophagosomal markers' signals correlate with SLC27A2-FLAG signal. Pearson's coefficient of LC3B co-distribution with SLC27A2-FLAG and GABARAP co-distribution with SLC27A2-FLAG. LC3B N=23 cells, GABARAP N=29 cells.

4.7.3.6. SLC27A2 contains evolutionarily conserved LIR domains

Given the possibility of a direct interaction of SLC27A2 with LC3 and GABARAP, we assessed whether SLC27A2 contains any domain of interaction with those proteins. It is known that ATG8-family proteins bind to domains of four amino acids that begin with tryptophan, phenylalanine or tyrosine and end with leucine, valine or isoleucine. These domains are known as LIR motifs. SLC27A2 amino acid sequence was analyzed in order to find potential LIRs (Figure 65). We observed that SLC27A2 contains 14 potential LIR domains. Interestingly, we noticed the presence of a region with 3 consecutive LIR motifs.

```

MLSAIYTVLAGLLFLPLLVNLCPPYFFQDIGYFLKVAAVGRRVRSY      46
GKRRPARTILRAFLEKARQTPHKPFLFRDETLTYAQVDRRSNQVA      92
RALHDHLGLRQGDCAVLLMGNEPAYVWLWLGLVKLGCAMACLNINI    138
RAKSLLHCFQCCGAKVLLVSPQLQAAVEEILPSLKKDDVSIYYVSR    184
TSNTDGDIDSLDKVDEVSTPEIPESWRSEVTFSTPALYIYTSGTTG    230
LPKAAMITHQRIWYGTGLTFVSGLKADDVIYITLPHYHSAALLIGI    276
HGCIVAGATLALRTKFSASQFWDDCRKYNVTVIQYIGELLRYLCNS    322
PQKPNDRDHKVRRLALGNGLRGDVRQFVKRFGDICIYEFYAATEGN    368
IGFMNYARKVAVGRVNYLQKKIITYDLIKYDVEKDEPVRDENGYC    414
VRVPKGEVGLLVCKITQLTPFNGYAGAKAQTEKKKLRDVFKKGDLY    460
FNSGDLLMVDHENFIYFHDRVGDTRFWKGENVATTEVADTVGLVDF    506
VQEVNVYGVHVPDHEGRIGMASIKMKNHEFDGKKLFOHIADYLPS    552
YARPRFLRIQDTIEITGTFKHKMTLVEEGFNPAVIKDALYFLDDT    598
AKMYVPMTEDIYNAISAKTLKL                                620

```

Figure 65. Human SLC27A2 contains 14 LIR motifs. Amino acid sequence of human SLC27A2. LIR domains are displayed in green. The region with 3 consecutive LIR motifs is highlighted with a red rectangle.

In order to assess if any of these potential LIR motifs could be more relevant for the interaction of SLC27A2 with ATG8-family proteins,

we hypothesized that it should be evolutionarily conserved. We used ClustalW²²² to align the human sequence of SLC27A2 with those of several species including *Drosophila melanogaster*, *Danio rerio*, *Gallus gallus*, *Xenopus laevis*, *Gorilla gorilla*, *Mus musculus*, *Rattus norvegicus* (Figure 66). We observed that almost all the LIR domains are evolutionarily conserved among these species. To assess how important these domains are for the interaction of SLC27A2 with ATG8 proteins, it would be necessary to perform site directed mutagenesis followed by co-IP of the SLC27A2 mutants with LC3 and GABARAP.

```

Drosophila  YLQWILAPVLTATISGLILYQGPWYGVATLYAALISILLVRPGWRWFYIAAVTTPRDITVA 120
Danio        -----MLCPLLGLLLSA-----LLFL-YIRFFPLP-----QDCAF 30
Gallus      ----MLGVLVAAVAGLLLLL-----LLH-GRWFPFLW-----ADLGA 32
Xenopus     ----MITLI FTALPGLLLP-----ILI-SFIFPYIF-----QDI AW 32
Homo        ----MLSAITYTVLAGLLFLP-----LLV-NLCCPYFF-----QDIGY 32
Gorilla     ----MLSAITYTVLAGLLFLP-----LLV-NLCCPYFF-----QDIGY 32
Mus         ----MLPVLYTGLAGLLLLP-----LLL-TCCCPYLL-----QDVR 32
Rattus      ----MLPVLYTGLAGLLLLP-----LLL-TCCCPYLL-----QDVR 32
          : : **:: : : :
    
```

```

Drosophila  LFAVIT--RVLLFIKRQERKNLNIIGDIFESNVARQPKLAIVSESQOMTFRQVNEHSNRVA 178
Danio       ALRTLNLGRLLARFGSRSPCFSTLERFAEVARKHPDKLFIVFGDERITYRDA DRISNRLA 90
Gallus      FVALVGSRLRCRWLSRRPPIITLLQVFQSHARRRPHPHLLLFQDEYVTFSDMERRSNRAA 92
Xenopus     FLTIIRFGIRTWRYVSKTPALTVVDLFLEKVERHPDKPFVLFKEEYVTVSHMKLSNQAA 92
Homo        FLKVAAVGRRVRSYGKRRPARTILRAFLEKARQTPHKPFLFRDETLTYAQVDRRSNQVA 92
Gorilla     FLKVAAVGRRVRSYGKRRPARTILRAFLEKARQTPHKPFLFRDETLTYAQVDRRSNQVA 92
Mus         FLRLANMARRVRSYRQRRPVRTILRAFLEQARKTPHKPFLFRDETLTYAQVDRRSNQVA 92
Rattus      FLOLANMARQVRSYRQRRPVRTILHVFLEQARKTPHKPFLFRDETLTYAQVDRRSNQVA 92
          . . . * . . : * : : : : * : . . ** : *
    
```

```

Drosophila  NVFHSN-GYKKGDVVGLLENRAQFVATWLGLSKIGVITPLINTNLRGASLQHSITVGGC 237
Danio       NALRD---RSGQIVALFHGNAPMYVFTWLALAKLGCTVALLNTNRSRSLVHCCECSGA 146
Gallus      RAFALRLGLQPGQTVAVFLPNVPAVYVWTWLALAKLGCAMAACLN CNVRGRALLHARSAARA 152
Xenopus     RALLTHAAVKS GDCVAIFMANAPYINIWLGVAKLGSSTACLN MNIRSKSFLHCFKCSGA 152
Homo        RALHDHLGLRQGD CVALFMGN EPAVYVWLWLGVLKLGCA MACLN YNIRAKSLLHCFQCCGA 152
Gorilla     RALHDHLGLRQGD CVALFMGN EPAVYVWLWLGVLKLGCA MACLN YNIRAKSLLHCFQCCGA 152
Mus         RALHDQLGLRQGD CVALFMGN EPAVYVWLWLGVLKLGCA MACLN YNIRAKSLLHCFQCCGA 152
Rattus      RALHDHLGLRQGD CVALFMGN EPAVYVWLWLGVLKLGCA MACLN YNIRAKSLLHCFQCCGA 152
          .. : : * : * : : * : : ** : : * * : : * * : : * : .
    
```

```

Drosophila  TALIYGASFRSAVMDIAKDLPAH-VGLYQFNDESQEWASEGLSQGLAQLNGLLETAA 296
Danio       KTLITAAELVPAVLEVLQSLRQQQVSVLMLSGEAE-----TQDIINLTNQVSRASE 197
Gallus      DIVLSCSELQA AAVEEVL PDLKQEGVRV FYLNSTSP-----TPGVEALLPAIEAASD 203
Xenopus     KVILAEPELKDVI EEMPEL RKNVRVFLTETVI-----SEGTFSLDKVKAASD 203
Homo        KVLLVSPPELQA AAVEEIL PSLKDDVSIYVSR TSN-----TDGIDSF LDKVDEVST 203
Gorilla     KVLLASPELQA AAVEEIL PSLKDDVSIYVSR TSN-----TDGIDSF LDKVDEVST 203
Mus         KVLLASPDLEA AAVEEVL PTLKDDAVSVFYVSR TSN-----TNGVDTILDKVDGVS A 203
Rattus      KVLLASPELHEA AAVEEVL PTLKKEGVSVFYVSR TSN-----TNGVDTVLDKVDGVS A 203
          : : . : . : : * . * : . . : : . : : : .
    
```

```

Drosophila  KDKVAAGASRADHHDKLVYIYTSGTTGLPKAAVITHSRVFFIAAGIHYTLGFKQDDVYIT 356
Danio       EAPPISLRQHITMKSPALYIYTSGTTGLPKAAVVTHEKVMV-MSFLQRLSGVCSDDIYI 256
Gallus      EPM PQYH-TNTTTASKAIYIYTSGTTGLPKAAVVT EMKVMV-VANLARI CGLRENDIYIT 261
Xenopus     ESVPKSLRSFVSGKSLAMYIYTSGTTGLPKAALINHYRLLL-ACGLFEICNVRAKDVYYS 262
Homo        EPIPE SNRSEVTFSTPALYIYTSGTTGLPKAAMITHQRIWY-GTGLTFVSGLKADDVYIYI 262
Gorilla     EPIPE SNRSEVTFSTPALYIYTSGTTGLPKAAMITHQRIWY-GTGLTFVSGLKADDVYIYI 262
Mus         EPTPE SNRSEVTF TTPAVYIYTSGTTGLPKAATINHRLWY-GTGLMSGITAQDVYIT 262
Rattus      DPIPE SNRSEVTF TTPAVYIYTSGTTGLPKAATINHRLWY-GTSLALRS GIKAHDVYIT 262
          . : ***** : : : : : . . * : *
    
```

```

Drosophila  PLYHTAGGVMSMGQALLFGSTVIRKKFSASGYFSDCARFQCTVGQYIGEMARYILAT 416
Danio       CLPLYHSAGFLAGLSGAI ERGITVVLKSKFSASRFWDDCREHNVTVIQYIGEMRYLCNT 316
Gallus      TLPYHSAGLLIGVGGCLEVGATCVLRKFSASQFWDCCRRYNVTVIQYVGLMRYLCNS 321
Xenopus     PLYHSANMIGVHGCIYK GATLVL RPKFSASQFWDCCRKYNVTVVQYIGELRYLCNV 322
Homo        TLPFYHSAALLIGIHGCI VAGATLALRTKFSASQFWDCCRKYNVTVIQYIGELRYLCNS 322
Gorilla     TLPFYHSAALLIGIHGCI VAGATLALRTKFSASQFWDCCRKYNVTVIQYIGELRYLCNS 322
Mus         TLPFYHSAALMIGLHGCI VVGATLALRSKFSASQFWDCCRKYNVTVIQYIGELRYLCNT 322
Rattus      TLPFYHSAALMIGLHGCI VVGATFALRSKFSASQFWDCCRKYNATVIQYIGELRYLCNT 322
          : * : * : : : : : * * : : ***** : : ** : : ** * : * : * : *
    
```

4 | Results

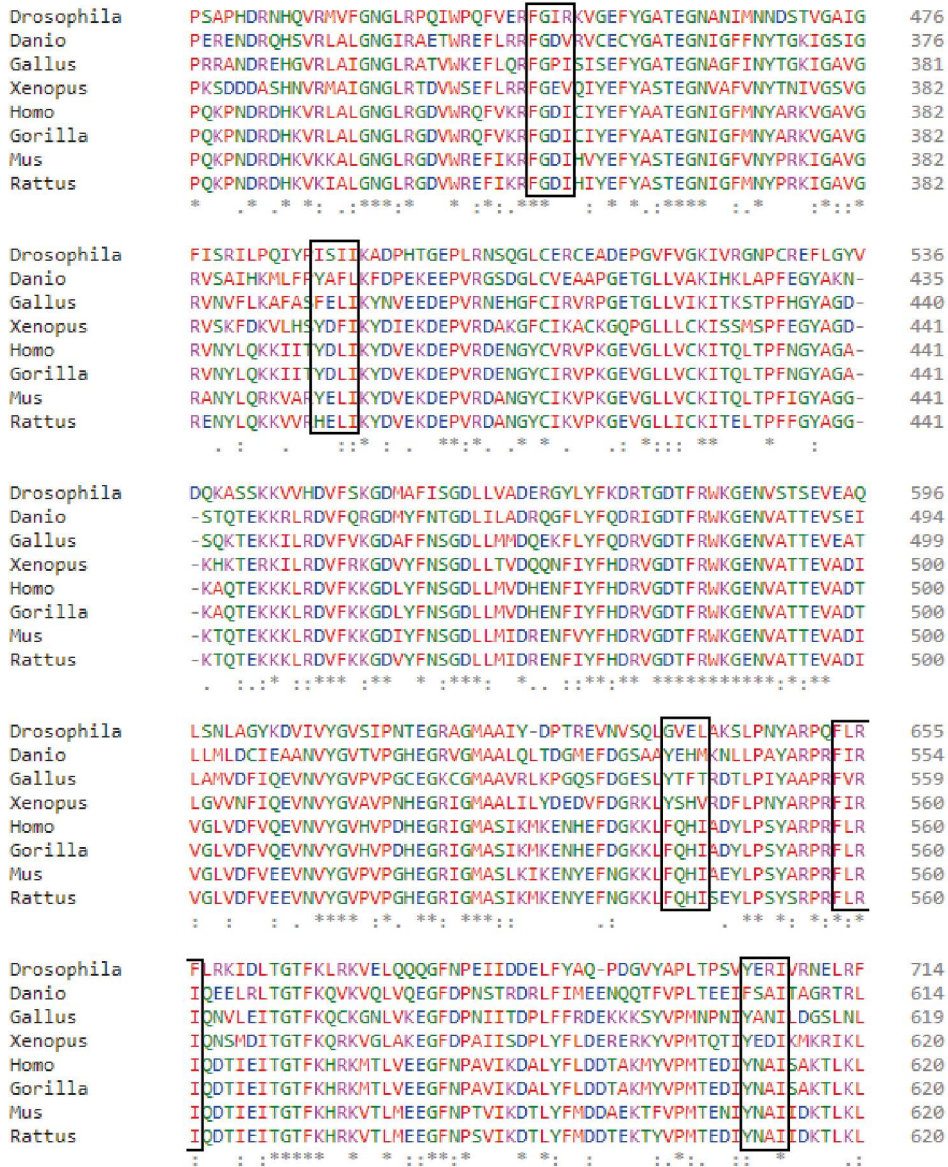


Figure 66. SLC27A2 LIR motifs are evolutionarily conserved. ClustalW alignment of SLC27A2 sequences of different species (*Drosophila melanogaster*, *Danio rerio*, *Gallus gallus*, *Xenopus laevis*, *Homo sapiens*, *Gorilla gorilla*, *Mus musculus*, *Rattus norvegicus*). LIR domains are shown inside black rectangles. Amino acids are represented in different colors depending on their sidechains: red stands for small and hydrophobic sidechains (A, V, F, P, M, I, L, W, Y), blue

represents acidic side chains (D, E), purple is used for basic sidechains (R, K), and green includes hydroxyl, sulfhydryl and amine sidechains and glycine (S, T, Y, H, C, N, G, Q).

4.7.3.7. Absence of SLC27A2 impairs MFN2 targeting by autophagosomes

MFN2 is necessary at ER-mitochondria contact sites for autophagosome formation. Thus, we hypothesized that LC3 could be able to target cellular domains enriched in MFN2. Since we observed that SLC27A2 can interact with ATG8-family proteins, we analyzed whether the ablation of *SLC27A2* could have an impact on LC3-MFN2 co-distribution (Figure 67). Cells were treated with a siRNA specific for *SLC27A2*, subjected to 1 hour of starvation, fixed and stained with antibodies against LC3 and MFN2. Confocal microscopy was performed to determine whether LC3 was able to reach MFN2 rich domains under basal and starvation conditions and whether the absence of SLC27A2 had an impact on LC3-MFN2 co-distribution. We observed that in basal conditions 30% of LC3 puncta co-distributed with MFN2 signal in control cells. We also noticed that the quantity of LC3 puncta that co-distributed with MFN2 in those cells increased to a 55% under starvation conditions. Both, under basal and starvation conditions, co-distribution of MFN2 signal and LC3 puncta was diminished in the absence of SLC27A2: 20% of LC3 puncta co-distributed with MFN2 in basal conditions and 30% after 1 hour of starvation.

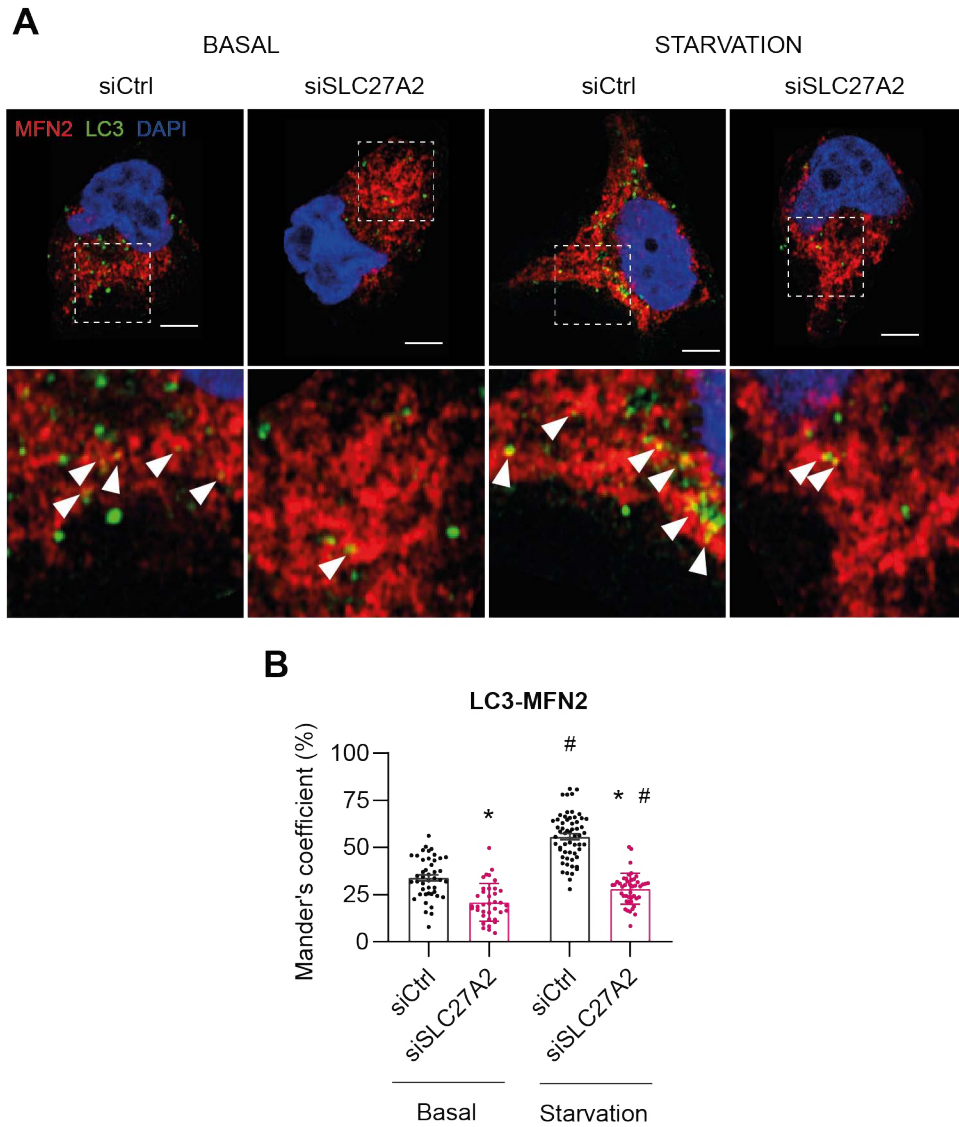


Figure 67. Silencing of *SLC27A2* results in impaired co-distribution of LC3B and MFN2. (A) Representative images of cells treated with control or *SLC27A2* specific siRNAs in basal or starvation conditions (1h EBSS) and stained with antibodies against MFN2 and LC3B and with Hoesch. Scale bar: 5 μ m. (B) Quantification of LC3B co-distribution with MFN2. siCtrl basal N=44 cells, siSLC27A2 basal N=59 cells, siCtrl starvation N=37 cells, siSLC27A2 N=45 cells. Data passed Saphiro-Wilk normality test and were compared using unpaired

T-test. * and # represent p-values ≤ 0.05 . * is used for siCtrl vs. siSLC27A2. # is used for basal vs. starvation.

4.7.3.8. MFN2 interacts with SLC27A2 and ATG2A in basal and starvation conditions

According to our mass spectrometry data, MFN2 and SLC27A2 interact under starvation conditions. We wanted to know whether MFN2 interacts with SLC27A2 under basal conditions and if MFN2 also interacts with ATG2A. MFN2-HA HeLa cells were used for endogenous IP of MFN2 with HA-beads (Figure 68).

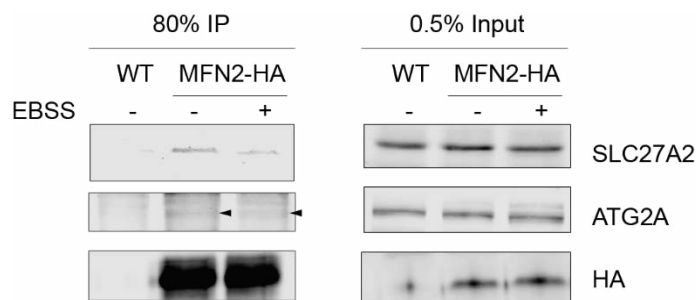


Figure 68. MFN2-HA co-immunoprecipitates with SLC27A2 and ATG2A in basal and starvation conditions. SLC27A2, ATG2A and HA immunoblots of HA-IP of WT and MFN2-HA cells in basal conditions and upon 1 hour of EBSS treatment. Eluate (IP) and input fractions are shown. Black arrows indicate the bands corresponding to ATG2A. N=1.

We observed that MFN2 also interacts with SLC27A2 under basal conditions. Nevertheless, to compare the interaction of MFN2 with SLC27A2 under basal and starvation conditions and determine how this interaction is influenced by nutrient availability we need more experimental replicates. Moreover, we noticed that MFN2 was capable to interact with ATG2 under basal and starvation conditions.

DISCUSSION



5. DISCUSSION

5.1. Endogenous IP coupled to MS is a physiological approach to identify MFN1 and MFN2 interactors

Most of the interactors of MFN1 and MFN2 have been described under overexpression conditions (Table 4). It is known that MFN2 overexpression results in abnormal mitochondrial distribution in clumps around the nucleus and induces cell death²⁰⁰. The overexpression of MFN1 can also cause aberrant mitochondrial distribution and morphology^{199,223}. Here, we edited HeLa cells with CRISPR/Cas9 technology with the aim of generating MFN1 and MFN2 HA-tagged cell lines with endogenous expression levels of MFN1 and MFN2. By applying this strategy, we avoided artifacts of protein overexpression such as protein aggregation, toxicity, mislocalization or organelle clumping. C-terminal tagging of MFN1 and MFN2 was selected over N-terminal tagging in order to prevent any interference between the HA-tag and the GTPase domain. By targeting the HA-tag insertion to the C-terminal domain we also labeled all the possible splicing variants of MFN1 and MFN2. We decided to use HA-tag because it is a short tag (9 amino acids) and there are highly specific antibodies for its detection and immunoprecipitation.

After transfecting the cells with the pSpCas9-gRNA plasmid and the ssODN, around 10% of the cells expressed high amounts of GFP and those were expanded until monoclonal cell lines were generated. From these clones around 1 out of 10 had integrated the HA-tag sequence in the genome. The estimated efficiency of our CRISPR/Cas9 system is 1%.

Although yielding a relatively small number of HA-positive clones, the main advantage of this strategy is that tedious cloning steps are avoided by using a commercially available ssODN and that it is a cost-effective approach. Moreover, selecting the cells that express GFP is more efficient than puromycin selection, which can lead to non-specific puromycin resistance or even to Cas9 integration in the genome.

Heterozygous cell lines expressing MFN1-HA or MFN2-HA at endogenous levels were obtained. We tagged 50% of the expressed MFN1 protein and 80% of the expressed MFN2 protein. We do not know how many alleles of *MFN1* and *MFN2* are present in HeLa cells nor which of them are preferentially expressed. Nevertheless, 50% HA-tagged MFN1 and 80% HA-tagged MFN2 were sufficient to perform HA-IP coupled to MS analysis to identify novel interactors.

We validated that the introduction of an HA-tag in *MFN1* and *MFN2* did not affect MFN1 nor MFN2 expression, the expression of other mitochondrial proteins nor mitochondrial morphology. Moreover, these cells presented normal functioning autophagy and normal mitochondrial hyperfusion. In all, these results demonstrated that CRISPR/Cas9 mediated insertion of a short tag is a clean, effective and simple strategy to develop a cellular model to perform biochemical analyses under our experimental conditions.

Most of the known interactors of MFN1 and MFN2 have been discovered under conditions of overexpression (Table 4). As we have previously mentioned, overexpression of MFN1 and MFN2 leads to aberrant mitochondrial morphology and distribution and in the case of MFN2

can eventually result in cell death^{199,200,223}. Therefore, it is not possible to ensure that the interactors described in conditions of MFN1 and MFN2 overexpression are occurring in the cell under physiological conditions. We have also noticed that many of the interactors of MFN1 and MFN2 described to date have been characterized after solubilizing the cells with Triton X-100 or NP-40. Those detergents, although being non-ionic can be too harsh to preserve protein-protein interactions. As revealed by our data, 1% Triton X-100 and 1% NP-40 are not able to preserve the interaction between MFN1 and MFN2 to the same extent as 1% CHAPS and 1% Digitonin. Moreover, in one of the first trials of HA-IP followed by MS that we performed, we used 1% Triton X-100 and we could not observe any of the already known partners of MFN1 or MFN2 (data not shown). Digitonin has been widely used to study mitochondrial complexes^{211,212,224} and has already been applied to reveal binding partners of MFN1 and MFN2 (Table 4). The interaction of overexpressed MIB (VAT1 orthologue in *Drosophila melanogaster*) with MFN1 and MFN2 was discovered after solubilizing HeLa cells with 1% Digitonin²²⁵. Moreover, in the study that described the interaction between overexpressed SLC25A46 and MFN1/2, the cells were lysed with 1 or 1.5% digitonin. Taking all these data into account, we chose 1% digitonin to solubilize the cells.

Table 4. MFN1 and MFN2 known interactors. Binding partners of MFN1 and MFN2 discovered by Co-IP. Experimental conditions in which Co-IP was performed have been included: overexpression or endogenous expression of MFN1 and MFN2 (O: Overexpression; E: Endogenous expression), detergent contained in lysis buffer and cell type in which Co-IP was performed. High

5 | Discussion

throughput screenings using BioID were excluded from this search.

Interactor ^f	MFN1	MFN2	Expression	Lysis buffer	Cell or tissue
BAD ²²⁶	X	X	O	2% CHAPS	HeLa
BAK ¹⁵⁶	X	X	E O	CHAPS	HeLa
BAT3 ²²⁷	X	X	O	0.5% Triton X-100	HeLa
BAX ²²⁶	X	X	O	2% CHAPS	HeLa
CADH5 ¹⁴²		X	O	1% Triton X-100	HLMVEC
CCNB1 ¹⁴⁵	X		E	0.1% NP-40	HeLa
CTNNB1 ¹⁴²		X	O	1% Triton X-100	HLMVEC
DRP1 ²²⁸		X	O	1% Triton X-100	BHK-21
eIF5A ²²⁹	X		E	-	Mouse VSMC
ERK ¹⁵⁰	X		O	6mM CHAPS	MEF
GASZ ¹⁶⁵	X	X	O	1% Triton X-100	HEK293T
GP78 ²³⁰	X	X	O	1% Triton X-100	COS-7
G-β2 ²³¹	X		E O	1.5% DDM	HeLa
HDAC6 ²³²	X	X	E	0.5% NP-40	MEF
HUWE1 ⁶⁹		X	O	0,6% Triton X-100	U2OS
JNK2 ⁶⁹		X	O	0,6% Triton X-100	U2OS
MARCHF5 ⁷²		X	E O	0,5% NP-40	HEK293T
MARCHF5 ²³³	X		O	-	HeLa
MARCHF5 ⁷¹		X	O	1% NP-40	COS-7, HeLa
MAVS ¹³⁴		X	E O	1% NP-40	HEK293T
MFN1 ⁶		X	O	1% Triton X-100	MEF
MFN1 ⁸²		X	O	1% NP-40	MEF
MFN2 ⁸²	X		O	1% NP-40	MEF
MGRN1 ²³⁴	X		E	0.1% Triton X-100, 1% NP-40	HeLa
MIB (VAT1) ²²⁵	X	X	O	1% Digitonin	Drosophila
MILTON1 ²¹	X	X	O	1% Triton X-100	HEK293T, rat DRG neurons
MILTON2 ²¹	X	X	O	1% Triton X-100	HEK293T, rat DRG neurons
MIRO2 ²¹	X	X	O	1% Triton X-100	HEK293T, rat DRG neurons
MIRO1 ²¹	X	X	O	1% Triton X-100	HEK293T, rat DRG neurons
MNS1 ²³⁵		X	E	1% NP-40	Mouse spermatogenic cells
MUL1 ²³⁶		X	O	RIPA	S2
NLRP3 ¹³⁹	X	X	E	1% Triton X-100	BMM
NME3 ²³⁷	X	X	O	-	HEK293T
NUMB ⁹⁶	X		E O	NP-40	MCF12A
OPA1 ²³⁸	X	X	E	0,8% Triton X-100	HeLa and 143B

PARK2 ²³⁹	X	X	E O	1% NP-40	SH-SY5Y
PERK ¹⁸		X	E	1% Triton X-100	MEF
PINK1 ²³⁹	X	X	E O	1% NP-40	SH-SY5Y
βIIPKC ⁷³	X		E	0.1% Triton X-100	Rat heart isolated mitochondria
PKC-ζ ⁹⁶	X		E O	NP-40	MCF12A
PLIN1 ⁸⁹		X	E	1% NP-40	Mouse BAT, mouse brown adipocytes
PRKAA1 ²⁴⁰		X	O	-	HeLa
PS2 ²⁴¹		X	O	1% NP-40, 0.01% SDS, 0.05% Na-DOC	MEF
RAB7A ⁹⁴		X	E	-	Mouse cardiomyocytes
RAF1 ²³⁹	X	X	E O	-	MEF
RAS ²⁴²		X	O	1% CHAPS	MEF
RAS ²³⁹	X	X	E O	-	MEF
RICTOR ²⁴³		X	E O	0.5% NP-40	MCF-7, A549
RIN1 ²⁴⁴		X	E O	1% NP-40	COS-7, HeLa, MEECs
SIRT1 ²⁴⁵	X	X	E O	1% NP-40	Normoxic hepatocytes MEF
SLC25A38 ²⁴⁶	X	X	E	-	HEK293T
SLC25A46 ²⁴⁷	X	X	E	1-1.5% digitonin	HEK293T
SMAD2 ²⁴⁴		X	E O	1% NP-40	COS-7, HeLa, MEECs
STOML2 ²⁴⁸		X	E	0.5% digitonin	HeLa
TCHP ⁴³		X	E O	1% Triton X-100, 0.1% SDS	HeLa
TDP-43 ²⁴⁹		X	E	1% NP-40, 0.5% Na-DOC	Human cortex tissue
TIP60 ²⁵⁰	X		O	1% NP-40, 0.1% Na-DOC, 0.1% SDS	HEK293T
USP30 ²⁵¹	X	X	O	1% NP-40	MEF
VCP ²⁵²		X	O	0,5% NP-40	HeLa

After applying MS to HA-IP, we could observe that already known interactors of MFN1 and MFN2 had been identified by mass spectrometry and reached statistical significance. We found MFN2 in the mass spectrometry of MFN1-HA IP and MFN1, MARCHF5 and MIRO2 (RHOT2) in the mass spectrometry of the IP of MFN2-HA.

Currently, the most commonly used method to identify protein-protein interactions is proximity biotinylation²⁵³. This method implies the

overexpression of the protein of interest fused to a biotinylation subunit of 35 kDa. Besides, this technique involves cell treatment with biotin with a duration from 10 minutes to 18 hours^{253,254}. This technique is applied for finding both stable and transient protein-protein interactions. Recently, a study of the protein composition in the different mitochondrial compartments using BioID technology has been published²⁵⁵. Proteins from the OMM, IMS, IMM and mitochondrial matrix were fused to the BirA biotinylating subunit and stable cell lines overexpressing these proteins were generated for further streptavidin pull-down coupled to MS analysis. One of the proteins analyzed was MFN2, which was overexpressed fused to a BirA subunit at its N-terminal region. The potential interactors of MFN2 obtained by this method were enriched in subunits of the proteasome, which could indicate that BirA-MFN2 fusion protein is not fully functional and is degraded in the proteasome. Moreover, MFN1 was not identified by MS. N-terminal localization of BirA subunit in MFN2 could be impeding its interaction with some of its binding partners, such as MFN1. As it is shown in Figure 69 and Figure 70, only three proteins (RHOT2, MARCHF5 and GEMIN4) identified in our study were significantly enriched in the results obtained by Antonicka et al. Part of these differences could be explained by the fact that BioID technology is more powerful than classical IP in identifying transient interactions. Other differences observed in the proteomes of MFN2 in both studies could be the consequence of artifacts of stable overexpression of MFN2 or impaired mitochondrial function due to the presence of an excess of MFN2 in the screening performed by Antonicka et al. Hence, we conclude that proximity biotinylation techniques are

not the best approach to study the stable complexes formed by MFN1 or MFN2.

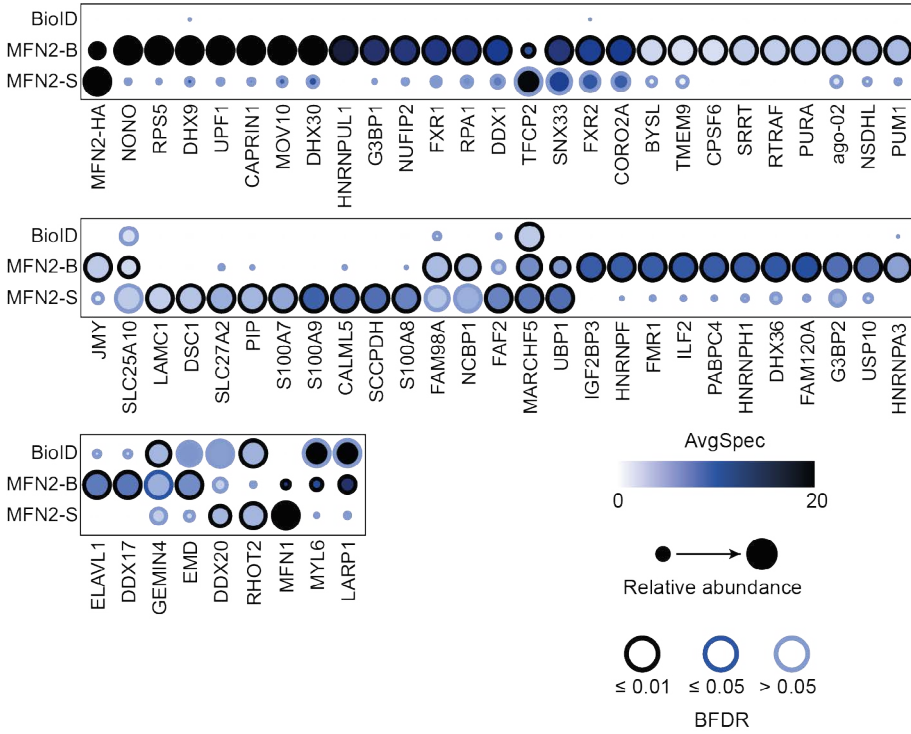


Figure 69. High confidence MFN2 interactors found in our study and their abundance in the screening performed by Antonicka et al. ²⁵⁵.

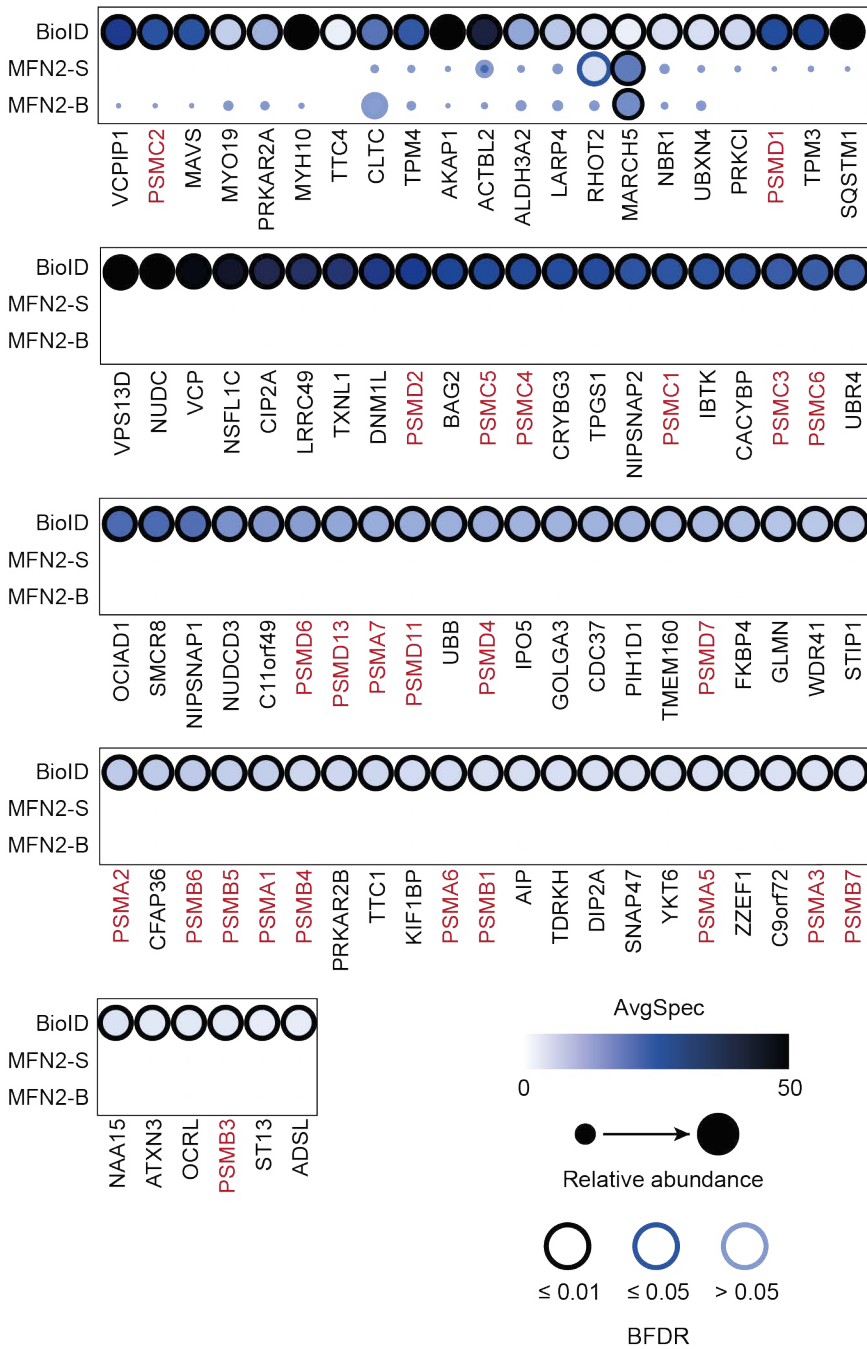


Figure 70. High confidence interactors found by Antonicka et al. and their abundance in our screening. Antonicka et al. binding partners identified with a BFDR of 0.01 or lower. Proteasome subunits are highlighted

in red.

5.2. MFN1 and MFN2 interactomes are dependent on the nutrient availability of the cell

Mitochondrial architecture is related to the balance between the energy demands of the cell and the energy that is supplied to the cell. When the cells are exposed to an oversupply of nutrients, their mitochondria divide ²⁵⁶, whereas mitochondria in cells that are deprived from nutrients undergo a hyperfusion process ²⁵⁷. Under fasting conditions, mitochondria elongate in order to increase cristae number and ATPase activity ²⁵⁷. Moreover, mitochondrial tubulation protects mitochondria from being degraded through mitophagy ^{14,257}. Thus, the interactome landscape of mitochondrial dynamics proteins could be also influenced by metabolic changes. Mass spectrometry revealed 44 binding candidates for MFN1 in basal conditions, 6 potential interactors for MFN1 after starvation treatment, 51 possible partners of MFN2 in basal conditions and 16 binding candidates of MFN2 upon starvation treatment. We have represented these results in Figure 71 and Figure 72, where we have included the organelles to which MFN1 and MFN2 possible interactors belong to.

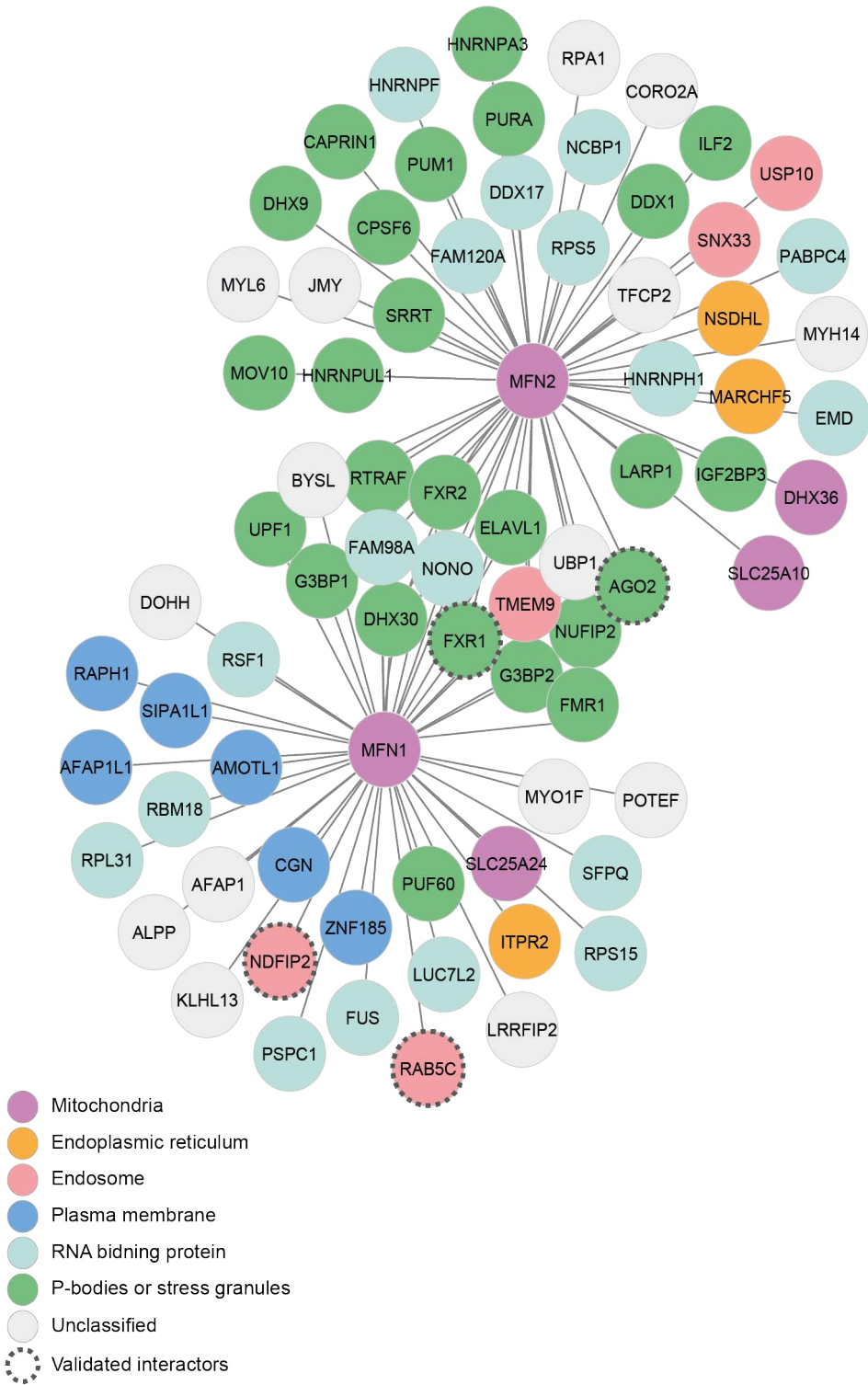
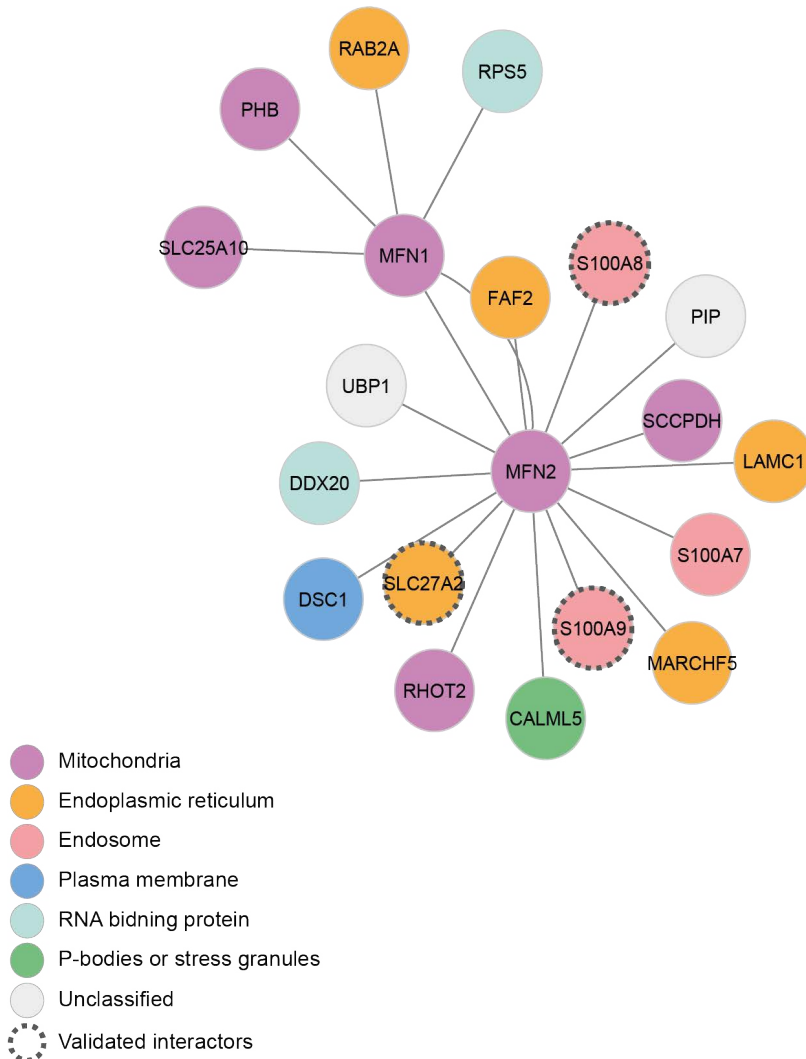


Figure 71. Interaction network of MFN1 and MFN2 in basal conditions.

Proteins from mitochondria, ER, endosomes, plasma membrane, RNA binding proteins and RNA-binding proteins localized in P-bodies or stress granules are highlighted. Interactions demonstrated in this thesis are emphasized with a darker edge.

**Figure 72. Interaction network of MFN1 and MFN2 in starvation conditions.**

Proteins from mitochondria, ER, endosomes compartment, plasma membrane, RNA binding proteins and RNA-binding proteins localized in

P-bodies or stress granules are highlighted. Interactions demonstrated in this thesis are emphasized with a darker edge.

These data show a dramatic decrease in the interactions of MFN1 and MFN2 when cells are deprived of amino acids, glucose and serum. Moreover, the only partner preserved by MFN1 upon nutrient deprivation is MFN2. In the case of MFN2, the binding candidates that are preserved in starvation are MFN1, MARCHF5 and UBP1. These changes in the interaction partners of MFN1 and MFN2 could be a consequence of a more specialized function of MFN1 and MFN2 in conditions of nutrient deprivation. MFN1 would be more actively participating in mitochondrial elongation and MFN2 would be mainly exerting its role in autophagy.

5.2.1. Nutrient availability determines MFN1- or MFN2-mediated mitochondrial tethering to other organelles

When cells are starved from serum for 24 hours, the mean distance between ER and mitochondria is decreased and the frequency of tight associations between these two organelles is increased ²⁵⁸. Moreover, cells deprived of serum, amino acids and glucose for 4 hours have a higher number of tight contacts between ER and mitochondria than cells in normal growth medium ²⁵⁹. MFN2 participates in ER-mitochondria contacts and several studies have demonstrated that its absence results in increased distance between mitochondria and ER or decreased contact sites ^{81,87,260–262}. Interestingly, we have identified more ER proteins in starvation conditions (FAF2, LAMC1, SLC27A2, MARCHF5) as possible interactors of MFN2 than in basal conditions (NSDHL, MARCHF5). These

proteins could participate in helping MFN2 to tether ER and mitochondria together during starvation. It is also known that autophagosomes arise from ER membranes at ER-mitochondria contact sites and that these are not formed in the absence of MFN2 ¹⁶. Thus, it is likely that ER interactors of MFN2 discovered in conditions of nutrient deprivation are related to the role of MFN2 in autophagosome formation, as we have demonstrated for SLC27A2.

MFN1 also participates in contacts of mitochondria and ER by interacting with MFN2 ¹⁹, but its depletion does not induce substantial changes in ER-mitochondria contacts ²⁶². Interestingly, in our mass spectrometry data, ITPR2 was identified by MS as a potential interactor of MFN1 under basal conditions. ITPR2 is a calcium channel in the endoplasmic reticulum important in the maintenance of ER-mitochondrial contacts and in calcium supply to mitochondria ²⁶³. Cardiac ablation of *Mfn1* in mice does not have an effect on mitochondrial calcium uptake, whereas the lack of *Mfn2* does decrease mitochondrial calcium uptake ²⁶⁴. This could indicate that MFN1 binding to the calcium channel does not influence its activity.

MFN1 has been found to anchor mitochondria to the plasma membrane in stem cells during cellular division ⁹⁶. Surprisingly, we found that MFN1 binding partners under basal conditions were enriched in plasma membrane proteins (AFAP1L1, ALPP, AMOTL1, RAPH1, SIPA1L1). This could indicate that MFN1 serves as an anchor of mitochondria to the plasma membrane through the interaction with these proteins.

5.2.2. Post-translational modifications of MFN1 and MFN2 are dependent on nutrient availability

MFN1 and MFN2 fusogenic activity is modulated by post-translational modifications. Ubiquitination, phosphorylation and acetylation of MFN1 and MFN2 are known to inhibit mitochondrial fusion. Ubiquitination of MFN1 and MFN2 by either PARK2 or MARCHF5 has been described to reduce mitochondrial fusion^{20,67–70}. Phosphorylation of MFN2 by PINK1 or JNK can enhance ubiquitination and, therefore, inhibit mitochondrial fusion^{69,239}. Phosphorylation of MFN1 by ERK or PKC β 2 isoform inhibits mitochondrial fusion^{73,150}. Acetylation of MFN1 reduces mitochondrial fusion and is reversed by HDAC6⁷⁴. In this study we have identified novel potential modifiers of MFN1 and MFN2 that participate in protein dephosphorylation, hypusination, ubiquitination and deubiquitination. Surprisingly, most of these proteins were identified among MFN1 binding candidates in basal conditions. We found the protein phosphatase ALPP^{265,266}, the hypusinase DOHH²⁶⁷ and the ubiquitination related proteins KLHL13, NDFIP2 and AMOTL1.

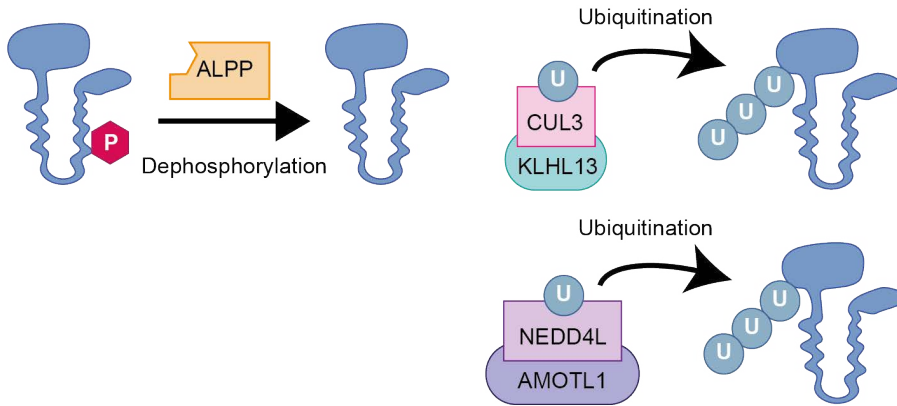
Since MFN1 activity is inhibited by phosphorylation, ALPP could reverse MFN1 inhibition and promotes mitochondrial fusion. Modification of lysine residues to hypusine by DOHH has only been described in the maturation of the translation initiation factor eIF5A²⁶⁷. Interestingly, a recent study in vascular smooth muscle cells showed that MFN1 interacts with eIF5A and that eIF5A transient ablation increases mitochondrial fission²²⁹. Conversely, overexpression of eIF5A resulted in augmented mitochondrial fusion. These data suggest that MFN1 activity could be

regulated by a positive feedback loop involving DOHH and eIF5A: MFN1 interacts with DOHH to activate eIF5A and then eIF5A promotes MFN1 participation in mitochondrial fusion. KLHL13 is an adaptor of the E3 ligase CUL3 ²⁶⁸. NDFIP2 activates the HECT domain of E3 ubiquitin ligases such as ITCH, NEDD4, NEDD4L, SMURF2, WWP1 and WWP2 ²³ and has been identified in mitochondria ²². We have validated that overexpressed NDFIP2 is able to interact with both MFN1 and MFN2. Nevertheless, we have not unraveled whether this interaction promotes MFN1 and MFN2 ubiquitination neither its effect on mitochondrial dynamics. AMOTL1 acts as a scaffold for the E3 ubiquitin ligase NEDD4L ²⁶⁹. The interaction of MFN1 with these three proteins could promote MFN1 ubiquitination and repression of its activity. These potential MFN1 modification mechanisms based on our mass spectrometry data are illustrated in Figure 73.

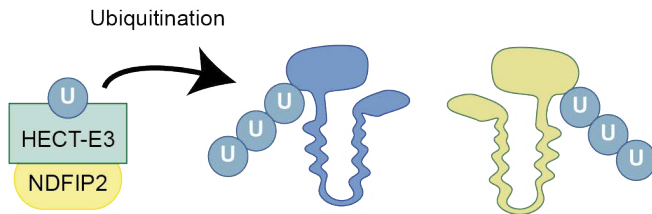
Among MFN2 potential interactors, we found more peptides of MARCHF5 in starvation than in basal conditions. It is known that MARCHF5 can promote the formation of MFN2 oligomers that tether ER and mitochondria ⁷². Thus, increased MARCHF5 interaction with MFN2 under starvation conditions could imply increased tethering activity of MFN2 during starvation. Moreover, our mass spectrometry data suggest that the de-ubiquitinase USP10 is a possible modifier of MFN2 under basal conditions and not under starvation conditions. USP10 could be promoting the fusogenic role of MFN2 by removing PARK2 or HUWE1-mediated ubiquitin modifications or could be preventing MFN2 tethering activity by removing MARCHF5-mediated ubiquitin chains. Possible

MFN2 modification mechanisms based on our mass spectrometry data are illustrated in Figure 73.

MFN1 modifications



MFN1 and MFN2 modifications



MFN2 modifications

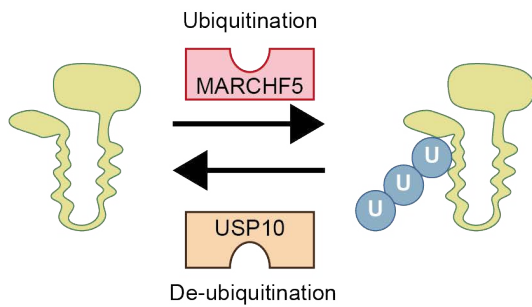


Figure 73. Proposed mechanisms of MFN1 and MFN2 post-translational modifications.

5.2.3. *MFN2 potential interactors link its function to autophagy*

During nutrient deprivation, autophagosomes arise at ER-mitochondria contact sites in a MFN2-dependent manner ^{16,270}. However, the precise role of MFN2 in starvation induced autophagy has not been elucidated yet. In our mass spectrometry data, we observed that MFN2 interacts with more proteins involved in autophagy than MFN1. Under basal conditions JMY and USP10 are potential interactors of MFN2. JMY is recruited to nascent autophagosomes through its LC3 interacting region where it promotes Arp2/3 complex mediated actin nucleation ²⁷¹. Actin filament nucleation in the autophagosome by the Arp2/3 complex is crucial for the correct formation of autophagosomes ²⁷². Lack of JMY results in a dramatic decrease in autophagosome formation ²⁷¹. USP10 is a de-ubiquitinase that interacts with BECN1 to remove ubiquitin chains and avoid its degradation ²⁷³. Moreover, USP10 has been shown to reverse LC3B ubiquitination, resulting in decreased proteasomal degradation of this protein ²⁷⁴. The authors of this study suggest that USP10 regulates autophagy through cycles of ubiquitination and de-ubiquitination of LC3B.

Under starvation conditions, mass spectrometry data show that MFN2 could interact with S100A8, S100A9 and SLC27A2. The complex formed by S100A8 and S100A9 promotes autophagy when administered to the cells ²⁷⁵. Moreover, S100A8 has been demonstrated to dissociate the complexes formed by BECN1 and BCL2 in order to promote the role of BECN1 in autophagy ^{220,276}. S100A9 has appeared as a high confidence

binding candidate of the autophagy proteins ATG5²⁷⁷ and P62²⁷⁸ after pulldown of these proteins coupled to MS analysis. We have validated that MFN2 interacts with S100A8 and S100A9. Nevertheless, we have not performed any functional experiments since these proteins are difficult to work with because they are secreted and because they form oligomers that account with an elevated number of subunits. This high degree of oligomerization complicates their denaturation for protein expression analyses. Moreover, when we attempted siRNA mediated silencing of *S100A8*, it increased its expression. *SLC27A2* belongs to the family of the yeast fatty acid transporter Faa1 that has been recently shown to fuel phospholipid synthesis with activated fatty acids for autophagosome formation²⁶ and its implication in autophagy has been demonstrated in this thesis. We have demonstrated that MFN2 interacts with *SLC27A2*.

Given the potential interaction of MFN2 with USP10 and JMY and the demonstrated interaction of MFN2 with S100A8, S100A9 and *SLC27A2*, we propose that MFN2 acts in ER-mitochondria contacts as a platform to recruit proteins that are necessary in autophagosome formation and its absence could impair the localization of these proteins in these sites and therefore abrogate autophagosome formation. The fact that some proteins are observed under basal conditions and other under starvation conditions, could be related to the stage of autophagy in which they are needed. JMY and USP10 could be necessary at ER-mitochondrial contact sites earlier than S100A8, S100A9 and *SLC27A2*.

5.3. RNA related structures interact with mitochondria in a MFN1/MFN2-dependent manner

Protein translation occurs at the ribosomes. Besides other localizations, these have been found in the proximity of mitochondria where they orchestrate the synthesis of most of the mitochondrial proteins which are then imported into mitochondria ^{279–282}. Protein import into mitochondria is not the only fate of mRNA translation in the proximity of mitochondria. It has been described in neurons, that mitochondria are needed at synapses to provide plasticity-induced protein synthesis with ATP ²⁸³. Localization of the translation machinery in the OMM can occur through peptide sequences of the newly synthesized protein or through untranslated sequences in the 3'-UTR domain ^{284,285}. Recently, a high throughput screening of the subcellular localization of RNA molecules revealed the localization of ribosome dependent and independent transcripts in the OMM ²⁸⁶. Moreover, they observed cytoskeleton dependent transport of RNAs to reach the mitochondrial surface ²⁸⁶. While mRNAs are transported for localized protein synthesis, translational activity is repressed until they reach their final destination ^{287,288}. When mRNAs specifically reach the OMM, PINK1 and PARK2 participate in de-repression of translation by ubiquitination of translation repressors ²⁸⁹. Translation can be repressed by the formation of condensates of proteins and mRNA molecules: P-bodies ³² and, in conditions of stress, stress granules ²⁹⁰. Nevertheless, it has been recently shown that translation can occur at stress granules ²⁹¹. Both of these structures can be transported in the cytosol through microtubules to

the regions where repressed mRNAs are needed ^{292,293}. CLUH granules are another type of granules of RNA and proteins, which have been described to both promote and repress protein synthesis depending on the metabolic state of the cell ³⁰. However, there is just one study that has reported CLUH granules and their protein composition has not been elucidated yet.

Among the potential interactors of MFN1 and MFN2, we observed an enrichment in RNA binding proteins under basal conditions. We crossed the lists of possible partners of MFN1 and MFN2 that we obtained with databases of core components of P-bodies and stress granules ^{27,28,294}. We detected that under basal conditions, around half of the interactors of MFN1 and MFN2 are components of P-bodies or stress granules. We validated the interactions of MFN1 and MFN2 with AGO2 and FXR1. Moreover, we observed that AGO2 structures (probably P-bodies) and G3BP1 structures (likely stress granules) interact with mitochondria in HeLa cells. It is not the first time that P-bodies and stress granules are observed in close apposition with mitochondria, however these interactions have not been deeply studied ^{31,295}. We propose that under basal conditions MFN1 and MFN2 link these structures to the mitochondrial surface and participate in the transport of the translation machinery to the sites in the OMM where required.

Under conditions of nutrient deprivation, global protein synthesis is decreased ²⁹⁶. Moreover, during starvation CLUH granules orchestrate the translation of proteins involved in catabolic pathways, such as amino acid degradation, fatty acid oxidation, and the Krebs cycle,

but inhibit the translation of other transcripts ³⁰. We propose that the arrest in global protein synthesis during starvation results in reduced OMM coupled translation and the release of MFN1 and MFN2 from the translation machinery in the shape of P-bodies or stress granules. Nevertheless, translation is still required in different parts of the cell or the mitochondrial network and there is a specific recruitment of the translation machinery and mRNAs independent of MFN1 and MFN2 that may involve CLUH granules. Knowing that MFN1 and MFN2 are necessary during nutrient deprivation for mitochondrial hyperfusion and autophagosome formation respectively, these roles of MFN1 and MFN2 could be more essential for the cell under lack of nutrients than the transport of the translational machinery for mitochondrial protein synthesis (Figure 74).

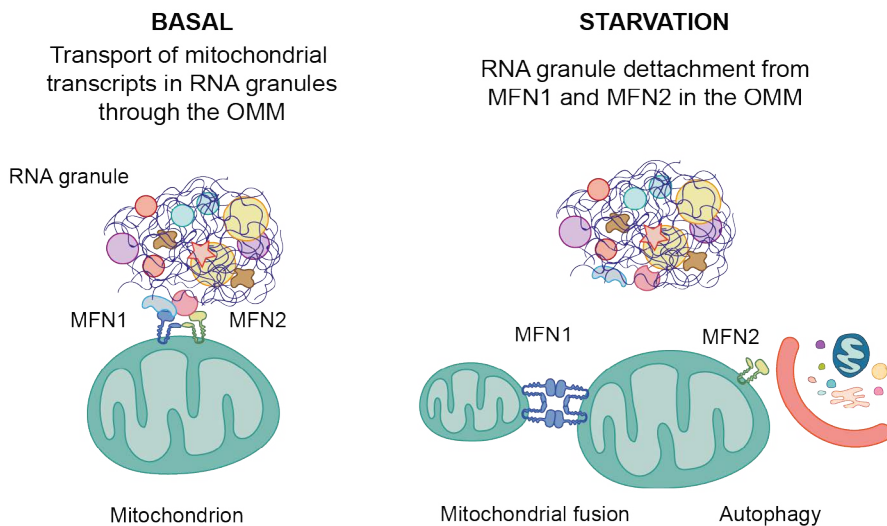


Figure 74. Proposed model for MFN1 and MFN2 anchoring of RNA granules under basal and starvation conditions. Under basal conditions MFN1 and MFN2 interact with RNA binding proteins to participate in the transport of

mitochondrial transcripts through the OMM. Under starvation conditions, there is a global arrest in protein translation and the cell prioritizes MFN1 role in mitochondrial fusion and MFN2 role in autophagy rather than the transport of transcripts across the OMM.

5.4. RAB5C interaction with MFN1 and MFN2 maintains mitochondrial morphology and prevents mitochondrial degradation

The contacts between endosomes and mitochondria are poorly studied. To date, it is known that these interactions are involved in iron transfer to mitochondria ²⁹⁷⁻²⁹⁹. Moreover, cholesterol is also transported from endosomes mitochondria at sites of close proximity ³⁰⁰. Mitochondrial quality control has also been shown to occur at the endosomal compartment ²¹⁸. During mitophagy, PINK1 is stabilized at the OMM of damaged mitochondria and PARK2 is recruited ²¹⁸. Endosomal RAB5C is bound to the OMM of those mitochondria and then exchanged by endosomal RAB7A ²¹⁸. Subsequently, other proteins are attracted to these sites to build the autophagosome ²¹⁸. Moreover, another study has shown that RAB5C is recruited to the OMM together with its guanyl-nucleotide exchange factors ALS and RABEX5 when mitochondria undergo acute oxidative stress ²¹⁷. The authors suggest that RAB5C targets stressed mitochondria as a cytoprotective mechanism to alleviate stress.

Early endosomes have been recently implicated in mitochondrial removal independently of mitophagy ³⁰¹. Mitochondria are targeted by PARK2, ubiquitinated and eventually engulfed by an early endosome

³⁰¹. RAB5A endosomes are capable of engulfing damaged mitochondria ³⁰¹. We have observed that co-distribution between mtDNA and EEA1 is increased in the absence of RAB5C, which is opposite to this result. However, the authors of the study did not demonstrate whether RAB5 proteins are crucial in this process. Another mechanism for mitochondrial quality control that involves the endosomal compartment is the formation of mitochondria-derived vesicles (MDVs). These vesicles arise from mitochondria in a PINK1/PARK2 dependent manner and fuse either to late endosomes or to lysosomes ^{302,303}. It has been recently reported that in the absence of mitophagy, cells exert mitochondrial quality control through elimination of defective fragments in MDVs ³⁰⁴. Nevertheless, little is known about MDVs biogenesis mechanisms, cargo specificity or other destinations of MDVs.

We have described that RAB5C interacts with MFN1 and MFN2 and that *RAB5C* ablation results in increased mitochondrial fragmentation. Therefore, mitochondria-endosome contacts mediated by RAB5C interaction with MFN1 and MFN2 are required for the maintenance of balanced mitochondrial dynamics. Moreover, we documented an increase in mitophagy genes (PINK1 and PARK2) and PINK1 protein levels accompanied by a substantial reduction in the number of mitochondrial nucleoids and TOM20. Furthermore, we demonstrated that mitochondrial nucleoids are accumulated in the presence of bafilomycin in *RAB5C* KO cells and co-localization between early endosomes and mtDNA is increased in *RAB5C* KO cells in basal conditions and with bafilomycin. Nonetheless, LC3 co-distribution with mtDNA

remains equal as in WT cells. These results suggest that an endosomal pathway is clearing defective mitochondria in the absence of RAB5C interaction with MFN1 and MFN2. However, the fact that mitochondrial mass is diminished in *RAB5C* KO cells only by a 5% compared to WT cells, could indicate that whole mitochondria are not being degraded, but only small portions that contain mtDNA and TOM20. This selective degradation of tiny mitochondrial fragments could be carried out in MDVs that fuse to endosomes (Figure 75). The increase in mitophagy genes and PINK1 protein levels that we observe in *RAB5C* KO cells also supports this hypothesis. Nevertheless, more insight is necessary to elucidate the precise mechanism of mitochondrial degradation in the absence of RAB5C-MFN1 and RAB5C-MFN2 interactions and other mitochondrial implications of these interactions.

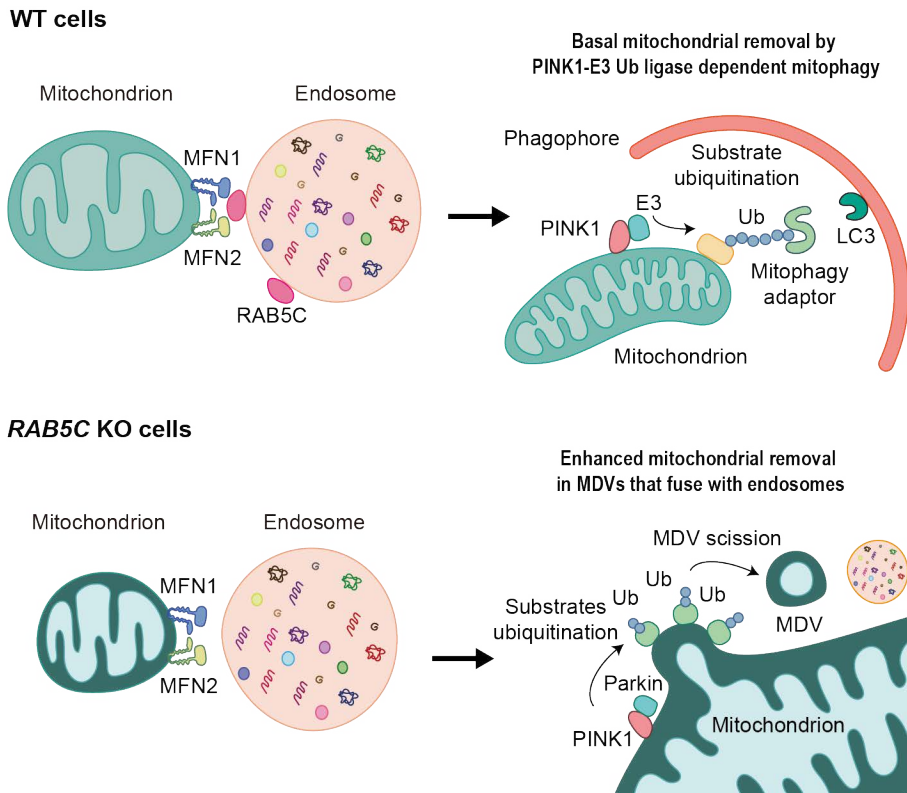


Figure 75. Proposed model for selective mitochondrial degradation by MDVs in *RAB5C* KO cells. In WT cells mitochondrial quality control occurs through defective mitochondria elimination by mitochondrial selective autophagy mediated by PINK1 and E3 ubiquitin ligases and dependent on LC3. In *RAB5C* KO cells, clearance of damaged mitochondria is exerted through MDVs that arise in a PINK1-dependent manner and that fuse with endosomes.

5.5. SLC27A2 interacts with MFN2 to orchestrate phagophore expansion

The contact sites between ER and mitochondria are a major source of autophagosomes during nutrient deprivation¹⁶. The presence of *MFN2* has been reported crucial for autophagosome formation in these

circumstances ^{16,270}. Our results have corroborated these observations: transient downregulation of *MFN2* results in diminished formation of autophagosomes upon nutrient starvation. Moreover, autophagic flux during starvation is also reduced upon *MFN2* silencing, which is in line with previously published data ¹⁸. Nevertheless, the precise role of *MFN2* in autophagy and which are its partners to accomplish its function remain elusive. By applying mass spectrometry to detect the interactors of *MFN2* under conditions of starvation, we have identified several proteins that could implicate *MFN2* in the process of autophagy, as described in the previous section. We have demonstrated that *MFN2* interacts with *SLC27A2*, which is a homologue of the yeast protein *faa1* that supplies fatty acids to the synthesis of phospholipids to be incorporated to the autophagosome ²⁶. This result suggests that *SLC27A2* is one of the binding partners of *MFN2* during autophagy and that together they could contribute to autophagosome formation.

Faa1 is an acyl-CoA synthetase that activates long chain fatty acids in yeast ³⁰⁵. *SLC27A2* is an acyl-CoA synthetase of long-chain and very long-chain fatty acids in mammals ³⁰⁶. *SLC27A2* and *Faa1* belong to the same protein family, nevertheless the yeast orthologue of *SLC27A2* is considered *Fat1*. Additionally, we have described that the absence of *SLC27A2* impairs autophagy similarly to the absence of *FAA1*. Silencing of *SLC27A2* results in diminished autophagic flux and decreased formation of autophagosomes, as it happens with the absence or mislocalization of *Faa1*. Nevertheless, Schütter et al. show that the ablation of the yeast orthologue of *SLC27A2*, *FAT1*, does not affect autophagy ²⁶. Furthermore,

we have shown that SLC27A2 co-localizes with autophagosomes, which is in line with Faa1 available data. However, Fat1 does not co-localize with Atg8 structures. Our results indicate that SLC27A2 plays the role of Faa1 in mammalian cells. Schütter et al. mutate the catalytic site of *FAA1* and observe an impairment of autophagy²⁶. Further work will implicate the characterization of the effects in autophagy of the inactivation of the catalytic site of SLC27A2.

The role described for Faa1 in autophagy by Schütter et al. is the supply of activated fatty acids to the pathway of *de novo* synthesis of phospholipids in yeast. *De novo* phospholipid synthesis has been demonstrated to contribute to autophagosome biogenesis in yeast and mammalian cells. In yeast, the enzymes related to the first steps of *de novo* phospholipid synthesis (Sct1, Gpt2, Ale1, Slc1) have been found to co-localize with Atg8 structures during starvation²⁶. Inducible mutants of these proteins show inhibited Atg8 degradation upon starvation induction of autophagy²⁶. The Kennedy pathway, which is implicated in *de novo* production of PC and PE in eukaryotes³⁰⁷, has recently been suggested to contribute to the expansion of lifespan in yeast through autophagy³⁰⁸. Ethanolamine external supply promotes PE synthesis and extends lifespan and the depletion of ethanolamine-phosphate cytidylyltransferase (*ECT1*) and choline-phosphate cytidylyltransferase (*PCT1*) enzymes from the Kennedy pathway suppresses this effect³⁰⁸. *ATG7* deletion to inhibit autophagy abolishes the effects of ethanolamine treatment on lifespan extension³⁰⁸. The authors of this study demonstrated as well that ethanolamine induces autophagy and reduces senescence in mammalian

cells. Nevertheless, a thorough characterization of the direct implication of the Kennedy pathway in autophagy in yeast and mammals is still elusive. In human cells, phosphatidylcholine (PC) synthesis *de novo* is activated during starvation induced autophagosome formation and perturbing this synthesis pathway results in impaired autophagy ³⁰⁹. Moreover, newly synthesized PC co-localizes LC3 ³⁰⁹. Loss of choline-phosphate cytidyltransferase A (PCYT1A) activity, the limiting enzyme during PC synthesis, results in impaired autophagosome formation ³⁰⁹.

Phospholipids contain two side chains derived from fatty acids. Free fatty acids in subcellular compartments have been shown to sustain autophagosome formation ³¹⁰. Moreover, lipid droplets can supply fatty acids to autophagosome biogenesis ³¹⁰. The impairment of lipid droplets formation results in the inhibition of autophagy and is not rescued by exogenous supply of fatty acids ³¹⁰. Nevertheless, a global vision of how autophagosomes are built from fatty acid activation is missing. The precise phospholipid composition of autophagosomes needs to be determined.

Another pathway to synthesize phospholipids is the Sphingosine 1-phosphate (S1P) pathway. The S1P metabolic pathway is the only pathway that allows the conversion of sphingosine from ceramide into glycerophospholipids (PI, PC, PS, PE, etc.) by the incorporation of an acyl-CoA molecule ³¹¹. In yeast this pathway is impaired by depleting the acyl-CoA synthetases Faa1 and Faa4 ¹⁹⁶. Human acyl-CoA synthetases can recover the phenotype of these yeast double null mutant strains and this suggests an important contribution of these enzymes in the synthesis of

glycerophospholipids. Namely, these acyl-CoA synthetases are: ACSBG1, ACSL1/3/4/5/6, or SLC27A2/4 ^{196,311}. Nevertheless, Schütter et al. have not analyzed the co-localization between the enzymes of the S1P pathway and Atg8 structures. Given the fact that both SLC27A2 and Faa1 provide the S1P pathway with activated fatty acids, this pathway could also be relevant for the synthesis of phospholipids to be incorporated in the phagophore. Interestingly, S1P has been described to positively regulate autophagy through mTORC1 inhibition in mammalian cells ³¹².

As documented for Faa1 in yeast, we have observed in HeLa cells that SLC27A2 co-localizes partially with LC3 and GABARAP puncta. Nevertheless, Schütter et al. rescue the phenotype observed in the absence of *FAA1* by expressing the human protein ACSL4 ²⁶, which belongs to the same family as SLC27A2. They also report ACSL4 partial co-localization with Atg8 structures in yeast ²⁶. ACSL4 also activates long chain fatty acids ¹⁹⁶. Interestingly, this protein localizes to ER-mitochondria contact sites ³¹³. As it has been described for SLC27A2, ACSL4 also recovers yeast double null mutants of *FAA1* and *FAA4* ¹⁹⁶. This could implicate a redundant role or a cell type specific role of these proteins in supplying fatty acids for the synthesis of phospholipids to contribute to the expansion of the phagophore.

Recently, ACSL3, which is also able of rescuing the phenotype of *FAA1* and *FAA4* double null mutants, has been found to interact and co-localize with GABARAPL2 ¹⁹⁷, a member of the Atg8-family. Nevertheless, autophagy seems to be unaffected by the absence of ACSL3 ¹⁹⁷. Interestingly, the authors observe that both GABARAPL2 and ACSL3 interact with UBA5,

the first enzyme of the ufmylation pathway¹⁹⁷. Ufmylation of ER substrates is crucial for reticulophagy³¹⁴. Further work is necessary to determine if ACSL3 contributes to reticulophagy.

Besides from the incorporation of phospholipids, autophagosomes require the presence of certain proteins on their membranes during and after their biogenesis. The phase of expansion of the phagophore involves the conjugation of Atg8-family proteins to PE in the autophagosome membrane and the incorporation of phospholipids which is mainly mediated by the presence of ATG2. Atg8-family proteins are lipidated by the cooperation of ATG7, ATG3 and the ATG12–ATG5–ATG16L1 complex³¹⁵. First, ATG7 binds to the Atg8 protein to be lipidated³¹⁵. Then the Atg8 protein is transferred to ATG3, which mediates the binding of PE headgroup to the C-terminal glycine of the Atg8 protein³¹⁵. ATG16L1 complex promotes this last step and determines the sites where conjugation has to occur¹⁸³. Under starvation conditions, we have reported that SLC27A2 interacts with ATG16L1, lipidated LC3B and lipidated GABARAP. We have also found a high co-distribution between SLC27A2 and LC3 or GABARAP positive puncta. These results indicate that SLC27A2 could contribute not only to PE synthesis, but to its conjugation with LC3B and GABARAP.

We have shown that the absence of SLC27A2 leads to decreased co-distribution of LC3 puncta with MFN2. This result indicates that SLC27A2–MFN2 interaction is necessary to connect forming phagophores to autophagic machinery at ER-mitochondria contact sites. We do not know whether these puncta are complete or incomplete autophagosomes.

Phagophore expansion requires the incorporation of phospholipids to its membrane. Several sources of phospholipids, where synthesis could occur or not *de novo* have been proposed: COP-II vesicles, mitochondria at ER-mitochondria contact sites, and ER membranes connected to the autophagosome³¹⁶. ATG2 has been proposed as the mediator of phospholipid transfer to the autophagosome membrane from the endoplasmic reticulum¹⁹³. ATG2, whose ablation impairs autophagosome biogenesis³¹⁷, has the capacity of membrane tethering and phospholipid transfer between membranes^{185,187,193,194}. Moreover, ATG2 interacts with TOM40 in the MAM upon induction of autophagy³¹⁸. We have described that SLC27A2 interacts with ATG2A. It has not been reported whether the yeast protein Faa1 interacts with Atg2. Moreover, we have also observed that MFN2 interacts with ATG2A. We think that MFN2, SLC27A2 and ATG2A belong to the same complex. SLC27A2 together with other proteins could be mediating the synthesis of phospholipids to be transferred to the phagophore from the endoplasmic reticulum by ATG2A and this complex would be anchored to ER-mitochondria contact sites by MFN2 and TOM40. Further analysis of the interactions of these proteins under starvation conditions needs to be performed. These interactions could occur under basal conditions but the activity of this complex could be repressed under basal conditions by post-translational modifications. Moreover, steps upstream or downstream the participation of this complex in autophagy could be inactive under basal conditions. It is necessary to characterize the whole autophagic cascade during starvation.

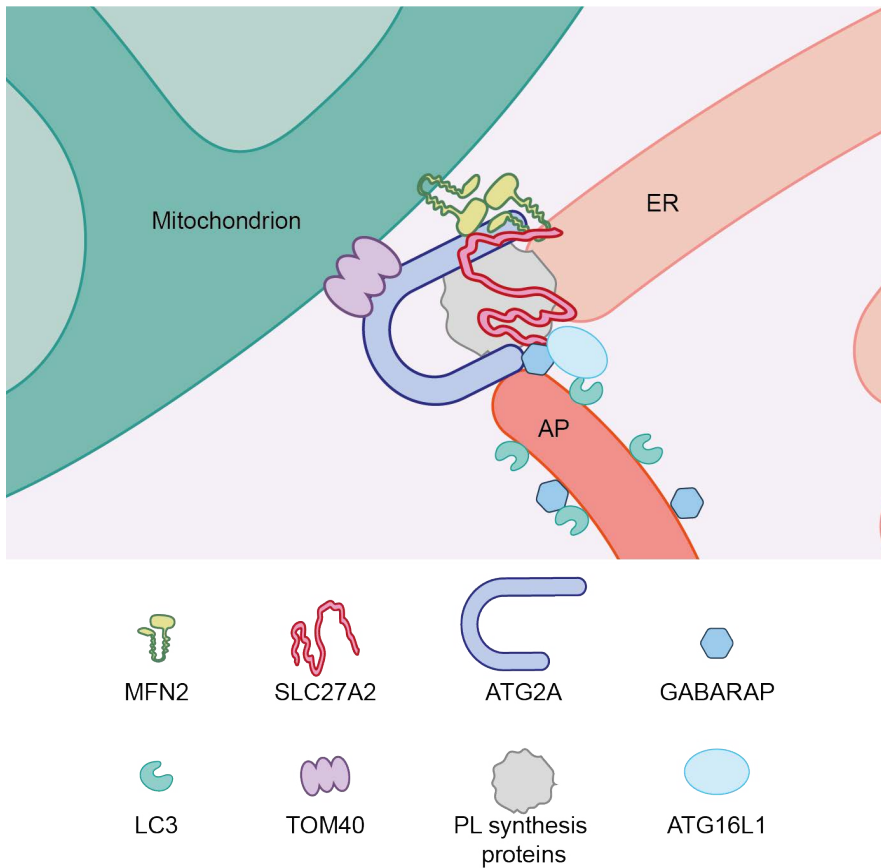


Figure 76. Proposed model for MFN2-SLC27A2 complex in autophagy.

In summary, we consider that MFN2 interaction with SLC27A2 and ATG2 occurs at ER-mitochondria contact sites and has the aim of fueling phagophore expansion with newly synthesized phospholipids. SLC27A2 is probably part of a bigger complex involving other enzymes that belong to the phospholipid synthesis pathway. Moreover, SLC27A2 interacts with ATG16L1, LC3B-II and GABARAP-II, thus we believe that it contributes to the conjugation of PE to LC3B and GABARAP. This model is represented in Figure 76.

Taking into account all the results obtained and discussed in this study we propose the following novel concepts regarding MFN1 and MFN2 functions (Figure 77):

1. Endosomal RAB5C interacts with MFN1 and MFN2 to maintain mitochondrial morphology and prevents mitochondrial degradation through MDVs.
2. Mitochondria interact with RNA granules through MFN1 and MFN2 that carry mitochondrial protein transcripts and this way they are transported to the sites of the mitochondrial network where they are required.
3. MFN2 interacts with SLC27A2 and ATG2A to promote the expansion of the phagophore through the incorporation of newly synthesized phospholipids.

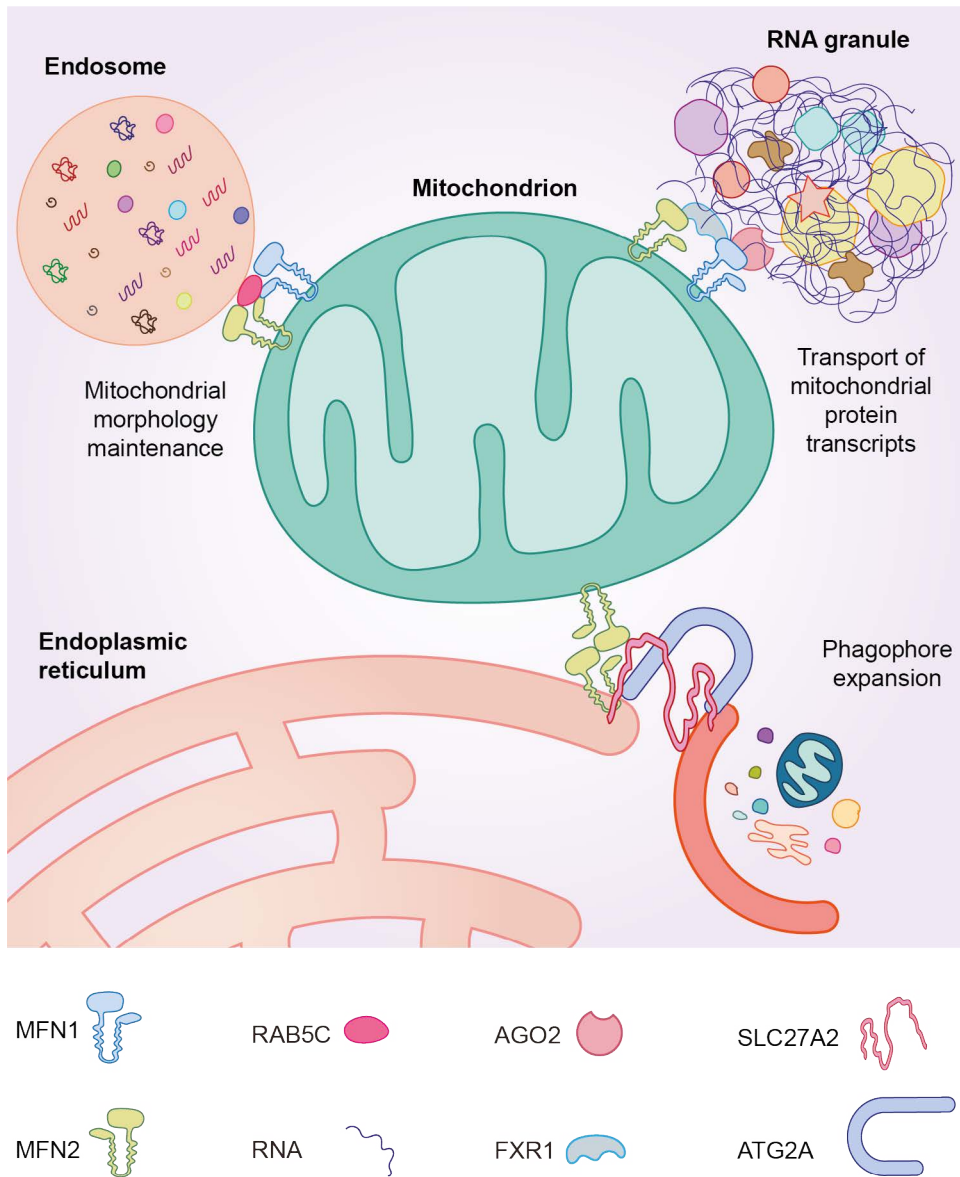


Figure 77. Proposed novel functions of MFN1 and MFN2.

CONCLUSIONS



6. CONCLUSIONS

The results obtained in this PhD thesis permit us to propose the following conclusions:

1. Endogenous expression of MFN1 and MFN2 with a C-terminal HA-tag does not alter mitochondrial morphology neither mitochondrial and autophagic responses to amino acid starvation.
2. MFN1 and MFN2 present different interaction networks depending on the feeding state of the cell. Endogenous IP revealed different binding partners of MFN1 and MFN2 upon starvation.
3. MFN1 and MFN2 interact with RNA-binding proteins in basal conditions. Mass spectrometry of MFN1 and MFN2 IP revealed that under basal conditions, MFN1 and MFN2 interact with RNA binding proteins. Endogenous MFN1 and MFN2 co-immunoprecipitate with AGO2 and FXR1.
4. RAB5C interacts with MFN1 and MFN2 and it is necessary to maintain mitochondrial morphology. RAB5C co-immunoprecipitates with MFN1 and MFN2 and its ablation results in increased mitochondrial fragmentation and degradation.
5. SLC27A2 interacts with MFN2 and it is essential for the correct functioning of autophagy. SLC27A2 co-immunoprecipitates with MFN2 and with proteins implicated in the expansion of the phagophore. The absence of SLC27A2 results in impaired autophagy.

MATERIALS AND METHODS



7. MATERIALS AND METHODS

All the reagents, plasmids, antibodies, siRNAs, PCR primers and ssODNs are listed in the following tables with the working concentrations used, applications and sources where they were obtained.

Table 5. Details of reagents.

Reagents	Working concentration	Application	Source
Ampicillin	100 mg/ml	Bacterial selection	Roche
Bafilomycin A1	200 nM	Autophagy completion inhibition	Santa Cruz Biotechnology
Hoesch 33342	1:10000	Nuclear staining	Thermo Fisher Scientific
Kanamycin	50mg/ml	Bacterial selection	Sigma Aldrich
Mitotracker Deep Red	100 nM	Mitochondrial staining	Thermo Fisher Scientific
Mitotracker Green	100 nM	Mitochondrial staining	Thermo Fisher Scientific
Puromycin	2 ug/ml	Cell line selection	Sigma-Aldrich

Table 6. Details of CRISPR/Cas9 and overexpression plasmids.

CRISPR/Cas9 vectors				
Bacterial				
Name	Reference	selection	Function	Source
pSpCas9(BB)-2A-GFP	Plasmid #48138	Ampicillin	gRNA and Cas9 delivery	Addgene
Rab 5C CRISPR/Cas9 KO Plasmid	sc-403247	-	gRNA and Cas9 delivery	Santa Cruz Biotechnology
Rab 5C HDR Plasmid	sc-403247-HDR	-	Homologous recombination	Santa Cruz Biotechnology
Overexpression vectors				
Name	Backbone	Reference	Bacterial selection	Source
AGO2-GFP	pCMV3	HG11079-ANG	Kanamycin	SinoBiological
G3BP1-GFP	pCMV3	HG16688-ANG	Kanamycin	SinoBiological
NDFIP2-FLAG	pDEST	-	Kanamycin	Gift from Stracker lab
RAB5C-FLAG	pCMV3	HG15817-NF	Kanamycin	SinoBiological
S100A8-FLAG	pCMV3	HG11138-NF	Kanamycin	SinoBiological
S100A9-FLAG	pCMV3	HG11145-NF	Kanamycin	SinoBiological
SLC27A2-FLAG	pCMV3	HG13155-NF	Kanamycin	SinoBiological

Table 7. List of primary antibodies used in this thesis.

Target	Host	Dilution	Reference	Source
α -TUBULIN	Mouse	WB: 1:20000	T5168	Sigma-Aldrich
AGO2	Rabbit	WB: 1:500	2897T	Cell Signaling
ATG14	Rabbit	WB: 1:1000	ab139727	Abcam
ATG16L1	Rabbit	WB: 1:1000	M150-3	MBL International Corporation
ATG2A	Rabbit	WB: 1:1000	NBP2-61690	Novus Biologicals
β -ACTIN	Mouse	WB: 1:20000	A1978	Sigma-Aldrich
BECN1	Rabbit	WB: 1:1000	3738S	Cell Signaling
dsDNA	Mouse	IF: 1:400	ab27156	Abcam
EEA1	Rabbit	IF: 1:200	3288S	Cell Signaling
FLAG	Mouse	IF: 1:100	F1804-200UG	Sigma-Aldrich
FLAG	Rabbit	WB: 1:1000 IF: 1:100	14793S	Cell Signaling
FXR1	Rabbit	WB: 1:500	12295T	Cell Signaling
GABARAP	Rabbit	WB: 1:1000 IF: 1:200	13733S	Cell Signaling
GAPDH	Mouse	WB: 1:20000	AM4300	Thermo Fischer
HA	Rabbit	WB: 1:1000	3724S	Cell Signaling
LC3B	Rabbit	WB: 1:1000	2775S	Cell Signaling
LC3B	Rabbit	WB: 1:1000 IF: 1:200	PM036	MBL International Corporation
LC3B	Mouse	WB: 1:1000 IF: 1:200	M186-3	MBL International Corporation
MFN1	Rabbit	WB: 1:1000	14739S	Cell Signaling

Table 8. List of secondary antibodies used in several assays of this thesis.

Target	Technique	Conjugate	Dilution	Reference	Source
Guinea pig	NIR-WB	DyLight 800	1:5000	SA5-10100	Thermo Fischer
Mouse	IF	Alexa Fluor 488	1:400-1:800	A-11001	Thermo Fischer
Mouse	IF	Alexa Fluor 647	1:400-1:802	A-21244	Thermo Fischer
Mouse	NIR-WB	DyLight 680	1:20000	35518	Thermo Fischer
Mouse	NIR-WB	DyLight 800 4X PEG	1:2000-1:10000	SA5-35521	Thermo Fischer
Mouse	ECL-WB	HRP	1:2000-1:40000	715-035-150	Jackson Immuno Research
Mouse	IF	Pacific Blue	1:400-1:804	P31582	Thermo Fischer
Rabbit	IF	Alexa Fluor 488	1:400-1:801	A-11008	Thermo Fischer
Rabbit	IF	Alexa Fluor 647	1:400-1:803	A-21235	Thermo Fischer
Rabbit	NIR-WB	DyLight 800 4X PEG	1:20000	SA5-35571	Thermo Fischer
Rabbit	ECL-WB	HRP	1:2000-1:40000	711-035-152	Jackson Immuno Research

Table 9. Commercially available siRNAs used in this thesis.

Target gene	Organism	Reference	Source
<i>MFN2</i>	Human	SASI_Hs02_00330014	Merck
<i>SLC27A2</i>	Human	SASI_Hs02_00336005	Merck

Table 10. Primers used in real time quantitative PCR to determine the

expression of human genes.

Gene	FW primer sequence	RV primer sequence
<i>MFN1</i>	TGGCTGTCTTGTACGTGTGT	AAGCCGCTCATTACCTTGT
<i>MFN2</i>	ACATAAACTGGCGCAATGTC	AACCTTTGACGTCCAGAACCT
<i>PINK1</i>	TCTTGAACACAATGAGCCAGGA	TAGTTGCTGGGACCTCTCTTG
<i>PARK2</i>	GTGTTTGTCAAGTTCAACTCCA	GAAAATCACACGCAACTGGTC

Table 11. Details of primers used in CRISPR/Cas9 strategy.

Gene	Sense	Sequence	Purpose
<i>MFN1</i>	FW	CACCGCCAAAGCAATCTCTATTGTT	gRNA insertion in Cas9 vector
	RV	AAACAACAATAGAGATTGCTGGC	
<i>MFN2</i>	FW	CACCGCTCAGGTGCCACTATCTGC	gRNA insertion in Cas9 vector
	RV	AAACGCAGATAGTGGGCACCTGAGC	
<i>HA</i>	RV	AGCGTAATCTGGAACATCGTATGGGTA	HA-integration validation by PCR
<i>MFN1</i>	FW	GTGGTGAAACTGTGCAGTAGA	HA-integration validation by PCR
	RV	CCAGGAAGCAGAGTTTTTCAG	
<i>MFN2</i>	FW	GGGTGTGTGTC AAGCCTCCTT	HA-integration validation by PCR
	RV	GAGCCACATGGCACTTAGGG	

Table 12. Sequences of ssODNs used in CRISPR/Cas9 strategy.

Gene	Sequence
<i>MFN1</i>	AATTTTACTAAGCAGTTTCTACCTTCAAGCAATGAAGAATCCTACCCATACGATG TTCCAGATTACGCTTAACAATAGAGATTGCTTTGGTGACCATGATAGGAGGAAAC
<i>MFN2</i>	AGCTCAACATGTTACACACCAGTACCTGCAGCCAGCAGATACCCATACGATGTT CCAGATTACGCTTAGTGGGCACCTGAGGCGGAGTCTGCGTGAGAGGGGCGGTG

7.1. Cell culture procedures

7.1.1. Cell Maintenance

The present work used HeLa cells as a cellular model. Cells were obtained from ATCC CCL-2™. Cells were grown in DMEM (Invitrogen) with 20mM HEPES (Sigma-Aldrich), 10% FBS and 100 U/ml of penicillin/

streptomycin (Life Technologies) at 37 °C in a humidified atmosphere of 5% CO₂ / 95% O₂. Once every two weeks mycoplasma detection test was performed to ensure no contamination of the cells. When mycoplasma was detected the cells were discarded. Maintenance of the different cell lines generated required regular split of the proliferating cells. Cells were split when they reached 100% confluence: medium was aspirated from the 10 cm dishes and 10 ml PBS were added to wash the remaining media from the cells. Then, 1 ml of trypsin was added and incubated for 1 min at RT. For cell recovery, 9 ml PBS were added to the dish and the 10 ml of 10 ml of cells in suspension recovered were transferred to a 15 or 50 ml tube for centrifugation. Cells were pelleted after spinning for 5 minutes at 1000 x g. The cell pellet was diluted according to the subsequent utilization of the cells, usually 1:10 to 1:30. In the case that a specific number of cells needed to be plated, cells were counted using Neubauer chamber. Trypan Blue (Gibco) was used in a 1:1 dilution of the cell suspension to ensure the counting of only alive unstained cells.

7.1.2. Freeze and Thaw cell aliquots

Cellular stocks were kept at -80°C. Cell Freezing was performed by centrifugation of trypsinized cell suspension at 1000 x g for 5 min and resuspension in 10% DMSO in FBS. This cellular suspension was distributed in cryovials of 2 ml at a concentration of 1-2 x 10⁶ cells in 1 ml. Cryovials were placed in a box at a -80°C freezer.

To thaw cell aliquots, cryovials are rapidly transferred from -80 °C to 37 °C water-bath to ensure rapid thawing. The thawed cell suspension was

mixed with 10 ml complete DMEM before centrifugation. To remove DMSO from the cells, the suspension was spun at 1000 x g for 5 min and resuspended in complete media for plating.

7.1.3. Cell treatments for autophagy assessment

HeLa cells were treated with EBSS medium (Gibco) in order to induce autophagy for different time durations. In order to block degradation of autophagosomes, Baf A1 was used at a concentration of 200 nM.

7.1.4. CRISPR/Cas9 HA-tagged cell line generation

7.1.4.1. gRNA design and cloning

A fragment containing the stop codon flanked by 50 nt upstream and 50 nt downstream was selected in ensembl.org from each gene to be edited. This sequence was loaded in the online tool of the Zhang lab (<http://crispr.mit.edu/>) to search for gRNAs and their specificity. The gRNA with the highest specificity score and nearest to the stop codon was selected. In order to clone the gRNAs in the pSpCas9 backbone vector (a pX330 based vector), the piece of DNA containing the gRNA must be double stranded and with cohesive ends compatible with the plasmid. This is achieved by annealing two primers. When designing the primers, the gRNA sequence picked from the Zhang lab tool, without the PAM sequence, was considered as the 5'-3' strand with the following modifications to fit in the vector:

5' CACCGNNNNNNNNNNNNNNNNNNNNNNNNNNNNNN 3' (oligo 1)

7 | Materials and Methods

A primer complementary to the previous one was designed also with some modifications:

3' CNNNNNNNNNNNNNNNNNNNNNNNCAAA 5' (oligo 2)

Primers were phosphorylated and annealed. From oligo 1 and oligo 2, 1 μ l at 100 μ M were mixed together and 1 μ l 10X T4 Ligation Buffer (NEB), 0.5 μ l T4 phosphonucleotide kinase (NEB) and 6.5 μ l of distilled water were added to the mix. A thermocycler was set to phosphorylate (37°C 30 min) and anneal the primers (95°C 5 min and slow cooldown to room temperature (RT)). The annealed sequences were diluted 1:250.

Next, a simultaneous digestion-ligation was performed. Reaction mix contained 100 ng of pSpCas9(BB)-2A-GFP (PX458) vector, 2 μ l phosphorylated and annealed oligo duplex 1:250 dilution from the previous step, 2 μ l 10X Tango buffer (or FastDigest Buffer), 2 μ l DTT (10 mM to a final concentration of 1 mM), 2 μ l ATP (10 mM to a final concentration of 1 mM), 1 μ l FastDigest BbsI (NEB), 0.5 μ l T7 DNA ligase, and distilled water up to 20 μ l. The reaction was incubated in a thermocycler during 6 cycles of 37°C 5 min, and 23°C 5 min.

A volume of 30 μ l of Top 10 competent *Escherichia coli* was mixed with 1 μ l of each digestion-ligation product in a 1.5 ml tube. The tubes were incubated on ice for 10 minutes. Next, each tube was transferred to a thermocycler at 42°C for 1 minute and then put back to the ice for 2 minutes. A volume of 700 μ l of LB medium was added to the tubes and then incubated at 37°C in a shaker for at least 30 min. Bacteria were pelleted by spinning the tubes at the maximum speed for 30 sec.

Supernatant was removed by inverting the tubes. A volume of 50 μl of bacteria and remaining medium was seeded into an LB agar Ampicillin plate per sample and incubated at 37°C o/n.

Grown colonies were amplified using Macherey-Nagel NucleoSpin Plasmid, Mini kit for plasmid DNA. One μg of each of the isolated plasmids was digested with 0.5 μl BbsI and 0.5 μl EcoRI in 1 μl 10X CutSmart Buffer and distilled water was added to a final volume of 10 μl . Samples were ran on an agarose gel. In the case of a correct integration of the gRNA primers in the vector, the expected digestion products were a fragment of 8500 bp and another fragment of 800 bp. Lack of integration would yield 3 digestion products: one of about 5000bp, another of 3500 bp and one of 800 bp.

7.1.4.2. CIRSPR/Cas9 HeLa cell clone generation

In a 10 cm dish, 2.2×10^6 HeLa cells were seeded. One day after seeding, HeLa cells were transfected with the gRNA-pSpCas9-GFP vector and the corresponding ssODN (ordered from Sigma Aldrich). In a 2ml tube, 6 μg of plasmid, 2 μg of ssODN, 1560 μl of 150 mM NaCl, and 96 μl of PEI were mixed. The tube was inverted 10 times and incubated for 15 minutes at room temperature. In the meantime, fresh medium was added to the cells. The transfection mix was added to the cells and incubated for 6 hours. After incubation, the medium was changed.

In order to check non-selectively whether cells had integrated the HA-tag, genomic DNA was isolated from these cells 48 hours after transfection by using Blood & Cell Culture DNA Mini Kit from QIAGEN (ID: 13323).

Two PCR reactions were performed: one to amplify a region of about 300bp around the site of integration, and a second one to selectively amplify the PCR products that contain the HA-tag sequence.

For selective growth of clones to identify HA-positive ones, 48 hours after transfection cells were trypsinized and sorted according to their GFP expression. GFP positive cells were isolated from the rest by FACS and grown individually in a 96wp. Each clone was expanded until there were more than 4×10^6 cells. From each clone, 2×10^6 cells were analyzed by westernblot using an antibody against HA to detect which clones expressed HA. Positive clones were sequenced for validation of the correct integration of HA.

7.1.5. CRISPR/Cas9 Knockout cell line generation

The necessary vectors for CRISPR/Cas9 KO of *RAB5C* in HeLa cells were acquired in Santa Cruz. In a 6 well plate, 0.3×10^6 HeLa cells were seeded per well. One day later, cells were transfected with *RAB5C* specific CRISPR/Cas9 gRNA plasmid and *RAB5C* specific HDR plasmid containing mCherry and a puromycin cassette. Per well, in one tube 1 μ g of *RAB5C* specific CRISPR/Cas9 gRNA plasmid and 1 μ g of *RAB5C* specific HDR plasmid, and 150 μ l of Opti-MEM (Gibco) were mixed. In a different tube, 3 μ l of PEI max 40K and 150 μ l of Opti-MEM were added. Each mixture was incubated separately at RT for 5 minutes. The content of both tubes was mixed and incubated at RT for 20 minutes. In the meantime, cell medium was replaced with fresh one. Transfection mix was added to the cells. Medium was changed 24 hours later. Puromycin selection was

carried out 36 hours after transfection using a concentration of 2 $\mu\text{g}/\text{ml}$ in the culture medium during 7 days. Cells that had survived puromycin selection and that presented more mCherry fluorescence were selected by using FACS and grown together to establish a polyclonal cell line. KO validation was performed by western blot analysis using an antibody against RAB5C.

7.1.6. Protein overexpression

For immunoprecipitation or microscopy assays, some proteins needed to be overexpressed. To achieve protein overexpression, cells were transfected with a plasmid containing the protein of interest. pCMV3-SP-N-FLAG or pCMV3-SP-C-FLAG plasmids containing the coding sequences from the proteins of interest were acquired from SinoBiological. Per 10 cm dish, 5 μg of plasmid DNA were incubated together with 750 μl of Opti-MEM in one 2ml tube for 5 min at RT. In a different tube, 15 μl PEI max 40K were mixed with 750 μl of Opti-MEM and were also incubated for 5 min at RT. Both solutions were mixed and incubated for 30 min RT. The final solution was added to a 10 cm dish and incubated during 24 hours. Medium was removed and fresh medium was added. Experiments were performed at least 24 hours after changing the medium.

7.1.7. Transient gene silencing

Genes were transiently silenced by transfecting the cells with siRNAs. Commercially available validated siRNAs were ordered from Sigma Aldrich. In a 6 well plate, 0.3×10^6 HeLa cells were seeded per well. One day later, cells were transfected with the appropriated siRNAs. Stocks

of siRNAs were prepared at 1 μM by adding 100 μl RNase free water to the siRNA commercial tube and diluting 10 μl of the previous solution in 1000 μl RNase free water. Per well, 125 μl OptiMEM were incubated with 2.5 μl lipofectamine 2000 (Thermo Fisher Scientific) in a 1.5 ml tube for 5 min at RT. In a different tube 125 μl OptiMEM were incubated with 60 μl siRNA (final concentration in 2ml of medium was 30nM) for 5 min at RT. Both solutions were mixed and incubated for 20 min at RT. The mixture was added to the cells and incubated for 48 or 72 hours.

7.2. Molecular biology techniques

7.2.1. Total protein extraction

RIPA buffer was prepared as explained in Table 13.

Table 13. RIPA buffer composition.

RIPA buffer
50 mM Tris pH 8.0
150 mM NaCl
0.1% w/v SDS
1% v/v NP-40
0.5% w/v Na-DOC
1mM EDTA

For total protein extraction, cells were cultured in 6 well plates of 9.6 cm^2 each well. When a confluency of 100% was reached, cells were scraped from the plate in growth medium and all the content of each well was transferred to a 2ml tube. Cellular suspensions were centrifuged for 5 minutes at 1000 x g at RT. Pellets were resuspended in PBS and

centrifuged with the same parameters as before. The obtained cellular pellets were resuspended in 100 μ l RIPA buffer (50 mM Tris pH 8.0, 150 mM NaCl, 0.1% w/v SDS, 1% v/v NP-40, 0.5% w/v Na-DOC, 1mM EDTA) and incubated for 30 min on ice. Samples were centrifuged for 20 min at 21000 x g at 4°C. Supernatants (90 μ l) were transferred to clean tubes and protein concentration was measured using Pierce™ BCA Protein Assay Kit (Thermo Fisher Scientific). A standard curve was generated by mixing in a 96 well plate different quantities (normally 0 mg, 2 mg, 4 mg, 6 mg and 8 mg) of BSA with 200 μ l of reaction mixture. Two μ l of each cellular lysate were mixed in the 96 well plate with 200 μ l of reaction mixture. The plate was incubated for 20 minutes at 37°C and absorbance was measured at 562 nm. After obtaining the standard curve, protein concentration was calculated by interpolation. Protein extract samples were prepared at the same concentration by adding the proper amounts of PBS if necessary. Then, 4X Laemmli (8% w/v SDS, 40% glycerol, 120 mM Tris-HCl pH 6.8, 8% β -mercaptoethanol) sample buffer was added in a proportion of 1:4 to make the samples suitable for western blot loading. Next, samples were boiled at 95°C for 5 min. Tubes were kept at -20°C until western blot was performed.

7.2.2. Western blot

Proteins were resolved by size by electrophoresis in an SDS-PAGE gel. The resolving gel had different concentrations of acrylamide depending on the size of proteins to be resolved (usually 7,5 %, 10 % 12,5 % or 15 %). Samples were run next to a molecular weight marker Spectra™ Multicolor Broad Range Protein Ladder (Thermo Fisher Scientific) for

chemiluminescence detection or Chameleon® Duo Pre-stained Protein Ladder (Li-COR) for near infra-red (NIR) fluorescence protein detection. Voltage was maintained at 90V until samples entered resolving gel, then voltage was increased to 100V - 150V until the desired resolution was achieved. Next, proteins were transferred to Immobilon-P PVDF membranes (Millipore) for chemiluminescence detection or Immobilon-FL PVDF membranes (Millipore) for NIR fluorescence detection. Transference was performed at 250 mA for 2 hours on ice or by o/n transference at 97mA at RT. Membranes were blocked in 5 % milk in PBS-Tween20 (PBST: 0,1 % Tween in PBS buffer) for 1 h at RT. Membranes were incubated in primary antibody diluted in PBST o/n at 4 °C. Membranes were washed three times for 5-15 min and then incubated in rotation for 1h at RT with the corresponding dilution in 5% milk PBST of horseradish peroxidase (HRP)-conjugated secondary antibodies or Fluorescent dye-conjugated secondary antibodies. Fluorescent dye-conjugated secondary antibodies were incubated in the dark. Then, membranes were washed three times with PBST for 5-15 min. Prior to chemiluminescence detection, membranes were exposed to Pierce™ ECL Western Blotting Substrate (Thermo Fisher Scientific) mixture for 1 min, and immediately after, placed into Li-COR Odyssey FC chemiluminescence detector. Images were obtained after 2, 5 or 10 minutes of exposure. For NIR fluorescence acquisition, membranes were washed once more in PBS without detergent for 5 minutes and placed in the LI-COR Odyssey® Infrared Imaging System. Signals were acquired at the appropriate wavelength (680 nm or 800 nm). Signal quantification was performed by using Image Studio™ Lite Software (Li-COR).

7.2.3. Immunoprecipitation

5.2.3.1. Endogenous denaturing HA-IP in RIPA buffer to validate HA-tagging of MFN1 and MFN

From each cell line or condition to be analyzed, cells were recovered from one 150 mm plate. For recovery, medium was discarded and the plate was rinsed in 10 ml PBS. One ml of ice cold PBS was added to the plate and cells were scraped and transferred to a 2 ml tube. Tubes were centrifuged at 1000 x g for 5 minutes at 4°C. Pelleted cells were resuspended in 1 ml of RIPA buffer and incubated 20 min on ice. Samples were centrifuged at maximum speed for 15 min at 4°C. During this step, beads were prepared for the binding step. Per lysate, 15 µl of HA-coupled dynabeads (Pierce™ Thermo Fisher Scientific) were washed three times in ice cold lysis buffer, separating the supernatant from the beads in a magnetic rack. Beads were incorporated into 1.5 ml tubes. Protein concentration of lysate supernatants was measured. Equal amounts of protein from each sample to be compared were added to the beads. A fraction of these lysates was kept as an input control. Samples were incubated at 4°C o/n in rotation. Next, a magnetic rack was used to separate the beads from the supernatant. A fraction of the supernatant was kept as an unbound control and the rest of the supernatant was discarded. Beads were washed 3 times in 1 ml ice cold RIPA buffer. Beads were eluted in 2X Laemmli buffer in a volume equal to the volume of beads and boiled for 5 min at 95°C.

5.2.3.2. Endogenous HA-IP coupled to mass spectrometry to identify MFN1 and MFN2 interactors

Lysis and wash buffers were prepared one day in advance as explained in Table 14. Protease inhibitors (Roche Complete EDTA Free diluted 1:50) and phosphatase inhibitors (Merck Cocktail set IV diluted 1:50) were added freshly to both buffers the same day when HA-IP was performed.

Table 14. Lysis and wash buffers used in endogenous HA-IP.

Lysis buffer	Wash buffer
50 mM Tris pH 7.4	50 mM Tris pH 7.4
150 mM NaCl	150 mM NaCl
5 mM EDTA	5 mM EDTA
1% Digitonin	0.1% Digitonin

Endogenous HA-IP was performed as follows:

1. From each cell line or condition to be analyzed, cells were recovered from 8 15 cm plates. For recovery, medium was discarded and each plate was rinsed in 10 ml PBS. One ml of ice cold PBS was added to each plate and cells were scraped and transferred to a 50 ml tube.
2. Tubes were centrifuged at 1000 x g for 5 minutes at 4°C.
3. Pelleted cells were resuspended in 2 ml of lysis buffer.
4. Cells were disrupted manually in a Dounce homogenizer after 20 strokes.
5. Lysates were transferred to 2 ml tubes and incubated on ice for at least 15 min.

6. Samples were centrifuged at maximum speed for 15 min at 4°C.
7. During step 6, beads were prepared for the binding step. Per lysate, 40 µl of HA-coupled dynabeads were washed three times in ice cold lysis buffer, separating the supernatant from the beads in a magnetic rack. Beads were incorporated into protein LoBind tubes (Eppendorf).
8. Protein concentration of lysate supernatants was measured.
9. Around twenty two mg of sample were used per 40 µl of dynabeads.
10. A fraction of these samples (100 µl) was kept as an input control.
11. Samples were incubated at 4°C in rotation.
12. Next, a magnetic rack was used to separate the beads from the supernatant.
13. A fraction of the supernatant was kept as an unbound control and the rest of the supernatant was discarded.
14. Beads were washed 5 times in 1 ml ice cold wash buffer. The last three washes were incubated in rotation for 5 minutes.
15. Beads were eluted in 2X Laemmli buffer in a volume equal to the volume of beads and boiled for 5 min at 95°C.
16. Next, samples were run on an 0.75 mm SDS-PAGE gel until they passed the stacking gel.
17. The gel was stained with InstantBlue® Coomassie Protein Stain (Abcam) and bands were cut.

Gel bands were reduced with DTT 10mM for 45min at 56°C and alkylated for 30 min in the dark with IAA 50 mM. Then, in-gel digestion was performed with trypsin (0.1 µg/µL) in 50mM NH₄HCO₃ at 37°C

overnight. The digestion was stopped by adding formic acid. Peptides were extracted with 100 % acetonitrile and completely evaporated. Samples were reconstituted in 20 μ L of 3% Acetonitrile (ACN) and 1% formic acid aqueous solution for MS analysis.

LC-MS coupling was performed with the Advion Triversa Nanomate (Advion BioSciences, Ithaca, NY, USA) as the nanoESI source performing nanoelectrospray through chip technology. The Nanomate was attached to an Orbitrap Fusion Lumos™ Tribrid mass spectrometer and operated at a spray voltage of 1.6 kV and a delivery pressure of 0.5 psi in positive mode.

The nano-LC-MS/MS set up was as follows. Digested peptides were diluted in 1% FA, 3% ACN. Samples were loaded to a 300 μ m \times 5 mm, C18 PepMap100 (Thermo Scientific) at a flow rate of 15 μ L/min using a Thermo Scientific Dionex Ultimate 3000 chromatographic system (Thermo Scientific). Peptides were separated using a C18 analytical column (NanoEase MZ HSS T3 column, 75 μ m \times 250 mm, 1.8 μ m, 100Å, Waters) with a 90 min run, comprising three consecutive steps with linear gradients from 3 to 35% B in 60 min, from 35 to 50% B in 5 min, and from 50 % to 85 % B in 2 min, followed by isocratic elution at 85 % B in 5 min and stabilization to initial conditions (A= 0.1% FA in water, B= 0.1% FA in CH₃CN). The column outlet was directly connected to an Advion TriVersa NanoMate (Advion) fitted on an Orbitrap Fusion Lumos™ Tribrid (Thermo Scientific). The mass spectrometer was operated in a data-dependent acquisition (DDA) mode. Survey MS scans were acquired in the orbitrap with the resolution (defined at 200

m/z) set to 120,000. The lock mass was user-defined at 445.12 m/z in each Orbitrap scan. The top speed (most intense) ions per scan were fragmented by CID and detected in the Ion Trap. The ion count target value was 400,000 for the survey scan and 50,000 for the MS/MS scan. Target ions already selected for MS/MS were dynamically excluded for 15 s. Spray voltage in the NanoMate source was set to 1.60 kV. RF Lens were tuned to 30%. Minimal signal required to trigger MS to MS/MS switch was set to 5000 and activation Q was 0.250. The spectrometer was working in positive polarity mode and singly charge state precursors were rejected for fragmentation.

A database search was performed with Proteome Discoverer software v2.3 (Thermo) using Sequest HT search engine, SwissProt Human release 2019_01 and Contaminants database. Search was run against targeted and decoy database to determine the false discovery rate (FDR). Search parameters included Trypsin (and Chymotrypsin) enzyme, allowing for two missed cleavage sites, carbamidomethyl in cysteine as static modification; methionine oxidation and acetylation in N-terminal as dynamic modifications. Peptide mass tolerance was 10 ppm and the MS/MS tolerance was 0.6 Da. Peptides with a FDR < 1% were considered as positive identifications with a high confidence level.

For the quantitative analysis, contaminant identifications were removed and unique peptide spectrum matches of protein groups identified with Sequest HT and Andromeda were analyzed with SAINTexpress-spc v3.11 [Teo, G. et al. J Proteomics, 2013]. SAINTexpress compares the prey control spectral counts with the prey test spectral counts for all available

replicates. For each available bait and for each available replicate, the maximum count result between PD and MQ was taken as prey count. Once obtained this combined dataset, SAINTexpress algorithm was ran twice, first with basal condition samples and second with starvation samples (refer as S). High confidence interactors were defined as those with Bayesian false discovery rate BFDR \leq 0.05.

5.2.3.3. FLAG-IP of overexpressed proteins

FLAG-IP lysis buffer and wash buffers were prepared in advanced as detailed in Table 15. Protease inhibitors (Roche Complete EDTA Free diluted 1:50) and phosphatase inhibitors (Merck Cocktail set IV diluted 1:50) were added freshly to both buffers the same day when FLAG-IP was performed.

Table 15. Lysis and wash buffers utilized in FLAG-IP.

Lysis buffer	Wash buffer
50 mM Tris pH 7.4	50 mM Tris pH 7.4
150 mM NaCl	150 mM NaCl
5 mM EDTA	5 mM EDTA
1% Digitonin or 1% Triton X-100	0.1% Digitonin or 1% Triton X-100

Around 2×10^7 HeLa cells in four 10 cm culture plates were transfected with a plasmid overexpressing the protein to be immunoprecipitated fused to a FLAG-tag. Two days after transfection, HeLa cells were recovered by scraping in PBS as explained before. Cell pellets were resuspended in 1 ml of lysis buffer and incubated on ice for at least 15 min. Samples were centrifuged at maximum speed for 15 min at 4°C.

During this step, beads were prepared for the binding step. Per lysate, 20 μ l of FLAG-coupled magnetic beads (Thermo Fisher Scientific) were washed three times in ice cold lysis buffer, separating the supernatant from the beads in a magnetic rack. Beads were incorporated into 1.5 ml tubes. Protein concentration of lysate supernatants was measured. From 2.5 mg to 5 mg of sample were used for immunoprecipitation. A fraction of these samples was kept as an input control. Samples were incubated at 4°C in rotation. Next, a magnetic rack was used to separate the beads from the supernatant. A fraction of the supernatant was kept as an unbound control, but the rest of the supernatant was discarded. Beads were washed 3 times in 1 ml ice cold wash buffer. Beads were eluted in 2X Laemmli buffer in a volume equal to the volume of beads and boiled for 5 min at 95°C.

7.2.4. Cell visualization by confocal microscopy

5.2.4.1. Immunostaining of fixed cells

Around 1.5×10^5 cells were plated on 12mm diameter coverslips in 6 well plates, expecting a confluence of ~50% two days later. If necessary, mitotracker deep red (Thermo Fisher Scientific) staining of mitochondria was performed in live cells by incubation during 30 min with the probe at 100 nM in complete medium, then cells were washed for 10min in complete medium before fixation. Paraformaldehyde (PFA) at a concentration of 4% in PBS was used for cell fixation. Cells were incubated in ice cold PFA for 20 min and then transferred to a 12 well plate for one wash with 50 mM NH_4Cl . If mtDNA needed to be stained,

cells were permeabilized in a buffer containing 0.1 % Triton X-100, and 3 % FBS in PBS for 30 min. If not, this step is skipped. Coverslips were incubated in blocking buffer (0.05 % Saponin, 2 % FBS in PBS) for at least 10 minutes. Primary antibodies were diluted in blocking buffer as specified. Coverslips were incubated in 80 μ l drops of antibody dilution upside down on a piece of parafilm for 1h at RT. Coverslips were return to the 12 well plate and washed three times for 10 min with blocking buffer. Fluorescent secondary antibodies were diluted in blocking buffer as specified. Coverslips were incubated upside down in 80 μ l drops of antibody dilution on a parafilm piece at RT in the dark for at least 30 min. Next, samples were returned to the 12 well plate and three washes of 10 min with blocking buffer were performed. If nuclei staining was performed, the coverslips were incubated in a 1:10000 dilution of Hoechst 33342 in PBS for 10 min followed by two washes of 10 min in PBS. Samples were rinsed in distilled water for 5 seconds and mounted onto microscope slides using 4 μ l of Flouromount (Sigma). Slides were dried o/n at RT in a dark chamber and then kept at 4°C in a dark chamber until imaging was performed.

5.2.4.2. Cell preparation for live imaging

Around 1.5×10^5 cells were grown in 25 mm coverslips inside 6 well plates or in 4 chamber 35mm glass bottom dishes. If necessary, cells were transfected with plasmids containing GFP-tagged proteins 48 hours before imaging. For visualization of mitochondria, either mitotracker deep red or mitotracker green were used. Cells were incubated with these probes at a concentration of 100 nM in DMSO for 30 minutes and

then incubated in normal medium until imaging was performed.

5.2.4.3. Image acquisition

Confocal images were obtained using Super Resolution Elyra PS1 + AiryScan Zeiss microscope with a PlanAchromat 63x oil objective lens with 1.40 NA, a pinhole diameter of 1 airy unit and a zoom between 1.0 and 2.0 units. Z-stacks were acquired with 0.25 μm steps. When live imaging was performed, the microscope imaging chamber was warmed up to 37°C and the flow of 5% CO₂ was activated. Image processing and quantification were performed using ImageJ software.

7.2.5. *Gene expression measurement by quantitative real time PCR*

5.2.5.1. RNA extraction

RNA was isolated from 1 x 10⁶ cells cultured in each well of a 6 well plate. RNeasy® minikit columns (Qiagen) were used for RNA extraction following the manufacturer's instructions. Briefly, cells were recovered from the wells by scraping in normal medium, centrifuged and washed in PBS. Clean cell pellets were resuspended in the lysis buffer provided in the kit after adding 1 % DTT. Samples were homogenized by passing through a 25G syringe 10 times and then spun at maximum speed for 10 min. The supernatants were mixed with equal volumes of 70 % ethanol in RNase-free water. The mixtures were transferred to RNase free spin cartridge with a collection tube and centrifuged at 12,000 x g for 30 s at RT. Flow-through was discarded and two washing steps with different buffers provided in the kit were performed. Spin cartridges were

spun at 12000 x g for drying the membrane and collection tubes were replaced by 1.5 ml tubes. A volume of 50 μ l of RNase-free water was added to each column membrane. Spin columns were incubated at RT for 1 minute. RNA was eluted by centrifugation at 12,000 x g for 2 min at RT. The concentration of RNA in the samples was quantified using the Nanodrop™ 2000/2000c spectrometer (Thermo Fisher Scientific) and the ND1000 software (Thermo Fisher Scientific). Isolated RNA was stored at -80 °C.

5.2.5.2. cDNA preparation

Reverse transcription was performed using qScript cDNA SuperMix™ (Quantabio) using a 2720™ Thermal Cycler (Applied Biosystems). Briefly, 6 μ g of RNA from each sample were added to PCR tubes, followed by 12 μ l of qScript reaction mix and RNase-free water to a final volume of 30 μ L. Reverse-Transcription Polymerase Chain Reaction (RT-PCR) was performed as follows: 5 min at 25°C, 30 min at 42°C and 5 min at 85°C. Generated cDNA was diluted to a working concentration of 10 ng/ μ l with distilled water and stored at -20 °C.

5.2.5.3. Quantitative real-time PCR

The reaction volume was set to 10 μ l per sample in a 384 well plate. Master Mix for SYBR Green analysis was prepared by mixing 5 μ l of SYBR Green PCR Master Mix (Applied Biosystems), with 0.25 μ l of 25 μ M primer solution (forward and reverse) per sample. Wells were loaded with 5 μ l of SYBR Green master mix and 5 μ l of 10 ng/ μ l cDNA sample were added to each well. Two or three technical replicates were analyzed

per sample. Quantitative real-time PCR was performed using the ABI Prism 7900 HT real-time PCR machine (Applied Biosystems) and the SYBR® Green PCR Master Mix (Applied Biosystems). All measurements were normalized to *GAPDH* or *TBP*.

7.3. Statistics

Statistical analyses were performed as explained in footnotes. Briefly, data were subjected to normality Saphiro-Wilk test. Data that passed normality test were compared using T-student test paired or unpaired. Data that did not pass normality test were compared using Wilcoxon test if values were paired or Mann-Whitney test if values were not paired. GraphPad Prism 8.0 software was used for these analyses.

REFERENCES



8. REFERENCES

1. Sebastián, D., Palacín, M. & Zorzano, A. Mitochondrial Dynamics: Coupling Mitochondrial Fitness with Healthy Aging. *Trends Mol. Med.* **23**, 201–215 (2017).
2. Ramachandran, R. & Schmid, S. L. The dynamin superfamily. *Curr. Biol.* **28**, R411–R416 (2018).
3. Smirnova, E., Griparic, L., Shurland, D. L., Blik, A. M. Van Der & Van der Blik, A. M. Dynamin-related Protein Drp1 Is Required for Mitochondrial Division in Mammalian Cells. *Mol. Biol. Cell* **12**, 2245–2256 (2001).
4. Chen, H., Chomyn, A. & Chan, D. C. Disruption of fusion results in mitochondrial heterogeneity and dysfunction. *J. Biol. Chem.* **280**, 26185–26192 (2005).
5. Santel, A. *et al.* Mitofusin-1 protein is a generally expressed mediator of mitochondrial fusion in mammalian cells. *J. Cell Sci.* **116**, 2763–2774 (2003).
6. Chen, H. *et al.* Mitofusins Mfn1 and Mfn2 coordinately regulate mitochondrial fusion and are essential for embryonic development. *J. Cell Biol.* **160**, 189–200 (2003).
7. Bach, D. *et al.* Mitofusin-2 determines mitochondrial network architecture and mitochondrial metabolism: A novel regulatory mechanism altered in obesity. *J. Biol. Chem.* **278**, 17190–17197 (2003).
8. Misaka, T., Miyashita, T. & Kubo, Y. Primary structure of a dynamin-related mouse mitochondrial GTPase and its distribution in brain, subcellular localization, and effect on mitochondrial morphology. *J. Biol. Chem.* **277**, 15834–15842 (2002).
9. Spinazzi, M. *et al.* A novel deletion in the GTPase domain of OPA1 causes defects in mitochondrial morphology and distribution, but not in function. *Hum. Mol. Genet.* **17**, 3291–3302 (2008).
10. Zanna, C. *et al.* OPA1 mutations associated with dominant optic atrophy impair oxidative phosphorylation and mitochondrial fusion. *Brain* **131**, 352–367 (2008).
11. Gordaliza-Alaguero, I., Cantó, C. & Zorzano, A. Metabolic implications of organelle–mitochondria communication. *EMBO Rep.* **20**, e47928 (2019).
12. Giacomello, M., Pyakurel, A., Glytsou, C. & Scorrano, L. The cell biology of mitochondrial membrane dynamics. *Nat. Rev. Mol. Cell Biol.* **21**, 204–224 (2020).
13. Schrepfer, E. & Scorrano, L. Mitofusins, from Mitochondria to Metabolism.

- Mol. Cell* **61**, 683–694 (2016).
14. Rambold, A. S., Kostecky, B., Elia, N. & Lippincott-Schwartz, J. Tubular network formation protects mitochondria from autophagosomal degradation during nutrient starvation. *Proc. Natl. Acad. Sci. U. S. A.* **108**, 10190–10195 (2011).
 15. Ding, Y., Gao, H., Zhao, L., Wang, X. & Zheng, M. Mitofusin 2-Deficiency Suppresses Cell Proliferation through Disturbance of Autophagy. *PLoS One* **10**, e0121328 (2015).
 16. Hamasaki, M. *et al.* Autophagosomes form at ER–mitochondria contact sites. *Nature* **495**, 389–393 (2013).
 17. Hailey, D. W. *et al.* Mitochondria Supply Membranes for Autophagosome Biogenesis during Starvation. *Cell* **141**, 656–667 (2010).
 18. Muñoz, J. P. *et al.* Mfn2 modulates the UPR and mitochondrial function via repression of PERK. *EMBO J.* **32**, 2348–2361 (2013).
 19. de Brito, O. M. & Scorrano, L. Mitofusin 2 tethers endoplasmic reticulum to mitochondria. *Nature* **456**, 605–610 (2008).
 20. Nakamura, N., Kimura, Y., Tokuda, M., Honda, S. & Hirose, S. MARCH-V is a novel mitofusin 2- and Drp1-binding protein able to change mitochondrial morphology. *EMBO Rep.* **7**, 1019–1022 (2006).
 21. Misko, A., Jiang, S., Wegorzewska, I., Milbrandt, J. & Baloh, R. H. Mitofusin 2 is necessary for transport of axonal mitochondria and interacts with the Miro/Milton complex. *J. Neurosci.* **30**, 4232–4240 (2010).
 22. Cristillo, A. D., Nie, L., Macri, M. J. & Bierer, B. E. Cloning and Characterization of N4WBP5A, an Inducible, Cyclosporine-sensitive, Nedd4-binding Protein in Human T Lymphocytes. *J. Biol. Chem.* **278**, 34587–34597 (2003).
 23. Mund, T. & Pelham, H. R. B. Control of the activity of WW-HECT domain E3 ubiquitin ligases by NDFIP proteins. *EMBO Rep.* **10**, 501–507 (2009).
 24. Ghavami, S. *et al.* S100A8/A9 induces autophagy and apoptosis via ROS-mediated cross-talk between mitochondria and lysosomes that involves BNIP3. *Cell Res.* **20**, 314–331 (2010).
 25. Yang, M. *et al.* S100A8 Contributes to drug resistance by promoting autophagy in leukemia cells. *PLoS One* **9**, (2014).
 26. Schütter, M., Giavalisco, P., Brodesser, S. & Graef, M. Local Fatty Acid Channeling into Phospholipid Synthesis Drives Phagophore Expansion during Autophagy. *Cell* **180**, 135–149 (2020).
 27. Jain, S. *et al.* ATPase-Modulated Stress Granules Contain a Diverse Proteome and Substructure. *Cell* **164**, 487–498 (2015).

28. Hubstenberger, A. *et al.* P-Body Purification Reveals the Condensation of Repressed mRNA Regulons. *Mol. Cell* **68**, 144–157.e5 (2017).
29. Wang, X. *et al.* MFN2 interacts with nuage-associated proteins and is essential for male germ cell development by controlling mRNA fate during spermatogenesis. *Dev.* **148**, 196295 (2021).
30. Pla-Martín, D. *et al.* CLUH granules coordinate translation of mitochondrial proteins with mTORC1 signaling and mitophagy. *EMBO J.* **39**, e102731 (2020).
31. Huang, L. *et al.* Mitochondria associate with P-bodies and modulate microRNA-mediated RNA interference. *J. Biol. Chem.* **286**, 24219–24220 (2011).
32. Parker, R. & Sheth, U. P Bodies and the Control of mRNA Translation and Degradation. *Mol. Cell* **25**, 635–646 (2007).
33. Mateju, D. *et al.* Single-Molecule Imaging Reveals Translation of mRNAs Localized to Stress Granules. *Cell* **183**, 1801–1812.e13 (2020).
34. Esser, C., Martin, W. & Dagan, T. The origin of mitochondria in light of a fluid prokaryotic chromosome model. *Biol. Lett.* **3**, 180–184 (2007).
35. Kölliker, A. von. Einige bemerkungen uber die endigung gen der hautnerven und den bau der muskeln. *Zwiss Zool* **8**, 311–325 (1857).
36. Kölliker, A. *Zur Kenntnis der quergestreiften Muskelfasern.* (Wilh. Engelmann, 1888).
37. Brenda, C. Ueber die Spermatogenese der Vertebraten und höherer Evertbraten. II. Theil: Die Histiogenese der Spermien. *Arch. Anal. Physiol.* 393–398 (1898).
38. Claude, A. Fractionation of mammalian liver cells by differential centrifugation: I. Problems, methods, and preparation of extract. *J. Exp. Med.* **84**, 51 (1946).
39. Kennedy, E. P. & Lehninger, A. L. Oxidation of fatty acids and tricarboxylic acid cycle intermediates by isolated rat liver mitochondria. *J. Biol. Chem.* **179**, 957–972 (1949).
40. Nass, M. M. K. & Nass, S. INTRAMITOCHONDRIAL FIBERS WITH DNA CHARACTERISTICS. I. Fixation and Electron Staining Reactions. *J. Cell Biol.* **19**, 593–611 (1963).
41. Sagan, L. On the origin of mitosing cells. *J. Theor. Biol.* **14**, 225–IN6 (1967).
42. Sprenger, H. G. & Langer, T. The Good and the Bad of Mitochondrial Breakups. *Trends Cell Biol.* **29**, 888–900 (2019).
43. Cerqua, C. *et al.* Trichoplein/mitostatin regulates endoplasmic reticulum-

- mitochondria juxtaposition. *EMBO Rep.* **11**, 854–860 (2010).
44. Wong, Y. C., Ysselstein, D. & Krainc, D. Mitochondria-lysosome contacts regulate mitochondrial fission via RAB7 GTP hydrolysis. *Nature* **554**, 382–386 (2018).
 45. Yu, R. *et al.* MIEF1/2 function as adaptors to recruit Drp1 to mitochondria and regulate the association of Drp1 with Mff. *Sci. Rep.* **7**, 1–16 (2017).
 46. Otera, H. *et al.* Mff is an essential factor for mitochondrial recruitment of Drp1 during mitochondrial fission in mammalian cells. *J. Cell Biol.* **191**, 1141–1158 (2010).
 47. Yoon, Y., Krueger, E. W., Oswald, B. J. & McNiven, M. A. The Mitochondrial Protein hFis1 Regulates Mitochondrial Fission in Mammalian Cells through an Interaction with the Dynamin-Like Protein DLP1. *Mol. Cell Biol.* **23**, 5409–5420 (2003).
 48. Friedman, J. R. *et al.* ER Tubules Mark Sites of Mitochondrial Division. *Science* **334**, 358–362 (2011).
 49. Korobova, F., Ramabhadran, V. & Higgs, H. N. An Actin-Dependent Step in Mitochondrial Fission Mediated by the ER-Associated Formin INF2. **339**, 464–468 (2013).
 50. Korobova, F., Gauvin, T. J. & Higgs, H. N. A Role for Myosin II in Mammalian Mitochondrial Fission. *Curr. Biol.* **24**, 409–414 (2014).
 51. Chakrabarti, R. *et al.* INF2-mediated actin polymerization at the ER stimulates mitochondrial calcium uptake, inner membrane constriction, and division. *J. Cell Biol.* **217**, 251–268 (2018).
 52. Lewis, S. C., Uchiyama, L. F. & Nunnari, J. ER-mitochondria contacts couple mtDNA synthesis with Mitochondrial division in human cells. *Science* **353**, (2016).
 53. Wu, W. *et al.* FUNDC1 regulates mitochondrial dynamics at the ER-mitochondrial contact site under hypoxic conditions. *EMBO J.* **35**, 1368–1384 (2016).
 54. Twig, G. *et al.* Fission and selective fusion govern mitochondrial segregation and elimination by autophagy. *EMBO J.* **27**, 433–446 (2008).
 55. Koshiba, T. *et al.* Structural Basis of Mitochondrial Tethering by Mitofusin Complexes. *Science* **305**, 858–862 (2004).
 56. Ishihara, N., Eura, Y. & Mihara, K. Mitofusin 1 and 2 play distinct roles in mitochondrial fusion reactions via GTPase activity. *J. Cell Sci.* **117**, 6535–6546 (2004).
 57. Ban, T. *et al.* Molecular basis of selective mitochondrial fusion by heterotypic action between OPA1 and cardiolipin. *Nat. Cell Biol.* **19**, 856–

- 863 (2017).
58. Yan, L. *et al.* Structural basis for GTP hydrolysis and conformational change of MFN1 in mediating membrane fusion. *Nat. Struct. Mol. Biol.* **25**, 233–243 (2018).
 59. Franco, A. *et al.* Correcting mitochondrial fusion by manipulating mitofusin conformations. *Nature* **540**, 74–79 (2016).
 60. Liu, J., Noel, J. K. & Low, H. H. Structural basis for membrane tethering by a bacterial dynamin-like pair. *Nat. Commun.* **9**, 1–12 (2018).
 61. Anand, R. *et al.* The i-AAA protease YME1L and OMA1 cleave OPA1 to balance mitochondrial fusion and fission. *J. Cell Biol.* **204**, 919–929 (2014).
 62. Low, H. H., Sachse, C., Amos, L. A. & Löwe, J. Structure of a Bacterial Dynamin-like Protein Lipid Tube Provides a Mechanism For Assembly and Membrane Curving. *Cell* **139**, 1342–1352 (2009).
 63. Low, H. H. & Löwe, J. A bacterial dynamin-like protein. *Nature* **444**, 766–769 (2006).
 64. Reubold, T. F. *et al.* Crystal structure of the dynamin tetramer. *Nature* **525**, 404–408 (2015).
 65. Cao, Y. L. *et al.* MFN1 structures reveal nucleotide-triggered dimerization critical for mitochondrial fusion. *Nature* **542**, 372–376 (2017).
 66. Li, Y. J. *et al.* Structural insights of human mitofusin-2 into mitochondrial fusion and CMT2A onset. *Nat. Commun.* **10**, 1–14 (2019).
 67. Burchell, V. S. *et al.* The Parkinson's disease-linked proteins Fbxo7 and Parkin interact to mediate mitophagy. *Nat. Neurosci.* **16**, 1257–1265 (2013).
 68. Ziviani, E., Tao, R. N. & Whitworth, A. J. Drosophila Parkin requires PINK1 for mitochondrial translocation and ubiquitinates Mitofusin. *Proc. Natl. Acad. Sci. U. S. A.* **107**, 5018–5023 (2010).
 69. Leboucher, G. P. *et al.* Stress-Induced Phosphorylation and Proteasomal Degradation of Mitofusin 2 Facilitates Mitochondrial Fragmentation and Apoptosis. *Mol. Cell* **47**, 547–557 (2012).
 70. Park, Y. Y. *et al.* Loss of MARCH5 mitochondrial E3 ubiquitin ligase induces cellular senescence through dynamin-related protein 1 and mitofusin 1. *J. Cell Sci.* **123**, 619–626 (2010).
 71. Nakamura, N., Kimura, Y., Tokuda, M., Honda, S. & Hirose, S. MARCH-V is a novel mitofusin 2- and Drp1-binding protein able to change mitochondrial morphology. *EMBO Rep.* **7**, 1019–1022 (2006).

72. Sugiura, A. *et al.* MITOL regulates endoplasmic reticulum-mitochondria contacts via Mitofusin2. *Mol. Cell* **51**, 20–34 (2013).
73. Ferreira, J. C. B. *et al.* A selective inhibitor of mitofusin 1- β IIPKC association improves heart failure outcome in rats. *Nat. Commun.* **10**, 1–14 (2019).
74. Lee, J. Y. *et al.* MFN1 deacetylation activates adaptive mitochondrial fusion and protects metabolically challenged mitochondria. *J. Cell Sci.* **127**, 4954–4963 (2014).
75. Song, Z., Chen, H., Fiket, M., Alexander, C. & Chan, D. C. OPA1 processing controls mitochondrial fusion and is regulated by mRNA splicing, membrane potential, and Yme1L. *J. Cell Biol.* **178**, 749–755 (2007).
76. Head, B., Griparic, L., Amiri, M., Gandre-Babbe, S. & Van Der Bliek, A. M. Inducible proteolytic inactivation of OPA1 mediated by the OMA1 protease in mammalian cells. *J. Cell Biol.* **187**, 959–966 (2009).
77. Yu, R., Jin, S., Lendahl, U., Nistér, M. & Zhao, J. Human Fis1 regulates mitochondrial dynamics through inhibition of the fusion machinery. *EMBO J.* **38**, e99748 (2019).
78. Valm, A. M. *et al.* Applying systems-level spectral imaging and analysis to reveal the organelle interactome. *Nature* **546**, 162–167 (2017).
79. Chen, H. *et al.* Mitofusins Mfn1 and Mfn2 coordinately regulate mitochondrial fusion and are essential for embryonic development. *J. Cell Biol.* **160**, 189–200 (2003).
80. Santel, A. & Fuller, M. T. Control of mitochondrial morphology by a human mitofusin. *J. Cell Sci.* **114**, 867–874 (2001).
81. Naon, D. *et al.* Critical reappraisal confirms that Mitofusin 2 is an endoplasmic reticulum–mitochondria tether. *Proc. Natl. Acad. Sci.* **113**, 11249–11254 (2016).
82. Brito, O. M. De & Scorrano, L. Mitofusin 2 tethers endoplasmic reticulum to mitochondria. *Nature* **456**, 605–610 (2008).
83. McLelland, G. *et al.* Mfn2 ubiquitination by PINK1 / parkin gates the p97-dependent release of ER from mitochondria to drive mitophagy. *Elife* **7**, 1–35 (2018).
84. Filadi, R. *et al.* Mitofusin 2 ablation increases endoplasmic reticulum – mitochondria coupling. *Proc. Natl. Acad. Sci.* **112**, E2174–E2181 (2015).
85. Santos Leal, N. *et al.* Mitofusin-2 knockdown increases ER– mitochondria contact and decreases amyloid b-peptide production. *J. Cell. Mol. Med.* **20**, 1686–1695 (2016).
86. Hernández-Alvarez, M. I. *et al.* Deficient Endoplasmic Reticulum-Mitochondrial Phosphatidylserine Transfer Causes Liver Disease Article

- Deficient Endoplasmic Reticulum-Mitochondrial Phosphatidylserine Transfer Causes Liver Disease. *Cell* **177**, 881–895 (2019).
87. Ainbinder, A., Boncompagni, S., Protasi, F. & Dirksen, R. T. Role of Mitofusin-2 in mitochondrial localization and calcium uptake in skeletal muscle. *Cell Calcium* **57**, 14–24 (2015).
 88. Wang, H. *et al.* Cardiomyocyte-specific perilipin 5 overexpression leads to myocardial steatosis and modest cardiac dysfunction. *J. Lipid Res.* **54**, 953–965 (2013).
 89. Boutant, M. *et al.* Mfn2 is critical for brown adipose tissue thermogenic function. *EMBO J.* **36**, 1543–1558 (2017).
 90. Tarnopolsky, M. A. *et al.* Influence of endurance exercise training and sex on intramyocellular lipid and mitochondrial ultrastructure, substrate use, and mitochondrial enzyme activity. *AJP Regul. Integr. Comp. Physiol.* **292**, R1271–R1278 (2006).
 91. Shiozaki, M. *et al.* Closer association of mitochondria with lipid droplets in hepatocytes and activation of Kupfer cells in resveratrol-treated senescence-accelerated mice. *Histochem. Cell Biol.* **136**, 475–489 (2011).
 92. Benador, I. Y. *et al.* Mitochondria Bound to Lipid Droplets Have Unique Bioenergetics, Composition, and Dynamics that Support Lipid Droplet Expansion. *Cell Metab.* **27**, 869–885.e6 (2018).
 93. Rambold, A. S., Cohen, S. & Lippincott-Schwartz, J. Fatty Acid Trafficking in Starved Cells: Regulation by Lipid Droplet Lipolysis, Autophagy, and Mitochondrial Fusion Dynamics. *Dev. Cell* **32**, 678–692 (2015).
 94. Zhao, T. *et al.* Central Role of Mitofusin 2 in Autophagosome-Lysosome Fusion in Cardiomyocytes. *J. Biol. Chem.* **287**, 23615–23625 (2012).
 95. Daniele, T. *et al.* Mitochondria and melanosomes establish physical contacts modulated by Mfn2 and involved in organelle biogenesis. *Curr. Biol.* **24**, 393–403 (2014).
 96. Wu, M. J. *et al.* Epithelial-Mesenchymal Transition Directs Stem Cell Polarity via Regulation of Mitofusin. *Cell Metab.* **29**, 993–1002.e6 (2019).
 97. Harding, H. P. *et al.* An Integrated Stress Response Regulates Amino Acid Metabolism and Resistance to Oxidative Stress. *Mol. Cell* **11**, 619–633 (2003).
 98. Blais, J. J. D. *et al.* Activating Transcription Factor 4 Is Translationally Regulated by Hypoxic Stress. *Mol. Cell Biol.* **24**, 7469–7482 (2004).
 99. Liang, S.-H., Zhang, W., Mcgrath, B. C., Zhang, P. & Cavener, D. R. PERK (eIF2 α kinase) is required to activate the stress-activated MAPKs and induce the expression of immediate-early genes upon disruption of ER

- calcium homeostasis. *Biochem. J.* **393**, 201–209 (2006).
100. Tessitore, A. *et al.* GM1 mediate activation of UPR. *Mol. Cell* **15**, 753–766 (2004).
 101. Kharroubi, I., Ladrie, LaurenceCardozo, A. K., Dogusan, Z., Cnop, M. & Eizirik, D. L. Free Fatty Acids and Cytokines Induce Pancreatic b-Cell Apoptosis by Different Mechanisms: Role of Nuclear Factor- κ B and Endoplasmic Reticulum Stress. *Endocrinology* **145**, 5087–5096 (2004).
 102. Lai, E., Bikopoulos, G., Wheeler, M. B., Rozakis-adcock, M. & Volchuk, A. Differential activation of ER stress and apoptosis in response to chronically elevated free fatty acids in pancreatic β -cells. *Am. J. Physiol. Endocrinol. Metab.* **294**, 540–550 (2008).
 103. Sidrauski, C., Chapman, R. & Walter, P. The unfolded protein response: An intracellular signalling pathway with many surprising features. *Trends Cell Biol.* **8**, 245–249 (1998).
 104. Haynes, C. M., Titus, E. A. & Cooper, A. A. Degradation of misfolded proteins prevents ER-derived oxidative stress and cell death. *Mol. Cell* **15**, 767–776 (2004).
 105. Hetz, C. & Saxena, S. ER stress and the unfolded protein response in neurodegeneration. *Nat. Rev. Neurol.* **13**, 477–491 (2017).
 106. Hetz, C. & Papa, F. R. The Unfolded Protein Response and Cell Fate Control. *Mol. Cell* **69**, 169–181 (2018).
 107. Harding, H. P. *et al.* Regulated Translation Initiation Controls Stress-Induced Gene Expression in Mammalian Cells. *Mol. Cell* **6**, 1099–1108 (2000).
 108. Han, J. *et al.* ER-stress-induced transcriptional regulation increases protein synthesis leading to cell death. *Nat. Cell Biol.* **15**, 481–490 (2013).
 109. Bravo, R. *et al.* Increased ER – mitochondrial coupling promotes mitochondrial respiration and bioenergetics during early phases of ER stress Increased ER – mitochondrial coupling promotes mitochondrial respiration and bioenergetics during early phases of ER stress. *J. Cell Sci.* **124**, 2143–2152 (2011).
 110. Ngoh, G. A., Papanicolaou, K. N. & Walsh, K. Loss of mitofusin 2 promotes endoplasmic reticulum stress. *J. Biol. Chem.* **287**, 20321–20332 (2012).
 111. Lamb, C. A., Yoshimori, T. & Tooze, S. A. The autophagosome: origins unknown, biogenesis complex. *Nat. Rev.* **14**, 759–774 (2013).
 112. Priault, M. *et al.* Impairing the bioenergetic status and the biogenesis of mitochondria triggers mitophagy in yeast. *Cell Death Differ.* **12**, 1613–1621 (2005).

113. Greene, J. C. *et al.* Mitochondrial pathology and apoptotic muscle degeneration in *Drosophila* parkin mutants. *Proc. Natl. Acad. Sci. U. S. A.* **100**, 4078–4083 (2003).
114. Sliter, D. A. *et al.* Parkin and PINK1 mitigate STING-induced inflammation. *Nature* **561**, 258–262 (2018).
115. Yamashita, S. I. *et al.* Mitochondrial division occurs concurrently with autophagosome formation but independently of Drp1 during mitophagy. *J. Cell Biol.* **215**, 649–665 (2016).
116. Matsuda, N. *et al.* PINK1 stabilized by mitochondrial depolarization recruits Parkin to damaged mitochondria and activates latent Parkin for mitophagy. *J. Cell Biol.* **189**, 211–221 (2010).
117. Vives-Bauza, C. *et al.* PINK1-dependent recruitment of Parkin to mitochondria in mitophagy. *Proc. Natl. Acad. Sci. U. S. A.* **107**, 378–383 (2010).
118. Narendra, D. P. *et al.* PINK1 is selectively stabilized on impaired mitochondria to activate Parkin. *PLoS Biol.* **8**, e1000298 (2010).
119. Narendra, D., Tanaka, A., Suen, D. F. & Youle, R. J. Parkin is recruited selectively to impaired mitochondria and promotes their autophagy. *J. Cell Biol.* **183**, 795–803 (2008).
120. Poole, A. C., Thomas, R. E., Yu, S., Vincow, E. S. & Pallanck, L. The Mitochondrial Fusion-Promoting Factor Mitofusin Is a Substrate of the PINK1/Parkin Pathway. *PLoS One* **5**, e10054 (2010).
121. Gegg, M. E. *et al.* Mitofusin 1 and mitofusin 2 are ubiquitinated in a PINK1/parkin-dependent manner upon induction of mitophagy. *Hum. Mol. Genet.* **19**, 4861–70 (2010).
122. Rakovic, A. *et al.* Mutations in PINK1 and Parkin Impair Ubiquitination of Mitofusins in Human Fibroblasts. *PLoS One* **6**, e16746 (2011).
123. Song, M., Mihara, K., Chen, Y., Scorrano, L. & Dorn, G. W. Mitochondrial fission and fusion factors reciprocally orchestrate mitophagic culling in mouse hearts and cultured fibroblasts. *Cell Metab.* **21**, 273–286 (2015).
124. Glater, E. E., Megeath, L. J., Stowers, R. S. & Schwarz, T. L. Axonal transport of mitochondria requires milton to recruit kinesin heavy chain and is light chain independent. *J. Cell Biol.* **173**, 545–557 (2006).
125. Misko, A. L., Sasaki, Y., Tuck, E., Milbrandt, J. & Baloh, R. H. Mitofusin2 mutations disrupt axonal mitochondrial positioning and promote axon degeneration. *J. Neurosci.* **32**, 4145–4155 (2012).
126. Sandoval, H. *et al.* Mitochondrial fusion but not fission regulates larval growth and synaptic development through steroid hormone production.

- Elife* **3**, 1–23 (2014).
127. Chen, H. *et al.* Mitochondrial fusion is required for mtDNA stability in skeletal muscle and tolerance of mtDNA mutations. *Cell* **141**, 280–289 (2010).
 128. Pich, S. *et al.* The Charcot-Marie-Tooth type 2A gene product, Mfn2, up-regulates fuel oxidation through expression of OXPHOS system. *Hum. Mol. Genet.* **14**, 1405–1415 (2005).
 129. Mourier, A. *et al.* Mitofusin 2 is required to maintain mitochondrial coenzyme Q levels. *J. Cell Biol.* **208**, 429–442 (2015).
 130. Banoth, B. & Cassel, S. L. Mitochondria in innate immune signaling. *Transl. Res.* **202**, 52–68 (2018).
 131. Akira, S., Uematsu, S. & Takeuchi, O. Pathogen recognition and innate immunity. *Cell* **124**, 783–801 (2006).
 132. Ablasser, A. & Hur, S. Regulation of cGAS- and RLR-mediated immunity to nucleic acids. *Nat. Immunol.* **21**, 17–29 (2020).
 133. Onoguchi, K. *et al.* Virus-infection or 5'ppp-RNA activates antiviral signal through redistribution of IPS-1 mediated by MFN1. *PLoS Pathog.* **6**, 1–17 (2010).
 134. Yasukawa, K. *et al.* Mitofusin 2 Inhibits Mitochondrial Antiviral Signaling. *Sci. Signal.* **2**, ra47 (2009).
 135. Castanier, C., Garcin, D., Vazquez, A. & Arnoult, D. Mitochondrial dynamics regulate the RIG-I-like receptor antiviral pathway. *EMBO Rep.* **11**, 133–138 (2010).
 136. Kanneganti, T.-D. *et al.* Autophagy proteins regulate innate immune responses by inhibiting the release of mitochondrial DNA mediated by the NALP3 inflammasome. *Nat. Immunol.* **11**, 401–414 (2006).
 137. Zhou, R., Yazdi, A. S., Menu, P. & Tschopp, J. A role for mitochondria in NLRP3 inflammasome activation. *Nature* **469**, 221–226 (2011).
 138. Swanson, K. V., Deng, M. & Ting, J. P. Y. The NLRP3 inflammasome: molecular activation and regulation to therapeutics. *Nat. Rev. Immunol.* **19**, 477–489 (2019).
 139. Ichinohe, T., Yamazaki, T., Koshiba, T. & Yanagi, Y. Mitochondrial protein mitofusin 2 is required for NLRP3 inflammasome activation after RNA virus infection. *Proc. Natl. Acad. Sci. U. S. A.* **110**, 17963–17968 (2013).
 140. Subramanian, N., Natarajan, K., Clatworthy, M. R., Wang, Z. & Germain, R. N. The adaptor MAVS promotes NLRP3 mitochondrial localization and inflammasome activation. *Cell* **153**, 348–361 (2013).

141. Tur, J. *et al.* Mitofusin 2 in Macrophages Links Mitochondrial ROS Production, Cytokine Release, Phagocytosis, Autophagy, and Bactericidal Activity. *Cell Rep.* **32**, 108079 (2020).
142. Kim, Y.-M. *et al.* Mitofusin-2 stabilizes adherens junctions and suppresses endothelial inflammation via modulation of β -catenin signaling. *Nat. Commun.* **12**, 2736 (2021).
143. Zhang, M. *et al.* Mitofusin 1 is required for female fertility and to maintain ovarian follicular reserve. *Cell Death Dis.* **10**, 560 (2019).
144. Salazar-Roa, M. & Malumbres, M. Fueling the Cell Division Cycle. *Trends Cell Biol.* **27**, 69–81 (2017).
145. Park, Y.-Y. Y. & Cho, H. Mitofusin 1 is degraded at G2/M phase through ubiquitylation by MARCH5. *Cell Div.* **7**, 25 (2012).
146. Meloche, S. & Pouysségur, J. The ERK1/2 mitogen-activated protein kinase pathway as a master regulator of the G1- to S-phase transition. *Oncogene* vol. 26 3227–3239 (2007).
147. Chen, K. H. *et al.* Role of mitofusin 2 (Mfn2) in controlling cellular proliferation. *FASEB J.* **28**, 382–394 (2014).
148. Karbowski, M. *et al.* Quantitation of mitochondrial dynamics by photolabeling of individual organelles shows that mitochondrial fusion is blocked during the Bax activation phase of apoptosis. *J. Cell Biol.* **164**, 493–499 (2004).
149. Karbowski, M., Norris, K. L., Cleland, M. M., Jeong, S. Y. & Youle, R. J. Role of Bax and Bak in mitochondrial morphogenesis. *Nature* **443**, 658–662 (2006).
150. Pyakurel, A., Savoia, C., Hess, D. & Scorrano, L. Extracellular Regulated Kinase Phosphorylates Mitofusin 1 to Control Mitochondrial Morphology and Apoptosis. *Mol. Cell* **58**, 244–254 (2015).
151. Peña-Blanco, A. & García-Sáez, A. J. Bax, Bak and beyond—mitochondrial performance in apoptosis. *FEBS J.* **285**, 416–431 (2018).
152. Namba, T. *et al.* CDIP1-BAP31 Complex Transduces Apoptotic Signals from Endoplasmic Reticulum to Mitochondria under Endoplasmic Reticulum Stress. *Cell Rep.* **5**, 331–339 (2013).
153. Korsmeyer, S. J. *et al.* Pro-apoptotic cascade activates BID, which oligomerizes BAK or BAX into pores that result in the release of cytochrome c. *Cell Death Differ.* **7**, 1166–1173 (2000).
154. Li, P. *et al.* Cytochrome c and dATP-Dependent Formation of Apaf-1 / Caspase-9 Complex Initiates an Apoptotic Protease Cascade. *Cell* **91**, 479–489 (1997).

155. Karbowski, M. *et al.* Spatial and temporal association of Bax with mitochondrial fission sites, Drp1, and Mfn2 during apoptosis. *J. Cell Biol.* **159**, 931–938 (2002).
156. Brooks, C. *et al.* Bak regulates mitochondrial morphology and pathology during apoptosis by interacting with mitofusins. *Proc. Natl. Acad. Sci. U. S. A.* **104**, 11649–11654 (2007).
157. Hoppins, S. *et al.* The Soluble Form of Bax Regulates Mitochondrial Fusion via MFN2 Homotypic Complexes. *Mol. Cell* **41**, 150–160 (2011).
158. Renault, T. T. *et al.* Mitochondrial shape governs BAX-induced membrane permeabilization and apoptosis. *Mol. Cell* **57**, 69–82 (2015).
159. Mai, S., Klinkenberg, M., Auburger, G., Bereiter-Hahn, J. & Jendrach, M. Decreased expression of Drp1 and Fis1 mediates mitochondrial elongation in senescent cells and enhances resistance to oxidative stress through PINK1. *J. Cell Sci.* **123**, 917–926 (2010).
160. Yoon, Y. S. *et al.* Formation of elongated giant mitochondria in DFO-induced cellular senescence: Involvement of enhanced fusion process through modulation of Fis1. *J. Cell. Physiol.* **209**, 468–480 (2006).
161. Lee, S. *et al.* Mitochondrial fission and fusion mediators, hFis1 and OPA1, modulate cellular senescence. *J. Biol. Chem.* **282**, 22977–22983 (2007).
162. Short, K. R. *et al.* Decline in skeletal muscle mitochondrial function with aging in humans. *Proc. Natl. Acad. Sci. U. S. A.* **102**, 5618–5623 (2005).
163. Zhang, J. H. *et al.* Mitofusin-2 is required for mouse oocyte meiotic maturation. *Sci. Rep.* **6**, 30970 (2016).
164. Varuzhanyan, G. *et al.* Mitochondrial fusion is required for spermatogonial differentiation and meiosis. *Elife* **8**, e51601 (2019).
165. Zhang, J. *et al.* GASZ and mitofusin-mediated mitochondrial functions are crucial for spermatogenesis. *EMBO Rep.* **17**, 220–234 (2016).
166. Sênos Demarco, R., Uyemura, B. S., D'Alterio, C. & Jones, D. L. Mitochondrial fusion regulates lipid homeostasis and stem cell maintenance in the *Drosophila* testis. *Nat. Cell Biol.* **21**, 710–720 (2019).
167. Bahat, A. *et al.* MTCH2-mediated mitochondrial fusion drives exit from naïve pluripotency in embryonic stem cells. *Nat. Commun.* **9**, 5132 (2018).
168. Son, M. J. *et al.* Mitofusins deficiency elicits mitochondrial metabolic reprogramming to pluripotency. *Cell Death Differ.* **22**, 1957–1969 (2015).
169. Kasahara, A., Cipolat, S., Chen, Y., Dorn, G. W. & Scorrano, L. Mitochondrial fusion directs cardiomyocyte differentiation via calcineurin and notch signaling. *Science* **342**, 734–737 (2013).

170. Jung, S. *et al.* Mitofusin 2, a mitochondria-ER tethering protein, facilitates osteoclastogenesis by regulating the calcium-calcineurin-NFATc1 axis. *Biochem. Biophys. Res. Commun.* **516**, 202–208 (2019).
171. Luchsinger, L. L., De Almeida, M. J., Corrigan, D. J., Mumau, M. & Snoeck, H. W. Mitofusin 2 maintains haematopoietic stem cells with extensive lymphoid potential. *Nature* **529**, 528–531 (2016).
172. Rabanal-Ruiz, Y., Otten, E. G. & Korolchuk, V. I. mTORC1 as the main gateway to autophagy. *Essays Biochem.* **61**, 565–584 (2017).
173. Kim, J., Kundu, M., Viollet, B. & Guan, K. L. AMPK and mTOR regulate autophagy through direct phosphorylation of Ulk1. *Nat. Cell Biol.* **13**, 132–141 (2011).
174. Farré, J. C. & Subramani, S. Mechanistic insights into selective autophagy pathways: Lessons from yeast. *Nat. Rev. Mol. Cell Biol.* **17**, 537–552 (2016).
175. Nishimura, T. *et al.* Autophagosome formation is initiated at phosphatidylinositol synthase-enriched ER subdomains. *EMBO J.* **36**, 1719–1735 (2017).
176. Moretti, F. *et al.* TMEM41B is a novel regulator of autophagy and lipid mobilization. *EMBO Rep.* **19**, e45889 (2018).
177. Suzuki, S. W. *et al.* Atg13 HORMA domain recruits Atg9 vesicles during autophagosome formation. *Proc. Natl. Acad. Sci. U. S. A.* **112**, 3350–3355 (2015).
178. Kageyama, S. *et al.* The LC3 recruitment mechanism is separate from Atg9L1-dependent membrane formation in the autophagic response against Salmonella. *Mol. Biol. Cell* **22**, 2290–2300 (2011).
179. Sawa-Makarska, J. *et al.* Reconstitution of autophagosome nucleation defines Atg9 vesicles as seeds for membrane formation. *Science* **369**, (2020).
180. Suzuki, K., Kubota, Y., Sekito, T. & Ohsumi, Y. Hierarchy of Atg proteins in pre-autophagosomal structure organization. *Genes to Cells* **12**, 209–218 (2007).
181. Obara, K., Sekito, T., Niimi, K. & Ohsumi, Y. The Atg18-Atg2 complex is recruited to autophagic membranes via phosphatidylinositol 3-phosphate and exerts an essential function. *J. Biol. Chem.* **283**, 23972–23980 (2008).
182. Dooley, H. C. *et al.* WIPI2 Links LC3 Conjugation with PI3P, Autophagosome Formation, and Pathogen Clearance by Recruiting Atg12-5-16L1. *Mol. Cell* **55**, 238–252 (2014).
183. Fujita, N. *et al.* The Atg16L complex specifies the site of LC3 lipidation for

- membrane biogenesis in autophagy. *Mol. Biol. Cell* **19**, 2092–2100 (2008).
184. Otomo, C., Metlagel, Z., Takaesu, G. & Otomo, T. Structure of the human ATG12~ATG5 conjugate required for LC3 lipidation in autophagy. *Nat. Struct. Mol. Biol.* **20**, 59–66 (2013).
 185. Maeda, S., Otomo, C. & Otomo, T. The autophagic membrane tether ATG2A transfers lipids between membranes. *Elife* **8**, e45777 (2019).
 186. Gómez-Sánchez, R. *et al.* Atg9 establishes Atg2-dependent contact sites between the endoplasmic reticulum and phagophores. *J. Cell Biol.* **217**, 2743–2763 (2018).
 187. Osawa, T., Ishii, Y. & Noda, N. N. Human ATG2B possesses a lipid transfer activity which is accelerated by negatively charged lipids and WIPI4. *Genes to Cells* **25**, 65–70 (2020).
 188. Nakatogawa, H., Ichimura, Y. & Ohsumi, Y. Atg8, a Ubiquitin-like Protein Required for Autophagosome Formation, Mediates Membrane Tethering and Hemifusion. *Cell* **130**, 165–178 (2007).
 189. Weidberg, H. *et al.* LC3 and GATE-16/GABARAP subfamilies are both essential yet act differently in autophagosome biogenesis. *EMBO J.* **29**, 1792–1802 (2010).
 190. Noda, N. N., Ohsumi, Y. & Inagaki, F. Atg8-family interacting motif crucial for selective autophagy. *FEBS Lett.* **584**, 1379–1385 (2010).
 191. Hayashi-Nishino, M. *et al.* A subdomain of the endoplasmic reticulum forms a cradle for autophagosome formation. *Nat. Cell Biol.* **11**, 1433–1437 (2009).
 192. Shima, T., Kirisako, H. & Nakatogawa, H. COPII vesicles contribute to autophagosomal membranes. *J. Cell Biol.* **218**, 1503–1510 (2019).
 193. Kotani, T., Kirisako, H., Koizumi, M., Ohsumi, Y. & Nakatogawa, H. The Atg2-Atg18 complex tethers pre-autophagosomal membranes to the endoplasmic reticulum for autophagosome formation. *Proc. Natl. Acad. Sci. U. S. A.* **115**, 10363–10368 (2018).
 194. Osawa, T. *et al.* Atg2 mediates direct lipid transfer between membranes for autophagosome formation. *Nat. Struct. Mol. Biol.* **26**, 281–288 (2019).
 195. Ishihara, N. *et al.* Autophagosome requires specific early sec proteins for its formation and NSF/SNARE for vacuolar fusion. *Mol. Biol. Cell* **12**, 3690–3702 (2001).
 196. Ohkuni, A., Ohno, Y. & Kihara, A. Identification of acyl-CoA synthetases involved in the mammalian sphingosine 1-phosphate metabolic pathway. *Biochem. Biophys. Res. Commun.* **442**, 195–201 (2013).
 197. Eck, F. *et al.* ACSL3 is a novel GABARAPL2 interactor that links ufmylation

- and lipid droplet biogenesis. *J. Cell Sci.* **133**, (2020).
198. Takahashi, Y. *et al.* An autophagy assay reveals the ESCRT-III component CHMP2A as a regulator of phagophore closure. *Nat. Commun.* **9**, 1–13 (2018).
 199. Park, K. S., Wiederkehr, A. & Wollheim, C. B. Defective mitochondrial function and motility due to mitofusin 1 overexpression in insulin secreting cells. *Korean J. Physiol. Pharmacol.* **16**, 71–77 (2012).
 200. Huang, P., Yu, T. & Yoon, Y. Mitochondrial clustering induced by overexpression of the mitochondrial fusion protein Mfn2 causes mitochondrial dysfunction and cell death. *Eur. J. Cell Biol.* **86**, 289–302 (2007).
 201. Hale, C. R. *et al.* RNA-Guided RNA Cleavage by a CRISPR RNA-Cas Protein Complex. *Cell* **139**, 945–956 (2009).
 202. Cong, L. *et al.* Multiplex Genome Engineering Using CRISPR/Cas Systems. *Science* **339**, 819–824 (2013).
 203. Zhang, Y., Vanoli, F., Larocque, J. R., Krawczyk, P. M. & Jasin, M. Biallelic targeting of expressed genes in mouse embryonic stem cells using the Cas9 system. *Methods* **69**, 171–178 (2014).
 204. Sung, Y. H. *et al.* Highly efficient gene knockout in mice and zebrafish with RNA-guided endonucleases. *Genome Res.* **24**, 125–131 (2014).
 205. Dickinson, D. J., Ward, J. D., Reiner, D. J. & Goldstein, B. Engineering the *Caenorhabditis elegans* genome using Cas9-triggered homologous recombination. *Nat. Methods* **10**, 1028–1033 (2013).
 206. Zhang, C., Meng, X., Wei, X. & Lu, L. Highly efficient CRISPR mutagenesis by microhomology-mediated end joining in *Aspergillus fumigatus*. *Fungal Genet. Biol.* **86**, 47–57 (2016).
 207. Chen, F. *et al.* Gene editing using ssODNs with engineered endonucleases. *Chromosom. Mutagen.* **1239**, 251–265 (2015).
 208. Zhang, X. A., Bontrager, A. L. & Hemler, M. E. Transmembrane-4 Superfamily Proteins Associate with Activated Protein Kinase C (PKC) and Link PKC to Specific β 1 Integrins. *J. Biol. Chem.* **276**, 25005–25013 (2001).
 209. Samovski, D. *et al.* Regulation of AMPK activation by CD36 links fatty acid uptake to β -oxidation. *Diabetes* **64**, 353–359 (2015).
 210. Robeson, A. C., Lindblom, K. R., Wojton, J., Kornbluth, S. & Matsuura, K. Dimer-specific immunoprecipitation of active caspase-2 identifies TRAF proteins as novel activators. *EMBO J.* **37**, (2018).
 211. Malty, R. H. *et al.* A Map of Human Mitochondrial Protein Interactions

- Linked to Neurodegeneration Reveals New Mechanisms of Redox Homeostasis and NF- κ B Signaling. *Cell Syst.* **5**, 564–577.e12 (2017).
212. Acín-Pérez, R., Fernández-Silva, P., Peleato, M. L., Pérez-Martos, A. & Enriquez, J. A. Respiratory Active Mitochondrial Supercomplexes. *Mol. Cell* **32**, 529–539 (2008).
213. Huckabee, D. B. & Jekabsons, M. B. Identification of Bax-voltage-dependent anion channel 1 complexes in digitonin-solubilized cerebellar granule neurons. *J. Neurochem.* **119**, 1137–1150 (2011).
214. Murphy, K. M., Streips, U. N. & Lock, R. B. Bcl-2 Inhibits a Fas-induced Conformational Change in the Bax N Terminus and Bax Mitochondrial Translocation*. *J. Biol. Chem.* **275**, 17225–17228 (2000).
215. Foot, N. J. *et al.* Regulation of the divalent metal ion transporter DMT1 and iron homeostasis by a ubiquitin-dependent mechanism involving Ndfips and WWP2. *Blood* **112**, 4268–4275 (2008).
216. Kang, Y., Guo, J., Yang, T., Li, W. & Zhang, S. Regulation of the human ether-a-go-go-related gene (hERG) potassium channel by Nedd4 family interacting proteins (Ndfips). *Biochem. J.* **472**, 71–82 (2015).
217. Hsu, F. S. *et al.* Rab5 and Alsln regulate stress-activated cytoprotective signaling on mitochondria. *Elife* **7**, e32282 (2018).
218. Yamano, K. *et al.* Endosomal rab cycles regulate parkin-mediated mitophagy. *Elife* **7**, e31326 (2018).
219. Sun, Z. *et al.* S100A8 transported by SEC23A inhibits metastatic colonization via autocrine activation of autophagy. *Cell Death Dis.* **11**, 650 (2020).
220. Yang, L. *et al.* S100A8-targeting siRNA enhances arsenic trioxide-induced myeloid leukemia cell death by down-regulating autophagy. *Int. J. Mol. Med.* **29**, 65–72 (2012).
221. Shabani, F., Farasat, A., Mahdavi, M. & Gheibi, N. Calprotectin (S100A8/S100A9): a key protein between inflammation and cancer. *Inflamm. Res.* **67**, 801–812 (2018).
222. Thompson, J. D., Higgins, D. G. & Gibson, T. J. CLUSTAL W: improving the sensitivity of progressive multiple sequence alignment through sequence weighting, position-specific gap penalties and weight matrix choice. *Nucleic Acids Res.* **22**, 4673–4680 (1994).
223. Santetl, A. *et al.* Mitofusin-1 protein is a generally expressed mediator of mitochondrial fusion in mammalian cells. *J. Cell Sci.* **116**, 2763–2774 (2003).
224. Maldonado, M., Guo, F., Letts, J. A. & Carter, A. P. Atomic structures of

- respiratory complex III2, complex IV, and supercomplex III2-IV from vascular plants. *Elife* **10**, 1–34 (2021).
225. Eura, Y., Ishihara, N., Oka, T. & Mihara, K. Identification of a novel protein that regulates mitochondrial fusion by modulating mitofusin (Mfn) protein function. *J. Cell Sci.* **119**, 4913–4925 (2006).
 226. Cleland, M. M. *et al.* Bcl-2 family interaction with the mitochondrial morphogenesis machinery. *Cell Death Differ.* **18**, 235–247 (2011).
 227. Saita, S. *et al.* Distinct types of protease systems are involved in homeostasis regulation of mitochondrial morphology via balanced fusion and fission. *Genes to Cells* **21**, 408–424 (2016).
 228. Huang, P., Galloway, C. A. & Yoon, Y. Control of mitochondrial morphology through differential interactions of mitochondrial fusion and fission proteins. *PLoS One* **6**, e20655–e20655 (2011).
 229. Ma, D. *et al.* Klf5 down-regulation induces vascular senescence through eIF5a depletion and mitochondrial fission. *PLOS Biol.* **18**, e3000808 (2020).
 230. Li, L. *et al.* p38 MAP kinase–dependent phosphorylation of the Gp78 E3 ubiquitin ligase controls ER–mitochondria association and mitochondria motility. *Mol. Biol. Cell* **26**, 3828–3840 (2015).
 231. Zhang, J. *et al.* G-protein $\beta 2$ subunit interacts with mitofusin 1 to regulate mitochondrial fusion. *Nat. Commun.* **1**, 101 (2010).
 232. HJ, K. *et al.* HDAC6 maintains mitochondrial connectivity under hypoxic stress by suppressing MARCH5/MITOL dependent MFN2 degradation. *Biochem. Biophys. Res. Commun.* **464**, 1235–1240 (2015).
 233. Park, Y.-Y. *et al.* Loss of MARCH5 mitochondrial E3 ubiquitin ligase induces cellular senescence through dynamin-related protein 1 and mitofusin 1. *J. Cell Sci.* **123**, 619–26 (2010).
 234. Mukherjee, R. & Chakrabarti, O. Regulation of Mitofusin1 by Mahogunin Ring Finger-1 and the proteasome modulates mitochondrial fusion. *Biochim. Biophys. Acta - Mol. Cell Res.* **1863**, 3065–3083 (2016).
 235. Vadnais, M. L., Lin, A. M. & Gerton, G. L. Mitochondrial fusion protein MFN2 interacts with the mitostatin-related protein MNS1 required for mouse sperm flagellar structure and function. *Cilia* **3**, 1–15 (2014).
 236. Yun, J. *et al.* MUL1 acts in parallel to the PINK1/parkin pathway in regulating mitofusin and compensates for loss of PINK1/parkin. *Elife* **3**, e01958 (2014).
 237. Chen, C. W. *et al.* Two separate functions of NME3 critical for cell survival underlie a neurodegenerative disorder. *Proc. Natl. Acad. Sci. U. S. A.* **116**,

- 566–574 (2019).
238. Guillery, O. *et al.* Metalloprotease-mediated OPA1 processing is modulated by the mitochondrial membrane potential. *Biol. Cell* **100**, 315–325 (2008).
239. Chen, Y. & Dorn, G. W. PINK1-Phosphorylated Mitofusin 2 Is a Parkin Receptor for Culling Damaged Mitochondria. *Science* **340**, 471–475 (2013).
240. Hu, Y. *et al.* The AMPK-MFN2 axis regulates MAM dynamics and autophagy induced by energy stresses. *Autophagy* **17**, 1142–1156 (2021).
241. Filadi, R. *et al.* Presenilin 2 Modulates Endoplasmic Reticulum-Mitochondria Coupling by Tuning the Antagonistic Effect of Mitofusin 2. *Cell Rep.* **15**, 2226–2238 (2016).
242. de Brito, O. M. & Scorrano, L. Mitofusin-2 regulates mitochondrial and endoplasmic reticulum morphology and tethering: The role of Ras. *Mitochondrion* **9**, 222–226 (2009).
243. Xu, K. *et al.* MFN2 suppresses cancer progression through inhibition of mTORC2/Akt signaling. *Sci. Rep.* **7**, 41718 (2017).
244. Kumar, S. *et al.* Activation of Mitofusin2 by Smad2-RIN1 Complex during Mitochondrial Fusion. *Mol. Cell* **62**, 520–531 (2016).
245. Biel, T. G. *et al.* Sirtuin 1 suppresses mitochondrial dysfunction of ischemic mouse livers in a mitofusin 2-dependent manner. *Cell Death Differ.* **23**, 279–290 (2016).
246. Zhang, C. *et al.* Apoptosin interacts with mitochondrial outer-membrane fusion proteins and regulates mitochondrial morphology. *J. Cell Sci.* **129**, 994–1002 (2016).
247. Steffen, J. *et al.* Rapid degradation of mutant SLC25A46 by the ubiquitin-proteasome system results in MFN1/2-mediated hyperfusion of mitochondria. *Mol. Biol. Cell* **28**, 600–612 (2017).
248. Hájek, P., Chomyn, A. & Attardi, G. Identification of a Novel Mitochondrial Complex Containing Mitofusin 2 and Stomatin-like Protein 2*. *J. Biol. Chem.* **282**, 5670–5681 (2007).
249. Davis, S. A. *et al.* TDP-43 interacts with mitochondrial proteins critical for mitophagy and mitochondrial dynamics. *Neurosci. Lett.* **678**, 8–15 (2018).
250. Oanh, N. T. K., Park, Y.-Y. & Cho, H. Mitochondria elongation is mediated through SIRT1-mediated MFN1 stabilization. *Cell. Signal.* **38**, 67–75 (2017).
251. Yue, W. *et al.* A small natural molecule promotes mitochondrial fusion through inhibition of the deubiquitinase USP30. *Cell Res.* **24**, 482–496

- (2014).
252. Kim, N. C. *et al.* VCP Is Essential for Mitochondrial Quality Control by PINK1/Parkin and this Function Is Impaired by VCP Mutations. *Neuron* **78**, 65–80 (2013).
 253. Roux, K. J., Kim, D. I., Raida, M. & Burke, B. A promiscuous biotin ligase fusion protein identifies proximal and interacting proteins in mammalian cells. *J. Cell Biol.* **196**, 801–810 (2012).
 254. Branon, T. C. *et al.* Efficient proximity labeling in living cells and organisms with TurboID. *Nat. Biotechnol.* **36**, 880–887 (2018).
 255. Antonicka, H. *et al.* A High-Density Human Mitochondrial Proximity Interaction Network. *Cell Metab.* **32**, 479–497.e9 (2020).
 256. Molina, A. J. A. *et al.* Mitochondrial networking protects β -cells from nutrient-induced apoptosis. *Diabetes* **58**, 2303–2315 (2009).
 257. Gomes, L. C., Benedetto, G. Di & Scorrano, L. During autophagy mitochondria elongate, are spared from degradation and sustain cell viability. *Nat. Cell Biol.* **13**, 589–598 (2011).
 258. Bravo-Sagua, R. *et al.* mTORC1 inhibitor rapamycin and ER stressor tunicamycin induce differential patterns of ER-mitochondria coupling. *Sci. Rep.* **6**, 36394 (2016).
 259. Cieri, D. *et al.* SPLICS: a split green fluorescent protein-based contact site sensor for narrow and wide heterotypic organelle juxtaposition. *Cell Death Differ.* **25**, 1131–1145 (2018).
 260. Tubbs, E. *et al.* Mitochondria-associated endoplasmic reticulum membrane (MAM) integrity is required for insulin signaling and is implicated in hepatic insulin resistance. *Diabetes* **63**, 3279–3294 (2014).
 261. Paillard, M. *et al.* Depressing mitochondria-reticulum interactions protects cardiomyocytes from lethal hypoxia-reoxygenation injury. *Circulation* **128**, 1555–1565 (2013).
 262. Casellas-Díaz, S. *et al.* Mfn2 localization in the ER is necessary for its bioenergetic function and neuritic development. *EMBO Rep.* **22**, e51954 (2021).
 263. Wu, S. *et al.* Binding of FUN14 Domain Containing 1 with Inositol 1,4,5-Trisphosphate Receptor in Mitochondria-Associated Endoplasmic Reticulum Membranes Maintains Mitochondrial Dynamics and Function in Hearts in Vivo. *Circulation* **136**, 2248–2266 (2017).
 264. Chen, Y. *et al.* Mitofusin 2-Containing Mitochondrial-Reticular Microdomains Direct Rapid Cardiomyocyte Bioenergetic Responses Via Interorganelle Ca²⁺ Crosstalk. *Circ. Res.* **111**, 863–875 (2012).

265. Solomon, A. L. *et al.* Placental alkaline phosphatase de-phosphorylates insulin-like growth factor (IGF)-binding protein-1. *Placenta* **35**, 520–522 (2014).
266. Du, M. H. Le, Stigbrand, T., Taussig, M. J., Ménez, A. & Stura, E. A. Crystal Structure of Alkaline Phosphatase from Human Placenta at 1.8 Å Resolution: Implication for a substrate specificity. *J. Biol. Chem.* **276**, 9158–9165 (2001).
267. Park, J.-H. *et al.* Molecular cloning, expression, and structural prediction of deoxyhypusine hydroxylase: A HEAT-repeat-containing metalloenzyme. *Proc. Natl. Acad. Sci.* **103**, 51–56 (2006).
268. Sumara, I. *et al.* A Cul3-Based E3 Ligase Removes Aurora B from Mitotic Chromosomes, Regulating Mitotic Progression and Completion of Cytokinesis in Human Cells. *Dev. Cell* **12**, 887–900 (2007).
269. Wei, Y. *et al.* NEDD4L-mediated Merlin ubiquitination facilitates Hippo pathway activation. *EMBO Rep.* **21**, e50642 (2020).
270. Hailey, D. W. *et al.* Mitochondria Supply Membranes for Autophagosome Biogenesis during Starvation. *Cell* **141**, 656–667 (2010).
271. Coutts, A. S. & La Thangue, N. B. Actin nucleation by WH2 domains at the autophagosome. *Nat. Commun.* **6**, 7888 (2015).
272. Kast, D. J. & Dominguez, R. The Cytoskeleton–Autophagy Connection. *Curr. Biol.* **27**, R318–R326 (2017).
273. Liu, J. *et al.* Beclin1 Controls the Levels of p53 by Regulating the Deubiquitination Activity of USP10 and USP13. *Cell* **147**, 223–234 (2011).
274. Jia, R. & Bonifacino, J. S. The ubiquitin isopeptidase USP10 deubiquitinates LC3B to increase LC3B levels and autophagic activity. *J. Biol. Chem.* **296**, 100405 (2021).
275. Ghavami, S. *et al.* S100A8/A9 induces autophagy and apoptosis via ROS-mediated cross-talk between mitochondria and lysosomes that involves BNIP3. *Cell Res.* **20**, 314–331 (2010).
276. Zhang, L. *et al.* S100A8 promotes chemoresistance via augmenting autophagy in B-cell lymphoma cells. *Oncol. Rep.* **45**, 151–158 (2021).
277. Bhushan, J. *et al.* Isg15 connects autophagy and ifn-dependent control of toxoplasma gondii infection in human cells. *MBio* **11**, 1–19 (2020).
278. Karras, P. *et al.* p62/SQSTM1 Fuels Melanoma Progression by Opposing mRNA Decay of a Selective Set of Pro-metastatic Factors. *Cancer Cell* **35**, 46–63.e10 (2019).
279. Suissa, M. & Schatz, G. Import of proteins into mitochondria. Translatable mRNAs for imported mitochondrial proteins are present in free as

- well as mitochondria-bound cytoplasmic polysomes. *J. Biol. Chem.* **257**, 13048–13055 (1982).
280. Kellems, R. E., Allison, V. I. ' & Butow, R. A. Cytoplasmic Type 80 S Ribosomes Associated with Yeast Mitochondria. *J. Biol. Chem.* **249**, 3297–3303 (1974).
 281. Kellems, R. E., Allison, V. F. & Butow, R. A. Cytoplasmic type 80S ribosomes associated with yeast mitochondria. IV. Attachment of ribosomes to the outer membrane of isolated mitochondria. *J. Cell Biol.* **65**, 1–14 (1975).
 282. Matsumoto, S. *et al.* Localization of mRNAs encoding human mitochondrial oxidative phosphorylation proteins. *Mitochondrion* **12**, 391–398 (2012).
 283. Rangaraju, V., Lauterbach, M. & Schuman, E. M. Spatially Stable Mitochondrial Compartments Fuel Local Translation during Plasticity. *Cell* **176**, 73-84.e15 (2019).
 284. Saint-Georges, Y. *et al.* Yeast Mitochondrial Biogenesis: A Role for the PUF RNA-Binding Protein Puf3p in mRNA Localization. *PLoS One* **3**, e2293 (2008).
 285. Corral-Debrinski, M., Blugeon, C. & Jacq, C. In Yeast, the 3' Untranslated Region or the Presequence of ATM1 Is Required for the Exclusive Localization of Its mRNA to the Vicinity of Mitochondria. *Mol. Cell. Biol.* **20**, 7881–7892 (2000).
 286. Fazal, F. M. *et al.* Atlas of Subcellular RNA Localization Revealed by APEX-Seq. *Cell* **178**, 473-490.e26 (2019).
 287. Paquin, N. *et al.* Local Activation of Yeast ASH1 mRNA Translation through Phosphorylation of Khd1p by the Casein Kinase Yck1p. *Mol. Cell* **26**, 795–809 (2007).
 288. Hüttelmaier, S. *et al.* Spatial regulation of β -actin translation by Src-dependent phosphorylation of ZBP1. *Nature* **438**, 512–515 (2005).
 289. Gehrke, S. *et al.* PINK1 and Parkin Control Localized Translation of Respiratory Chain Component mRNAs on Mitochondria Outer Membrane. *Cell Metab.* **21**, 95–108 (2015).
 290. Protter, D. S. W. & Parker, R. Principles and Properties of Stress Granules. *Trends Cell Biol.* **26**, 668–679 (2016).
 291. Mateju, D. *et al.* Single-Molecule Imaging Reveals Translation of mRNAs Localized to Stress Granules. *Cell* **183**, 1801-1812.e13 (2020).
 292. Nadezhdina, E. S., Lomakin, A. J., Shpilman, A. A., Chudinova, E. M. & Ivanov, P. A. Microtubules govern stress granule mobility and dynamics. *Biochim. Biophys. Acta - Mol. Cell Res.* **1803**, 361–371 (2010).

293. Aizer, A. *et al.* The Dynamics of Mammalian P Body Transport, Assembly, and Disassembly In Vivo. *Mol. Biol. Cell* **19**, 4154 (2008).
294. Youn, J.-Y. *et al.* High-Density Proximity Mapping Reveals the Subcellular Organization of mRNA-Associated Granules and Bodies. *Mol. Cell* **69**, 517-532.e11 (2018).
295. Amen, T. & Kaganovich, D. Stress granules inhibit fatty acid oxidation by modulating mitochondrial permeability. *Cell Rep.* **35**, 109237 (2021).
296. Gameiro, P. A. & Struhl, K. Nutrient Deprivation Elicits a Transcriptional and Translational Inflammatory Response Coupled to Decreased Protein Synthesis. *Cell Rep.* **24**, 1415–1424 (2018).
297. Sheftel, A. D., Zhang, A.-S., Brown, C., Shirihai, O. S. & Ponka, P. Direct interorganellar transfer of iron from endosome to mitochondrion. *Hematopoiesis* **110**, 125–132 (2007).
298. Hamdi, A. *et al.* Erythroid cell mitochondria receive endosomal iron by a “kiss-and-run” mechanism. *Biochim. Biophys. Acta - Mol. Cell Res.* **1863**, 2859–2867 (2016).
299. Das, A., Nag, S., Mason, A. B. & Barroso, M. M. Endosome–mitochondria interactions are modulated by iron release from transferrin. *J. Cell Biol.* **214**, 831–845 (2016).
300. Charman, M., Kennedy, B. E., Osborne, N. & Karten, B. MLN64 mediates egress of cholesterol from endosomes to mitochondria in the absence of functional Niemann-Pick Type C1 protein. *J. Lipid Res.* **51**, 1023–1034 (2010).
301. Hammerling, B. C. *et al.* A Rab5 endosomal pathway mediates Parkin-dependent mitochondrial clearance. *Nat. Commun.* **8**, 14050 (2017).
302. Sugiura, A., Mcllelland, G., Fon, E. A. & McBride, H. M. A new pathway for mitochondrial quality control: mitochondrial-derived vesicles. *EMBO J.* **33**, 2142–2156 (2014).
303. Soubannier, V. *et al.* A Vesicular Transport Pathway Shuttles Cargo from Mitochondria to Lysosomes. *Curr. Biol.* **22**, 135–141 (2012).
304. Towers, C. G. *et al.* Mitochondrial-derived vesicles compensate for loss of LC3-mediated mitophagy. *Dev. Cell* **56**, 2029-2042.e5 (2021).
305. Knoll, L. J., Johnson, D. R. & Gordon, J. I. Biochemical studies of three *Saccharomyces cerevisiae* acyl-CoA synthetases, Faa1p, Faa2p, and Faa3p. *J. Biol. Chem.* **269**, 16348–16356 (1994).
306. Steinberg, S. J., Wang, S. J., Kim, D. G., Mihalik, S. J. & Watkins, P. A. Human very-long-chain Acyl-CoA synthetase: Cloning, topography, and relevance to branched-chain fatty acid metabolism. *Biochem. Biophys.*

- Res. Commun.* **257**, 615–621 (1999).
307. Gibellini, F. & Smith, T. K. The Kennedy pathway—De novo synthesis of phosphatidylethanolamine and phosphatidylcholine. *IUBMB Life* **62**, 414–428 (2010).
 308. Rockenfeller, P. *et al.* Phosphatidylethanolamine positively regulates autophagy and longevity. *Cell Death Differ.* **22**, 499–508 (2015).
 309. Andrejeva, G. *et al.* De novo phosphatidylcholine synthesis is required for autophagosome membrane formation and maintenance during autophagy. *Autophagy* **16**, 1044–1060 (2019).
 310. Shpilka, T. *et al.* Lipid droplets and their component triglycerides and steryl esters regulate autophagosome biogenesis. *EMBO J.* **34**, 2117–2131 (2015).
 311. Nakahara, K. *et al.* The Sjögren-Larsson syndrome gene encodes a hexadecenal dehydrogenase of the sphingosine 1-phosphate degradation pathway. *Mol. Cell* **46**, 461–471 (2012).
 312. Yang, L. G. *et al.* Sphingosine-1-phosphate induces myocyte autophagy after myocardial infarction through mTOR inhibition. *Eur. J. Pharmacol.* **907**, 174260 (2021).
 313. Lewin, T. M., Kim, J.-H., Granger, D. A., Vance, J. E. & Coleman, R. A. Acyl-CoA Synthetase Isoforms 1, 4, and 5 Are Present in Different Subcellular Membranes in Rat Liver and Can Be Inhibited Independently. *J. Biol. Chem.* **276**, 24674–24679 (2001).
 314. Liang, J. R. *et al.* A Genome-wide ER-phagy Screen Highlights Key Roles of Mitochondrial Metabolism and ER-Resident UFMylation. *Cell* **180**, 1160-1177.e20 (2020).
 315. Martens, S. & Fracchiolla, D. Activation and targeting of ATG8 protein lipidation. *Cell Discov.* **6**, 1–11 (2020).
 316. Nakatogawa, H. Mechanisms governing autophagosome biogenesis. *Nature Reviews Molecular Cell Biology* vol. 21 439–458 (2020).
 317. Bozic, M. *et al.* A conserved ATG2-GABARAP family interaction is critical for phagophore formation. *EMBO Rep.* **21**, e48412 (2020).
 318. Tang, Z., Takahashi, Y., Chen, H., Young, M. M. & Correspondence, H.-G. W. TOM40 Targets Atg2 to Mitochondria-Associated ER Membranes for Phagophore Expansion. *Cell Rep.* **28**, 1744–1757 (2019).

PUBLICATIONS



REVIEW ARTICLE:



**Metabolic implications of organelle-mitochondria
communication**

Isabel Gordaliza-Alaguero, Carlos Cantó, Antonio Zorzano

EMBO Reports (2019) 20: e47928

doi.org/10.15252/embr.201947928

Metabolic implications of organelle–mitochondria communication

Isabel Gordaliza-Alaguero^{1,2,3} , Carlos Cantó^{4,5} & Antonio Zorzano^{1,2,3,*} 

Abstract

Cellular organelles are not static but show dynamism—a property that is likely relevant for their function. In addition, they interact with other organelles in a highly dynamic manner. In this review, we analyze the proteins involved in the interaction between mitochondria and other cellular organelles, especially the endoplasmic reticulum, lipid droplets, and lysosomes. Recent results indicate that, on one hand, metabolic alterations perturb the interaction between mitochondria and other organelles, and, on the other hand, that deficiency in proteins involved in the tethering between mitochondria and the ER or in specific functions of the interaction leads to metabolic alterations in a variety of tissues. The interaction between organelles is an emerging field that will permit to identify key proteins, to delineate novel modulation pathways, and to elucidate their implications in human disease.

Keywords contact sites; diabetes; endoplasmic reticulum; insulin resistance; lipid droplets

DOI 10.15252/embr.201947928 | Received 15 February 2019 | Revised 10 May 2019 | Accepted 28 May 2019 | Published online 14 August 2019

EMBO Reports (2019) 20: e47928

See the Glossary for abbreviations used in this article.

Contacts between mitochondria and other organelles

Mitochondria are highly dynamic and social organelles. They undergo continuous morphological changes to maintain cellular homeostasis; i.e., they fuse in response to specific physiological conditions, they divide to facilitate their removal by autophagy, and they maintain dynamic contacts with other membranous compartments of the cell. Mitochondria communicate with the endoplasmic reticulum (ER), lipid droplets (LDs), Golgi apparatus, lysosomes, melanosomes, and peroxisomes by establishing physical contacts (Fig 1). Fluorescent labeling of all these organelles *in vivo* has recently revealed cellular regions where three or more of these organelles physically interact [1]. Mitochondria and ER actively communicate, and their contact sites are important hubs for lipid

trafficking, mitochondrial dynamics, Ca²⁺ signaling, ER stress, apoptosis, and macroautophagy. Mitochondria–ER contact sites are also referred to as MERCs or when studied at a biochemical level MAMs (mitochondria-associated membranes). The contacts between mitochondria and LD functionally support triacylglyceride synthesis [2], and they are sustained by the interaction between MFN2 and PLIN1 [3]. Apposition of the Golgi apparatus and mitochondria has been demonstrated by microscopy techniques; however, the molecular features of this interaction remain poorly understood [4,5]. Mitochondria incorporate Ca²⁺ excess from the Golgi apparatus and have been proposed as a source of ATP for this organelle [4]. The contacts between mitochondria and lysosomes have been described to regulate mitochondrial fission, as well as lysosomal dynamics, by RAB7 GTP hydrolysis [6]. Melanosomes, which are lysosome-related organelles that store pigments, also interact with mitochondria [7]. These sites are associated with the process of melanogenesis [7]. MFN2 has been found at these areas of juxtaposition, and its knockdown reduces these interorganelle connections [7]. Peroxisomes and mitochondria interact through TOM20 in the mitochondria and ECI2 in peroxisomes. This interaction has functional implications in steroid biosynthesis in mouse Leydig cells [8]. Of all the mitochondrial contacts, those with ER are the best characterized to date, and some metabolic implications of those contacts have been also documented. The contacts between mitochondria and LDs or lysosomes are currently gaining insight and relevance and their potential metabolic implications are in the spotlight. In this review, we focus mainly on the molecular biology of mitochondria–ER, mitochondria–LD, and mitochondria–lysosome contacts and their involvement in metabolism.

Architecture of mitochondria–ER tethers

The structural scaffold of ER-mitochondria contact sites consists of proteins inserted in the outer mitochondrial membrane (OMM) that interact with those in the ER membrane. Available data indicate that ER bridging to mitochondria is governed by the following protein complexes (Fig 2): VAPB in the ER and PTPIP51 in mitochondria [9]; inositol 1,4,5-triphosphate receptors (IP3R1/2/3) in the ER and GRP75, together with VDAC1 in mitochondria [10]; BAP31 in the ER

1 Institute for Research in Biomedicine (IRB Barcelona), Barcelona Institute of Science and Technology (BIST), Barcelona, Spain

2 CIBER de Diabetes y Enfermedades Metabólicas Asociadas, Barcelona, Spain

3 Departamento de Bioquímica i Biomedicina Molecular, Facultat de Biologia, Universitat de Barcelona, Barcelona, Spain

4 Nestlé Institute of Health Sciences (NIHS), Lausanne, Switzerland

5 School of Life Sciences, Ecole Polytechnique Fédérale de Lausanne (EPFL), Lausanne, Switzerland

*Corresponding author. Tel: +34 93 40 37197; E-mail: antonio.zorzano@irbbarcelona.org

Glossary

ABHD5	1-acylglycerol-3-phosphate O-acyltransferase	MFN1	Mitofusin 1
ACSL1	Acyl-CoA synthase long chain family member 1	MFN2	Mitofusin 2
AgRP	Agouti-related protein	MiD49/51	Mitochondrial dynamics proteins 49 and 51
AKT	Protein kinase B	MOSPD2	Motile sperm domain containing 2
ATAD3A	ATPase family, AAA domain containing 3A	MPTP	Mitochondrial permeability transition pore
ATF4	Activating transcription factor 4	mRNA	Messenger ribonucleic acid
ATF6	Activating transcription factor 6	mtDNA	Mitochondrial deoxyribonucleic acid
ATG12	Autophagy related 12	mTORC1	Mammalian target of rapamycin complex 1
ATG14	Autophagy related 14	mTORC2	Mammalian target of rapamycin complex 2
ATG16L1	Autophagy related 16 like 1	mTOR	Mammalian target of rapamycin
ATC5	Autophagy related 5	OMM	Outer mitochondrial membrane
ATGL	Adipose triglyceride lipase	OPA1	Optic atrophy 1
BAK	Bcl-2 homologous antagonist/killer	ORP5	Oxysterol-binding protein-related protein 5
BAP31	B-cell receptor-associated protein 31	ORP8	Oxysterol-binding protein-related protein 8
BAT	Brown adipose tissue	OSBP	Oxysterol-binding protein
BAX	BCL2-associated X	OXPHOS	Oxidative phosphorylation
BCL2	Apoptosis regulator B-cell lymphoma 2	PACS2	Phosphofurin acidic cluster sorting protein 2
BECN1	Beclin 1	PC	Phosphatidylcholine
BioID	Proximity dependent biotin identification	PKD4	Pyruvate dehydrogenase kinase 4
BiP	Binding immunoglobulin protein	PDZD8	PDZ domain-containing protein 8
Ca²⁺	Calcium	PEMT	Phosphatidylethanolamine N-methyltransferase
Ccl2	C-C motif chemokine ligand 2	PE	Phosphatidylethanolamine
CDIP	Cell death-inducing p53-target protein 1	PERK	Protein kinase RNA-like endoplasmic reticulum kinase
CEBPA	CCAAT/enhancer-binding protein alpha	PI3K	Phosphatidylinositol-3-kinase
CHOP	CCAAT/enhancer-binding protein homologous protein	PI4P	Phosphatidylinositol 4-phosphate
CIDEA	Cell death-inducing DFFA-like effector a	PISD	Phosphatidylserine decarboxylase proenzyme
CYP11A1	Cytochrome P450 family 11 subfamily A member 1	PLIN1	Perilipin 1
CypD	Cyclophilin D	PLIN5	Perilipin 5
DRP1	Dynamin-related protein 1	POMC	Pro-opiomelanocortin
ECI2	Enoyl-CoA delta isomerase 2	PPARγ	Peroxisome proliferator-activated receptor gamma
eIF2α	Eukaryotic initiation factor 2 alpha	PS	Phosphatidylserine
ER	Endoplasmic reticulum	PSS1	Phosphatidylserine synthase-1
ERK	Extracellular signal-regulated kinase	PSS2	Phosphatidylserine synthase-2
ERLIN2	ER lipid raft associated 2	PTPIP51	Protein tyrosine phosphatase interacting protein 51
ERMES	ER-mitochondria encounter structure	RAB5	Ras-related protein Rab-5
FACL4	Fatty acid-CoA ligase 4	RAB7	Ras-related protein Rab-7
FDB	Flexor digitorum brevis	ROS	Reactive oxygen species
FGF21	Fibroblast growth factor 21	RYR1/2/3	Ryanodine receptors 1, 2, and 3
FIS1	Mitochondrial fission 1	SEC61	Protein transport protein Sec61
FUNDC1	FUN14 domain-containing protein 1	SERCA	Sarco/endoplasmic reticulum Ca ²⁺ -ATPase
GLUT4	Glucose transporter type 4	SLC	Solute carrier protein
GM1	Gangliosidosis-1	SMP	Synaptotagmin-like mitochondrial-lipid-binding domain
GRP75	Glucose-regulated protein 75	SNAP23	Synaptosomal-associated protein 23
GRP94	Glucose-regulated protein 94	SREBP1C	Sterol regulatory element-binding protein 1
GTPase	GTP hydrolase	STARD1/3/4	Steroidogenic acute regulatory lipid transfer domain proteins 1, 3, and 4
GTP	Guanosine 5'-triphosphate	StAR	Steroidogenic acute regulatory protein
H₂O₂	Hydrogen peroxide	START	StAR-related lipid transfer
HDL	High-density lipoprotein	STX17	Syntaxin 17
HFD	High-fat diet	TAG	Triacylglycerides
IL6	Interleukin 6	TBC1D15	TBC1 domain family member 15
IMM	Inner mitochondrial membrane	TCHP	Trichoplein
INF2	Inverted formin 2	TG2	Transglutaminase 2
IP3R1/2/3	Inositol 1,4,5-triphosphate receptors 1, 2 and 3	Tnfrα	Tumor necrosis factor alpha
IRE1α	Inositol-requiring enzyme 1 alpha	TOM20	Translocase of outer mitochondrial membrane 20
JNK	c-Jun N-terminal kinase	TOM22	Translocase of outer mitochondrial membrane 22
LC3	Microtubule-associated protein 1A/1B-light chain 3	TOM40	Translocase of outer mitochondrial membrane 40
LD	Lipid droplet	TOM70	Translocase of outer mitochondrial membrane 70
M1	Classically activated macrophages	TSP0	Translocator protein
MAM	Mitochondria-associated membranes	UCP1	Uncoupling protein 1
MAPK	Mitogen-activated protein kinase	UPR	Unfolded protein response
MCU	Mitochondrial calcium uniporter	VAMP4	Vesicle-associated membrane protein 4
MDV	Mitochondria-derived vesicle	VAPB	VAMP-associated Protein B
MEF	Mouse embryonic fibroblasts	VDAC1	Voltage-dependent anion channel 1
MEK	Mitogen-activated protein kinase kinase	VDAC2	Voltage-dependent anion channel 2
MERC	Mitochondria-ER contact sites	VDAC	Voltage-dependent anion channels
MFF	Mitochondria fission factor		

Glossary (continued)

VPS13A	Vacuolar protein sorting-associated protein 13 A	WASF3	Wiskott–Aldrich syndrome protein family member 3
VPS15	Vacuolar protein sorting-associated protein 15	WAT	White adipose tissue
VPS34	Vacuolar protein sorting-associated protein 34	XBP1	X-box binding protein 1
Vps39	Vacuolar protein sorting-associated protein 39	Ypt7	GTP-binding protein YPT7

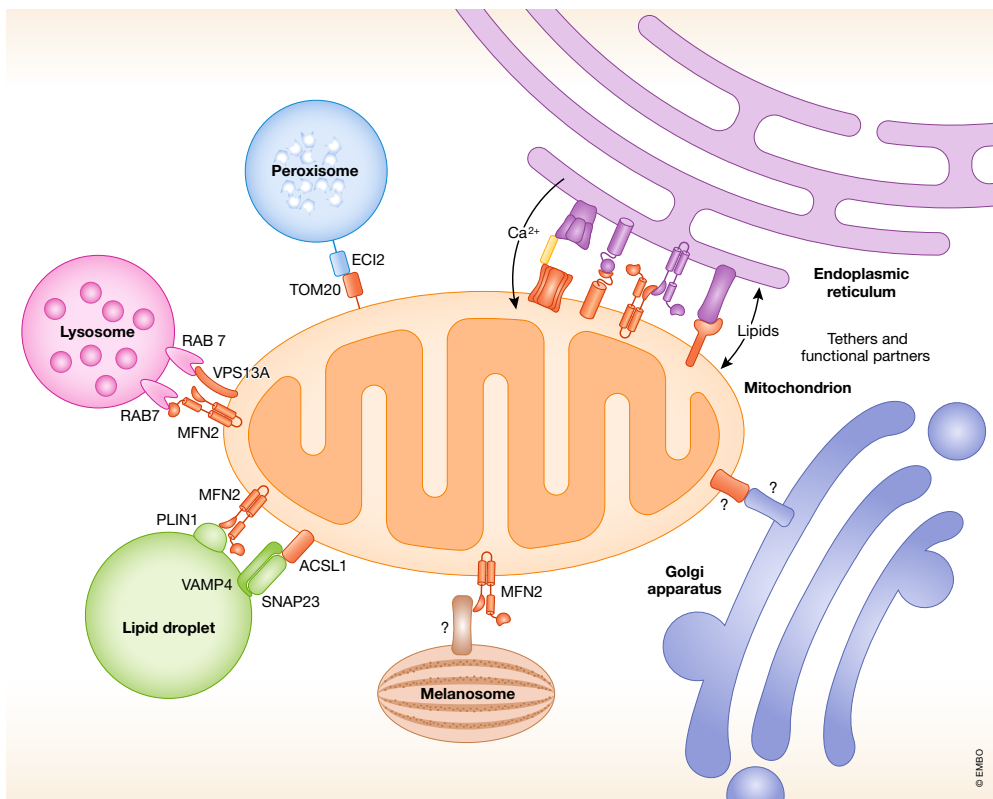


Figure 1. Contacts between mitochondria and other organelles.

Mitochondria interact with other membranous compartments in the cell. Mitochondria interact with the Golgi apparatus; however, the identities of the proteins involved in this interaction have not been discovered yet. Mitochondria are also in contact with lysosomes, but the mediators of these contacts remain unknown. MFN2 in mitochondria interacts with melanosomes. ECI2 and TOM20 bridge the peroxisome to the mitochondria. Mitochondria are anchored to lipid droplets by the MFN2–PLIN1 interaction. Mitochondria–ER contacts harbor a singular architecture and are hubs for several cellular processes such as Ca^{2+} signaling and lipid trafficking (see further details in Figs 2 and 3).

and FIS1 in mitochondria [11]; and MFN2 both in the ER and mitochondria [12]. These proteins not only shape mitochondria–ER contacts but also participate in the functions associated with these domains. PTPIP51 and VAPB are necessary to maintain Ca^{2+} transport between the ER and mitochondria [13]. Recently, MOSPD2 has

been proposed as a new tethering protein in the ER that interacts with PTPIP51 [14]. MOSPD2 is located at the contact sites of the ER with other organelles [14]. IP3Rs, GRP75, and VDAC1 form the gate through which Ca^{2+} leaves the ER and enters mitochondria [10]. These proteins are core components of a bigger complex specialized

in calcium channeling. Tethering capacity and calcium flux are sustained by the mitochondrial proteins PDK4 and TG2 [15]. The BAP31-FIS1 interaction is established at the MAM, upstream of apoptosis induction [11]. Moreover, this complex also participates in mitochondrial fission: FIS1 is a receptor for DRP1 in mitochondria, the major player in mitochondrial fission [16], and BAP31, once cleaved, is able to induce mitochondrial fission [17]. MFN2 is localized both in the mitochondria and in the ER, and in both cases, it is able to homo-oligomerize and to hetero-oligomerize with MFN1 to tether both organelles or to promote mitochondrial fusion [18,19]. Furthermore, the lack of MFN2 results in reduced mitochondrial Ca^{2+} uptake and in autophagosome formation arrest [12,20]. Although several studies argue that MFN2 is an organelle spacer [21,22], rather than a tether, we consider that the available data strongly support the role of MFN2 as a tether [12,23,24]. A recent study has suggested that another mitochondria-ER tethering complex could exist containing BiP in the ER membrane toward the ER lumen, WASF3 at the cytoplasm, and ATAD3A in the inner mitochondrial membrane (IMM) [25] (Fig 2). ATAD3A, WASF3, and BiP co-immunoprecipitate and silencing of *ATAD3A* downregulates BiP and WASF3 [25]. Given the location of these proteins in the cell, it is likely that they are part of a larger complex whose components remain undescribed.

Partial or total ablation of tethering proteins influences the architecture of mitochondria-ER contact sites. *GRP75* silencing decreases the interaction between IP3R1 and VDAC1 both in

HT22 mouse hippocampal neurons cells and in HuH7 human hepatocarcinoma cells [26,27]. This effect is also observed upon *MFN2* knockdown in HuH7 cells and H9c2 rat cardiomyoblasts [27,28]. *VDAC1* partial ablation diminishes the number of interaction spots between GRP75 and IP3R1 in HuH7 cells [27]. *IP3R1* silencing in hepatocytes does not alter the protein levels of the other IP3Rs [29]. *Pdk4* ablation in mice results in decreased MAM formation in skeletal muscle [15]. *Tg2* ablation in mouse embryonic fibroblasts (MEF) decreases the quantity of mitochondria-ER contact sites [30]. *Vapb* knockdown does not affect PTPIP51 expression or vice versa in NSC34 mouse motor neuron-like cells; however, it does reduce mitochondria-ER association [13]. In line with this, *Ptip51* silencing in rat neonatal cardiomyocytes reduces mitochondria-ER contacts [31]. Moreover, the downregulation of *Vapb* or *Ptip51* in NSC34 cells does not affect total MFN2 expression [13]. *MFN2* knockdown in human lung cancer H838 cells leads to an increase in ATAD3A localization to the MAM [32]. Both total and partial ablation of *Mfn2* in MEF cells increases the distance between the ER and mitochondria [23]. In agreement with this finding, in flexor digitorum brevis (FDB) muscles, mitochondria and ER apposition is reduced upon temporal *Mfn2* depletion [33]. It is likely that additional tethers or spacers will be identified in the future and that they will allow a more global view of the proteins involved in the maintenance of mitochondria-ER contacts. In addition, further studies are needed to determine whether the ablation of a single protein modifies the

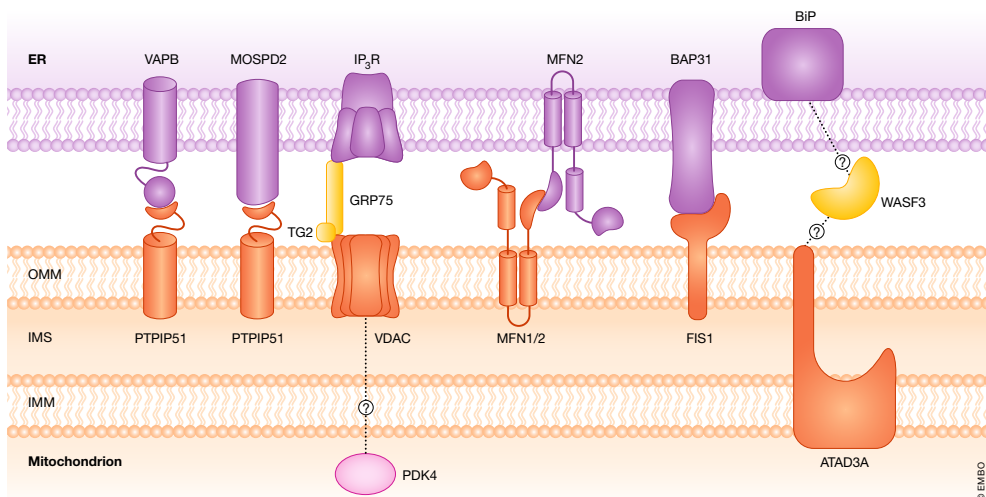


Figure 2. The architecture of mitochondria-ER contact sites: tethering complexes.

Mitochondria are bridged to the ER by several protein complexes. In the ER, VAPB or MOSPD2 bind to PTPIP51 in mitochondria. IP3R in the ER is anchored to VDAC in the OMM by the cytosolic protein GRP75. MFN2 is present both at the ER and in the OMM. From the ER, MFN2 interacts with either MFN1 or MFN2 in the mitochondria. BAP31 in the ER partners up with FIS1 in the mitochondria. BiP in the ER, WASF3 in the cytosol, and ATAD3A in the IMM have been suggested to form a complex that tethers both organelles.

expression of proteins or of genes involved in a different tether and to know whether these structures cooperate.

Functions linked to the mitochondria–ER contacts

The interface between ER and mitochondria harbors processes that are essential for the cell (Fig 3; Table 1). In this review, we have classified these processes in six groups: traffic of lipids, mitochondrial dynamics, Ca^{2+} signaling, ER stress, apoptosis initiation, and autophagosome formation.

Lipid trafficking

Intracellular lipid transport can occur by flip-flop from one side of a bilayer to the other, by vesicular trafficking, by lipid transfer proteins, or by diffusion within a bilayer [34]. MAMs are hubs for non-vesicular phospholipid and cholesterol transport, and this

process is linked to the synthesis of phospholipid and cholesterol intermediates. In this chapter, we analyze the progress in the traffic of lipids between ER and mitochondria and we highlight the remaining unexplored questions. Most of the advances so far have been obtained in cellular models, and *in vivo* assays would provide these findings with more robustness.

At the ER, phosphatidylcholine (PC) is converted into phosphatidylserine (PS) by PSS1 [35]. Mitochondria are not able to synthesize PS and therefore receive it from the ER [36,37]. The decarboxylation of PS in the mitochondria by PISD produces phosphatidylethanolamine (PE) [36,38]. This newly synthesized PE can then be translocated to the ER [37], where it is converted to PC by PEMT [39] or, less likely, to PS by PSS2 [35]. The discovery that newly synthesized PS and PE are transported between ER and mitochondria in a non-vesicular manner [37,40] was a key finding in the lipid trafficking field and an outstanding contribution to the understanding of the molecular biology of mitochondria and ER

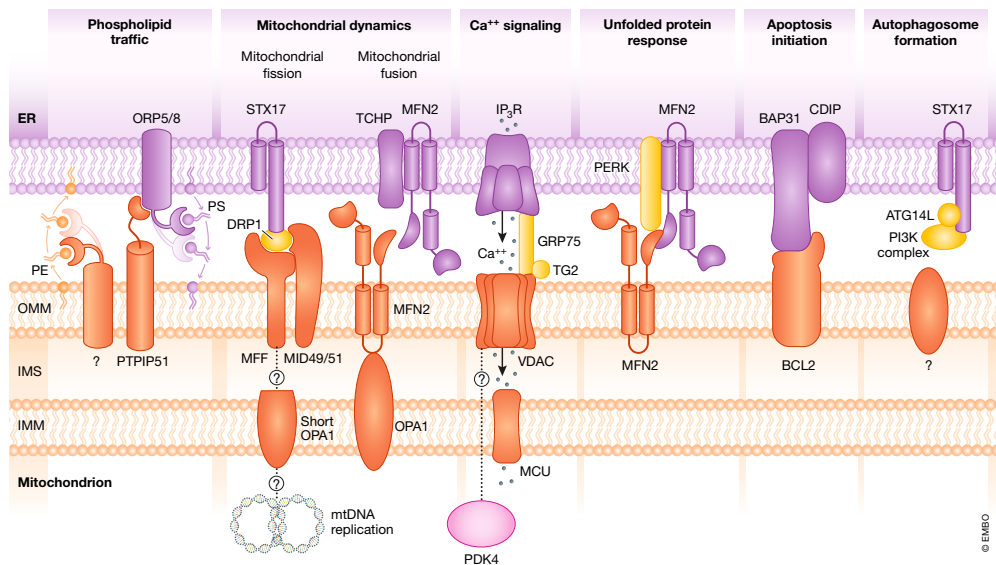


Figure 3. Cellular functions at mitochondria–ER contact sites.

The main processes that take place at the MAM are as follows: phospholipid trafficking, mitochondrial dynamics, Ca^{2+} signaling, unfolded protein response (UPR), apoptosis initiation, and autophagosome formation. MAMs are hubs for phospholipid exchange between the ER and mitochondria. Mitochondria take phosphatidylserine from the ER, which is supplied with phosphatidylethanolamine by mitochondria. Mitochondrial dynamics processes are regulated at the interface between the ER and mitochondria. The mitochondrial fission effector DRP1 is recruited by MFF and MID49/51 to the mitochondrial surface, and it interacts with STX17 in the ER membrane. The ER wraps around the mitochondrion, which is finally excised into two daughter mitochondria after mtDNA replication. Mitochondrial fusion is promoted by TCHP binding to MFN2. This interaction separates MFN2 tethers and promotes the fusogenic function of mitochondrion-bound MFN2. The ER is the cellular Ca^{2+} reservoir. IP3R, GRP75, and VDAC form a Ca^{2+} channelling complex that allows Ca^{2+} flux from the ER to mitochondria. MCU transports the intermembrane Ca^{2+} to the mitochondrial matrix. The UPR is regulated at the interface between mitochondria and the ER. One of the key regulators is MFN2, which inhibits the UPR by interacting with PERK. It is not known whether PERK interacts with MFN2 in mitochondria, MFN2 in the ER or with both. MAMs are also involved in the initiation of apoptosis. Sustained pro-apoptotic stimuli lead to BCL2 sequestration by the reticulum proteins BAP31 and CDIP in order to initiate apoptotic signaling cascades. Autophagosomes arise from mitochondria–ER contact sites. Proteins involved in autophagosome formation are recruited to these locations. STX17 in the ER attracts ATG14L and the PI3K complex. The mitochondrial component involved in this process is still not known.

Table 1. Mitochondria–ER contact sites proteins.

Protein	Location	Function in the MAM
ATAD3A	IMM	ER-mt tethering [25], lipid trafficking [52]
ATF6	ER	UPR [106]
ATG14	ER	Autophagosome formation [20]
BAK	OMM	Apoptosis [126]
BAP31	ER	ER-mt tethering [11], Apoptosis [11]
BAX	Cyt, OMM	Apoptosis [126]
BCL2	OMM	Apoptosis [126]
BiP	ER	ER-mt tethering [25]
CDIP1	ER	Apoptosis [126]
CypD	IMM	Apoptosis [125]
DRP1	OMM	Mitochondrial dynamics [252]
FIS1	OMM	ER-mt tethering [11], Mitochondrial dynamics [16], Apoptosis [11]
FUNDC1	OMM	Ca ²⁺ signaling [76], Mitochondrial dynamics [68]
GRP75	Mt	ER-mt tethering [10], Ca ²⁺ signaling [10]
INF2	ER	Mitochondrial dynamics [59]
IP3R	ER	ER-mt tethering [10], Ca ²⁺ signaling [10]
IRE1 α	ER	UPR [106]
MCU	IMM	Ca ²⁺ signaling [253]
MFF	OMM	Mitochondrial dynamics [62]
MFN1	OMM	ER-mt tethering [12], Mitochondrial dynamics [69]
MFN2	ER, OMM	ER-mt tethering [12], Mitochondrial dynamics [69], UPR [97]
MiD49	OMM	Mitochondrial dynamics [62]
MiD51	OMM	Mitochondrial dynamics [62]
ORP5	ER	Lipid trafficking [43]
ORP8	ER	Lipid trafficking [43]
PACS2	Cyt	ER-mt tethering maintenance [55]
PDZD8	ER	Lipid trafficking(?) [46]
PERK	ER	UPR [106]
PTPIP51	OMM	ER-mt tethering [9]
RyR	ER	Ca ²⁺ signaling [8]
SEC61	ER	Ca ²⁺ signaling [42]
SERCA1	ER	UPR [114]
STARD1	Cyt	Lipid trafficking [48]
STX17	ER	Autophagosome formation [20], Mitochondrial dynamics [65]
TSPO	OMM	Lipid trafficking [52]
VAPB	ER	ER-mt tethering [9]
VDAC1	OMM	ER-mt tethering [10], Ca ²⁺ signaling [10], Lipid trafficking [53]
WASF3	Cyt	ER-mt tethering [25]

apposition. It is not fully understood how PS is transported from the ER to mitochondria in mammalian cells; however, members of the oxysterol-binding protein (OSBP) family have been proposed to participate in this process. OSBP family proteins contain an OSBP-related ligand-binding domain that has the structure of a beta-barrel and binds PI4P and, in some cases, sterols [34]. Two members of this family, ORP5 and ORP8, localize at the ER

membrane facing the cytosol (Fig 3). ORP5 was first discovered to catalyze the exit of cholesterol from endosomes [41]. Later, it was found that ORP5 and ORP8 counter-exchange PS and phosphatidylinositol 4-phosphate (PI4P) between the ER and plasma membrane [42]. ORP5 and ORP8 are present at mitochondria–ER contact sites, where they interact with the tethering protein PTPIP51 [43] and could be responsible for PS transport to

mitochondria. In addition to the OSBP family, in yeast, the ERMES complex, which has no homology with any mammalian complex, tethers mitochondria to the ER and transfers PS from the ER to mitochondria [44]. Mmm1 and Mdm12, components of the ERMES complex, have been found to harbor an SMP domain that is responsible for phospholipid transfer [44,45]. This domain shows functional orthology with the SMP domain of mammalian proteins that localize at the ER, such as extended synaptotagmins and PDZD8 [45,46]. Expression of a chimeric form of Mmm1 containing the PDZD8 SMP domain in deficient *MMM1* yeast rescues mitochondrial defects. PDZD8 localizes at the ER fraction of MAMs [46]. The fact that PDZD8 harbors an SMP domain makes it a potential candidate for phospholipid exchange between the ER and mitochondria.

Sterols, oxysterol, and bile acids are synthesized in mitochondria. These molecules originate from cholesterol that is imported into mitochondria from several sources: ER, LD, and endosomes (reviewed by Elustondo *et al* [47]). Here, we focus on cholesterol transport from the ER, which is performed by STARD1 [48]. STARD1 contains a lipid binding domain known as START, which particularly in this protein has specificity for sterols [49,50]. In mitochondria-ER contact sites, STARD1 is recruited to the OMM where it forms a complex with the OMM proteins TOM22 and VDAC2 and the ER proteins BiP, ERLIN2, and SLC [48]. STARD1 incorporates ER-cholesterol into the OMM so that it can be transported to the IMM, where CYP11A1 further processes it [51]. The complex that moves cholesterol from the OMM to the IMM is formed by VDAC1 and TSPO in the OMM and by ATAD3A and CYP11A1 in the IMM [52]. STARD1 interacts with members of this complex, namely VDAC1 and TSPO [53], thus linking cholesterol incorporation from the ER to its processing in the mitochondrial matrix.

The modification of proteins involved in lipid trafficking in the MAM influences other protein complexes and functions that take place at the MAM, and it also affects the interaction between mitochondria and the ER. Moreover, the alteration of tethering proteins has an impact on lipid transport between the two organelles. *ORP5* and *ORP8* depletion from HeLa cells alters mitochondrial morphology and respiration; however, the number of mitochondria-ER contact sites is not affected [43]. Overexpression of *ORP5* and *ORP8* increases mitochondrial Ca^{2+} concentration in HeLa cells after histamine treatment, although depletion of these proteins does not alter Ca^{2+} signaling [54]. Also, when the tethering protein PTPIP51 is overexpressed in HeLa cells, the presence of *ORP5/8* at mitochondria-ER contact sites is increased [43]. However, it has not been assessed whether PS transport is increased upon PTPIP51 overexpression. Depletion of *PDZD8* leads to reduced contact surface between the ER and mitochondria and to reduced Ca^{2+} flux into mitochondria in HeLa cells [46]. The expression of a loss-of-function mutant of *PACS2*, a cytosolic protein involved in tether maintenance, in A7 human skin melanoma cells diminishes the levels of *PSS1* and *FACL4*, a fatty acid metabolism enzyme [55]. Regarding cholesterol trafficking proteins, *TSPO* downregulation is observed upon the deletion of the tethering protein *VDAC1* in U87 MG human glioma cells [56]. Furthermore, *TSPO* was demonstrated to inhibit mitochondrial Ca^{2+} uptake by promoting *VDAC1* phosphorylation [57]. The available evidence for the role of different proteins in lipid trafficking is limited to cultured cells, and further studies should be done to validate their function in the context of the whole animal.

Mitochondrial dynamics

Mitochondria change their morphology in order to efficiently adapt to the energetic demands of the cell, to respond to stress conditions (such as nutrient deprivation), or to react to apoptotic stimuli. Mitochondria-ER contacts are crucial for mitochondrial fission, since ER tubules surround and constrict mitochondria at the sites of division [58]. This constriction is mediated by actin filaments that accumulate between mitochondria and the ER and that are polymerized at the ER membrane by INF2 [59]. INF2-mediated actin polymerization leads to an accumulation of myosin type II [60], an increase in mitochondria-ER contacts, and the subsequent stimulation of mitochondrial Ca^{2+} uptake before constriction of the IMM and mitochondrial division [61]. The main driver of mitochondrial fission is the dynamin-related GTPase *DRP1*, which moves from the cytosol to the OMM, where it interacts with membrane proteins such as *FIS1*, *MFF*, *MiD49*, and *MiD51* [62]. *MFF*, *MiD49*, and *MiD51* recruit *DRP1* at the mitochondrial surface to form trimeric complexes in which *MiD49/51* compete with *MFF* for *DRP1* interaction [63]. *DRP1* activity can be regulated by redox signals. *PDIA1* modifies *DRP1* to negatively regulate its activity and to maintain mitochondrial reactive oxygen species (ROS) at low levels [64]. Conversely, an increase in mitochondrial ROS results in oxidation of *DRP1* and in increased mitochondrial fission which favors mitochondrial ROS accumulation [64]. However, further insight is necessary for a deep characterization of how redox states of cells influence mitochondrial dynamics. At mitochondria-ER contact sites, the ER protein *STX17* interacts with mitochondria-bound *DRP1* to support fission [65] (Fig 3). Under starvation conditions, *STX17* releases *DRP1* to initiate autophagosome formation and to promote the elongation of mitochondria to be protected from autophagy [65,66]. Recent findings have revealed that mitochondria-ER contacts are sites for mitochondrial DNA (mtDNA) synthesis and that nascent mtDNA stays in the daughter mitochondria after fission [67]. How the mitochondrial fission machinery is coupled to mtDNA replication has not been explained to date. Mitochondrial fission is a process coupled to mitochondrial removal by mitophagy. The link between these two processes is the OMM protein *FUNDC1*, which localizes at mitochondria-ER contact sites and interacts with calnexin in the ER and *DRP1* on the mitochondrial surface [68]. *FUNDC1* promotes both autophagosome recruitment and mitochondrial fission [68].

Furthermore, the interaction between the ER and mitochondria is a key player in the regulation of mitochondrial fusion. This process occurs first by fusion of the OMMs, followed by fusion of the IMM [69]. The key players in these two processes are the dynamin-like GTPases *MFN1* and *MFN2* in the OMM and *OPA1* in the IMM [69]. Mitofusins present in mitochondria interact with each other to fuse the OMMs. After OMM fusion, *OPA1* oligomerizes and IMM fuse. A cleaved isoform of *OPA1* is associated with mitochondrial fission rather than fusion [70]. It is still not clear how many *MFN1*, *MFN2*, and *OPA1* molecules oligomerize to carry out this function. Dimeric and tetrameric interaction models have been proposed [71–73]. As mentioned before, *MFN2* is present at both sides of the MAM, and it participates in mitochondria-ER tethering complexes [74]. These two roles of *MFN2* are mutually exclusive and determined by its interaction with *TCHP* (Fig 3). *TCHP*, a MAM protein localized at the ER, prevents mitochondria-ER tethering and favors mitochondrial elongation when it is bound to *MFN2* [74].

The alteration of mitochondrial dynamics proteins has an impact on MAM functions. Moreover, changes in certain tethering proteins alter mitochondrial morphology. Regarding the mitochondrial fission machinery, the induction of INF2-mediated actin polymerization with ionomycin in U2OS human osteosarcoma cells leads to an increase in mitochondrial Ca^{2+} and mitochondria-ER contact sites [61]. Moreover, the chemical inhibition of DRP1 in PC12 rat pheochromocytoma cells leads to a reduction in ER Ca^{2+} release compared to untreated cells and concomitantly decreases mitochondrial Ca^{2+} intake [75]. *Fundc1* overexpression in mouse cardiomyocytes increases Ca^{2+} release from the ER to mitochondria [76]. The role of FUNDC1 in Ca^{2+} release will be further assessed in this review. Concerning mitochondrial fusogenic proteins, the lack of MFN1 and MFN2 produces an aberrant distribution of pro-apoptotic proteins in the OMM, thus reducing apoptotic signaling [77]. *Mfn2* ablation in mouse hearts increases the levels of the anti-apoptotic protein BCL2 [78]. Loss of function of the tethering protein VAPB in *Caenorhabditis elegans* impairs mitochondrial dynamics [79], although this has not been reported in mammals to date. The depletion of the tether maintainer PACS2 in A7 cells results in mitochondrial fragmentation and uncoupling from the ER [55].

Ca^{2+} signaling

Before MAMs were studied at the molecular level, there was evidence that regions of mitochondria in close proximity to the ER participated in Ca^{2+} signaling [80]. The ER lumen is the cell Ca^{2+} storage area and the sites of proximity of the ER to mitochondria harbor high Ca^{2+} microdomains. The ER incorporates Ca^{2+} from the cytoplasm by SERCA1/2/3 ATPases [81,82]. ATP is hydrolyzed by SERCA transporters in order to allow Ca^{2+} entry to the ER lumen [81]. Ca^{2+} is released from the ER by the IP3R1/2/3 and the ryanodine receptors (RyR1/2/3), transferred to the mitochondrial intermembrane space by VDAC porins, and finally introduced into the mitochondrial matrix by the mitochondrial Ca^{2+} uniporter (MCU) complex (reviewed by Giorgi *et al* [83]). Ca^{2+} transport at the MAMs is depicted in Fig 3. In the OMM, TOM70 recruits IP3R to favor Ca^{2+} transference to mitochondria [84] and, in the cytosolic part of the MAM, GRP75 couples IP3Rs to VDAC [10], thereby allowing rapid Ca^{2+} flux into mitochondria. CypD, a protein involved in apoptosis initiation and in mitochondrial ATP synthase modulation [85], interacts with and maintains the VDAC1-GRP75-IP3R1 complex [28]. Another Ca^{2+} channel in the ER is the SEC61 complex, a translocon at the ER from which Ca^{2+} leaks passively to the cytosol [86,87], and once in the cytosol, it can be sequestered into mitochondria by VDAC. Ca^{2+} import to mitochondria stimulates the translocation of cristae accumulated H_2O_2 to MAMs, which results in the appearance of redox nanodomains at the mitochondria-ER interface which enhance Ca^{2+} efflux from the ER [88]. The accumulations of ROS at the MAMs arise as a consequence of active Ca^{2+} exit from the ER and do not occur with passive Ca^{2+} leakage. Mitochondrial ROS can regulate as well Ca^{2+} flux to the mitochondrial matrix by MCU oxidation, which increases the MCU oligomerization and thus its activity [89]. Insulin signaling modulates IP3R Ca^{2+} flux to mitochondria via mTORC2. After insulin stimuli, mTORC2 in the MAM phosphorylates AKT [90], which in turn phosphorylates IP3Rs to reduce Ca^{2+} release from the ER [91,92]. BiP limits ER Ca^{2+} leakage through the Sec61 complex by binding to the ER luminal region of Sec61 α [93].

Alterations in Ca^{2+} trafficking between the ER and mitochondria affect mitochondrial morphology. Mitochondria of brown adipose tissue (BAT) of mice fed on Ca^{2+} excess for 3 days are larger and fewer than in control mice [94]. MFN1 and MFN2 are increased in the BAT of these mice, whereas DRP1 is decreased [94]. Mitochondria-ER contacts are also increased in BAT after Ca^{2+} treatment [94]. Moreover, *MCU* ablation in U2OS cells prevents mitochondrial division [61]. In addition to its role in mitochondrial dynamics, FUNDC1 interacts with the ER Ca^{2+} channel IP3R2 and promotes Ca^{2+} flux to mitochondria [76]. The depletion of *Fundc1* in mouse cardiomyocytes and H9c2 myoblasts leads to a decrease in IP3R2 and colocalization between mitochondria and the ER [76]. The authors of this study proposed that FUNDC1 and IP3R2 act together as a tethering complex of mitochondria and the ER. FUNDC1 ablation also decreases the levels of the MAM maintenance protein PACS2 [76]. Inhibition of ER Ca^{2+} uptake by SERCA initiates UPR and eventually provokes apoptosis [95]. PDK4 inhibition decreases Ca^{2+} flux in C2C12 myoblasts [15]. *Tg2* ablation impairs Ca^{2+} flux in MEF [30]. The alteration of mitochondria-ER tethers also has an impact on Ca^{2+} trafficking [76]. Disruption of PTPIP51 and VAPB tethering complex impairs Ca^{2+} homeostasis in HEK293 cells [9]. The knock-down of either *VAPB* or *PTPIP51* decreases Ca^{2+} uptake into mitochondria [9], and overexpression of these proteins increases Ca^{2+} flux to mitochondria [96]. *MFN2* depletion has been reported to cause both increase and decrease in Ca^{2+} uptake [33,97]. In FDB muscles, mitochondrial Ca^{2+} uptake decreased upon temporal *Mfn2* depletion [33]. However, the protein levels of Ca^{2+} transport proteins (MCU, SERCA1, RyR1) remained unchanged [33]. In contrast to this result, *Mfn2* depletion in MEF cells caused Ca^{2+} overload in mitochondria [97].

ER stress

When protein folding efficiency is disturbed at the ER, misfolded proteins accumulate in the lumen and cause ER stress. This can happen as a result of certain conditions, such as nutrient deprivation, hypoxia, loss of Ca^{2+} homeostasis, free fatty acids, and GMI ganglioside accumulation [98–103]. Why stress conditions lead to protein misfolding remains unknown. The accumulation of large amounts of these misfolded proteins activates the unfolded protein response (UPR) in order to restore protein homeostasis or to induce apoptosis [104,105]. The UPR has three main branches, which are interconnected after the signal transducers in the ER, namely PERK, ATF6, and IRE1 α , have been stimulated [106]. What is known about UPR branches has been discovered by treating cells and animals with exogenous compounds or unphysiological harvesting conditions to provoke protein misfolding; nevertheless, the natural cause of protein folding defects and their accumulation is not known. The activation of PERK induces eIF2 α phosphorylation. Phosphorylated eIF2 α inhibits global protein translation and activates ATF4, which translocates to the nucleus to induce the expression of survival genes [107]. Prolonged UPR activation induces apoptosis through the activation of CHOP by ATF4 [108]. The ATF6 branch of the UPR starts with the translocation of ATF6 from the ER to the Golgi apparatus for cleavage [109]. Cleaved ATF6 is a transcription factor that induces ER-associated degradation genes [110] and XBP1 [111]. IRE1 α activation induces splicing of XBP1 mRNA to enhance cell survival [111], activation of MAPK [112] to modulate autophagy and apoptosis, and IRE1 α -dependent mRNA decay [113]. ER stress

signaling can be amplified at MAMs by SERCA1 truncated isoform (ER), which acts upstream of the PERK-eIF2 α -ATF4-CHOP pathway [114]. Moreover, the location of PERK at MAMs contributes to the maintenance of mitochondria-ER contact sites and to the enhancement of ROS-mediated mitochondrial apoptosis signaling [115]. UPR mission is to restore cellular homeostasis by correcting protein folding and recovering damaged ER environment [116]. As long as protein folding efficiency is not resolved, UPR is activated [116]. ER stress results in increased mitochondria coupling to ER, which increases ATP production, oxygen consumption, and mitochondrial Ca²⁺ uptake [117]. Chronic UPR signaling initiates a signaling cascade in the MAM that eventually leads to apoptosis [116]. This signaling pathway is discussed in the following section.

The alteration of ER stress proteins, especially the IRE1 α branch, impairs lipid handling. The hepatic depletion of *Xbp1* in mice decreases circulating levels of fatty acids, triglycerides, and sterols, compared to control mice [118]. Lack of XBP1 in the liver impairs cholesterol processing for the generation of bile acids in these mice [119]. This phenotype is recovered by overfeeding the mice with cholesterol [119]. A separate study using liver *Xbp1* knockout mice also reports decreased plasma levels of cholesterol and triglycerides compared to control mice [120]. This effect is prevented by knocking down IRE1 α [120]. The modification of mitochondria-ER tethering proteins leads to ER stress. MFN2 interacts with PERK and represses its activity [97]. MFN2 loss of function in MEF cells dysregulates the three branches of the UPR by enhancing the PERK-eIF2 α -ATF4-CHOP pathway [97]. Ablation of *Mfn2* results in the continuous activation of PERK, and PERK silencing in these cells causes ROS production, the restoration of mitochondrial Ca²⁺ levels, and an improvement of mitochondrial morphology [97]. However, it is not known whether PERK interacts with mitochondrial MFN2, ER MFN2, or both (Fig 3). The increase in mitochondria coupling to ER upon ER stress [117] is coherent with the upregulation of MFN2 expression observed in MEFs upon ER-stress induction with thapsigargin and tunicamycin [121]. In the same study, the authors show that ablation of *Mfn2* in MEFs upregulates ER stress markers (BiP, GRP94, and ATF4) [121]. Specific ablation of *Mfn2* in mouse cardiac myocytes also causes an increase in the expression of BiP, GRP94, and ATF4 [121]. Another tethering protein, VAPB, represses the UPR by binding to ATF6 [122]. Overexpression of *VAPB* both in HEK293 and NSC34 cells decreases ATF6/XBP1-induced luciferase activity upon tunicamycin stimulation, even in combination with ATF6 overexpression [122].

Apoptosis initiation and ER stress-mediated apoptosis

When cells cannot adequately handle certain stress stimuli, they activate pathways that lead to cell death. A complex formed by BAP31 and FIS1 at mitochondria-ER contact sites is able to transfer apoptotic signals back and forth from the mitochondria to the ER [11]. In response to apoptotic stimulus, the FIS1-BAP31 complex recruits procaspase-8 to be activated [11]. Active caspase 8 cleaves BAP31 into a pro-apoptotic form that, together with FIS1, promotes Ca²⁺ release from the ER [11,123] and mitochondrial fission [17]. Mitochondrial Ca²⁺ increase leads to CYPD activation in the IMM to open the permeability transition pore from which molecules that drive apoptosis are released [124,125]. Under sustained ER stress conditions, CDIP and BAP31 interact at the ER side of the MAM to

sequester the anti-apoptotic factor BCL2 located at the OMM, in order to promote apoptosis (Fig 3) [126]. The protein PACS2, which localizes in MAMs, has been reported to promote the translocation of the pro-apoptotic protein BID to mitochondria [55]. The CDIP1-BAP31-BCL2 complex, together with the truncated form of Bid and caspase-8 activation, promotes BAX and BAK oligomerization [126]. BAX translocates from the cytosol to the OMM, where BAK locates constitutively. The activation of these two molecules occurs after their oligomerization [127]. Although not yet demonstrated, it is believed that cytochrome *c* exits mitochondria from the pores formed by these oligomers [128]. After cytochrome *c* release, an apoptotic protease cascade is initiated [129].

Since MAMs are hubs for apoptosis initiation and this process involves Ca²⁺ signaling at the MAM and mitochondrial fission, the alteration of some apoptosis initiators has an impact on these MAM functions. *BCL2* loss-of-function mutations in Jurkat T cells decreases mitochondrial Ca²⁺ uptake [130]. When *Bak* is knocked out in MEF cells, mitochondria are not fragmented in response to apoptotic stimulus [131]. Overexpression of *Bax* promotes MFN2-mediated mitochondrial fusion in MEFs [132]. It has been proposed that BAX plays a dual role: The soluble cytoplasmic form promotes mitochondrial fusion and, when activated and recruited to the OMM, it participates in apoptosis [132].

Autophagosome formation

In order to preserve cellular homeostasis, damaged or unnecessary components of the cell must be degraded or recycled. This process is achieved by autophagy. Autophagosomes engulf damaged or needless components and can originate from ER-mitochondria contact sites [20]. The ER side of the MAM region, where proteins related to autophagosome formation start to accumulate, is known as the isolation membrane. This structure protrudes from the ER and finally closes around the cellular components to be eliminated, forming a vesicle named the autophagosome [133]. After starvation stimulus, ATG14 is recruited to the MAM by STX17 [20]. This results in accumulation of the components of the class III PI3K complex (ATG14, BECN1, VPS34, and VPS15) at the MAM [20] (Fig 3) and contributes to the initiation and nucleation of the isolation membrane. Next, the ATG16L1 complex (ATG5-ATG12-ATG16L) is recruited to the isolation membrane, where it binds PE to LC3 [134]. Lipidated LC3 molecules associate with the isolation membrane and remain attached once the autophagosome is closed [133]. How the isolation membrane closes is still poorly understood.

Alterations in tethering proteins have an impact on autophagosome formation. The absence of MFN2 or PACS2 at the MAM impedes STX17-mediated ATG14 recruitment to this area in HeLa cells [20]. MFN2 and PACS2 seem to be crucial for autophagosome biogenesis; nevertheless, their role in this process has not been described yet. Moreover, the tightening of mitochondria-ER contact sites by overexpression of *VAPB* and *PTPIP51* results in decreased autophagosome formation after torin-1 or rapamycin stimulus in HeLa and HEK293T cells [135]. Conversely, the opposite effect is observed when *PTPIP51* and *VAPB* are ablated in HeLa and HEK293T cells [135]. Future work will unravel what is the precise role of the MAM in autophagosome formation and which MAM proteins recruit the autophagosome biogenesis machinery. Moreover, since membrane contact sites from other

organelles have also been proposed as autophagosome factories [20,136–138], a remaining open question in the field is whether autophagosomal content to be degraded is influenced by the origin of the autophagosome.

Consequences of metabolic challenge in mitochondria–ER contacts

Human, animal, and cellular studies have revealed that metabolic alterations can perturb mitochondria–ER contact sites. In this section, we review the observations that document the impact of altered metabolic homeostasis on the architecture and functioning of MAMs, and also the impact of nutrient availability and lysosomal storage disorders.

The impact of metabolic disorders on the architecture and functioning of mitochondria–ER contacts

Some studies have reported alterations in mitochondria–ER contacts in liver and in muscle cells upon metabolic dysregulation. Surprisingly, there is considerable discrepancy in the data available. Thus, liver analysis of ob/ob obese mice and mice subjected to a high-fat diet (HFD) showed an increased abundance of MFN2, IP3R, and PACS2 in MAM fractions, in parallel to increased mitochondria–ER contacts, and an excess of mitochondrial Ca^{2+} accumulation [29]. Moreover, a forced increase in the mitochondria–ER contacts, induced by expression of an artificial linker in livers from control mice, caused an increased mitochondrial Ca^{2+} uptake and impaired glucose homeostasis [29]. Conversely, *Ip3r1* knockdown in obese mice caused a reduced Ca^{2+} flux, and similarly, *Pacs2* knockdown led to a decreased physical interaction between the ER and mitochondria, and to improved glucose homeostasis [29].

In contrast to the results obtained by Arruda *et al*, Tubbs *et al* [27] detected that mitochondria–ER contacts (measured by quantifying VDAC1–IP3R1 interaction) were decreased in hepatocytes isolated from mice subjected to diet-induced diabetes and from ob/ob mice. Moreover, the overexpression of *CypD* in these hepatocytes increased mitochondria–ER contacts and improved the effects of insulin. A third study revealed that HepG2 hepatoma cells treated with palmitate showed reduced mitochondrial Ca^{2+} flux, lower mitochondria–ER contacts, and impaired insulin sensitivity [139]. Under these conditions, *Mfn2* overexpression ameliorated the mitochondria–ER contact area and insulin sensitivity. We do not yet know whether the opposite observations are a consequence of differences in the methodology used (proximity ligation assays or transmission electron microscopy, or tissue sections versus isolated hepatocytes), or whether they are based on subtle differences in the nutritional state of the animals studied. Regarding the impact of metabolic alterations in liver ER stress and ER Ca^{2+} homeostasis, the main studies of the field show more consensus. Livers of obese mice show increased ER stress [140,141] and reduced cellular SERCA2b levels [140] or impaired SERCA activity in the ER [141]. Glucose tolerance was increased and ER stress was alleviated in obese and diabetic mice by liver exogenous expression of SERCA2b [140,141].

In the skeletal muscle of ob/ob mice or in mice subjected to a high-fat, high-sucrose diet, Tubbs *et al* found impaired insulin

signaling and decreased levels of MAM proteins, accompanied by a decrease in mitochondria–ER contacts (measured by quantifying VDAC1–IP3R1 interaction). In human myotubes from healthy patients, mitochondria–ER contacts were also diminished after palmitate treatment [142]. Mitochondrial Ca^{2+} concentration was somewhat decreased compared to untreated cells. *Mfn2* or *Grp75* overexpression reversed the effects of palmitate on MAM proteins and on insulin signaling [142]. Moreover, myotubes from obese patients and from obese patients with type 2 diabetes showed decreased mitochondria–ER contacts compared to those of healthy patients [142]. In contrast to these results, Arruda *et al* [29] found an increase in the MAM proteins MCU and RyR in soleus muscles from ob/ob and HFD-fed mice, suggesting an enrichment in MAMs under these conditions. In line with these results, Thoudam *et al* [15] found increased levels of IP3R1, VDAC1, and GRP75 in the MAM fraction of skeletal muscle of HFD-fed mice and ob/ob mice. Furthermore, they observed increased levels of MFN2 in HFD-fed mice. Moreover, using proximity ligation assays, they detected increased IP3R1–GRP75–VDAC1 interactions in HFD-fed mice and ob/ob mice [15]. Transmission electron microscopy of muscle MAM surface revealed increased MAM area in HFD-fed mice compared to animals on a chow diet [15]. Interestingly, the authors quantified the distance between juxtaposed ER and mitochondria and found that in HFD-fed mice the proportion of loose contacts between the ER and mitochondria was increased. As mentioned in the liver studies, we do not know whether the differing observations detected in muscles of obese mice are due to differences in the methodology used or to differences in the nutritional state of the animals studied. In any case, further studies are required to clarify the nature and kinetics of the changes that occur in mitochondria–ER contacts during metabolic dysregulation in muscle and in liver.

Insulin-resistant conditions such as obesity and type 2 diabetes are characterized by altered muscle expression of MFN2, which may participate in the alterations in mitochondria–ER contacts. Thus, *Mfn2* is repressed in the muscles of obese Zucker rats [143]. Obesity induced by a HFD during 40 weeks also reduces MFN2 and MFN1 expression in muscle [144]. In addition, the muscles of obese subjects also show a reduced expression of MFN2 compared with lean subjects [143,145]. In contrast, bariatric surgery-induced body weight loss was reported to increase *MFN2* gene expression in the skeletal muscle of morbidly obese subjects [146–148] in parallel with increased insulin sensitivity [146–148]. Type 2 diabetic patients also show reduced MFN2 expression in the skeletal muscle compared with control subjects [145,149], and this occurs both in obese and non-obese type 2 diabetic patients [145]. The dysregulation of *MFN2* is unlikely to be a consequence of reduced insulin action because the expression of this gene in lean, obese, or type 2 diabetic subjects is not altered in response to 3 h of hyperinsulinemia during clamp studies. Neither is the expression of this protein affected when cultured muscle cells are chronically incubated in the presence of insulin [145,150]. Induced insulin resistance in rats by high sucrose diet provokes slower contraction and elongation of cardiomyocytes [151]. ER Ca^{2+} uptake by SERCA is impaired in these cardiomyocytes although the levels of this protein remain unchanged [151].

Studies in beta-cells also indicate the existence of alterations in response to metabolic stress. Thivolet *et al* [152] reported an

increased IP3R2 and decreased VDAC1 expression, accompanied by reduced mitochondria-ER contact sites in beta-cells from type 2 diabetic patients. In addition, Min6-B1 beta-cells exposed to palmitate show ER stress, reduced mitochondria-ER contacts, and impaired insulin secretion [152]. Zhang *et al* [153] reported increased VDAC1 abundance accompanied by mislocalization of part of VDAC1 to the plasma membrane. INS1E beta-cells also respond to elevated glucose concentrations in the culture medium by upregulating VDAC1 [154]. High glucose environment increases *Bax* mRNA levels and stimulates BAX-dependent apoptosis in mouse islets [155].

POMC neurons respond to a HFD by reducing the number of mitochondria-ER contacts compared to mice on a regular diet [156]. Under these conditions, MFN2 levels are reduced in HFD mice [156]. In HFD-fed mice, stimulation of DRP1-dependent mitochondrial fission in the dorsal vagal complex induces ER stress and insulin resistance [157], and inhibition of DRP1 restores ER stress, insulin resistance, and hepatic glucose metabolism.

An increase in mitochondria-ER contacts, increased expression of IP3R1, IP3R2, and PACS2 protein levels, and greater mitochondrial Ca^{2+} uptake and apoptosis has been documented in oocytes from HFD-treated mice [158]. These changes compromise oocyte maturation.

In conclusion, available data suggest that metabolic stress linked to insulin resistance, obesity, or type 2 diabetes affects mitochondria-ER contacts, and may occur in various cells or tissues. Liver and muscle have been deeply analyzed in this context, and the observations annotated by the authors differ across the studies that we have discussed. Whether the consequence of this metabolic stress in liver and muscle is to increase or to reduce the surface of contact between the ER and the mitochondria is still under debate. Moreover, current data regarding the expression levels of the tethering proteins MFN2, IP3R, VDAC, and GRP75 under conditions of insulin resistance, obesity, or type 2 diabetes annotated across several studies are not uniform. As a consequence, the functional impact of the modification of these contacts is not known. An example that illustrates this lack of consensus is the persistent discrepancy on the observations regarding Ca^{2+} influx into mitochondria under metabolic stress conditions. In order to solve this puzzle, there is need of a precise characterization of the molecular mechanisms involved in the response to metabolic stress as well as the establishment of standard procedures to perform this characterization.

The adaptation of mitochondria-ER contact sites to nutrient availability

Mitochondria-ER contact sites respond to changes in nutrient availability by modifying Ca^{2+} signaling, initiating autophagy or activating the UPR. The first evidence for this response was observed by Sood *et al* [159] in postprandial mouse livers. Five hours postprandial livers showed larger mitochondria-ER contact sites than 2 h postprandial livers. In agreement with this study, livers of fed mice show reduced mitochondria-ER contacts compared to those of overnight fasted mice, and this occurs without a significant modification of the ER or mitochondrial content [160]. The interactions between VDAC1 and IP3R1 are reduced in fed compared to fasted mice. VDAC1 and GRP75 are also decreased upon feeding in mouse liver, whereas IP3R1 protein expression remains unchanged [160]. In a different study, mice

refed after 22 h of fasting showed a 50% decrease in hepatic IP3R1 levels compared to fasted animals [161]. Interestingly, primary hepatocytes cultured in the presence of high glucose (17 mM) also show a reduced VDAC1-IP3R1 interaction compared to cells cultured in the presence of 5 mM glucose. In conclusion, these data suggest that glucose availability is a key signal in the regulation of mitochondria-ER contacts in liver cells.

Genetic obesity appears to alter the dynamics of mitochondria-ER contacts. Thus, the livers of obese ob/ob mice do not reproduce the mitochondria-ER uncoupling during fed to fasted transition. MAMs are reduced in fasting conditions in ob/ob compared to lean mice, and no differences are detectable compared to obese mice analyzed during fed conditions [160]. Moreover, the interaction between IP3R1 and VDAC1 is reduced in fasted ob/ob mice compared to lean mice and no significant differences are observed in ob/ob mice when comparing fed and fasted states [160]. In keeping with these data, ob/ob hepatocytes cultured in the presence of high glucose do not show a reduced VDAC1-IP3R1 interaction compared to cells cultured in the presence of 5 mM glucose, again indicating that obesity disrupts glucose-induced control over mitochondria-ER contacts.

Nutrient deprivation causes the inhibition of mTOR activity, which activates autophagy [162] and promotes the formation of autophagosomes. In this regard, autophagosomes originate at mitochondria-ER contact sites [20], and the disruption of MAMs by depletion of *Mfn2* or *Pacs2* results in impaired autophagosome formation [20,163]. Moreover, glucose and amino acid deprivation causes mitochondrial elongation [66], which occurs through inhibition of DRP1 and activation of MFN1, thus protecting mitochondria against autophagic degradation. In all, available data allow us to propose that the modulation of mitochondria-ER contact sites is linked to the modulation of autophagosome formation and mitochondrial morphology through mechanisms that require extensive research efforts. It is likely that signals such as mTOR, and ER stress response, which are modulated by nutrient availability [164,165], participate in mitochondria-ER contacts during fed to fasted transitions.

In summary, ER and mitochondria contact surface increases in response to lack of nutrients. This adaptive increase in contact sites is impaired under obesogenic conditions. However, it is still uncertain whether these changes in the MAM are accompanied by a modification in the expression levels of tethering proteins. Enhanced autophagosome formation and ER-stress response are probably the functional consequences of MAM enlargement.

Metabolic impact of alterations in proteins participating in mitochondria-ER contacts

The concept that metabolic homeostasis is determined by modulation of mitochondria-ER contact sites arose after several reports documenting that *Mfn2* deficiency disrupts metabolism in cells and in animal models [97,156,166,167]. In addition, the metabolic effects caused by *Mfn2* deficiency differ to those detected upon *Mfn1* ablation, thereby indicating that they are probably due to compromised mitochondria-ER contacts rather than to impaired mitochondrial fusion. Subsequent mouse studies have revealed that ablation of proteins participating in mitochondria-ER contacts

causes three distinct phenotypes, namely (i) reduced glucose tolerance and insulin signaling; (ii) improved glucose tolerance; and (iii) disrupted lipid metabolism. In this chapter, we analyze the data currently available with respect to these three categories (Fig 4).

Proteins whose depletion causes deficient insulin signaling and glucose intolerance

There is extensive evidence of a major metabolic role of MFN2 in mouse tissues. Thus, muscle-specific ablation of *Mfn2* causes age-dependent glucose intolerance and deficient insulin signaling [166,167] (Fig 4A). *Mfn2*-deficient muscles also show reduced muscle autophagy, muscle atrophy, and loss of muscular function [167]. *Mfn2* repression in cultured muscle cells also reduces insulin signaling [142].

Mfn2 deficiency in liver is also associated with disrupted insulin signaling, enhanced hepatic glucose production, enhanced expression of gluconeogenic genes, and glucose intolerance [166]. *Mfn2* repression also reduces insulin signaling in human liver cells [27]. Notably, the phenotype linked to *Mfn2* deficiency is opposite to what occurs in mice upon ablation of *Mfn1*, which show protection against HFD-induced insulin resistance, and enhanced mitochondrial respiration [168]. These observations suggest that the mechanisms linked to *Mfn2* deficiency are not a consequence of alterations in mitochondrial fusion but are rather linked to its tethering function. *Mfn2* ablation in adipose tissues obtained by crossing *Mfn2^{loxP/loxP}* mice with mice expressing the Cre recombinase under the adiponectin promoter leads to enhanced body weight and fat mass, which was linked to a reduction in energy expenditure and in BAT thermogenesis [3]. In keeping with these data, BAT-specific *Mfn2* deletion through *Ucp1*-Cre causes BAT lipohypertrophy and cold intolerance [169]. The effects linked to *Mfn2* ablation in adipose depots are not detected upon ablation of *Mfn1* [3]. These findings thus support the notion that the alterations detected in BAT are not dependent on mitochondrial fusion, but on a different function of MFN1 and MFN2.

Specific ablation of *Mfn2* in pro-opiomelanocortin (POMC) neurons of the hypothalamus results in defective POMC processing, leptin resistance, hyperphagia, reduced energy expenditure, and obesity [156]. These data establish MFN2 in POMC neurons as an essential regulator of systemic energy balance. Along the same lines, interfering with mitochondrial fusion mechanisms in *Agrp* neurons by selectively knocking down *Mfn2* results in altered mitochondrial size and density in these cells. *Agrp*-specific *Mfn2* knockout mice gain less weight when fed a HFD due to decreased fat mass [170]. Available data in POMC neurons also indicate that the effects caused by *Mfn2* ablation differ greatly from what is detected for *Mfn1* ablation. Thus, mice lacking MFN1 in POMC neurons exhibit attenuated hypothalamic gene expression programs during the fast-to-fed transition [171]. This loss of mitochondrial flexibility in POMC neurons alters glucose sensing, causing abnormal glucose homeostasis as a result of defective insulin secretion by pancreatic β cells [171]. In conclusion, available data in conditional knockout mouse models indicate that *Mfn2* ablation causes defects in metabolism that are very different to those effects that result from ablation of *Mfn1*. These observations are compatible with MFN2 exerting metabolic effects in tissues via modulation of the mitochondria-ER contact sites.

In connection with the effects of the ER triggered by *Mfn2* deficiency, a potent UPR has been documented both in cells and in tissues [97,156,166]. Thus, *Mfn2* ablation in liver or in skeletal muscle causes chronic activation of the UPR, which involves the three UPR arms, i.e., the PERK, IRE-1 α , and the ATF6 pathways [166]. Furthermore, treatment of liver-specific *Mfn2* knockout mice with an ER stress blocker restores insulin sensitivity and glucose homeostasis [166], thereby suggesting that the functional link between MFN2 and the UPR has metabolic relevance.

Ablation of *GRP75*, the bridge between IP3R and VDAC, has been reported to cause a reduction in VDAC1/IP3R1 interactions in human liver cells and in myotubes [27,142]. Moreover, *GRP75* deficiency reduces insulin signaling and insulin action in HuH7 liver cells [27,142] (Fig 4A). The depletion of *GRP75* in medullary thyroid carcinoma cells induces the MEK/ERK pathway and increases oxidative stress [172]. Both in *GRP75* knockdown SH-SY5Y bone marrow neuroblasts and in fibroblasts derived from a Parkinson's disease patient with *GRP75* loss of function, increased mitochondrial UPR (UPR^{MT}) was reported [173].

Hepatocyte-specific deletion of the tethering protein BAP31 is linked to metabolic defects in mice. *Bap31*-deficient mice show enhanced body weight, increased food intake, and greater liver steatosis after exposure to a HFD [174]. Another study with these mice reported the same effects upon tunicamycin treatment, as well as increased levels of ER-stress markers [175]. In *Bap31*-deficient mice, although not statistically significant, a trend toward increased p-*eIF2 α* , ATF4, and CHOP signaling was observed [175]. Moreover, hepatocytes of these mice show increased lipogenic gene expression and SREBP1C expression, and activation of SREBP signaling. *Bap31*-deficient mice show impaired glucose tolerance and reduced insulin responsiveness under normal diet or a HFD challenge (Fig 4A).

Depletion of the modulator of the permeability transition pore, *CypD*, in mice has been reported to enhance hepatic gluconeogenesis, as assessed by the pyruvate tolerance test [27]. In addition, *CypD* deficiency is associated with deficient insulin signaling and a reduced number of VDAC1/IP3R1 interactions in human liver cells [27]. The metabolic effects detected under conditions of *CypD* deficiency in mice and in human liver cells were characterized by UPR^{ER} [176]. In conclusion, these data are coherent with a model in which CYPD plays an important role in the maintenance of mitochondria-ER contact sites, which, upon dysregulation, trigger ER stress and metabolic alterations, namely deficient insulin signaling and insulin resistance (Fig 4A).

A shared feature of the absence of MFN2, GRP75, BAP31, or CYPD is the activation of UPR [97,156,166,173,175,176]. ER stress was initially proposed as a mechanism that drives insulin resistance-related diseases [177], and altered reticulum proteostasis alteration has also been in the spotlight as a possible driver of metabolic diseases [178]. Insulin resistance observed upon ablation of MFN2, GRP75, BAP31, or CYPD may arise as a result of altered mitochondria and/or ER protein homeostasis. The signaling pathways activated upon loss of protein homeostasis in both organelles converge in ATF4 and CHOP upregulation [179,180]. JNK activation is as well a consequence of ER stress that impairs insulin signaling, eventually leading to insulin resistance [177]. ER stress provokes hyperactivation of JNK, which phosphorylates and inhibits the insulin receptor IRS1 [177]. MFN2, BAP31, and CYPD ablation provoke an increase in activated JNK [156,175,176]; however, there

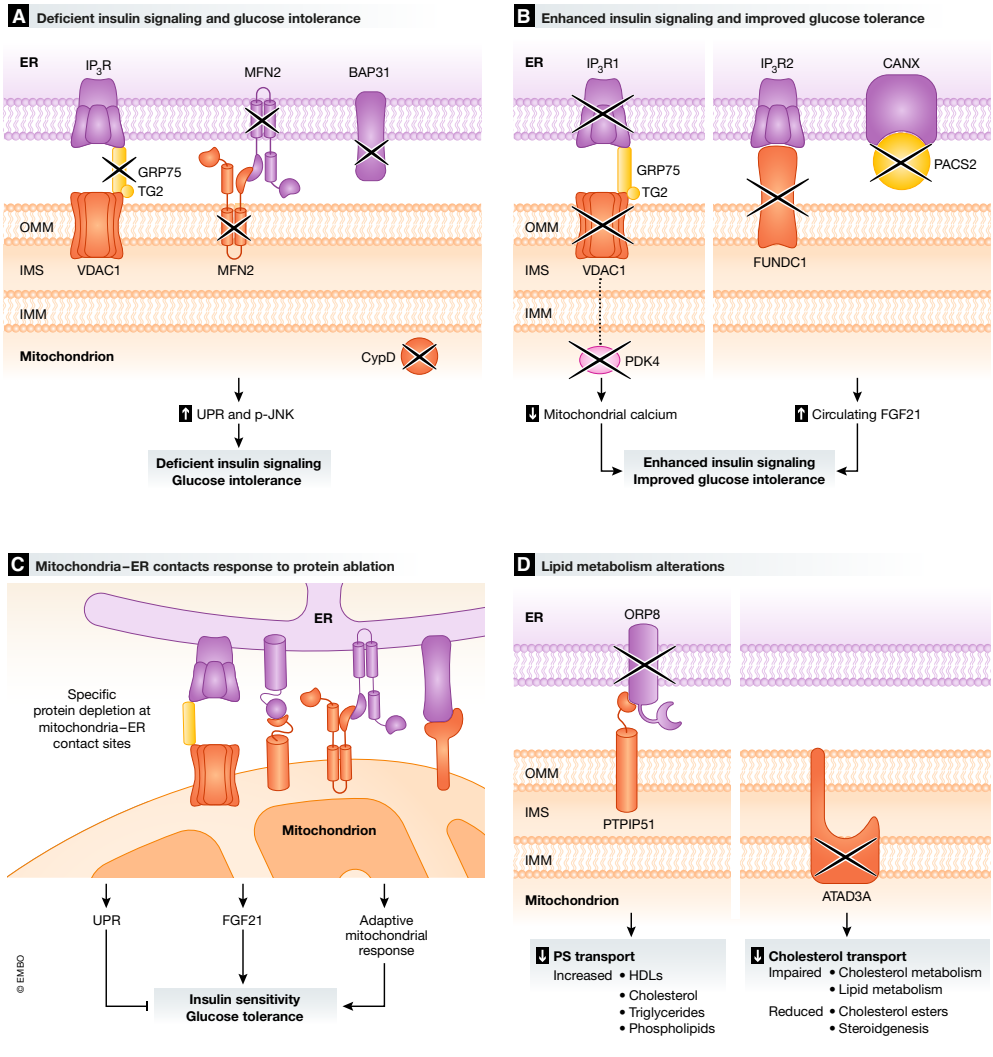


Figure 4. Metabolic impact of alterations in proteins participating in mitochondria-ER contacts.

(A) GRP75, MFN2, BAP31, or CypD depletion leads to deficient insulin signaling and glucose intolerance. The lack of GRP75, MFN2, BAP31, or CypD at mitochondria-ER contact sites causes deficient insulin signaling and glucose intolerance, probably through a mechanism that involves ^{ER}UPR or ^{MM}UPR. (B) IP3R1, VDAC1, FUNDC1, or PACS2 ablation results in enhanced insulin signaling and improved glucose tolerance. The lack of IP3R1, VDAC1, FUNDC1, or PACS2 at mitochondria-ER contact sites potentiates insulin signaling and improves glucose tolerance. The mechanism by which FUNDC1 or PACS2 causes these effects is mediated by the release of FGF21. As a result of decreased mitochondrial Ca²⁺ accumulation, IP3R1 or VDAC1 ablation may result in enhanced insulin signaling and improved glucose tolerance. (C) Mitochondria-ER contacts response to protein ablation. The deletion of proteins that participate in the MAM results in the activation of signaling pathways that either enhance or impair insulin sensitivity and glucose tolerance. It has been proposed that these signaling pathways are related to UPR, FGF21, and an adaptive mitochondrial response that may lead to an improved or to a worsened response to insulin and glucose handling. (D) ORP8 or ATAD3A deficiency causes lipid metabolism alterations. Various alterations in lipid metabolism are observed upon ORP8 and ATAD3A ablation. ORP8 deficiency causes an increase in circulating HDL, cholesterol, triglycerides, and phospholipids. On the other hand, a lack of ATAD3A results in impaired cholesterol and lipid metabolism, reduced cholesterol esters, and decreased steroidgenesis.

are no data available on the levels of activated JNK in the absence of GRP75. Another common pathway that could be involved in insulin resistance upon depletion of *Mfn2*, *Grp75*, *Bap31*, or *CypD* is the MEK/ERK signaling cascade. MFN2 is a repressor of the MEK/ERK signaling pathway by its interaction with RAS [181]. ERK is hyperactivated upon *Mfn2* ablation in MEFs [182]. Ablation of *GRP75* stimulates the MEK/ERK signaling pathway in medullary thyroid carcinoma cells [172]. Moreover, the ERK signaling pathway is more active in *CypD* knockout mice hearts than in hearts of control animals [183]. Moreover, *BAP31* depletion in human embryonic stem cells leads to a mild increase in ERK phosphorylation [184]. Active ERK phosphorylates PPAR γ , which in turn stimulates the expression of genes related to diabetes [185,186].

Proteins whose depletion enhances insulin signaling and improves glucose tolerance

In addition to participating in mitophagy, FUNDC1 mediates the formation of mitochondria-ER contact sites and promotes Ca $^{2+}$ flux from the ER to mitochondria through binding to IP3R2 in cardiac cells [76]. Cardiomyocyte-specific ablation of *Fundc1* results in decreased mitochondrial and cytosolic Ca $^{2+}$ levels [76]. *Fundc1* ablation in mouse muscle causes mitochondrial dysfunction characterized by lower ATP and enhanced ROS [187]. In addition, *Fundc1*-ablated muscles show a reduced capacity to exercise, probably as a consequence of reduced fat oxidation [187]. Nevertheless, *Fundc1* knockout mice show improved glucose tolerance, insulin responsiveness, and less adiposity upon treatment with a HFD (Fig 4B). The process responsible for this reduced susceptibility to obesity is the activation of adaptive thermogenesis of adipose tissue driven by ROS-dependent muscle expression of FGF21 [187].

The downregulation of hepatic *Pacs2* in ob/ob mice increases maximal mitochondrial respiration and reduces JNK [29]. Under these conditions, *Pacs2* deficiency improves glucose tolerance and increases hepatic insulin signaling [29]. In oocytes from obese mice, genetic repression of *Pacs2* decreases Ca $^{2+}$ influx into mitochondria and ROS production [158]. In *Pacs2* knockout mice, liver expression of FGF21 is increased and mice are resistant to diet-induced obesity [188] (Fig 4B).

FGF21 is a systemic regulator of energy homeostasis and insulin sensitivity [189]. Its expression is activated upon detection of low protein and high carbohydrate levels. In mouse models of diabetes, this protein improves insulin sensitivity and reduces circulating glucose and triglyceride levels [190]. FGF21 upregulation in *Fundc1*- and *Pacs2*-deficient mice explains the improvement in glucose handling and insulin signaling observed in these mice.

The inhibition of the anti-apoptotic protein BCL2 mimics glucose stimulation by increasing mitochondrial activity and ATP production in pancreatic b-cells [191]. Pancreatic islets isolated from *Bcl2* $^{-/-}$ mice show enhanced insulin secretion in response to glucose stimulation [191]. The knockout of *Bak* and *Bax* in β -cells does not involve metabolic changes, indicating a role for BCL2 in metabolism besides its anti-apoptotic function [191]. In keeping with these results, induced insulin resistance in HepG2 cells upregulates BCL2 [192]. How *Bcl2* suppression leads to improved response to glucose has not been elucidated.

In contrast to the above data on the ablation of the Ca $^{2+}$ channeling protein GRP75, adenoviral-induced hepatic deficiency of *Ip3r1* enhances mitochondrial respiration, lowers JNK activity, enhances

insulin signaling, and improves glucose tolerance in mice [29] (Fig 4B). Analysis of the *Ip3r1* heterozygous mutant (opt/C) mouse indicates defects in beta-pancreatic cells, with reduced beta-cell mass, and impaired glucose tolerance [193]. In oocytes from obese mice, genetic repression of *Ip3r1* reduces Ca $^{2+}$ influx into mitochondria and also leads to a decrease in ROS production [158].

In line with these results, the downregulation of VDAC1 in pancreatic beta-cells has a protective effect against high glucose concentrations and maintains cellular reductive capacity [153]. *VDAC1* depletion in cancer cells has been shown to reprogram metabolism toward a decrease in energy production, accompanied by growth arrest [194,195]. Moreover, insulin release and ATP production in response to high glucose concentrations are improved in *VDAC1*-depleted cells [153]. In pancreatic islets from db/db mice, *VDAC1* inhibition leads to enhanced ATP generation and glucose-stimulated insulin secretion in response to high glucose levels [196] (Fig 4B).

To explain the hepatic increase in IP3R1-observed obese mice, in 2014 Arruda *et al* hypothesized that excessive Ca $^{2+}$ accumulation in mitochondria was the cause of impaired glucose metabolism and insulin sensitivity. In the same study, they showed improved glucose tolerance when they knocked down IP3R1 [29]. Since the ablation of *VDAC1* in pancreatic cells also has a protective effect against high glucose concentrations [153], it is possible that decreased mitochondrial Ca $^{2+}$ accumulation drives an improvement in insulin signaling.

Another important player in insulin signaling at the MAMs is mTORC2. mTORC2 signaling is essential for an adequate response to insulin [197]. Moreover, mTORC2 is implicated in the regulation of MAM integrity and its ablation results in decreased MAM formation and insulin resistance [90,197]. Insulin enhances mTORC2 localization at the MAMs [90]. Here, mTORC2 activation induces inhibitory phosphorylation of IP3R and PACS2 by AKT [90]. PACS2 ablation and IP3R ablation could have a synergistic effect with mTORC2 signaling in response to insulin stimuli.

Surprisingly, current data indicate that the repression of some proteins involved in mitochondria-ER contacts enhances glucose tolerance and insulin sensitivity by inducing the expression of FGF21, and perhaps by an independent mechanism related to an adaptive response of mitochondria which implies reduced mitochondrial Ca $^{2+}$ or mTORC2 signaling. Further studies are required to determine whether those processes are indeed independent or whether they share common mechanisms.

Why the deletion of certain proteins that participate in mitochondria-ER contacts results in enhanced or in impaired insulin sensitivity and glucose tolerance is not known yet. We believe that the absence of these proteins stimulates several signaling pathways that are related to UPR, FGF21, and an adaptive mitochondrial response (Fig 4C). The final output, i.e., the observed phenotype, will depend in each case on the sum of all the pathways that have been activated. We propose that a sum of stimuli that results in UPR and therefore JNK activation will provoke impaired response to insulin and glucose handling. On the other hand, if the combination of all the stimuli leads to increased circulating FGF21 and/or an adaptive mitochondrial response (which would include decreased mitochondrial Ca $^{2+}$ accumulation), the phenotype observed will be an improved response to insulin and glucose tolerance.

Proteins whose depletion alters lipid metabolism

Skeletal muscle-specific *Atad3* knockout mice show muscle atrophy in combination with mitochondrial abnormalities that include lack of cristae, reduced OXPHOS complexes and OPA1 expression, and progressive mtDNA depletion [198]. Fibroblasts derived from patients suffering from *ATAD3* gene cluster deletions show impaired cholesterol metabolism and mtDNA damage, as well as impaired lipid metabolism [199] (Fig 4D). In agreement with these data, muscle *ATAD3* deficiency reduces the levels of cholesterol esters in muscle, probably due to reduced Acetyl-CoA acetyltransferase [199]. The effects of *ATAD3* ablation on substrate handling have not been analyzed. Moreover, *ATAD3* ablation decreases steroidogenesis in a mouse cell line derived from Leydig cell tumor [200].

ORP5 and *ORP8* depletion leads to altered mitochondria morphology and function in HeLa cells [43]. The global ablation of *Orp8* in mice causes a marked elevation of high-density lipoprotein (HDL) cholesterol and phospholipids, which occurs in the absence of changes in apolipoprotein A-I [201]. Moreover, the secretion of nascent HDL particles is enhanced in primary *ORP8*-deficient hepatocytes, thereby suggesting altered biosynthesis of HDL [201] (Fig 4D). No information on the impact of *ORP8* depletion on glucose homeostasis is available.

In conclusion, available data suggest that some proteins of mitochondria-ER contacts play a pivotal role in the modulation of lipid metabolism. Future studies should address the mechanisms by which given proteins specifically modulate lipid metabolism in the absence of changes in energy metabolism.

Architectural, functional, and metabolic aspects of mitochondria-LD contact sites

Mitochondria and LDs are in active communication in highly metabolic tissues such as BAT, skeletal muscle, and heart [3,202-204]. It has been reported that the properties of the mitochondria surrounding LDs differ to those of mitochondria in the cytoplasm [2,205], which suggests a context-specific metabolic behavior of mitochondria. A study conducted by Benador *et al* [2] in BAT revealed that mitochondria surrounding LDs oxidize pyruvate, generate ATP, and use fatty acids for triacylglycerol (TAG) synthesis, whereas cytosolic mitochondria oxidize fatty acids. In addition, it has been reported in cultured cells that, under nutrient deprivation conditions, mitochondria and LDs interact in order to favor fatty acid oxidation [206,207]. This observation is in keeping with prior findings

indicating that lack of nutrients enhances fatty acid oxidation [208]. The variable impact of the interaction of LD with mitochondria on beta-oxidation will require a precise molecular explanation.

Proteins involved in mitochondria-LD contacts

The protein components of mitochondria-LD contact sites have been only partially characterized (Table 2). A tethering complex identified to operate in BAT is MFN2-PLIN1 [3] (MFN2 is located in the mitochondria and PLIN1 in LDs; Fig 5). Another mitochondrial protein that interacts with LD proteins is ACSL1 (acyl-CoA synthase long chain family member 1). BioID technology has revealed the interaction between ACSL1 and SNAP23 and VAMP4 in LDs [209] (Fig 5). The LD protein SNAP23 was first suggested to mediate the interaction between mitochondria and LDs since it was observed that its ablation reduced the contacts between these two organelles [210]. Moreover, SNAP23, together with VAMP4, is involved in LD fusion [211]. The LD protein PLIN5 has been described to localize at mitochondria-LD contacts; however, the mitochondrial partner of this protein is unknown [212,213]. PLIN5 interacts with ATGL and ABDH5 [214] on the LD surface (Fig 5).

Functional implications of the interaction between mitochondria and LDs

The associations between mitochondria and LDs influence LD size and mitochondrial dynamics. Thus, the interaction of mitochondria with LDs promotes the expansion of the latter [2]. PLIN5 overexpression increases mitochondrial recruitment to LDs and LD total area relative to control cells [2]. Mitochondrial morphology is also somehow regulated by interaction with LDs [2]: Mitochondria associated with LDs are more elongated than free mitochondria and contain reduced levels of DRP1 and cleaved OPA1 [2]. In turn, mitochondrial dynamics also influence LD size and distribution. Thus, impaired mitochondrial fusion causes an heterogeneous distribution of lipids throughout the mitochondrial network, greater accumulation of fatty acids in LDs, and increased fatty acid release from the cell [206]. This increase in fatty acids accumulation and release probably occurs due to impaired fatty acid oxidation in fragmented mitochondria.

PLIN5 is likely to promote the mitochondrial uptake of fatty acids since it interacts with adipose triglyceride lipase (ATGL) and its activator ABDH5 on the LD surface [214], leading to enhanced lipolysis. During glucose deprivation, ACSL1 interacts with SNAP23 and VAMP4 and thus increases mitochondria-LD contact sites [209]. Under these conditions, ACSL1 promotes the synthesis of acyl-CoA

Table 2. Mitochondria-LD contact sites proteins.

Protein	Location	Function in the mitochondria-LD contacts
ABDH5	LD	Lipolysis [214] (coupled to fatty acid transport into mitochondria?)
ACSL1	OMM	Mitochondria-LD tether (?)
ATGL	LD	Lipolysis [214] (coupled to fatty acid transport into mitochondria?)
MFN2	OMM	Mitochondria-LD tether [3] (?), Fatty acid transport into mitochondria [3] (?)
PLIN1	LD	Mitochondria-LD tether [3] (?), Fatty acid transport into mitochondria [3] (?)
PLIN5	LD, OMM	Fatty acid transport into mitochondria [214] (?)
SNAP23	LD	Mitochondria-LD tether [210] (?), LD fusion [211]
VAMP4	LD	Mitochondria-LD tether (?), LD fusion [211]

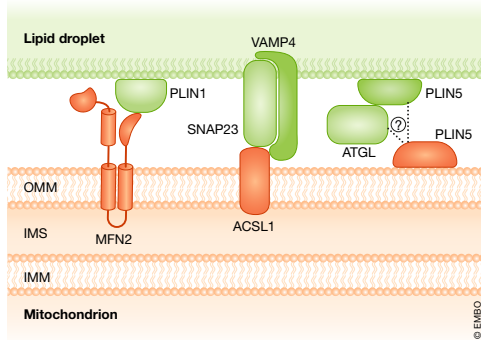


Figure 5. The architecture of mitochondria-LD contact sites.

Mitochondria establish contacts with lipid droplets (LDs). Although these contacts are poorly studied, several proteins have been found to participate in them. MFN2 in mitochondria interacts with the LD protein PLIN1. Mitochondrial ACSL1 has been found to form a complex with SNAP23 and VAMP4, both present on the LD surface. Moreover, PLIN5 has been found both on the surface of LDs and in the OMM. It is known that PLIN5 interacts with ATGL; however, the protein complex through which PLIN5 anchors LDs to mitochondria is still uncharacterized.

from fatty acids released by LDs, which are then channeled through mitochondrial beta-oxidation. Such a process may sustain the thermogenic capacity of BAT during its activation [215].

The MFN2-PLIN1 complex may be key for the maintenance of fatty acid oxidation in BAT and thus for thermogenesis [3]. Moreover, proteomic analysis of the LD-enriched fraction of BAT has identified the mitochondrial thermogenic protein UCP1 upon cold treatment [205], thereby suggesting increased cooperation of mitochondria and LDs for heat production.

Mitochondria-LD contacts respond to metabolic alterations

Mitochondria-LD contacts are modulated by nutrient availability in various tissues. Thus, glucose deficiency promotes LD interaction with mitochondria in monkey kidney Vero cells and in mouse primary hepatocytes [209,216]. The interaction of ACSL1 with SNAP23 and VAMP4 is enhanced upon glucose deprivation in mouse primary hepatocytes [209]. In agreement with these observations, SNAP23 expression increases in rat livers during fasting [217]. Proteomic analysis of purified LDs from mouse livers revealed that PLIN5 and ACSL1 proteins are more abundant in fasted mice [218]. It is likely that the enhanced mitochondria-LD contacts favor fatty acid oxidation in mitochondria under conditions of nutrient deprivation or during physiological fasting.

Mitochondria-LD contacts are also modified in BAT under conditions of thermogenic activity. In this regard, Benador *et al* [2] reported a 50% decrease in mitochondria contacts with LDs in primary cultures of BAT from mice maintained at 6°C compared to BAT of mice under thermoneutral conditions. In contrast, Boutant *et al* [3] observed that PLIN1-MFN2 interaction is enhanced upon treatment with an adrenergic agonist in brown adipocytes. In

agreement with the latter findings, Yu *et al* [205] detected increased expression of PLIN1 and ATGL in BAT of mice subjected to cold. No explanation for the reduced mitochondria-LD interaction upon cold exposure, under conditions which are linked to greater beta-oxidation, has been put forward to date.

The effects of a HFD, obesity, diabetes, and exercise on mitochondria-LD apposition have not been studied in depth. However, it has been reported that these conditions have an impact on proteins that operate at the interface of these two organelles. PLIN1 protein levels are decreased in the WAT of mice on a HFD in comparison with that of animals on a normal chow diet [219]. In skeletal muscle, two independent studies found that PLIN5 protein expression is increased in mice upon exposure to a HFD [220,221]. These findings are in agreement with a study performed in human muscle biopsies, in which PLIN5 protein levels were higher in obese and diabetic patients compared to those of healthy subjects [222].

Exercise influences the expression of proteins located at the mitochondria-LD interface. Both control and HFD-fed mice subjected to chronic exercise show increased levels of muscle PLIN1 [221]. Furthermore, the levels of this protein are higher in trained HFD-fed mice compared to trained mice under a normal diet. Interestingly, triglycerides tended to accumulate more in the muscle of trained animals and of those on HFD.

In turn, PLIN5 is upregulated in the primary myotubes of physically active subjects upon lipolytic stimulation [223]. In agreement with this, PLIN5-positive LDs are higher in muscle sections from trained individuals and total PLIN5 is higher in these subjects [222]. Upregulation of PLIN1 and PLIN5 in skeletal muscle of trained subjects may participate in the increased contacts that occur between mitochondria and LDs.

Metabolic impact of alterations in proteins participating in mitochondria-LD contacts

Disruption of the contacts between mitochondria and LDs may affect metabolism. However, information in this regard is scarce. Some animal and cellular models lacking proteins involved in these contacts have been generated, but the effects observed may not be fully attributable to the disruption of mitochondria-LD contact sites.

The specific ablation of *Mfn2* in BAT in mice impairs lipolysis, fatty acid oxidation, and respiration, and thus decreases the thermogenic capacity of this tissue [3]. Moreover, that study showed that the lack of MFN2 disrupts fatty acid flux into mitochondria, probably as a result of impairment of mitochondria and LD contacts. *Mfn2*-deficient BAT shows an enhanced expression of FGF21 when mice are subjected to a HFD, leading to increased circulating levels of FGF21. Whether FGF21 induction is due to cellular stress that is specifically dependent on alterations in mitochondria-LD contacts or to other biological effects of MFN2 remains unknown. However, under these conditions, the enhanced levels of FGF21 protect *Mfn2* knockout mice against lipid accumulation in the liver and lead to improved hepatic fatty acid oxidation.

Liver-specific *Plin5* knockout mice show reduced mitochondria-LD contacts in hepatocytes, decreased fatty acid oxidation, and reduced triglyceride secretion [224]. Treatment of these mice with a HFD induces greater accumulation of TAG, the activation of JNK, and insulin resistance. Partial ablation of *Plin5* in muscle leads to insulin resistance with improved insulin responsiveness under HFD feeding [220]. Complete ablation of *Plin5* in skeletal

muscle results in glucose intolerance, insulin resistance in adipose tissue, and reduced circulating insulin levels [225]. After HFD feeding, *Plin5* knockout animals show decreased ER stress markers (p-IRE1 α , spliced XBP1, *Atf4*), reduced activation of JNK, and diminished levels of proinflammatory markers (*Tnfa*, *Il6*, *Ccl2*), as well as decreased levels of muscle, circulating, and hepatic FGF21 compared to wild-type mice. These metabolic alterations are reversed upon injection of recombinant FGF21. Moreover, in agreement with these findings, *Plin5* overexpression in skeletal muscle causes increased energy metabolism and accumulation of more TAG in skeletal muscle under conditions of normal glucose and insulin tolerance [226]. Upon HFD, the expression of inflammatory markers in the liver is lower and muscle and plasma levels of FGF21 are increased. Moreover, when mice overexpressing *Plin5* are subjected to a HFD, they show upregulation of browning markers (*Ucp1*, *Cidea*, *Adiponectin*, *Cebpa*) in WAT, in comparison with wild-type mice. In line with these results, another study found that overexpression of *PLIN5* reduces lipolysis and fatty acid oxidation and increases glycogen synthesis and glucose oxidation in human primary myotubes [220]. Nevertheless, augmented energy demand by forskolin application increases lipid oxidation in conditions of *PLIN5* overexpression to a higher rate than in control myotubes. Laurens *et al* proposed that higher energy demands increase the contacts between mitochondria and LDs in order to optimize fatty acid oxidation and that HFD uncouples LD from mitochondria.

Total *Plin1* knockout mice are resistant to insulin [219]. Livers of *Plin1* knockout mice show spontaneous hepatosteatosis, impaired glucose metabolism, increased synthesis of TAG, and decreased fatty acid oxidation [227]. Furthermore, these mice suffer from hypertrophic cardiomyopathy [228] and increased atherosclerosis [229]. The depletion of *Plin1* causes increased circulating levels of proinflammatory cytokines, TAGs, and free fatty acids accompanied by white adipose tissue inflammation with higher M1 macrophage infiltration [219]. This proinflammatory phenotype is driven by enhanced lipolysis in adipocytes, which leads to increased production and the release of prostaglandins.

Snap23 knockdown in HL-1 cardiomyocytes causes insulin resistance *in vitro* [211]. In the same study, wild-type HL-1 cells exposed to oleic acid showed increased recruitment of SNAP23 to LDs and insulin resistance. Insulin resistance was rescued by *Snap23* overexpression. Since SNAP23 also localizes to the plasma membrane where it translocates GLUT4, insulin resistance might be caused by the absence of this protein in the plasma membrane.

Functional and metabolic aspects of mitochondria-lysosome contact sites

The interaction between mitochondria and lysosomes has been widely studied upon stress or mitochondrial damage conditions. Damaged mitochondria are degraded by selective autophagy (mitophagy), and this process implies the fusion of the mitophagosome with a lysosome (reviewed by Nguyen *et al* [230]). Moreover, mitochondria generate vesicles that trigger lysosomes, mitochondria-derived vesicles (MDVs), and this process is considered as a way for mitochondria to degrade proteins or oxidized components (reviewed by Sugiura *et al* [231]). Besides these studies performed

under stress conditions and revealing indirect interaction between mitochondria and lysosomes, little is known about physical apposition of mitochondria and lysosomes in basal conditions. In this section, we review the recent advances on this field and we analyze the functional aspects of the apposition between lysosomes and mitochondria and its crosstalk with metabolism.

Composition and functions of contacts between mitochondria and lysosomes

Over the past decade, although physical interaction between mitochondria and lysosomes had not yet been described, there was evidence for mitochondria and lysosome crosstalk since disruption of mitochondria affects lysosomal function and dynamics and lysosomal damage triggers mitochondrial homeostasis impairment (reviewed by Raimundo *et al* [232]). Recently, cutting-edge microscopy studies have detected the establishment of physical contacts between lysosomes and mitochondria in healthy cells in the absence of damage stimulus [1,233]. Besides, the latest discoveries in the field point to RAB7 as a master coordinator of these contacts [6,7,234–236] (Fig 6).

Lysosome-mitochondria contacts are promoted by GTP-bound lysosomal RAB7 [6]. When a constitutively active GTP-bound RAB7 mutant is expressed, contacts between lysosomes and mitochondria increase and these are more stable over time. TBC1D15 is a GTPase activating protein that governs RAB7 activity [237]. Recruitment of TBC1D15 to mitochondria by FIS1 favors GTP hydrolysis and separates lysosomes from mitochondria [6] (Fig 6). TBC1D15 inactive mutants can still be recruited to mitochondria; however, they do not uncouple mitochondria from lysosomes and lysosomes become larger [6]. Interaction between RAB7 and TBC1D15 has not been described yet. Confocal microscopy has revealed colocalization between lysosomes and sites for mitochondrial division [6] in which, as we described before, ER tubules participate [58]. These findings suggest that the interface between these two organelles plays a major role in the regulation of mitochondrial and lysosomal dynamics.

It has been discovered in retinal ganglion cells of *Xenopus laevis* embryos that late endosomes can associate with ribosomes in axons through RAB7 and RAB5 and protein translation can occur at the endosomal membrane [235]. Some mitochondrial proteins such as VDAC2 can be translated at the surface of these late endosomes and then be transferred to mitochondria [235] (Fig 6). Mutations in *rab7* associated with Charcot-Marie-Tooth disease cause downregulation of mitochondrial protein translation, mitochondrial elongation, and diminished mitochondrial membrane potential in the axons [235]. Currently, the proteins in the interorganelle surface that contribute to mitochondrial incorporation of the newly synthesized peptides remain unknown.

Melanogenesis is a process influenced by the apposition between melanosomes and mitochondria [7]. Melanosomes, which are lysosomal related organelles that accumulate melanin in pigmented cells, establish contacts with mitochondria through MFN2 in melanocytes [7] (Fig 6). However, the melanosomal component of these junctions remains unknown. MFN2 ablation decreases the interaction between mitochondria and melanosomes and arrests melanogenesis activation [7].

The interface between mitochondria and lysosomes could play a role in autophagy. It is known that MFN2 interacts with RAB7 in mouse hearts [234] (Fig 6). This interaction increases upon

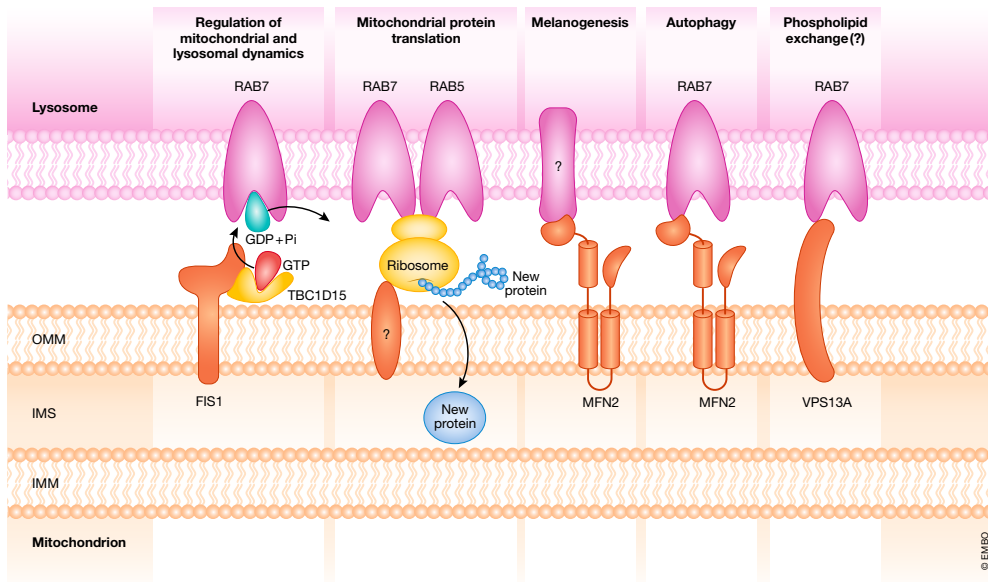


Figure 6. Mitochondria–lysosome interface.

Several processes take place at the contacts between mitochondria and lysosomes: (A) Regulation of mitochondrial and lysosomal dynamics by RAB7, TBC1D15, and FIS1 coordination; (B) mitochondrial protein translation in ribosomes anchored to the endosomal surface by interaction with RAB7 and RAB5 in close proximity to mitochondria; (C) melanogenesis in melanosomes that interact with mitochondria through MFN2; (D) autophagosome to lysosome fusion, which is supported by MFN2–RAB7 interaction; and (E) possible phospholipid exchange through VPS13A interaction with RAB7.

autophagy induction by starvation and has been proposed to be key for autophagosome–lysosome fusion [234].

A recent study indicates that lysosomal RAB7 immunoprecipitates and partially colocalizes with mitochondrial VPS13A in HeLa cells and that the absence of VPS13A causes impaired lysosomal degradation [236]. Moreover, a different study has identified a hydrophobic cavity in the structure of this protein and has proved its capacity to bind and transfer phospholipids between two membranes [238]. However, it has not been elucidated whether mitochondria and lysosomes exchange phospholipids in a non-vesicular manner (Fig 6).

A long DRP1 isoform present in mitochondria, lysosomes, and plasma membrane is highly enriched in mitochondrial contacts with lysosomes [239]. This isoform is mainly expressed in the brain and conserves mitochondrial division capacity [239]. When overexpressed in MEF, DRP1 long isoform colocalizes with RAB7; nevertheless, it is not known whether RAB7 and DRP1 interact [239]. GTPase activity and oligomerization capacity of DRP1 long isoform are necessary for its localization to lysosomes [239]. The role of this isoform of DRP1 in membrane junctions remains uncharacterized, although a role in lysosomal dynamics has already been discarded [239].

Besides the participation of mitochondria–lysosome contacts in organelle dynamics regulation, mitochondrial protein translation

and melanogenesis, and their possible contribution to autophagy and phospholipid exchange, communication between mitochondria and lysosomes has been associated with iron translocation to mitochondria [240] and lipofuscin deposit formation in lysosomes [241]. Nevertheless, mechanisms for these processes are poorly described and it is not known whether they take place in a vesicular or non-vesicular manner.

The effects of mitochondria–lysosome contact modification on metabolism

Little is known about how the modification of the contacts between mitochondria and lysosomes affects metabolism. RAB7 role in fat storage has been reported in *C. elegans*, in which neuronal silencing of *rab7* results in reduced fat storage [242]. *Rab7* knockdown in mouse bone marrow cells decreases glucose consumption and ROS excess [243]. The knockout of *TBC1D15* decreases glucose uptake in L02 human fetal hepatocytes [244]. Moreover, *TBC1D15* ablation reduces GLUT4 mRNA and protein levels and this effect is more dramatic in the presence of insulin [244]. In the absence of TBC1D15, GLUT4 colocalizes with lysosomes, where it could be degraded [244]. The authors suggest that TBC1D15 is necessary for GLUT4 translocation to the plasma membrane. There are no studies

Box: In need of answers

- (i) What is the precise composition of tethering (and spacer) complexes responsible for the contacts of mitochondria with other organelles (ER, lipid droplets, lysosomes, Golgi, peroxisomes, etc.)?
- (ii) How do the tethering (and spacer) complexes undergo modulation in a tissue-specific manner in response to hormonal or nutritional alterations? What are the mechanisms involved?
- (iii) Do the tethering complexes functionally interact with other tethering/spacer complexes or with functional proteins present in contacts? If so, what is the nature of the mechanisms involved?
- (iv) Identification of the precise functions operating in the different contact sites, and characterization of the complexes involved in the catalysis present in those contacts. Analysis of the modes of regulation of the functional complexes in response to hormonal and/or nutritional cues.
- (v) What are the mechanisms by which mitochondria within a specific cell type show a heterogeneous interaction with specific organelles such as lipid droplets?
- (vi) Because some of the proteins involved in tethering or in function in contact sites are present in multiple locations in cells, there is a need to design strategies to identify the specific function of the protein located in the contact site rather in other locations.
- (vii) How do alterations in proteins present in contact sites impact on metabolic homeostasis? Why do some proteins mediate enhanced anabolism whereas others mediate inhibited anabolism, and other alterations in lipid metabolism? What is the physiological meaning, and what the mechanisms in place?

linking these observations on RAB7 and TBC1D15 with mitochondria-lysosome interaction.

Impact of metabolism on mitochondria-lysosome contacts

The influence of metabolic homeostasis on mitochondria-lysosome contacts in mammalian cells is an unexplored field. Related findings have been discovered in yeast [245]. Yeast vacuoles interact with mitochondria through Ypt7, the yeast homologue of RAB7, and Vps39 in the vacuole [245] and Tom40 in the mitochondria [246]. In the absence of glucose, vacuole-mitochondria contacts are lost, but upon addition of glucose to the growth medium, these contacts slowly reappear [245]. This study is the first evidence that glucose levels modulate mitochondria-lysosome contacts in yeast cells; nevertheless, more insight is necessary into how glucose deprivation affects these contacts in mammalian cells.

Under insulin or amino acid stimuli in mammalian cells, lysosomal mTORC1 is activated and stimulates mitochondrial oxidative pathways and mtDNA synthesis [247]. RAB7 interacts with mTOR in mouse bone marrow cells [243]. It is not known whether this interaction occurs in other cell types. Given the importance of mTOR in response to nutrient availability and RAB7 in the interaction between mitochondria and lysosomes, this complex is a potential candidate to modulate mitochondria-lysosome contacts in response to metabolism.

Contacts of mitochondria with peroxisomes and the Golgi apparatus

Peroxisomes and mitochondria establish physical contacts, and this interaction influences cell metabolism [1,8,248]. ECI2, a

peroxisomal enoyl-CoA isomerase, is so far the only protein established as part of a mitochondria-peroxisome tethering complex [8]. A proximity ligation assay has revealed that peroxisomal ECI2 and mitochondrial TOM20 interact in MA-10 Leydig-like cells [8], although more precise analyses of this interaction such as co-immunoprecipitation or two-hybrid screening have not been performed. Overexpression of *ECI2* results in increased steroid biosynthesis [8], a metabolic process that takes place in mitochondria. Moreover, MAMs associate with peroxisomes during antiviral immune signaling [249,250]. Beta-oxidation needs the interplay between both compartments: Very long chain fatty acids (> 16 carbons) are shortened in peroxisomes (to 6–8 carbons fatty acids) and then preferentially translocated to mitochondria for complete oxidation [251]. How shortened fatty acids are shuttled from peroxisomes to mitochondria remains unknown.

Golgi apparatus and mitochondria also communicate with each other by physical interaction [1,4]. Nevertheless, the key players of this apposition remain unknown. The existence of Ca^{2+} gradients from the Golgi apparatus to mitochondria has been discovered in pancreatic acinar cells [4], although the existence of calcium channels for active or passive calcium transport has not been clarified yet.

Future perspectives

The interaction between organelles is an emerging field that is gaining importance due to the physiological implications of organelle contact sites. In this regard, mitochondria contacts with the ER are the better characterized ones to date and their functional and metabolic aspects have already been highlighted. Nevertheless, the full composition of tethering complexes still needs to be discovered. Mitochondria interacting with lipid droplets show different metabolic behavior compared with those mitochondria that are free in the cytosol. Studies on the interaction of LD and mitochondria have generated two hypotheses: The first hypothesis is that mitochondria-LD interaction favors beta-oxidation, and the second hypothesis is that mitochondria-LD interaction results in increased TAG synthesis. More insight is needed to determine whether metabolic behavior of mitochondria associated with LDs depends on the energetic demands of the tissue or the whole body. Lysosome-mitochondria contacts in mammalian cells are still poorly described but currently in the spotlight of research. Whether reciprocal dynamics regulation exerted between mitochondria and lysosomes has any metabolic implications is yet to be discovered. The key players in the communication between mitochondria and peroxisomes have not been deciphered. Future characterization of this interaction will be metabolically relevant since peroxisomes and mitochondria interact during beta-oxidation of fatty acids. Although several studies have revealed an interaction between mitochondria and the Golgi apparatus, the functional and structural features of this interaction remain unknown. How Ca^{2+} is transferred from the Golgi apparatus to mitochondria and what Ca^{2+} flux between these organelles signals for has not been discovered yet. It is possible that metabolic features of mitochondria could depend on their interaction with other organelles, which we hypothesize would be determined by the organ or tissue energetic requirements. A tissue/cell-specific characterization of

contact sites is lacking, but it will be fundamental for a better understanding of contact sites influence on metabolism. Future discoveries on organelle contact sites will fill these gaps and transform our understanding of cellular physiology and metabolism regulation and likely will provide us with new tools for targeting metabolic disorders.

Acknowledgements

I.G. is a recipient of a PhD fellowship from the Ministerio de Economía y Competitividad (MINECO). This study was supported by research grants from the MINECO (SAF2016-75246R), the Generalitat de Catalunya (Grant 2017SGR1015), INFLAMES (PIE-14/00045, Instituto de Salud Carlos III, CIBERDEM ("Instituto de Salud Carlos III"), the Marató de TV3, the Fundación BBVA, and the Fundación Ramon Arcecs. We gratefully acknowledge institutional funding from MINECO through the Centres of Excellence Severo Ochoa Award, and from the CERCA Programme of the Generalitat de Catalunya.

Conflict of interest

The authors declare that they have no conflict of interest.

References

- Valm AM, Cohen S, Legant WR, Melunis J, Hershberg U, Wait E, Cohen AR, Davidson MW, Betzig E, Lippincott-Schwartz J (2017) Applying systems-level spectral imaging and analysis to reveal the organelle interactome. *Nature* 546: 162–167
- Benador IY, Veliova M, Mahdaviyani K, Petcherski A, Wikstrom JD, Assali EA, Acín-Pérez R, Shum M, Oliveira MF, Cinti S et al (2018) Mitochondria bound to lipid droplets have unique bioenergetics, composition, and dynamics that support lipid droplet expansion. *Cell Metab* 27: 869–885.e6
- Boutant M, Kulkarni SS, Joffraud M, Ratajczak J, Valera-Albarni M, Combe R, Zorzano A, Cantó C (2017) Mfn2 is critical for brown adipose tissue thermogenic function. *EMBO J* 36: 1543–1558
- Dolman NJ, Gerasimenko JV, Gerasimenko OV, Voronina SG, Petersen OH, Tepikin AV (2005) Stable Golgi-mitochondria complexes and formation of Golgi Ca²⁺ gradients in pancreatic acinar cells. *J Biol Chem* 280: 15794–15799
- Marsh BJ, Mastroratte DN, Buttler KF, Howell KE, McIntosh JR (2001) Organellar relationships in the Golgi region of the pancreatic beta cell line, HIT-T15, visualized by high resolution electron tomography. *Proc Natl Acad Sci USA* 98: 2399–2406
- Wong YC, Ysselstein D, Krainc D (2018) Mitochondria-lysosome contacts regulate mitochondrial fission via RAB7 GTP hydrolysis. *Nature* 554: 382–386
- Daniele T, Hurbain I, Vago R, Casari G, Raposo G, Tacchetti C, Schiaffino MV (2014) Mitochondria and melanosomes establish physical contacts modulated by Mfn2 and involved in organelle biogenesis. *Curr Biol* 24: 393–403
- Fan J, Li X, Issop L, Culty M, Papadopoulos V (2016) ACBD2/ECI2-mediated peroxisome-mitochondria interactions in Leydig cell steroid biosynthesis. *Mol Endocrinol* 30: 763–782
- De Vos KJ, Mórotz GM, Stoica R, Tudor EL, Lau KF, Ackerley S, Warley A, Shaw CE, Miller CJ (2012) VAPB interacts with the mitochondrial protein PTP1P51 to regulate calcium homeostasis. *Hum Mol Genet* 21: 1299–1311
- Szabadkai G, Bianchi K, Várnai P, De Stefani D, Wieckowski MR, Cavagna D, Nagy AI, Balla T, Rizzuto R (2006) Chaperone-mediated coupling of endoplasmic reticulum and mitochondrial Ca²⁺ channels. *J Cell Biol* 175: 901–911
- Iwasawa R, Mahul-Mellier AL, Datler C, Pazarentzos E, Grimm S (2011) Fis1 and Bap31 bridge the mitochondria-ER interface to establish a platform for apoptosis induction. *EMBO J* 30: 556–568
- de Brito OM, Scorrano L (2008) Mitofusin 2 tethers endoplasmic reticulum to mitochondria. *Nature* 456: 605–610
- Stoica R, De Vos KJ, Paillusson S, Mueller S, Sancho RM, Lau KF, Vizcay-Barrena G, Lin WL, Xu YF, Lewis J et al (2014) ER-mitochondria associations are regulated by the VAPB-PTPIP51 interaction and are disrupted by ALS/FTD-associated TDP-43. *Nat Commun* 5: 3996
- Di Mattia T, Wilhelm LP, Ikhlef S, Wendling C, Spohner D, Nominé Y, Giordano F, Mathelin C, Drin G, Tomasetto C et al (2018) Identification of MOSPD2, a novel scaffold for endoplasmic reticulum membrane contact sites. *EMBO Rep* 19: e45453
- Thoudam T, Ha C, Leem J, Chanda D, Park J, Kim H, Jeon J-H, Choi Y-K, Liangpunsakul S, Huh YH et al (2019) PDK4 augments ER-mitochondria contact to dampen skeletal muscle insulin signaling during obesity. *Diabetes* 68: 571–586
- Yoon Y, Krueger EW, Oswald BJ, McNiven MA (2003) The mitochondrial protein hFis1 regulates mitochondrial fission in mammalian cells through an interaction with the dynamin-like protein DLP1. *Mol Cell Biol* 23: 5409–5420
- Breckenridge DG, Stojanovic M, Marcellus RC, Shore GC (2003) Caspase cleavage product of BAP31 induces mitochondrial fission through endoplasmic reticulum calcium signals, enhancing cytochrome c release to the cytosol. *J Cell Biol* 160: 1115–1127
- Chen H, Detmer SA, Ewald AJ, Griffin EE, Fraser SE, Chan DC (2003) Mitofusins Mfn1 and Mfn2 coordinately regulate mitochondrial fusion and are essential for embryonic development. *J Cell Biol* 160: 189–200
- Santel A, Fuller MT (2001) Control of mitochondrial morphology by a human mitofusin. *J Cell Sci* 114: 867–874
- Hamasaki M, Furuta N, Matsuda A, Nezu A, Yamamoto A, Fujita N, Oomori H, Noda T, Haraguchi T, Hiraoka Y et al (2013) Autophagosomes form at ER-mitochondria contact sites. *Nature* 495: 389–393
- Filadi R, Gretti E, Turacchio G, Luini A, Pozzan T, Pizzo P (2015) Mitofusin 2 ablation increases endoplasmic reticulum-mitochondria coupling. *Proc Natl Acad Sci USA* 112: E2174–E2181
- Santos Leal N, Schreiner B, Moreira C, Filadi R, Wiehager B, Karlstr H, Pizzo P, Ankarcrone M (2016) Mitofusin-2 knockdown increases ER-mitochondria contact and decreases amyloid β -peptide production. *J Cell Mol Med* 20: 1686–1695
- Naon D, Zaninello M, Giacomello M, Varanita T, Grespi F, Lakshminarayanan S, Serafini A, Semenzato M, Herkenne S, Hernández-Alvarez MI et al (2016) Critical reappraisal confirms that Mitofusin 2 is an endoplasmic reticulum-mitochondria tether. *Proc Natl Acad Sci USA* 113: 11249–11254
- Mclelland G, Goiran T, Yi W, Chen CX, Lauinger ND, Krahn AI, Valimehr S, Rakovic A, Rouiller I, Durcan TM (2018) Mfn2 ubiquitination by PINK1/parkin gates the p97-dependent release of ER from mitochondria to drive mitophagy. *Elife* 7: 1–35
- Teng Y, Ren X, Li H, Shull A, Kim J, Cowell JK (2016) Mitochondrial ATAD3A combines with GRP78 to regulate the WASF3 metastasis-promoting protein. *Oncogene* 35: 333–343
- Honrath B, Metz I, Bendridi N, Rieusset J, Cuijsee C, Dolga AM (2017) Glucose-regulated protein 75 determines ER-mitochondrial coupling

- and sensitivity to oxidative stress in neuronal cells. *Cell Death Discov* 3: 17076
27. Tubbs E, Theurey P, Vial G, Bendridi N, Bravard A, Chauvin MA, Ji-Cao J, Zoulim F, Bartosch B, Ovize M et al (2014) Mitochondria-associated endoplasmic reticulum membrane (MAM) integrity is required for insulin signaling and is implicated in hepatic insulin resistance. *Diabetes* 63: 3279–3294
 28. Paillard M, Tubbs E, Thiebaut PA, Gomez L, Fauconnier J, Da Silva CC, Teixeira G, Mewton N, Belaidi E, Durand A et al (2013) Depressing mitochondria-reticulum interactions protects cardiomyocytes from lethal hypoxia-reoxygenation injury. *Circulation* 128: 1555–1565
 29. Arruda AP, Pers BM, Parlakgöl G, Güney E, Inouye K, Hotamisligil GS (2014) Chronic enrichment of hepatic endoplasmic reticulum-mitochondria contact leads to mitochondrial dysfunction in obesity. *Nat Med* 20: 1427–1435
 30. Eletto MD, Rossin F, Occhigrossi L, Pinton P, Eletto MD, Rossin F, Occhigrossi L, Farrace MG, Faccenda D, Desai R (2018) Transglutaminase type 2 regulates ER-mitochondria contact sites by interacting with report transglutaminase type 2 regulates ER-mitochondria contact sites by interacting with GRP75. *Cell Rep* 25: 3573–3581
 31. Qiao X, Jia S, Ye J, Fang X, Zhang C, Cao Y, Xu C, Zhao L, Zhu Y, Wang L et al (2017) PTP1P51 regulates mouse cardiac ischemia/reperfusion through mediating the mitochondria-SR junction. *Sci Rep* 7: 1–14
 32. Chiang SF, Huang CY, Lin TY, Chiou SH, Chow KC (2012) An alternative import pathway of AIF to the mitochondria. *Int J Mol Med* 29: 365–372
 33. Ainbinder A, Boncompagni S, Protasi F, Dirksen RT (2015) Role of mitofusin-2 in mitochondrial localization and calcium uptake in skeletal muscle. *Cell Calcium* 57: 14–24
 34. Kentalha H, Weber-Boyvatt M, Olkkonen VM (2016) OSBP-related protein family: mediators of lipid transport and signaling at membrane contact sites. *Int Rev Cell Mol Biol* 321: 299–340
 35. Kuge O, Nishijima M (1997) Phosphatidylserine synthase I and II of mammalian cells. *Biochim Biophys Acta* 1348: 151–156
 36. McMurray W (1986) Origins of the phospholipids in animal mitochondria. *Biochem Cell Biol* 64: 1115–1124
 37. Vance JE (1991) Newly made phosphatidylserine and phosphatidylethanolamine are preferentially translocated between rat liver mitochondria and endoplasmic reticulum. *J Biol Chem* 266: 89–97
 38. Dennis EA, Kennedy EP (1972) Intracellular sites of lipid synthesis and the biogenesis of mitochondria. *J Lipid Res* 13: 263–267
 39. Blusztajn JK, Zeisel SH, Wurtman RJ (1979) Synthesis of lecithin (phosphatidylcholine) from phosphatidylethanolamine in bovine brain. *Brain Res* 179: 319–327
 40. Vance JE (1990) Phospholipid synthesis in a membrane fraction associated with mitochondria. *J Biol Chem* 265: 7248–7257
 41. Du X, Kumar J, Ferguson C, Schulz TA, Ong YS, Hong W, Prinz WA, Parton RG, Brown AJ, Yang H (2011) A role for oxysterol-binding protein-related protein 5 in endosomal cholesterol trafficking. *J Cell Biol* 192: 121–135
 42. Chung J, Torta F, Masai K, Lucast L, Czaplá H, Tanner LB, Narayanaswamy P, Wenk MR, Nakatsu F, De Camilli P (2015) PI4P/phosphatidylserine countertransport at ORP5- and ORP8-mediated ER-plasma membrane contacts. *Science* 349: 428–432
 43. Galmes R, Houcine A, van Vliet AR, Agostinis P, Jackson CL, Giordano F (2016) ORP5/ORP8 localize to endoplasmic reticulum-mitochondria contacts and are involved in mitochondrial function. *EMBO Rep* 17: 800–810
 44. AhYoung AP, Jiang J, Zhang J, Khoi Dang X, Loo JA, Zhou ZH, Egea PF (2015) Conserved SMP domains of the ERMES complex bind phospholipids and mediate tether assembly. *Proc Natl Acad Sci USA* 112: E3179–E3188
 45. Schauder CM, Wu X, Saheki Y, Narayanaswamy P, Torta F, Wenk MR, De Camilli P, Reinisch KM (2014) Structure of a lipid-bound extended synaptotagmin indicates a role in lipid transfer. *Nature* 510: 552–555
 46. Hirabayashi Y, Kwon SK, Paek H, Pernice WM, Paul MA, Lee J, Erfani P, Raczkowski A, Petrey DS, Pon LA et al (2017) ER-mitochondria tethering by PDZD8 regulates Ca²⁺ dynamics in mammalian neurons. *Science* 358: 623–630
 47. Elustondo P, Martin LA, Karten B (2017) Mitochondrial cholesterol import. *Biochim Biophys Acta* 1862: 90–101
 48. Prasad M, Kaur J, Pawlak KJ, Bose M, Whittall RM, Bose HS (2015) Mitochondria-associated endoplasmic reticulum membrane (MAM) regulates steroidogenic activity via steroidogenic acute regulatory protein (StAR)-voltage-dependent anion channel 2 (VDAC2) interaction. *J Biol Chem* 290: 2604–2616
 49. Reitz J, Gehrig-burger K, Iii JFS, Gimpl G (2008) Cholesterol interaction with the related steroidogenic acute regulatory lipid-transfer (START) domains of StAR (STARD1) and MLN64 (STARD3). *FEBS J* 64: 1790–1802
 50. Tsujishita Y, Hurley JH (2000) Structure and lipid transport mechanism of a StAR-related domain. *Nat Struct Biol* 7: 408–414
 51. Strushkevich N, Mackenzie F, Cherkesova T, Grabovec I, Usanov S, Park H-W (2011) Structural basis for pregnenolone biosynthesis by the mitochondrial monooxygenase system. *Proc Natl Acad Sci USA* 108: 10139–10143
 52. Rone MB, Midzak AS, Issop L, Rammouz G, Jagannathan S, Fan J, Ye X, Blonder J, Veenstra T, Papadopoulos V (2012) Identification of a dynamic mitochondrial protein complex driving cholesterol import, trafficking, and metabolism to steroid hormones. *Mol Endocrinol* 26: 1868–1882
 53. Liu J, Rone MB, Papadopoulos V (2006) Protein-protein interactions mediate mitochondrial cholesterol transport and steroid biosynthesis. *J Biol Chem* 281: 38879–38893
 54. Pulli I, Lassila T, Pan G, Yan D, Olkkonen VM, Törnquist K (2018) Oxysterol-binding protein related-proteins (ORPs) 5 and 8 regulate calcium signaling at specific cell compartments. *Cell Calcium* 72: 62–69
 55. Simmen T, Aslan JE, Blagoveshchenskaya AD, Thomas L, Wan L, Xiang Y, Felciangeli SF, Hung CH, Crump CM, Thomas G (2005) PACS-2 controls endoplasmic reticulum-mitochondria communication and Bid-mediated apoptosis. *EMBO J* 24: 717–729
 56. Arif T, Krelin Y, Shoshan-Barmatz V (2016) Reducing VDAC1 expression induces a non-apoptotic role for pro-apoptotic proteins in cancer cell differentiation. *Biochim Biophys Acta* 1857: 1228–1242
 57. Gatliff J, East DA, Singh A, Alvarez MS, Frison M, Matic I, Ferraina C, Sampson N, Turkheimer F, Campanella M (2017) A role for TSP0 in mitochondrial Ca²⁺ homeostasis and redox stress signaling. *Cell Death Dis* 8: 1–15
 58. Friedman JR, Lackner LL, West M, DiBenedetto JR, Nunnari J, Voeltz GK (2011) ER tubules mark sites of mitochondrial division. *Science* 334: 358–362
 59. Korobova F, Ramabhadran V, Higgs HN (2013) An actin-dependent step in mitochondrial fission mediated by the ER-associated formin INF2. *Science* 339: 464–468
 60. Korobova F, Gauvin TJ, Higgs HN (2014) A role for myosin II in mammalian mitochondrial fission. *Curr Biol* 24: 409–414

61. Chakrabarti R, Ji WK, Stan RV, de Juan Sanz J, Ryan TA, Higgs HN (2018) INF2-mediated actin polymerization at the ER stimulates mitochondrial calcium uptake, inner membrane constriction, and division. *J Cell Biol* 217: 251–268
62. Loson OC, Song Z, Chen H, Chan DC (2013) Fis1, Mff, MID49, and MID51 mediate Drp1 recruitment in mitochondrial fission. *Mol Biol Cell* 24: 659–667
63. Yu R, Liu T, Jin S, Ning C, Lendahl U, Nistér M, Zhao J (2017) MIEF1/2 function as adaptors to recruit Drp1 to mitochondria and regulate the association of Drp1 with Mff. *Sci Rep* 7: 880
64. Kim Y, Youn S, Sudhakar V, Das A, Chandhri R, Cuervo Grajal H, Kwon J, Leanhart S, He L, Toth PT et al (2018) Redox regulation of mitochondrial fission protein Drp1 by protein disulfide isomerase limits endothelial senescence. *Cell Rep* 23: 3565–3578
65. Arasaki K, Shimizu H, Mogari H, Nishida N, Hirota N, Furuno A, Kudo Y, Baba M, Baba N, Cheng J et al (2015) A role for the ancient SNARE syntaxin 17 in regulating mitochondrial division. *Dev Cell* 32: 304–317
66. Rambold AS, Kostecky B, Elia N, Lippincott-Schwartz J (2011) Tubular network formation protects mitochondria from autophagosomal degradation during nutrient starvation. *Proc Natl Acad Sci USA* 108: 10190–10195
67. Lewis SC, Uchiyama LF, Nunnari J (2016) ER-mitochondria contacts couple mtDNA synthesis with mitochondrial division in human cells. *Science* 353: aaf5549
68. Wu W, Lin C, Wu K, Jiang L, Wang X, Li W, Zhuang H, Zhang X, Chen H, Li S et al (2016) FUNDC1 regulates mitochondrial dynamics at the ER-mitochondrial contact site under hypoxic conditions. *EMBO J* 35: 1368–1384
69. Chan DC (2006) Dissecting mitochondrial fusion. *Dev Cell* 11: 592–594
70. Anand R, Wai T, Baker MJ, Kladt N, Schauss AC, Rugarli E, Langer T (2014) The γ -AAA protease YME1L and OMA1 cleave OPA1 to balance mitochondrial fusion and fission. *J Cell Biol* 204: 919–929
71. Yan L, Qi Y, Huang X, Yu C, Lan L, Guo X, Rao Z, Hu J, Lou Z (2018) Structural basis for GTP hydrolysis and conformational change of MFN1 in mediating membrane fusion. *Nat Struct Mol Biol* 25: 233–243
72. Franco A, Kitsis RN, Fleischer JA, Gavathiotis E, Kornfeld OS, Gong G, Biris N, Benz A, Qvit N, Donnelly SK et al (2016) Correcting mitochondrial fusion by manipulating mitofusin conformations. *Nature* 540: 74–79
73. Liu J, Noel JK, Low HH (2018) Structural basis for membrane tethering by a bacterial dynamin-like pair. *Nat Commun* 9: 1–12
74. Cerqua C, Anesti V, Pyakurel A, Liu D, Naon D, Wiche G, Baffa R, Dimmer KS, Scorrano L (2010) Trichoplein/mitostatin regulates endoplasmic reticulum-mitochondria juxtaposition. *EMBO Rep* 11: 854–860
75. Tian Y, Li B, Shi WZ, Chang MZ, Zhang CJ, Di ZL, Liu Y (2014) Dynamin-related protein 1 inhibitors protect against ischemic toxicity through attenuating mitochondrial Ca^{2+} uptake from endoplasmic reticulum store in PC12 cells. *Int J Mol Sci* 15: 3172–3185
76. Wu S, Lu Q, Wang Q, Ding Y, Ma Z, Mao X, Huang K, Xie Z, Zou MH (2017) Binding of FUN14 domain containing 1 with inositol 1,4,5-trisphosphate receptor in mitochondria-associated endoplasmic reticulum membranes maintains mitochondrial dynamics and function in hearts *in vivo*. *Circulation* 136: 2248–2266
77. Weaver D, Eisner V, Liu X, Várnai P, Hunyady L, Gross A, Hajnóczky G (2014) Distribution and apoptotic function of outer membrane proteins depend on mitochondrial fusion. *Mol Cell* 54: 870–878
78. Papanicolaou KN, Khairallah RJ, Ngho GA, Chikando A, Luptak I, O'Shea KM, Riley DD, Lugus JJ, Colucci WS, Lederer WJ et al (2011) Mitofusin-2 maintains mitochondrial structure and contributes to stress-induced permeability transition in cardiac myocytes. *Mol Cell Biol* 31: 1309–1328
79. Han SM, Tsuda H, Yang Y, Vibbert J, Cottee P, Lee SJ, Winek J, Haueter C, Bellen HJ, Miller MA (2012) Secreted VAPB/ALS8 major sperm protein domains modulate mitochondrial localization and morphology via growth cone guidance receptors. *Dev Cell* 22: 348–362
80. Rizzuto R, Pinton P, Carrington W, Fay FS, Fogarty KE, Lifshitz LM, Tuft RA, Pozzan T (1998) Close contacts with the endoplasmic reticulum as determinants of mitochondrial Ca^{2+} responses. *Science* 280: 1763–1766
81. Lytton J, Westlin M, Burk SE, Shull E, MacLennan H (1992) Functional comparisons between isoforms of the sarcoplasmic or endoplasmic reticulum family of calcium pumps. *J Biol Chem* 267: 14483–14489
82. Miller KK, Verma A, Snyder SH, Ross CA (1991) Localization of an endoplasmic reticulum calcium ATPase mRNA in rat brain by *in situ* hybridization. *Neuroscience* 43: 1–9
83. Giorgi C, Marchi S, Pinton P (2018) The machineries, regulation and cellular functions of mitochondrial calcium. *Nat Rev Mol Cell Biol* 19: 713–730
84. Filadi R, Leal NS, Schreiner B, Rossi A, Dentoni G, Pinho CM, Wiehager B, Cieri D, Cali T, Pizzo P et al (2018) TOM70 sustains cell bioenergetics by promoting IP3R3-mediated ER to mitochondria Ca^{2+} transfer. *Curr Biol* 28: 369–382.e6
85. Giorgio V, Bisetto E, Soriano ME, Dabbeni-sala F, Basso E, Petronilli V, Forte MA, Bernardi P, Lippe G (2009) Cyclophilin D modulates mitochondrial FOF1-ATP synthase by interacting with the lateral stalk of the complex. *J Biol Chem* 284: 33982–33988
86. Ong HL, Liu X, Sharma A, Hegde RS, Ambudkar IS (2007) Intracellular Ca^{2+} release via the ER translocon activates store-operated calcium entry. *Pflugers Arch Eur J Physiol* 453: 797–808
87. Giunti R, Gamberucci A, Fulceri R, Bánhegyi G, Benedetti A (2007) Both translocon and a cation channel are involved in the passive Ca^{2+} leak from the endoplasmic reticulum: a mechanistic study on rat liver microsomes. *Arch Biochem Biophys* 462: 115–121
88. Booth DM, Enyedi B, Geiszt M, Várnai P, Hajnóczky G (2016) Redox nanodomains are induced by and control calcium signaling at the ER-mitochondrial interface. *Mol Cell* 63: 240–248
89. Dong Z, Shanmughapriya S, Tomar D, Siddiqui N, Lynch S, Nemani N, Breves SL, Zhang X, Tripathi A, Palaniappan P et al (2017) Mitochondrial Ca^{2+} uniporter is a mitochondrial luminal redox sensor that augments MCU channel activity. *Mol Cell* 65: 1014–1028
90. Betz C, Stracka D, Prescianotto-baschong C, Frieden M, Demaurex N, Hall MN (2013) mTOR complex 2-Akt signaling at mitochondria associated endoplasmic reticulum membranes (MAM) regulates mitochondrial physiology. *Proc Natl Acad Sci USA* 110: 12526–12534
91. Khan MT, Wagner L, Yule DI, Bhanumathy C, Joseph SK (2006) Akt kinase phosphorylation of inositol 1,4,5-trisphosphate receptors. *J Biol Chem* 281: 3731–3737
92. Szado T, Vanderheyden V, Parys JB, De Smedt H, Rietdorf K, Kotelevets L, Chastre E, Khan F, Landegren U, Söderberg O et al (2008) Phosphorylation of inositol 1,4,5-trisphosphate receptors by protein kinase B/Akt inhibits Ca^{2+} release and apoptosis. *Proc Natl Acad Sci USA* 105: 2427–2432
93. Schäuble N, Lang S, Jung M, Cappel S, Schorr S, Ulucan Ö, Linxweijer J, Dudek J, Blum R, Helms V et al (2012) BiP-mediated closing of the Sec61 channel limits Ca^{2+} leakage from the ER. *EMBO J* 31: 3282–3296
94. Golic I, Velickovic K, Markecic M, Stancic A, Jankovic A, Vucetic M, Otasevic V, Buzadzic B, Korac B, Korac A (2014) Calcium-induced

- alteration of mitochondrial morphology and mitochondrial-endoplasmic reticulum contacts in rat brown adipocytes. *Eur J Histochem* 58: 2377
95. Sehgal P, Szalai XP, Olesen XC, Praetorius XHA, Nissen XP, Christensen SB, Engedal XN, Møller JV (2017) Inhibition of the sarco/endoplasmic reticulum (ER) Ca^{2+} -ATPase by thapsigargin analogs induces cell death via ER Ca^{2+} depletion and the unfolded protein response. *J Biol Chem* 292: 19656–19673
 96. Gomez-Suaga P, Paillusson S, Miller CCJ (2017) ER-mitochondria signaling regulates autophagy. *Autophagy* 13: 1250–1251
 97. Muñoz JP, Ivanova S, Sánchez-Wandelmer J, Martínez-Cristóbal P, Noguera E, Sancho A, Díaz-Ramos A, Hernández-Alvarez MI, Sebastián D, Mauvezin C et al (2013) Mfn2 modulates the UPR and mitochondrial function via repression of PERK. *EMBO J* 32: 2348–2361
 98. Harding HP, Zhang Y, Zeng H, Novoa I, Lu PD, Calfon M, Sadri N, Yun C, Popko B, Paules R et al (2003) An integrated stress response regulates amino acid metabolism and resistance to oxidative stress. *Mol Cell* 11: 619–633
 99. Blais JJD, Filipenko V, Bi M, Harding HHP, Ron D, Koumenis C, Wouters BC, Bell JC (2004) Activating transcription factor 4 is translationally regulated by hypoxic stress. *Mol Cell Biol* 24: 7469–7482
 100. Liang S-H, Zhang W, McGrath BC, Zhang P, Cavener DR (2006) PERK (eIF2 α kinase) is required to activate the stress-activated MAPKs and induce the expression of immediate-early genes upon disruption of ER calcium homeostasis. *Biochem J* 393: 201–209
 101. Tessitore A, Martin MP, Sano R, Ma Y, Mann L, Ingrassia A, Laywell ED, Steindler DA, Hendershot LM, Azzo A (2004) GM1-ganglioside-mediated activation of the unfolded protein response causes neuronal death in a neurodegenerative gangliosidosis. *Mol Cell* 15: 753–766
 102. Kharroubi I, Ladrie L, Cardozo AK, Dogusan Z, Cnop M, Eizrik DL (2004) Free fatty acids and cytokines induce pancreatic β -cell apoptosis by different mechanisms: role of nuclear factor- κ B and endoplasmic reticulum stress. *Endocrinology* 145: 5087–5096
 103. Lai E, Bikopoulos G, Wheeler MB, Rozakis-adcock M, Volchuk A (2008) Differential activation of ER stress and apoptosis in response to chronically elevated free fatty acids in pancreatic β -cells. *Am J Physiol Endocrinol Metab* 294: 540–550
 104. Sidrauski C, Chapman R, Walter P (1998) The unfolded protein response: an intracellular signalling pathway with many surprising features. *Trends Cell Biol* 8: 245–249
 105. Haynes CM, Titus EA, Cooper AA (2004) Degradation of misfolded proteins prevents ER-derived oxidative stress and cell death. *Mol Cell* 15: 767–776
 106. Hetz C, Saxena S (2017) ER stress and the unfolded protein response in neurodegeneration. *Nat Rev Neurol* 13: 477–491
 107. Harding HP, Novoa I, Zhang Y, Zeng H, Wek R, Schapira M, Ron D (2000) Regulated translation initiation controls stress-induced gene expression in mammalian cells. *Mol Cell* 6: 1099–1108
 108. Han J, Back SH, Hur J, Lin YH, Gildersleeve R, Shan J, Yuan CL, Krokowski D, Wang S, Hatzoglou M et al (2013) ER-stress-induced transcriptional regulation increases protein synthesis leading to cell death. *Nat Cell Biol* 15: 481–490
 109. Chen X, Shen J, Prywes R (2002) The luminal domain of ATF6 senses endoplasmic reticulum (ER) stress and causes translocation of ATF6 from the ER to the Golgi. *J Biol Chem* 277: 13045–13052
 110. Yamamoto K, Sato T, Matsui T, Sato M, Okada T, Yoshida H, Harada A, Mori K (2007) Transcriptional induction of mammalian ER quality control proteins is mediated by single or combined action of ATF6 α and XBP1. *Dev Cell* 13: 365–376
 111. Yoshida H, Matsui T, Yamamoto A, Okada T, Mori K (2001) XBP1 mRNA is induced by ATF6 and spliced by IRE1 in response to ER stress to produce a highly active transcription factor. *Cell* 107: 881–891
 112. Urano F, Urano F, Wang X, Bertolotti A, Zhang Y, Chung P, Harding HP, Ron D (2008) Coupling of stress in the ER to activation of JNK protein kinases by transmembrane protein kinase IRE1. *Science* 664: 664–667
 113. Hollien J, Weissman JS (2006) Decay of endoplasmic reticulum-localized mRNAs during the unfolded protein response. *Science* 313: 104–107
 114. Chami M, Oulès B, Szabadkai G, Tacine R, Rizzuto R, Paterlini-Bréchet P (2008) Role of SERCA1 truncated isoform in the proapoptotic calcium transfer from ER to mitochondria during ER stress. *Mol Cell* 32: 641–651
 115. Verfaillie T, Rubio N, Garg AD, Bultynck G, Rizzuto R, Decuypere JP, Piette J, Linehan C, Gupta S, Samali A et al (2012) PERK is required at the ER-mitochondrial contact sites to convey apoptosis after ROS-based ER stress. *Cell Death Differ* 19: 1880–1891
 116. Hetz C, Papa FR (2018) The unfolded protein response and cell fate control. *Mol Cell* 69: 169–181
 117. Bravo R, Vicencio JM, Parra V, Troncoso R, Munoz JP, Bui M, Quiroga C, Rodriguez AE, Verdejo HE, Ferreira J et al (2011) Increased ER – mitochondrial coupling promotes mitochondrial respiration and bioenergetics during early phases of ER stress Increased ER – mitochondrial coupling promotes mitochondrial respiration and bioenergetics during early phases of ER stress. *J Cell Sci* 124: 2143–2152
 118. Lee A, Scapa EF, Cohen DE, Glimcher LH (2008) Regulation of hepatic lipogenesis by the transcription factor XBP1. *Science* 319: 1492–1497
 119. Liu X, Henkel AS, LeCuyer BE, Hubchak SC, Schipma MJ, Zhang E, Green RM (2017) Hepatic deletion of X-box binding protein 1 impairs bile acid metabolism in mice. *J Lipid Res* 58: 504–511
 120. So JS, Hur KY, Tarrío M, Ruda V, Frank-Kamenetsky M, Fitzgerald K, Kotliansky V, Lichtman AH, Iwawaki T, Glimcher LH et al (2012) Silencing of lipid metabolism genes through ire1 α -mediated mRNA decay lowers plasma lipids in mice. *Cell Metab* 16: 487–499
 121. Ngho GA, Papanicolaou KN, Walsh K (2012) Loss of mitofusin 2 promotes endoplasmic reticulum stress. *J Biol Chem* 287: 20321–20332
 122. Gkogkas C, Middleton S, Kremer AM, Wardrope C, Hannah M, Gillingwater TH, Skehel P (2008) VAPB interacts with and modulates the activity of ATF6. *Hum Mol Genet* 17: 1517–1526
 123. Ng FWH, Nguyen M, Kwan T, Branton PE, Nicholson DW, Cromlish JA, Shore GC (1997) p28 Bap31, a Bcl-2/Bcl-XL – and procaspase-8-associated protein in the endoplasmic reticulum. *J Cell Biol* 139: 327–338
 124. Hirsch T, Marzo I, Kroemer G (1997) Role of the mitochondrial permeability transition pore in apoptosis. *Biosci Rep* 17: 67–76
 125. Schinzel AC, Takeuchi O, Huang Z, Fisher JK, Zhou Z, Rubens J, Hetz C, Dhanil NN, Moskowitz MA, Korsmeyer SJ (2005) Cyclophilin D is a component of mitochondrial permeability transition and mediates neuronal cell death after focal cerebral ischemia. *Proc Natl Acad Sci USA* 102: 12005–12010
 126. Namba T, Tian F, Chu K, Hwang SY, Yoon KW, Byun S, Hiraki M, Mandinova A, Lee SW (2013) CDIP1-BAP31 complex transduces apoptotic signals from endoplasmic reticulum to mitochondria under endoplasmic reticulum stress. *Cell Rep* 5: 331–339
 127. Peña-Blanco A, García-Sáez AJ (2018) Bax, Bak and beyond — mitochondrial performance in apoptosis. *FEBS J* 285: 416–431
 128. Korsmeyer SJ, Wei MC, Saito M, Weiler S, Oh KJ, Schlesinger PH (2000) Pro-apoptotic cascade activates BID, which oligomerizes BAK or BAX

- into pores that result in the release of cytochrome c. *Cell Death Differ* 7: 1166–1173
129. Li P, Nijhawan D, Budihardjo I, Srinivasula SM, Ahmad M, Alnemri ES, Wang X (1997) Cytochrome c and dATP-dependent formation of Apaf-1/caspase-9 complex initiates an apoptotic protease cascade. *Cell* 91: 479–489
 130. Bassik MC, Scorrano L, Oakes SA, Pozzan T, Korsmeyer SJ (2004) Phosphorylation of BCL-2 regulates ER Ca²⁺ homeostasis and apoptosis. *EMBO J* 23: 1207–1216
 131. Brooks C, Wei Q, Feng L, Dong G, Tao Y, Mei L, Xie Z, Dong Z (2007) Bak regulates mitochondrial morphology and pathology during apoptosis by interacting with mitofusins. *Proc Natl Acad Sci USA* 104: 11649–11654
 132. Hoppins S, Edlich F, Cleland MM, Banerjee S, Mccaffery JM, Youle RJ (2011) The soluble form of bax regulates mitochondrial fusion via MFN2 homotypic complexes. *Mol Cell* 41: 150–160
 133. Lamb CA, Yoshimori T, Toozze SA (2013) The autophagosome: origins unknown, biogenesis complex. *Nat Rev* 14: 759–774
 134. Tanida I, Ueno T, Kominami E (2004) LC3 conjugation system in mammalian autophagy. *Int J Biochem Cell Biol* 36: 2503–2518
 135. Gomez-Suaga P, Paillusson S, Stoica R, Noble W, Hanger DP, Miller CCJ (2017) The ER-mitochondria tethering complex VAPB-PTPIP51 regulates autophagy. *Curr Biol* 27: 371–385
 136. Ge L, Schekman R (2014) The ER-Golgi intermediate compartment feeds the phagophore membrane. *Autophagy* 10: 170–172
 137. Appenzeller-Herzog C, Hauri H (2006) The ER-Golgi intermediate compartment (ERGIC): in search of its identity and function. *J Cell Sci* 119: 2173–2183
 138. Nascimbeni AC, Giordano F, Codogno P, Morel E, Dupont N, Grasso D, Maria I (2017) ER – plasma membrane contact sites contribute to autophagosome biogenesis by regulation of local PI3P synthesis. *EMBO J* 36: 2018–2033
 139. Shinjo S, Jiang S, Nameta M, Suzuki T, Kanai M, Nomura Y, Goda N (2017) Disruption of the mitochondria-associated ER membrane (MAM) plays a central role in palmitic acid-induced insulin resistance. *Exp Cell Res* 359: 86–93
 140. Park SW, Zhou Y, Lee J, Lee J, Ozcan U (2010) Sarco(endo)plasmic reticulum Ca²⁺-ATPase 2b is a major regulator of endoplasmic reticulum stress and glucose homeostasis in obesity. *Proc Natl Acad Sci USA* 107: 19320–19325
 141. Fu S, Yang L, Li P, Hofmann O, Dicker L, Hide W, Lin X, Watkins SM, Ivanov AR (2011) Aberrant lipid metabolism disrupts calcium homeostasis causing liver endoplasmic reticulum stress in obesity. *Nature* 473: 528–531
 142. Tubbs E, Chanon S, Robert M, Bendridi N, Bidaux G, Chauvin MA, Ji-Cao J, Durand C, Gauvrit-Ramette D, Vidal H et al (2018) Disruption of mitochondria-associated endoplasmic reticulum membrane (MAM) integrity contributes to muscle insulin resistance in mice and humans. *Diabetes* 67: 636–650
 143. Bach D, Pich S, Soriano FX, Vega N, Baumgartner B, Oriola J, Daugaard JR, Lloberas J, Camps M, Zierath JR et al (2003) Mitofusin-2 determines mitochondrial network architecture and mitochondrial metabolism. A novel regulatory mechanism altered in obesity. *J Biol Chem* 278: 17190–17197
 144. Liu R, Jin P, Yu L, Wang Y, Han L, Shi T, Li X (2014) Impaired mitochondrial dynamics and bioenergetics in diabetic skeletal muscle. *PLoS One* 9: e92810
 145. Bach D, Naon D, Pich S, Soriano FX, Vega N, Rieusset J, Laville M, Cuillet C, Boirie Y, Wallberg-henriksson H et al (2005) Expression of Mfn2, the charcot-marie-tooth neuropathy type 2A gene, in human skeletal muscle: effects of type 2 diabetes, obesity, weight loss, and the regulatory role of tumor necrosis factor alpha and interleukin-6. *Diabetes* 54: 2685–2693
 146. Gastaldi G, Russell A, Golay A, Giacobino JP, Habicht F, Barthassat V, Muzzin P, Bobbioni-Harsch E (2007) Upregulation of peroxisome proliferator-activated receptor gamma coactivator gene (PGC1A) during weight loss is related to insulin sensitivity but not to energy expenditure. *Diabetologia* 50: 2348–2355
 147. Hernández-Alvarez MI, Chiellini C, Manco M, Naon D, Liesa M, Palacín M, Mingrone G, Zorzano A (2009) Genes involved in mitochondrial biogenesis/function are induced in response to bilio-pancreatic diversion in morbidly obese individuals with normal glucose tolerance but not in type 2 diabetic patients. *Diabetologia* 52: 1618–1627
 148. Mingrone G, Manco M, Calvani M, Castagneto M, Naon D, Zorzano A (2005) Could the low level of expression of the gene encoding skeletal muscle mitofusin-2 account for the metabolic inflexibility of obesity? *Diabetologia* 48: 2108–2114
 149. Hernández-Alvarez MI, Thabit H, Burns N, Shah S, Brema I, Hatunic M, Finucane F, Liesa M, Chiellini C, Naon D et al (2010) Subjects with early-onset type 2 diabetes show defective activation of the skeletal. *Diabetes Care* 33: 645–651
 150. Yang C, Aye CC, Li X, Diaz Ramos A, Zorzano A, Mora S (2012) Mitochondrial dysfunction in insulin resistance: differential contributions of chronic insulin and saturated fatty acid exposure in muscle cells. *Biosci Rep* 32: 465–478
 151. Wold LE, Dutta K, Mason MM, Ren J, Cala SE, Schwanke ML, Davidoff AJ (2005) Impaired SERCA function contributes to cardiomyocyte dysfunction in insulin resistant rats. *J Mol Cell Cardiol* 39: 297–307
 152. Thivolet C, Vial G, Cassel R, Rieusset J, Madec A-M (2017) Reduction of endoplasmic reticulum mitochondria interactions in beta cells from patients with type 2 diabetes. *PLoS One* 12: e0182027
 153. Zhang E, Mohammed Al-Amily I, Mohammed S, Luan C, Asplund O, Ahmed M, Ye Y, Ben-Hail D, Soni A, Vishnu N et al (2018) Preserving insulin secretion in diabetes by inhibiting VDAC1 overexpression and surface translocation in β cells. *Cell Metab* 29: 64–77
 154. Ahmed M, Muhammed SJ, Kessler B, Salehi A (2010) Mitochondrial proteome analysis reveals altered expression of voltage dependent anion channels in pancreatic β -cells exposed to high glucose. *Islets* 2: 283–292
 155. Mckenzie MD, Jamieson E, Jansen ES, Scott CL, Huang DCS, Bouillet P, Allison J, Kay TWH, Strasser A, Thomas HE (2010) Glucose induces pancreatic islet cell apoptosis that requires the BH3-only proteins bim and puma and multi-bh domain protein bax. *Diabetes* 59: 644–652
 156. Schneeberger M, Dietrich MO, Sebastián D, Imbernón M, Castaño C, García A, Esteban Y, Gonzalez-Franquesa A, Rodríguez IC, Bortolozzi A et al (2013) Mitofusin 2 in POMC neurons connects ER stress with leptin resistance and energy imbalance. *Cell* 155: 172–187
 157. Filipilli BM, Abraham MA, Silva PN, Rasti M, LaPierre MP, Bauer PV, Rocheleau JV, Lam TKT (2017) Dynamin-related protein 1-dependent mitochondrial fission changes in the dorsal vagal complex regulate insulin action. *Cell Rep* 18: 2301–2309
 158. Zhao L, Lu T, Gao L, Fu X, Zhu S, Hou Y (2017) Enriched endoplasmic reticulum-mitochondria interactions result in mitochondrial dysfunction and apoptosis in oocytes from obese mice. *J Anim Sci Biotechnol* 8: 1–8
 159. Sood A, Vijey D, Prudent J, Caron A, Lemieux P, McBride HM, Laplante M, Tóth K, Pellegrini L (2014) A mitofusin-2 – dependent inactivating

- cleavage of Opa1 links changes in mitochondria cristae and ER contacts in the postprandial liver. *Proc Natl Acad Sci USA* 111: 16017–16022
160. Theurey P, Tubbs E, Vial G, Jacquemetton J, Bendridi N, Chauvin MA, Alam MR, Le Romancer M, Vidal H, Rieusset J (2016) Mitochondria-associated endoplasmic reticulum membranes allow adaptation of mitochondrial metabolism to glucose availability in the liver. *J Mol Cell Biol* 8: 129–143
161. Báez-Ruiz A, Cázares-Gómez K, Vázquez-Martínez O, Aguilar-Roblero R, Díaz-Muñoz M (2013) Diurnal and nutritional adjustments of intracellular Ca^{2+} release channels and Ca^{2+} ATPases associated with restricted feeding schedules in the rat liver. *J Circadian Rhythms* 11: 1–17
162. Levine B (2005) Eating oneself and uninvited guests: autophagy-related pathways in cellular defense. *Cell* 120: 159–162
163. Hailey DW, Rambold AS, Satpute-Krishnan P, Mitra K, Sougrat R, Kim PK, Lippincott-Schwartz J (2010) Mitochondria supply membranes for autophagosome biogenesis during starvation. *Cell* 141: 656–667
164. Mihai AD, Schröder M (2015) Glucose starvation and hypoxia, but not the saturated fatty acid palmitic acid or cholesterol, activate the unfolded protein response in 3T3-F442A and 3T3-L1 adipocytes. *Adipocyte* 4: 188–202
165. Shao M, Shan B, Liu Y, Deng Y, Yan C, Wu Y, Mao T, Qiu Y, Zhou Y, Jiang S et al (2014) Hepatic IRE1 α regulates fasting-induced metabolic adaptive programs through the XBP1s-PPAR α axis signalling. *Nat Commun* 5: 3528
166. Sebastian D, Hernandez-Alvarez MI, Segales J, Sorianello E, Munoz JP, Sala D, Waget A, Liesa M, Paz JC, Gopalacharyulu P et al (2012) Mitofusin 2 (Mfn2) links mitochondrial and endoplasmic reticulum function with insulin signaling and is essential for normal glucose homeostasis. *Proc Natl Acad Sci USA* 109: 5523–5528
167. Sebastián D, Sorianello E, Segalés J, Irazoki A, Ruiz-Bonilla V, Sala D, Planet E, Berenguer-Llergo A, Muñoz JP, Sánchez-Feutrie M et al (2016) Mfn2 deficiency links age-related sarcopenia and impaired autophagy to activation of an adaptive mitophagy pathway. *EMBO J* 35: 1677–1693
168. Kulkarni SS, Joffraud M, Boutant M, Ratajczak J, Gao AW, MacLachlan C, Hernandez Alvarez MI, Raymond F, Metairon S, Descombes P et al (2016) Mfn1 deficiency in the liver protects against diet-induced insulin resistance and enhances the hypoglycemic effect of metformin. *Diabetes* 65: 3552–3560
169. Mahdavian K, Benador IY, Su S, Gharakhanian RA, Stiles L, Trudeau KM, Cardamone M, Enriquez-Zarralanga V, Ritou E, Aprahamian T et al (2017) Mfn2 deletion in brown adipose tissue protects from insulin resistance and impairs thermogenesis. *EMBO Rep* 18: 1123–1138
170. Dietrich MO, Liu ZW, Horvath TL (2013) Mitochondrial dynamics controlled by mitofusins regulate agrp neuronal activity and diet-induced obesity. *Cell* 155: 188–199
171. Ramírez S, Gómez-Valadés AG, Schneeberger M, Varela L, Haddad-Tóvelli R, Altirriba J, Noguera E, Drougard A, Flores-Martínez Á, Imbernon M et al (2017) Mitochondrial dynamics mediated by mitofusin 1 is required for POMC neuron glucose-sensing and insulin release control. *Cell Metab* 25: 1390–1399.e6
172. Starecki D, Hong SK, Lloyd RV, Park JJ (2015) Mortalin (GRP75/HSPA9) upregulation promotes survival and proliferation of medullary thyroid carcinoma cells. *Oncogene* 34: 4624–4634
173. Burbulla LF, Fitzgerald JC, Stegen K, Westermeier J, Thost AK, Kato H, Mokranjac D, Sauerwald J, Martins LM, Weitalla D et al (2014) Mitochondrial proteolytic stress induced by loss of mortalin function is rescued by Parkin and PINK1. *Cell Death Dis* 5: 1–19
174. Xu J-L, Li L-Y, Wang Y-Q, Li Y-Q, Shan M, Sun S-Z, Yu Y, Wang B (2018) Hepatocyte-specific deletion of BAP31 promotes SREBP1C activation, promotes hepatic lipid accumulation, and worsens IR in mice. *J Lipid Res* 59: 35–47
175. Wu Z, Yang F, Jiang S, Sun X, Xu J (2018) Induction of liver steatosis in BAP31-deficient mice burdened with tunicamycin-induced endoplasmic reticulum stress. *Int J Mol Sci* 19: 1–16
176. Rieusset J, Fauconnier J, Paillard M, Belaidi E, Tubbs E, Chauvin M, Durand A, Bravard A, Teixeira G, Bartosch B et al (2016) Disruption of calcium transfer from ER to mitochondria links alterations of mitochondria-associated ER membrane integrity to hepatic insulin resistance. *Diabetologia* 59: 614–623
177. Özcan U, Cao Q, Yilmaz E, Lee A-H, Iwakoshi NN, Özdelen E, Tuncman G, Görgün C, Glimcher LH, Hotamisligil GS (2004) Endoplasmic reticulum stress links obesity, insulin action, and type 2 diabetes. *Science* 306: 457–461
178. Baiceanu A, Mesdom P, Lagoue M, Foufelle F (2016) Endoplasmic reticulum proteostasis in hepatic steatosis. *Nat Rev Endocrinol* 12: 710–722
179. Frakes AE, Dillin A (2017) The UPRER: sensor and coordinator of organismal homeostasis. *Mol Cell* 66: 761–771
180. Shpilka T, Haynes CM (2018) The mitochondrial UPR: mechanisms, physiological functions and implications in ageing. *Nat Rev Mol Cell Biol* 19: 109–120
181. Chen KH, Dasgupta A, Ding J, Indig FE, Ghosh P, Longo DL (2014) Role of mitofusin 2 (Mfn2) in controlling cellular proliferation. *FASEB J* 28: 382–394
182. de Brito OM, Scorrano L (2009) Mitofusin-2 regulates mitochondrial and endoplasmic reticulum morphology and tethering: the role of Ras. *Mitochondrion* 9: 222–226
183. Klawitter J, Seres T, Pennington A, Beatty JT, Klawitter J, Christians U (2017) Ablation of cyclophilin D results in an activation of FAK, Akt, and ERK pathways in the mouse heart. *J Cell Biochem* 118: 2933–2940
184. Kim W-T, Choi HS, Lee HM, Jang Y-J, Ryu CJ (2014) B-cell receptor-associated protein 31 regulates human embryonic stem cell adhesion, stemness, and survival via control of epithelial cell adhesion molecule. *Stem Cells* 32: 2626–2641
185. Choi JH, Banks AS, Estall JL, Kajimura S, Boström P, Laznik D, Ruas JL, Chalmers MJ, Kamenecka TM, Blüher M et al (2010) Anti-diabetic drugs inhibit obesity-linked phosphorylation of PPAR γ 3 by Cdk5. *Nature* 466: 451–456
186. Banks AS, McAllister FE, Camporez JPC, Zushin PJH, Jurczak MJ, Laznik-Bogoslavski D, Shulman GI, Gygi SP, Spiegelman BM (2015) An ERK/Cdk5 axis controls the diabetogenic actions of PPAR γ . *Nature* 517: 391–395
187. Fu T, Xu Z, Liu L, Guo Q, Wu H, Liang X, Zhou D, Xiao L, Liu L, Liu Y et al (2018) Mitophagy directs muscle-adipose crosstalk to alleviate dietary obesity. *Cell Rep* 23: 1357–1372
188. Krzyśiak TC, Thomas L, Choi Y, Auclair S, Qian Y, Luan S, Krasnow SM, Thomas LL, Koharudin LMI, Benos PV et al (2018) An insulin-responsive sensor in the SIRT1 disordered region binds DBC1 and PACS-2 to control enzyme activity. *Mol Cell* 72: 985–998.e7
189. Potthoff MJ (2017) FGF21 and metabolic disease in 2016: a new frontier in FGF21 biology. *Nat Rev Endocrinol* 13: 74–76
190. Kharitononkov A, Shyanova TL, Koester A, Ford AM, Micanovic R, Galbreath EJ, Sandusky GE, Hammond LJ, Moyers JS, Owens RA et al

- (2005) FGF-21 as a novel metabolic regulator. *J Clin Invest* 115: 1627–1635
191. Luciani DS, White SA, Widenmaier SB, Saran VV, Taghizadeh F, Hu X, Allard MF, Johnson JD (2013) Bcl-2 and Bcl-xl suppress glucose signaling in pancreatic b-cells. *Diabetes* 62: 170–182
 192. Liu X, Li L, Li J, Cheng Y, Chen J (2016) Insulin resistance contributes to multidrug resistance in HepG2 cells via activation of the PERK signaling pathway and upregulation of Bcl-2 and P-gp. *Oncol Rep* 35: 3018–3024
 193. Ye R, Ni M, Wang M, Luo S, Zhu G, Chow RH, Lee AS (2011) Inositol 1,4,5-trisphosphate receptor 1 mutation perturbs glucose homeostasis and enhances susceptibility to diet-induced diabetes. *J Endocrinol* 210: 209–217
 194. Arif T, Paul A, Krelin Y, Shteinfer-Kuzmine A, Shoshan-Barmatz V (2018) Mitochondrial VDAC1 silencing leads to metabolic rewiring and the reprogramming of tumour cells into advanced differentiated states. *Cancers (Basel)* 10: E499
 195. Arif T, Krelin Y, Nakdimon I, Benharroch D, Paul A, Dadon-Klein D, Shoshan-Barmatz V (2017) VDAC1 is a molecular target in glioblastoma, with its depletion leading to reprogrammed metabolism and reversed oncogenic properties. *Neuro Oncol* 19: 951–964
 196. Chen H, Gao W, Yang Y, Guo S, Wang H, Wang W, Zhang S, Zhou Q, Xu H, Yao J et al (2014) Inhibition of VDAC1 prevents Ca²⁺-mediated oxidative stress and apoptosis induced by 5-aminolevulinic acid mediated sonodynamic therapy in THP-1 macrophages. *Apoptosis* 19: 1712–1726
 197. Lamming DW, Ye L, Katajisto P, Goncalves MD, Saitoh M, Stevens DM, Davis JG, Salmon AB, Richardson A, Ahima RS et al (2012) Rapamycin-induced insulin resistance is mediated by mTORC2 loss and uncoupled from longevity. *Science* 335: 1638–1643
 198. Peralta S, Goffart S, Williams SL, Diaz F, Garcia S, Nissanka N, Area-Gomez E, Pohjoismäki J, Moraes CT (2018) ATAD3 controls mitochondrial cristae structure in mouse muscle, influencing mtDNA replication and cholesterol levels. *J Cell Sci* 131: jcs217075
 199. Desai R, Frazier AE, Durigon R, Patel H, Jones AW, Rosa ID, Lake NJ, Compton AG, Mountford HS, Tucker EJ et al (2017) ATAD3 gene cluster deletions cause cerebellar dysfunction associated with altered mitochondrial DNA and cholesterol metabolism. *Brain* 140: 1595–1610
 200. Issop L, Fan J, Lee S, Rone MB, Basu K, Mui J, Papadopoulos V (2015) Mitochondria-associated membrane formation in hormone-stimulated leydig cell steroidogenesis: role of ATAD3. *Endocrinology* 156: 334–345
 201. Beaslas O, Metso J, Nissila E, Laurila PP, Kaiharju E, Batchu KC, Kaipainen L, Mayranpaa MI, Yan D, Gylling H et al (2013) Osbp18 deficiency in mouse causes an elevation of high-density lipoproteins and gender-specific alterations of lipid metabolism. *PLoS One* 8: e58856
 202. Wang H, Sreenivasan U, Gong D-W, O'Connell KA, Dabkowski ER, Hecker PA, Ionica N, Konig M, Mahurkar A, Sun Y et al (2013) Cardiomyocyte-specific perilipin 5 overexpression leads to myocardial steatosis and modest cardiac dysfunction. *J Lipid Res* 54: 953–965
 203. Tarnopolsky MA, Rennie CD, Robertshaw HA, Fedak-Tarnopolsky SN, Devries MC, Hamadeh MJ (2006) Influence of endurance exercise training and sex on intramyocellular lipid and mitochondrial ultrastructure, substrate use, and mitochondrial enzyme activity. *Am J Physiol Regul Integr Comp Physiol* 292: R1271–R1278
 204. Shiozaki M, Hayakawa N, Shibata M, Koike M, Uchiyama Y, Gotow T (2011) Closer association of mitochondria with lipid droplets in hepatocytes and activation of Kupfer cells in resveratrol-treated senescence-accelerated mice. *Histochem Cell Biol* 136: 475–489
 205. Yu J, Zhang S, Cui L, Wang W, Na H, Zhu X, Li L, Xu G, Yang F, Christian M et al (2015) Lipid droplet remodeling and interaction with mitochondria in mouse brown adipose tissue during cold treatment. *Biochim Biophys Acta* 1853: 918–928
 206. Rambold AS, Cohen S, Lippincott-Schwartz J (2015) Fatty acid trafficking in starved cells: regulation by lipid droplet lipolysis, autophagy, and mitochondrial fusion dynamics. *Dev Cell* 32: 678–692
 207. Nguyen TB, Louie SM, Daniele JR, Tran Q, Dillin A, Zoncu R, Nomura DK, Olzmann JA (2017) DGAT1-dependent lipid droplet biogenesis protects mitochondrial function during starvation-induced autophagy. *Dev Cell* 42: 9–21.e5
 208. Cahill GF (1970) Starvation in man. *N Engl J Med* 282: 668–675
 209. Young PA, Senkal CE, Suchanek AL, Grevengoed TJ, Lin DD, Zhao L, Crunk AE, Klett EL, Füllekrug J, Obeid LM et al (2018) Long-chain acyl-CoA synthetase 1 interacts with key proteins that activate and direct fatty acids into niche hepatic pathways. *J Biol Chem* 293: 16724–16740
 210. Jägerström S, Polesie S, Wickström Y, Johansson BR, Schröder HD, Højlund K, Boström P (2009) Lipid droplets interact with mitochondria using SNAP23. *Cell Biol Int* 33: 934–940
 211. Boström P, Andersson L, Rutberg M, Perman J, Lidberg U, Johansson BR, Fernandez-Rodriguez J, Ericson J, Nilsson T, Borén J et al (2007) SNARE proteins mediate fusion between cytosolic lipid droplets and are implicated in insulin sensitivity. *Nat Cell Biol* 9: 1286–1293
 212. Wang H, Sreenivasan U, Hu H, Saladino A, Polster BM, Lund LM, Gong D, Stanley WC, Sztalryd C (2011) Perilipin 5, a lipid droplet-associated protein, provides physical and metabolic linkage to mitochondria. *J Lipid Res* 52: 2159–2168
 213. Bosma M, Minnaard R, Sparks LM, Schaart G, Losen M, De Baets MH, Duimel H, Kersten S, Bickel PE, Schrauwen P et al (2012) The lipid droplet coat protein perilipin 5 also localizes to muscle mitochondria. *Histochem Cell Biol* 137: 205–216
 214. Granneman JG, Moore HPH, Mottillo EP, Zhu Z, Zhou L (2011) Interactions of Perilipin-5 (Plin5) with adipose triglyceride lipase. *J Biol Chem* 286: 5126–5135
 215. Calderon-Dominguez M, Mir JF, Fucho R, Weber M, Serra D, Herrero L (2016) Fatty acid metabolism and the basis of brown adipose tissue function. *Adipocyte* 5: 98–118
 216. Herms A, Bosch M, Reddy BJN, Schieber NL, Fajardo A, Ruperez C, Fernandez-Vidal A, Ferguson C, Rentero C, Tebar F et al (2015) AMPK activation promotes lipid droplet dispersion on detyrosinated microtubules to increase mitochondrial fatty acid oxidation. *Nat Commun* 6: 1–14
 217. Sath K, Rai P, Mallik R (2017) Feeding-fasting dependent recruitment of membrane microdomain proteins to lipid droplets purified from the liver. *PLoS One* 12: e0183022
 218. Kramer DA, Quiroga AD, Lian J, Fahlman RP, Lehner R (2018) Fasting and refeeding induces changes in the mouse hepatic lipid droplet proteome. *J Proteomics* 181: 213–224
 219. Sohn JH, Lee YK, Han JS, Jeon YG, Kim JI, Cho SS, Kim SJ, Yoo HJ, Kim JB (2018) Perilipin 1 (Plin1) deficiency promotes inflammatory responses in lean adipose tissue through lipid dysregulation. *J Biol Chem* 293: 13974–13988
 220. Laurens C, Bourlier V, Mairal A, Louche K, Badin PM, Mouiel E, Montagner A, Marette A, Tremblay A, Weinsagel JS et al (2016) Perilipin 5 fine-tunes lipid oxidation to metabolic demand and protects against lipotoxicity in skeletal muscle. *Sci Rep* 6: 1–12

221. Morton TL, Galior K, McGrath C, Wu X, Uzer G, Uzer GB, Sen B, Xie Z, Tyson D, Rubin J et al (2016) Exercise increases and browns muscle lipid in high-fat diet-fed mice. *Front Endocrinol (Lausanne)* 7: 1–8
222. Gemmink A, Daemen S, Brouwers B, Huntjens PR, Schaart G, Moonen-Kornips E, Jörgensen J, Hoeks J, Schrauwen P, Hesselink MKC (2018) Dissociation of intramyocellular lipid storage and insulin resistance in trained athletes and type 2 diabetes patients; involvement of perilipin 5? *J Physiol* 596: 857–868
223. Covington JD, Noland RC, Hebert RC, Masinter BS, Smith SR, Rustan AC, Ravussin E, Bajpeyi S (2015) Perilipin 3 differentially regulates skeletal muscle lipid oxidation in active, sedentary, and type 2 diabetic males. *J Clin Endocrinol Metab* 100: 3683–3692
224. Keenan SN, Meex RC, Lo JCY, Ryan A, Nie S, Magdalene K (2019) Perilipin 5 deletion in hepatocytes remodels lipid metabolism and causes hepatic insulin resistance in mice. *Diabetes* 68: 543–555
225. Montgomery MK, Mokhtar R, Bayliss J, Parkinson HC, Suturin VM, Bruce CR, Watt MJ (2018) Perilipin 5 deletion unmasks an endoplasmic reticulum Stress-Fibroblast growth factor 21 axis in skeletal muscle. *Diabetes* 67: 594–606
226. Harris LALS, Skinner JR, Shew TM, Pietka TA, Abumrad NA, Wolins NE (2015) Perilipin 5-driven lipid droplet accumulation in skeletal muscle stimulates the expression of fibroblast growth factor 21. *Diabetes* 64: 2757–2768
227. Wei S, Liu S, Su X, Wang W, Li F, Deng J, Lyu Y, Geng B, Xu G (2018) Spontaneous development of hepatosteatosis in perilipin-1 null mice with adipose tissue dysfunction. *Biochim Biophys Acta* 1863: 212–218
228. Liu S, Geng B, Zou L, Wei S, Wang W, Deng J, Xu C, Zhao X, Lyu Y, Su X et al (2015) Development of hypertrophic cardiomyopathy in perilipin-1 null mice with adipose tissue dysfunction. *Cardiovasc Res* 105: 20–30
229. Langlois D, Forcheron F, Li JY, Del Carmine P, Neggazi S, Beylot M (2011) Increased atherosclerosis in mice deficient in perilipin1. *Lipids Health Dis* 10: 1–6
230. Nguyen TN, Padman BS, Lazarou M (2016) Deciphering the molecular signals of PINK1/parkin mitophagy. *Trends Cell Biol* 26: 733–744
231. Sugiura A, Mclelland G, Fon EA, McBride HM (2014) A new pathway for mitochondrial quality control: mitochondrial-derived vesicles. *EMBO J* 33: 2142–2156
232. Raimundo N, Fernández-mosquera L, Yambire KF, Diogo CV (2016) Mechanisms of communication between mitochondria and lysosomes. *Int J Biochem Cell Biol* 79: 345–349
233. Han Y, Li M, Qiu F, Zhang M, Zhang Y-H (2017) Cell-permeable organic fluorescent probes for live-cell long-term super-resolution imaging reveal lysosome-mitochondrion interactions. *Nat Commun* 8: 1307–1316
234. Zhao T, Huang X, Han L, Wang X, Cheng H, Zhao Y, Chen Q, Chen J, Cheng H, Xiao R et al (2012) Central role of mitofusin 2 in autophagosome-lysosome fusion in cardiomyocytes. *J Biol Chem* 287: 23615–23625
235. Cioni J, Lin JQ, Holtermann AV, Franze K, Harris WA, Holt CE, Cioni J, Lin JQ, Holtermann AV, Koppers M et al (2019) Late endosomes act as mRNA translation platforms and sustain mitochondria in axons article late endosomes act as mRNA translation platforms and sustain mitochondria in axons. *Cell* 176: 56–72.e15
236. Muñoz-Braceras S, Tornero-Écija AR, Vincent O, Escalante R (2019) VPS13A is closely associated with mitochondria and is required for efficient lysosomal degradation. *Dis Model Mech* 12: 1–13
237. Zhang X, Walsh B, Mitchell CA, Rowe T (2005) TBC domain family, member 15 is a novel mammalian Rab GTPase-activating protein with substrate preference for Rab7. *Biochem Biophys Res Commun* 335: 154–161
238. Kumar N, Leonzino M, Cerutti WH, Horenkamp FA, Li P, Lees JA (2018) VPS13A and VPS13C are lipid transport proteins differentially localized at ER contact sites. *J Cell Biol* 217: 3625–3639
239. Itoh K, Adachi Y, Yamada T, Suzuki TL, Otomo T, McBride HM, Yoshimori T, Iijima M, Sesaki H (2018) A brain-enriched Drp1 isoform associates with lysosomes, late endosomes, and the plasma membrane. *J Biol Chem* 293: 11809–11822
240. Kon K, Kim J, Uchiyama A, Jaeschke H, Lemasters JJ (2010) Lysosomal iron mobilization and induction of the mitochondrial permeability transition in acetaminophen-induced toxicity to mouse hepatocytes. *Toxicol Sci* 117: 101–108
241. König J, Ott C, Hugo M, Jung T (2017) Mitochondrial contribution to lipofuscin formation. *Redox Biol* 11: 673–681
242. Mukhopadhyay A, Pan X, Lambright DG, Tissenbaum HA (2007) An endocytic pathway as a target of tubby for regulation of fat storage. *EMBO Rep* 8: 931–938
243. Ding X, Zhang W, Zhao T, Yan C, Du H (2017) Rab7 GTPase controls lipid metabolic signaling in myeloid-derived suppressor cells. *Oncotarget* 8: 30123–30137
244. Wu J, Cheng D, Liu L, Lv Z, Liu K (2019) TBC1D15 affects glucose uptake by regulating GLUT4 translocation. *Gene* 683: 210–215
245. Hönscher C, Mari M, Auffarth K, Bohnert M, Griffith J, Ceerts W, Van Der Laan M (2014) Cellular metabolism regulates contact sites between vacuoles and mitochondria. *Dev Cell* 30: 86–94
246. Gonzalez Montoro A, Kathrin A, Honscher C, Bohnert M, Becker T, Warscheid B, Reggiori F, van der Laan M, Frohlich F, Ungermann C (2018) Vps39 interacts with Tom40 to establish one of two functionally distinct vacuole-mitochondria contact sites. *Dev Cell* 45: 621–636
247. Norambuena A, Wallrabe H, Cao R, Wang DB, Silva A, Svindrych Z, Periasamy A, Hu S, Tanzi RE, Kim DY et al (2018) A novel lysosome-to-mitochondria signaling pathway disrupted by amyloid- β oligomers. *EMBO J* 37: 1–18
248. Islinger M, Lüers GH, Zischka H, Ueffing M, Völkl A (2006) Insights into the membrane proteome of rat liver peroxisomes: microsomal glutathione-S-transferase is shared by both subcellular compartments. *Proteomics* 6: 804–816
249. Horner SM, Wilkins C, Badil S, Iskarpatyoti J (2015) Proteomic analysis of mitochondrial-associated ER membranes (MAM) during RNA virus infection reveals dynamic changes in protein and organelle trafficking. *PLoS One* 10: e0117963
250. Horner SM, Liu HM, Park HS, Briley J, Gale M (2011) Mitochondrial-associated membranes (MAM) form innate immune synapses and are targeted by hepatitis C virus. *Proc Natl Acad Sci USA* 108: 14590–14595
251. Schrader M, Costello J, Godinho LF, Islinger M (2015) Peroxisome-mitochondria interplay and disease. *J Inherit Metab Dis* 38: 681–702
252. Otera H, Mihara K (2011) Discovery of the membrane receptor for mitochondrial fission GTPase Drp1. *Small GTPases* 2: 167–172
253. Kirichok Y, Krapivinsky G, Clapham DE (2004) The mitochondrial calcium uniporter is a highly selective ion channel. *Nature* 427: 360–364

RESEARCH ARTICLE:

**Deficient Endoplasmic Reticulum-Mitochondrial
Phosphatidylserine Transfer Causes Liver Disease**

María Isabel Hernández-Alvarez, David Sebastián, Sara Vives, Saška Ivanova, Paola Bartoccioni, Pamela Kakimoto, Natalia Plana, Sónia R. Veiga, Vanessa Hernández, Nuno Vasconcelos, Gopal Peddinti, Anna Adrover, Mariona Jové, Reinald Pamplona, Isabel Gordaliza-Alaguero, Enrique Calvo, Noemí Cabré, Rui Castro, Antonija Kuzmanic, Marie Boutant, David Sala, Tuulia Hyotylainen, Matej Orešič, Joana Fort, Ekaitz Errasti-Murugarren, Cecilia M.P. Rodrigues, Modesto Orozco, Jorge Joven, Carles Cantó, Manuel Palacin, Sonia Fernández-Veledo, Joan Vendrell, Antonio Zorzano

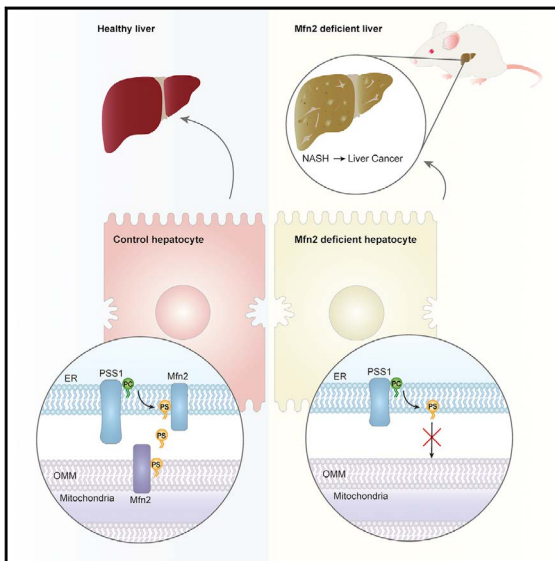
Cell, Vol. 117(4), pp. 881-895, May 2019

doi.org/10.1016/j.cell.2019.04.010

Cell

Deficient Endoplasmic Reticulum-Mitochondrial Phosphatidylserine Transfer Causes Liver Disease

Graphical Abstract



Authors

María Isabel Hernández-Alvarez, David Sebastián, Sara Vives, ..., Sonia Fernández-Veledo, Joan Vendrell, Antonio Zorzano

Correspondence

misabel.hernandez.alvarez@gmail.com (M.I.H.-A.), antonio.zorzano@irbbarcelona.org (A.Z.)

In Brief

The mitochondrial protein mitofusin 2 binds and transfers phosphatidylserine across mitochondria-ER contacts, and perturbation of this process leads to aberrant lipid metabolism and liver diseases like NASH, NAFLD, and cancer.

Highlights

- Mfn2 binds directly and specifically to phosphatidylserine (PS)
- Hepatic Mfn2 deficiency causes a reduced transfer of PS from ER to mitochondria
- Mfn2 ablation in liver causes a NASH-like phenotype and liver cancer
- A defective transfer of PS from ER to mitochondria causes liver disease



Hernández-Alvarez et al., 2019, *Cell* 177, 881–895
 May 2, 2019 © 2019 Published by Elsevier Inc.
<https://doi.org/10.1016/j.cell.2019.04.010>

CellPress

Article

Deficient Endoplasmic Reticulum-Mitochondrial Phosphatidylserine Transfer Causes Liver Disease

María Isabel Hernández-Alvarez,^{1,2,4,12,*} David Sebastián,^{1,3,4} Sara Vives,¹ Saska Ivanova,^{1,3,4} Paola Bartoccioni,^{1,5} Pamela Kakimoto,^{1,16} Natalia Plana,¹ Sónia R. Veiga,⁶ Vanessa Hernández,¹ Nuno Vasconcelos,¹ Gopal Peddinti,⁷ Anna Adrover,¹ Mariona Jové,¹⁸ Reinald Pamplona,¹⁸ Isabel Gordaliza-Alaguero,^{1,3,4} Enrique Calvo,^{2,12} Noemí Cabré,^{2,14,15} Rui Castro,⁸ Antonija Kuzmanic,¹ Marie Boutant,⁹ David Sala,¹⁷ Tuulia Hyötyläinen,¹⁰ Matej Orešič,¹¹ Joana Fort,^{1,3,5} Ekaitz Errasti-Murugarren,¹ Cecilia M.P. Rodrigues,⁸ Modesto Orozco,¹ Jorge Joven,^{2,14,15} Carles Cantó,⁹ Manuel Palacin,^{1,3,5} Sonia Fernández-Veledo,^{2,4,12} Joan Vendrell,^{2,4,12,19} and Antonio Zorzano^{1,3,4,19,*}

¹Institute for Research in Biomedicine (IRB Barcelona), The Barcelona Institute of Science and Technology, Barcelona, Spain

²Institut Investigació Sanitària Pere Virgili (IISPV), Reus, Spain

³Departament de Bioquímica i Biomedicina Molecular, Facultat de Biologia, Barcelona, Spain

⁴CIBER de Diabetes y Enfermedades Metabólicas Asociadas (CIBERDEM), Instituto de Salud Carlos III, Madrid, Spain

⁵CIBERER, Instituto de Salud Carlos III, Madrid, Spain

⁶Laboratory of Metabolism and Cancer, Catalan Institute of Oncology, ICO, Bellvitge Biomedical Research Institute (IDIBELL), Barcelona, Spain

⁷VTT Technical Research Center of Finland, Espoo, Finland

⁸Research Institute for Medicines (iMed.Ulisboa), and Department of Biochemistry and Human Biology, Faculty of Pharmacy, Universidade de Lisboa, Lisboa, Portugal

⁹Nestlé Institute of Health Sciences SA, Lausanne, Switzerland

¹⁰Department of Chemistry, University of Örebro, Örebro, Sweden

¹¹Turku Centre for Biotechnology, University of Turku and Åbo Akademi University, Turku, Finland

¹²Hospital Universitari de Tarragona Joan XXIII, Tarragona, Spain

¹³Universitat Rovira i Virgili, Tarragona, Spain

¹⁴Universitat Rovira i Virgili, Department of Medicine and Surgery, Reus, Spain

¹⁵Unitat de Recerca Biomèdica, Hospital Universitari Sant Joan, Reus, Spain

¹⁶Departamento de Bioquímica, Instituto de Química, Universidad de São Paulo, São Paulo, Brazil

¹⁷Development, Aging and Regeneration Program, Sanford Burnham Prebys Medical Discovery Institute, La Jolla, CA, USA

¹⁸Department of Experimental Medicine, University of Lleida-Lleida Biomedical Research Institute (UdL-IRBLleida), Lleida, Spain

¹⁹Lead Contact

*Correspondence: misabel.hernandez.alvarez@gmail.com (M.I.H.-A.), antonio.zorzano@irbbarcelona.org (A.Z.)

<https://doi.org/10.1016/j.cell.2019.04.010>

SUMMARY

Non-alcoholic fatty liver is the most common liver disease worldwide. Here, we show that the mitochondrial protein mitofusin 2 (Mfn2) protects against liver disease. Reduced Mfn2 expression was detected in liver biopsies from patients with non-alcoholic steatohepatitis (NASH). Moreover, reduced Mfn2 levels were detected in mouse models of steatosis or NASH, and its re-expression in a NASH mouse model ameliorated the disease. Liver-specific ablation of Mfn2 in mice provoked inflammation, triglyceride accumulation, fibrosis, and liver cancer. We demonstrate that Mfn2 binds phosphatidylserine (PS) and can specifically extract PS into membrane domains, favoring PS transfer to mitochondria and mitochondrial phosphatidylethanolamine (PE) synthesis. Consequently, hepatic Mfn2 deficiency reduces PS transfer and phospholipid synthesis, leading to endoplasmic reticulum (ER) stress and the development of a NASH-like phenotype and liver cancer. Ablation of Mfn2 in liver reveals that disrup-

tion of ER-mitochondrial PS transfer is a new mechanism involved in the development of liver disease.

INTRODUCTION

Non-alcoholic fatty liver disease (NAFLD) represents a clinical spectrum ranging from simple steatosis and non-alcoholic steatohepatitis (NASH) to cirrhosis and hepatocellular carcinoma (HCC) (Chalasani et al., 2012). NASH is accompanied by inflammation, cell death, and fibrosis and is characterized histologically by the presence of ballooning hepatocytes and lobular inflammation with or without perisinusoidal fibrosis and steatosis (Yeh and Brunt, 2014). In the course of the inflammatory process, liver hepatocytes frequently die by programmed cell death. The persistent cycle of “necro-inflammation” and hepatocyte regeneration is believed to enhance the risk of genetic mutation in hepatocytes, promoting survival and expansion of initiated cells. The result is increased cell growth, also referred to as compensatory proliferation, which can lead to tumor development (Aravalli et al., 2008). In this context, epidemiological and clinical studies have provided convincing evidence that chronic inflammation leads to carcinogenesis (Mantovani et al., 2008).



Several potential factors influencing NASH progression are known to interact (Tig and Hotamisligil, 2006) such as endoplasmic reticulum (ER) stress, oxidative stress, mitochondrial dysfunction, and lipotoxicity. Mitochondrial function is governed by the preservation of a normal lipid composition (Schenkel and Bakovic, 2014), which is dependent on the capacity of mitochondria to synthesize phospholipids, and by the traffic of lipids from the ER to mitochondria (Osman et al., 2011). Specifically, phosphatidylserine (PS) is primarily synthesized in the ER and is imported into mitochondria by transient membrane contact between mitochondria-associated ER membranes (MAMs) and the mitochondrial outer membrane (Vance and Vance, 2004). In mitochondria, PS is converted into phosphatidylethanolamine (PE), which is then imported into the ER for conversion to phosphatidylcholine (PC). Accordingly, MAMs are key sites for synthesis and traffic of phospholipids (Flis and Daum, 2013).

Mitofusin 2 (Mfn2) is a mitochondrial membrane protein with a role connecting ER membranes to mitochondria (de Brito and Scorrano, 2008; Leal et al., 2016), and its depletion causes ER stress and plays a relevant role in the maintenance of mitochondrial metabolism, insulin signaling, and energy homeostasis (Bach et al., 2003; Pich et al., 2005; Muñoz et al., 2013; Schneeberger et al., 2013; Sebastián et al., 2012). Cancer cells of different origin show a low expression of Mfn2 (Cheng et al., 2013; Rehman et al., 2012). In addition, Mfn2 levels are significantly downregulated in HCC tissue compared with corresponding adjacent normal tissue, and there is a negative correlation between Mfn2 levels and the prognosis of cancer (Wu et al., 2016; Zhou et al., 2016). Mfn2 overexpression in hepatocellular carcinoma or colorectal cancer cells reduces cell proliferation and induces spontaneous apoptosis (Wang et al., 2012). However, it is unknown whether Mfn2 downregulation is a cause or a consequence of cancer, and there are no data linking Mfn2 to NALFD progression.

Here, we show that hepatic Mfn2 is downregulated both in patients with NASH and in subjects' borderline for NASH. Further, mouse models of hepatic lipid accumulation or NASH present lower levels of Mfn2 in liver, and the re-expression of Mfn2 in liver ameliorates the NASH phenotype. We also demonstrate that hepatic Mfn2 ablation causes a NASH-like phenotype that progresses to liver cancer with age. We show that Mfn2 binds to and participates in the transfer of PS. Accordingly, hepatic Mfn2 deficiency causes a reduced transfer of PS from ER to mitochondria, which leads to reduced PS synthesis and ER stress, in turn causing inflammation, fibrosis, and liver cancer. Overall, our data strongly suggest that Mfn2 constitutes a new target for the treatment of NALFD.

RESULTS

Human Liver Samples of Non-alcoholic Steatohepatitis Present Low Levels of Mfn2

To investigate whether Mfn2 is dysregulated in NASH, we compared its expression in liver biopsies from patients with steatosis or NASH. Clinical, anthropometric, and biochemical data of this cohort have been reported previously (Ferreira et al., 2011). Results showed that Mfn2 levels were significantly lower in liver from patients with NASH than in subjects with simple steatosis

(Figure 1A). We also analyzed human liver biopsies from a second cohort of subjects without NASH (NAS index ≤ 3) and close to borderline NASH (NAS index ≥ 5). NAS scoring was performed according to Takeda et al. (2013). Clinical characteristics of these patients are shown in Table S1. Both Mfn2 mRNA and protein levels were significantly decreased in patients with borderline NASH (Figures S1A–S1C). We did not discriminate whether the reduction in Mfn2 expression was different in women and in men due to insufficient statistical power. By contrast, expression of the Mfn2 homolog Mfn1 was unaltered in this group (Figure S1D). Overall, these data show that Mfn2 is downregulated in human liver during progression from steatosis to NASH.

Mouse Models of Non-alcoholic Liver Disease Have Low Hepatic Levels of Mfn2

To document the possible involvement of Mfn2 in NALFD, we studied its expression in C57BL6/J mice with steatosis induced by high-fat diet (HFD) over 3 weeks, a time sufficient to trigger hepatic steatosis (Gaemers et al., 2011). Mfn2 protein expression in liver was significantly lower in the HFD group than in controls (Figures 1B and S1E). Because mice on HFD show fatty liver and obesity but not fibrosis, we used a well-established mouse model of NASH consisting of a methionine and choline-deficient diet combined with 45% HFD and supplemented with 0.1% L-methionine in drinking water to avoid weight loss (Matsumoto et al., 2013) (hereafter termed MCD). C57BL6/J mice on MCD diet for 3 weeks showed substantial fat accumulation and liver fibrosis (Figure 1C). Further, liver triglyceride (TAG) and mRNA levels of inflammatory and the fibrotic marker transforming growth factor β (TGF- β) were significantly higher in mice on MCD diet than on control diet (Figures 1D, S1F, and S1G). Under these conditions, Mfn2 levels were diminished (Figures 1E and S1H), and this decrease was greater in mice on MCD diet than on HFD (Figures 1B and 1E). Consistent with the data in human biopsies, Mfn1 protein levels were unaltered in mice on MCD diet (Figure S1I). These results are consistent with a specific progressive repression of Mfn2 in mouse liver disease.

Mfn2 Ablation Causes Chronic Hepatic Inflammation and Abnormal Lipid Metabolism

To substantiate the role of Mfn2 in liver as a trigger of the NASH-like phenotype, we analyzed liver-specific Mfn2 knockout mice (L-KO) generated in our laboratory (Sebastián et al., 2012). Under normal chow diet, 8-week-old L-KO mice showed a significant increase in the abundance of hepatic and plasma pro-inflammatory cytokines (Figures 1F, S1J, and S1K), expression of hepatic pro-inflammatory genes (Figure S1L), and a modest but significant accumulation of TAG (Figure 1G). This occurred in the absence of changes in body weight, food intake, or circulating lipids (Figures S1M–S1Q). Further analysis of lipid metabolism in hepatocytes isolated from L-KO and control mice revealed that the esterification of oleate into diacylglycerol and triacylglycerol was enhanced in the former, but their incorporation into phospholipids was decreased (Figure 1H). Under these conditions, oleate β -oxidation was decreased in Mfn2-deficient hepatocytes (Figure S1R). Further, the expression of *de novo* lipogenesis and esterification genes was modestly elevated in liver from

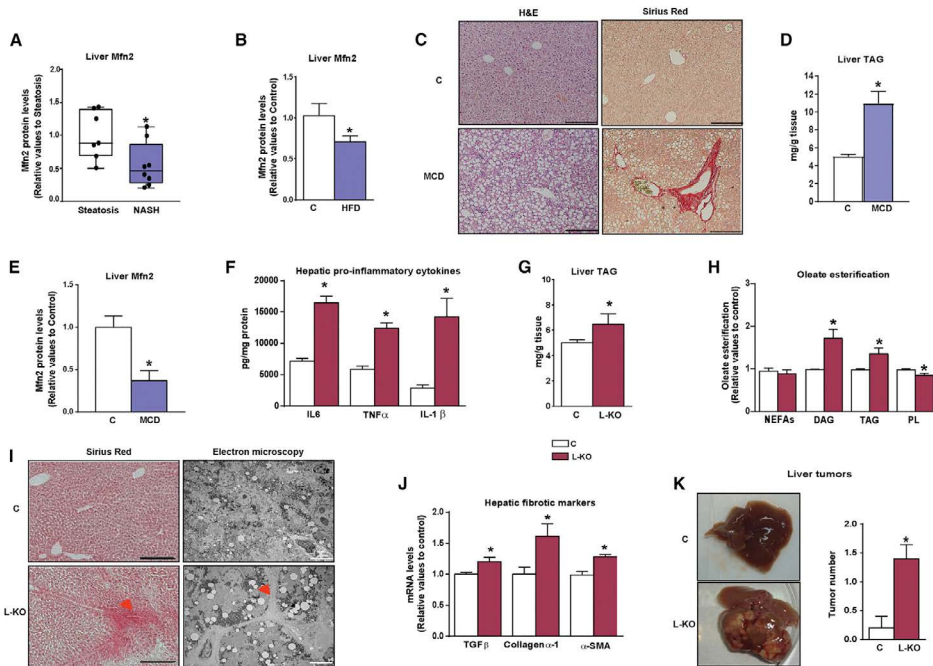


Figure 1. Mfn2 Is Reduced in NASH and Liver-Specific Mfn2 Ablation in Mice Causes a NASH-like Phenotype

(A) Mfn2 protein in liver biopsies from steatotic (n = 7 patients) and NASH (n = 8 patients).
 (B) Mfn2 protein in liver from mice on chow diet (C) or high-fat diet (HFD) (n = 4 mice).
 (C) H&E and Sirius red staining images in liver sections from C57Bl6/J mice fed either a C diet or a methionine and choline-deficient diet combined with HFD and supplemented with 0.1% L-methionine in drinking water (MCD) (scale bar, 200 μ m).
 (D) Liver TAG from mice on C and MCD (n = 5 mice).
 (E) Liver Mfn2 protein from C (n = 5 mice) and MCD mice (n = 4 mice).
 (F) Hepatic pro-inflammatory factors in control (C) and liver-specific Mfn2 KO (L-KO) (n = 8 mice).
 (G) TAG levels in C and L-KO mice (n = 8–12).
 (H) Oleate incorporation in hepatocytes isolated from C and L-KO mice (n = 4 mice; each experiment performed in triplicate).
 (I) Sirius red staining and TEM images in liver sections from 27-week-old C and L-KO mice fed a normal diet (scale bars, 200 μ m in Sirius Red and 5 μ m in TEM images).
 (J) Hepatic expression of genes involved in collagen synthesis in C and L-KO mice (n = 5 mice).
 (K) Images and tumor quantification of liver from 24 month-old C and L-KO (n = 5 mice).
 In (A), data are expressed as mean \pm SD. In (B)–(K), data are mean \pm SE. *p < 0.05 versus control group in each case. See also [Figures S1, S2 and S3](#) and [Table S1](#).

L-KO mice ([Figure S1S](#)). In sum, L-KO mice show a pattern typical of disturbances in hepatic lipid metabolism.

Mfn2 Ablation Causes Apoptosis, Increased Cell Growth, Fibrosis, and Liver Cancer

It is known that chronic hepatic inflammation is associated with enhanced apoptosis, leading to compensatory cell proliferation and fibrosis, which are known risk factors for liver cancer ([Malhi et al., 2010](#); [Sun and Karin, 2012](#)). Given the chronic inflammation detected in L-KO mice, we analyzed whether Mfn2

deficiency leads to liver cancer progression. Under normal conditions, apoptosis was higher in liver from L-KO mice than from controls, as demonstrated by increased levels of cleaved PARP-1 and cleaved caspase-3 ([Figures S2A and S2B](#)), and was accompanied by a higher number of Ki67-positive cells ([Figure S2C](#)), indicating enhanced proliferation. Furthermore, the expression of genes encoding fibrotic markers was also elevated in L-KO livers ([Figure 1J](#)), and Sirius red staining and transmission electron microscopy revealed a marked accumulation of extracellular collagen in livers at 27 weeks of age ([Figure 1I](#)).

We next explored whether Mfn2 deficiency promotes liver cancer as a consequence of the natural progression of liver disease. Accordingly, L-KO and control mice on normal diet were examined for liver tumors at 24 months of age. Analysis showed that the number of tumors and volume were significantly higher in L-KO than in control mice (Figures 1K and S2D). To validate these results, we investigated whether L-KO mice showed a predisposition to the liver-specific carcinogen diethylnitrosamine (DEN). Treatment of mice with DEN triggers a well-known cascade of events in liver that include DNA damage and apoptosis of centrilobular hepatocytes, production of proinflammatory cytokines, and compensatory proliferation (Herranz et al., 2010). As a first approach, we induced liver DNA damage with a single high-dose intraperitoneal injection of DEN (50 mg/kg) to assess the acute liver response. Immunohistological examination of livers 48 h after DEN revealed a stronger DNA damage response in centrilobular regions in L-KO mice than in controls, and this accompanied by greater levels of compensatory proliferation (Figures S2E–S2G). We next treated control and L-KO mice with a single lower dose of DEN (5 mg/kg), followed by continued exposure to HFD. After 7 months, L-KO mice subjected to DEN-HFD showed a larger number of tumors and greater tumor size compared to control treated mice (Figure S2H). Thus, our data indicate that hepatic Mfn2 ablation leads to apoptosis, increased cell proliferation, fibrosis, and a greater susceptibility to develop liver cancer.

Mfn2 Re-expression Restores Normal Liver Metabolism in L-KO Mice

To assess whether the alterations detected in Mfn2-deficient livers were attributable to Mfn2 loss-of-function or to compensatory mechanisms, we re-expressed Mfn2 in L-KO mice by intravenous administration of adenoviruses encoding either Mfn2 or LacZ (AdC, used as a control). Upon Mfn2 re-expression (Figure S3A), hepatic and plasma cytokines returned to control levels (Figures S3B–S3D), and the expression of fibrosis and pro-inflammatory genes were markedly downregulated (Figures S3E and S3G). Moreover, TAG levels were normalized (Figure S3F), and oleate β -oxidation was enhanced (Figure S3H).

We have previously reported that L-KO mice present an elevated unfolded protein response (UPR) (Sebastián et al., 2012). Thus, we surveyed the impact of Mfn2 re-expression on ER stress markers. Results showed that Mfn2 re-expression normalized the different UPR parameters (Figure S3I). These data strongly suggest that Mfn2 is directly responsible for the liver abnormalities found in L-KO mice.

Normalization of ER Stress Triggered by Mfn2 Deficiency Ameliorates Inflammation and Fibrosis, but Not the Impaired Lipid Metabolism

The upregulation of UPR proteins, such as CHOP, is sufficient to promote liver apoptosis, inflammation, compensatory proliferation, fibrosis, and liver cancer (DeZwaan-McCabe et al., 2013). We then examined the contribution of ER stress to these processes in the L-KO model. We blocked ER stress by overexpressing a critical regulator of UPR signaling, BIP (GRP-78). Because hepatic BIP gain-of-function in control mice has been shown to cause hypoglycemia and sudden death, even upon

administration of very low levels of adenovirus, in models that do not present UPR activation (data not shown and previous reports) (Lee, 2001), we expressed BIP by adenoviral intravenous injection only in L-KO mice, which show chronic ER stress.

Acute BIP overexpression decreased UPR signaling in L-KO mice (Figures 2A and S3J). Moreover, liver and plasma pro-inflammatory cytokines were normalized by BIP (Figure 2B, and 2C), and the expression of genes encoding pro-inflammatory or fibrotic factors was also markedly lower than that seen in equivalent controls (Figures 2D and S3K). Similarly, apoptosis and cell proliferation were decreased in L-KO mice expressing BIP (Figures S3L and S3M). In the context of mitochondrial metabolism, BIP expression enhanced oleate oxidation (Figure S3N) and reduced ROS production (Figure S3O), thereby recovering mitochondrial function, which is in keeping with previous data (Muñoz et al., 2013). Intriguingly, BIP overexpression failed to restore TAG levels (Figure 2E) or the incorporation of oleate into lipids (Figure 2F). These data indicate that the mitochondrial dysfunction, inflammation, fibrosis, apoptosis, and increased proliferation detected in L-KO mice lies downstream of ER stress and UPR signaling.

Mfn2 Plays a Crucial Role in Hepatic Phospholipid Metabolism

It has been reported that an aberrant phospholipid composition of the ER membrane is a potent activator of the UPR (Fagone and Jackowski, 2009; Fu et al., 2011). Accordingly, we studied the total hepatic phospholipid content in L-KO mice in an attempt to identify mechanisms linking Mfn2 deficiency and UPR. Results from lipidomics analysis showed that L-KO mice had a decreased abundance of total hepatic PE and PC species (Figure 3A; Table S2). Consistent with these data, the lipidomics profile of hepatic MAMs and mitochondrial fractions from L-KO and control mice was different (Figures S4A and S4D), with a decrease in the abundance of PE and PC species in the former (Figures S4B, S4C, S4E, and S4F; Table S3). Because Mfn2 and some proteins of phospholipid synthesis are localized in mitochondria-ER contact sites (schematic shown in Figure 3B) (de Brito and Scorrano, 2008; Stone and Vance, 2000), we monitored the incorporation of radiolabeled L-serine (L-Ser) into PS, PE, and PC in MAM fractions from control and L-KO mice. We found that this incorporation was significantly decreased in MAM fractions from L-KO mice (Figures 3C–3E).

We next questioned whether ER stress plays a role in the defects detected in phospholipid synthesis by analyzing BIP-expressing L-KO mice. BIP failed to improve the incorporation of L-Ser into PS, PE, or PC (Figure 3F); however, re-expression of Mfn2 completely rescued L-Ser incorporation into phospholipids (Figure 3G). Overall, our data indicate that hepatic Mfn2 depletion alters phospholipid synthesis and that these effects are not a consequence of ER stress.

Phospholipid metabolism in mammalian cells depends on the activity of many enzymes including phosphatidylserine synthase 1 (PSS1), phosphatidylserine synthase 2 (PSS2), and PE N-methyltransferase (PEMT), which are localized in MAMs and the ER, and PS decarboxylase (PLSD), which is found in mitochondria (Flis and Daum, 2013; Osman et al., 2011). We therefore analyzed whether loss of Mfn2 altered the expression of these

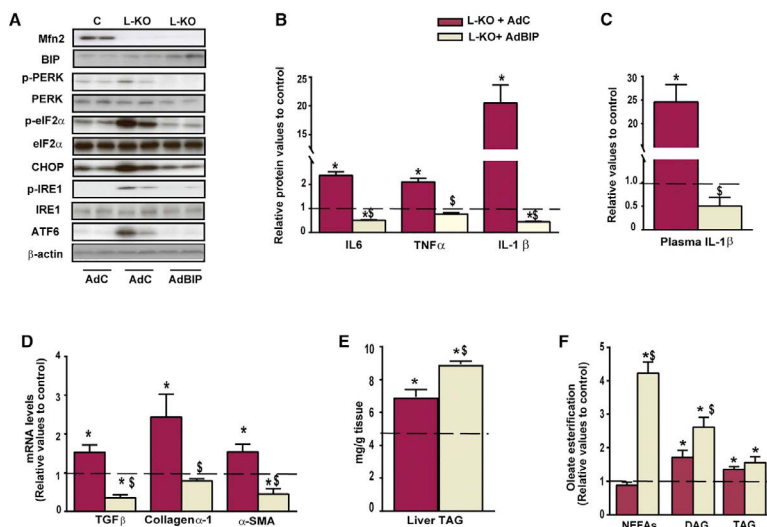


Figure 2. Normalization of ER Stress Ameliorates Inflammation and Fibrosis, but Not Lipid Metabolism, in L-KO Mice

Data are expressed as values relative to control LacZ group (shown as a discontinuous line) ($n = 4$ mice).

(A) Protein expression of hepatic ER stress markers.

(B) Hepatic pro-inflammatory factors.

(C) Plasma levels of interleukin (IL)-1 β .

(D) Expression of genes involved in collagen synthesis.

(E) TAG levels.

(F) Oleate incorporation in isolated hepatocytes. Data are expressed as mean \pm SE. * $p < 0.05$ L-KO versus C mice, $^{\$}p < 0.05$ L-KO+AdBIP versus L-KO+AdC mice.

See also [Figure S3](#).

proteins. Analysis by western blotting showed that the hepatic expression of PSS1 and PSS2 proteins was significantly lower in L-KO than in control mice ([Figure 3H](#)), whereas no changes were observed for PEMT ([Figure S4G](#)) or PISD (data not shown).

We next assessed the protein composition in MAMs by examining the abundance of MAM-enriched proteins in liver upon subcellular fractionation ([Figures 3I](#) and [S4H](#)). Western blotting of MAM fractions revealed a 50% reduction in PSS1 expression in L-KO mice ([Figure 3I](#)), whereas no changes were found for PSS2 whose expression was barely detectable ([Figures 3I](#) and [S4I](#)). Moreover, levels of PACS-2, Sig1R, and calnexin were elevated in MAMs from L-KO mice ([Figures 3I](#), [S4H](#), and [S4I](#)), which resembles the alterations in MAM composition in models of insulin resistance and aberrant lipid metabolism ([Arruda et al., 2014; Fu et al., 2011](#)). Thus, our results suggest that Mfn2 regulates phospholipid biosynthesis through PSS1 and PSS2 protein levels.

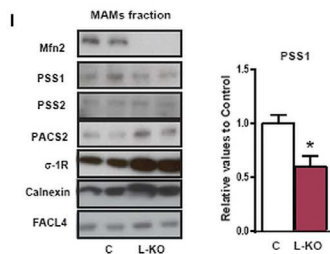
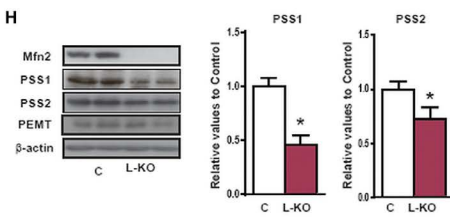
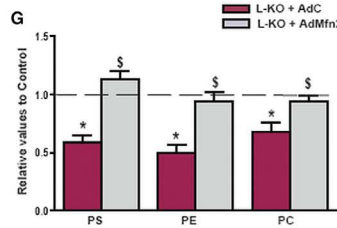
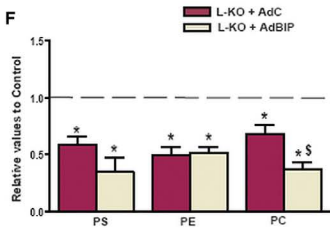
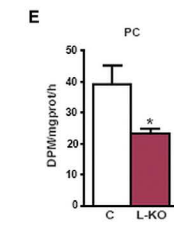
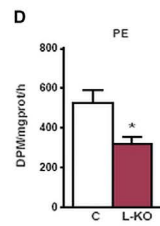
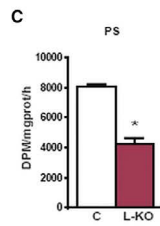
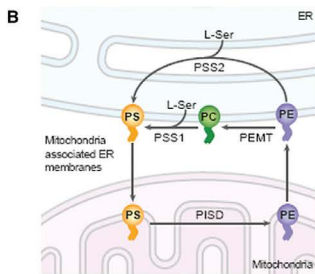
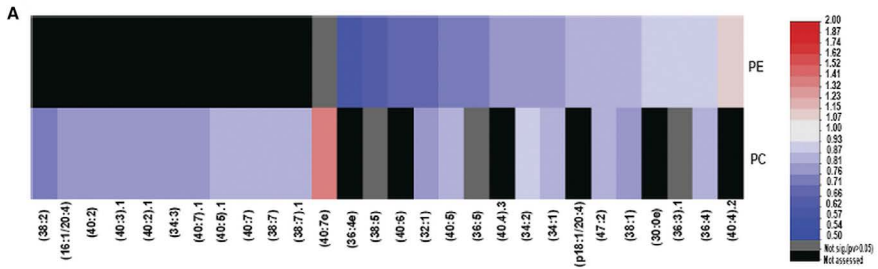
Alterations of Lipid Metabolism in L-KO Mice Are Independent of the Distance between ER and Mitochondria

Given the role of Mfn2 in tethering ER to mitochondria, we explored whether the distance between mitochondria and ER might regulate phospholipid synthesis in L-KO mice. To do

this, we used a recombinant adenovirus construct encoding a synthetic linker (RFP-linker) that increases the number ER-mitochondria contact sites, thus forcing ER-mitochondria interactions in L-KO mice ([Arruda et al., 2014](#)). Western blot analysis of RFP expression confirmed the expression of the linker ([Figure S5A](#)). L-KO mice expressing this linker showed a normalization of L-Ser incorporation into PS ([Figure S5B](#)); however, it failed to correct the PE or PC synthesis, TAG levels, ER stress, or PSS1 expression ([Figures S5B–S5F](#)). Under these conditions, PSS2 abundance was actually enhanced in L-KO mice ([Figure S5F](#)), which may explain the normalization of PS synthesis ([Figure S5B](#)). These results indicate that altered ER-mitochondria contact does not explain the lower synthesis of PE and PC in MAMs of Mfn2-deficient livers.

Downregulation of Hepatic PSS1/2 Phenocopies Mfn2 Ablation

In light of the above findings, we hypothesized that a decrease in phospholipid synthesis in MAMs causes TAG accumulation and ER stress in liver. To test this, we induced downregulation of either PSS1 or PSS2 in wild type mice. Silencing of PSS1 by intravenous injection of a specific shRNA adenovirus caused the upregulation of hepatic PSS2 and vice versa ([Figures S6A](#)



(legend on next page)

and S6B), observations that are in agreement with previous data (Steenbergen et al., 2006; Stone and Vance, 1999). On the basis of these findings, which point to a strong adaptation process, we silenced both PSS1 and PSS2 in wild type mice using two specific short hairpin RNA (shRNA) adenoviruses, which decreased the hepatic expression of both proteins by ~90% (Figures 4A and S6C). Analysis of MAM fractions showed a significant decrease of PSS1 in PSS1/2 knockdown (hereafter termed KD) mice (Figure 4B). This resulted in a decrease in the incorporation of L-Ser into PS and PE (Figure 4C) and an increase in TAG and oleate incorporation into lipids (Figures 4D and S6D). KD mice also showed ER stress (Figures 4E and S6E) and a higher expression of pro-inflammatory and fibrosis genes (Figures 4F and S6F). In keeping with these observations, levels of hepatic pro-inflammatory cytokines were elevated in KD livers (Figure S6G); however, mitochondrial function (oleate oxidation or liver hydrogen peroxide production) was unaltered (Figures S6H and S6I).

Analysis of MAMs protein composition revealed alterations in response to PSS1/2 silencing, with a significant decrease of Mfn2 expression in KD mice (Figure 4G). PACS-2, Sig1R, and calnexin proteins were more abundant in MAMs from KD mice (Figures S6J–S6L), thus mirroring the alterations in MAMs composition in Mfn2 L-KO mice. Overall, these results indicate that hepatic PSS1/2 deficiency recapitulates many of the alterations caused by Mfn2 ablation. We next attempted to counter the liver alterations in L-KO mice by overexpressing PSS1 (Figure 4H). PSS1 overexpression led to an upregulation of Ptdss2 mRNA in L-KO mice (Figure 4I). As expected, we also found an increase in the synthesis of PS (Figure 4J), and surprisingly, the normalization of liver TAG (Figure 4K). By contrast, PSS1 overexpression failed to rescue the synthesis of PE or PC (Figure 4J) or ameliorate the UPR (Figures 4L and S6M). Taken together, our data show that Mfn2 depletion causes a fundamental defect that prevents the synthesis of PE from PS.

Mfn2 Is a PS-Binding Protein and Generates PS-Rich Domains in Membranes

A key process in the synthesis of phospholipids in MAMs is the transfer of PS and PE between the ER and mitochondria. To determine whether Mfn2 was involved in PS transfer, we first investigated whether it binds phospholipids by assaying binding of Mfn2 to lipid strips. Mfn2 was specifically isolated under denaturing immunoprecipitation conditions with a polyclonal antibody. Mfn2 specifically bound phosphatidate (PA) and PS but not phosphatidylinositol (PI), PE, or PC (Figure 5A). To validate this binding to phospholipids and to exclude the possibility that

it was due to transmembrane domains, we constructed a truncated version of Mfn2 lacking the transmembrane domains and the C-terminal cytosolic portion (1–613), but preserving some metabolic characteristics of the full-length protein (Segalés et al., 2013). L-KO mice were tail vein injected with an adenoviral vector permitting the hepatic expression of this short form containing a 6× His tag at the N terminus. We then purified the recombinant Mfn2 protein under denaturing conditions by affinity chromatography. Results showed that Mfn2 (1–613) could also specifically bind PS and PA (Figure 5B). To determine its potential *in vivo* role on phospholipid synthesis, we analyzed the effects on phospholipid synthesis by monitoring the incorporation of labeled L-Ser. Data revealed that Mfn2 (1–613) enhanced the incorporation of L-Ser into PS, PE, and PC (Figure 5C).

For *in vitro* analysis, Mfn2 (1–613) was re-cloned, expressed in *E. coli*, and purified by affinity chromatography to >60% purity as assessed by a Coomassie blue-stained protein SDS-PAGE (Figure 5D). Eluted Mfn2 (1–613) was also identified by mass spectrometry and contaminants were detected at very low levels (Table S5). When we analyzed the capacity of the recombinant protein to bind phospholipids, we observed specific binding to PS and to PA in lipid strip assays (Figure 5E), consistent with the results in liver. To exclude false positive binding due to phospholipid positioning in the strip, we performed liposome flotation assays, which confirmed that Mfn2 (1–613) mainly bound PS conjugated to a fluorophore (NBD) and also natural PS (Figures 5F and S7A) in liposomes. Overall, these data indicate that Mfn2 shows a capacity to selectively bind PS with minimal binding to natural PA and PI.

We next determined whether Mfn2 participates in the transfer of PS between membranes. We first evaluated its capacity to extract PS from liposomes, which may account for the alterations in the synthesis of PE in L-KO liver, even upon PSS1 overexpression. Phospholipid extraction was performed as described (Kawano et al., 2018). Purified Mfn2 (1–613) was incubated with liposomes containing labeled phospholipids (NBD-PS or NBD-PE), and the mixture was then separated by gradient centrifugation (Figure 5G). Subsequently, we analyzed the liposome-containing fraction and the non-liposome-containing fraction. Analysis of the distribution of NBD fluorescence in the presence of Mfn2 revealed that the fluorescence of NBD-PS decreased in the liposome fraction and increased in the non-liposome fraction (Figure 5H), whereas the distribution of NBD-PE fluorescence was unchanged in the presence of Mfn2 (Figure S7B).

In accord with these data, confocal microscopy revealed that Mfn2 (1–613) induced the formation of rigid domains containing

Figure 3. Mfn2 Ablation Alters Hepatic Phospholipid Metabolism Independently of ER Stress

(A) Hepatic phosphatidylcholine (PC) and phosphatidylethanolamine (PE) content measured by lipidomics in C (n = 11 mice) and L-KO (n = 13 mice). Data are expressed as fold-change versus C mice. Significant compounds are shown in the heatmap (p < 0.05) out of 128 phospholipids analyzed.

(B) Graphical scheme of phosphatidylserine (PS), PE, and PC synthesis in MAMs.

(C–E) ³H-L-serine incorporation into PS (C), PE (D), and PC (E) in MAMs fractions from C and L-KO mice (n = 5–7).

(F and G) ³H-L-serine incorporation into PS, PE, and PC (n = 4 mice), BIP overexpression (F) and Mfn2 re-expression experiment (G). Data are expressed as values relative to C+AdC group (shown as a discontinuous line).

(H) Hepatic expression of PSS1, PSS2 and PEMT proteins (n = 4 mice).

(I) Hepatic expression of MAM proteins from C and L-KO mice (n = 4 mice). Data are expressed as mean ± SE. *p < 0.05 L-KO versus C mice, [§]p < 0.05 versus L-KO+AdC mice.

See also Figures S4 and S5 and Tables S2 and S3.

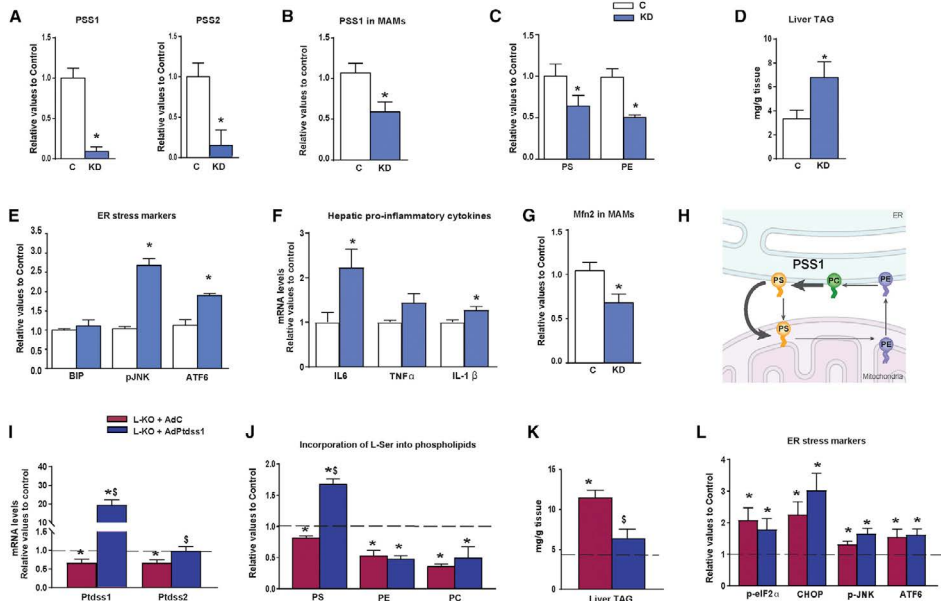


Figure 4. Deficiency of Hepatic Phosphatidylserine Synthase 1 and 2 Phenocopies Mfn2 Ablation

(A) Hepatic protein expression of PSS1 and PSS2 with control LacZ (C) or Ptdss1/Ptdss2 (KD) siRNA adenoviruses (n = 5 mice).

(B) PSS1 protein in MAM fractions obtained from C or KD mice (n = 5 mice).

(C) ³H-L-serine incorporation into PS and PE (n = 4).

(D) TAG levels (n = 4 mice).

(E) Protein expression of ER stress markers (n = 4 mice).

(F) Hepatic expression of genes involved in inflammation (n = 5 mice).

(G) Mfn2 protein in MAMs.

(H) Scheme of PSS1 overexpression in mice.

(I) mRNA levels of Ptdss1 and Ptdss2 from control, and L-KO mice (n = 3–5 mice).

(J) ³H-L-serine incorporation into PS, PE, and PC (n = 3–5 mice).

(K) TAG levels (n = 4 mice).

(L) Protein expression of ER stress markers (n = 3–5 mice). Data are expressed as values relative to C+AdC group (shown as a discontinuous line). Data are expressed as mean ± SE. *p < 0.05 versus C mice, [§]p < 0.05 versus L-KO+AdC mice.

See also Figure S6.

exclusively NBD-PS from liposomes containing both NBD-PS (green) and Rhodamine-PE (red) (Figure 5). Lipid domains were not generated when Mfn2 (1–613) was exposed to liposomes containing NBD-PC and Rhodamine-PE (Figure S7C). Given the unexpected capacity of Mfn2 (1–613) to generate PS-rich domains in membranes, we evaluated whether this capacity showed time-dependence and if it occurred with different types of liposomes. We incubated control and Mfn2 (1–613) proteins with a mix of donor liposomes (containing NBD-phospholipids and Rhodamine-PE) and acceptor liposomes (non-fluorescent). The presence of Mfn2 (1–613) induced the release of NBD fluorescence in a time-dependent manner in liposomes containing NBD-PS but not NBD-PE (Figures 5J and S7D). Similar results were obtained using liposomes containing fluorescent TopFluor

(TopFluor-PS or TopFluor-PE) derivatives of phospholipids, which are smaller in size than NBD-phospholipids (Figures S7E and S7F). Our results support the view that Mfn2 binds PS and has the capacity to isolate it from membranes and to form rigid domains enriched in PS. These findings are consistent with a role for Mfn2 in exchanging lipids from different membranes or remodeling them in membranes, which may be due to lipid rearrangement.

PS-Dependent Remodeling Activity of Mfn2 Requires an Intact N-Terminal Region

To address the specificity of Mfn2 functions, we tested whether Mfn1 has the same activities. To evaluate similar protein fragments in Mfn1 and in Mfn2, a recombinant truncated version of

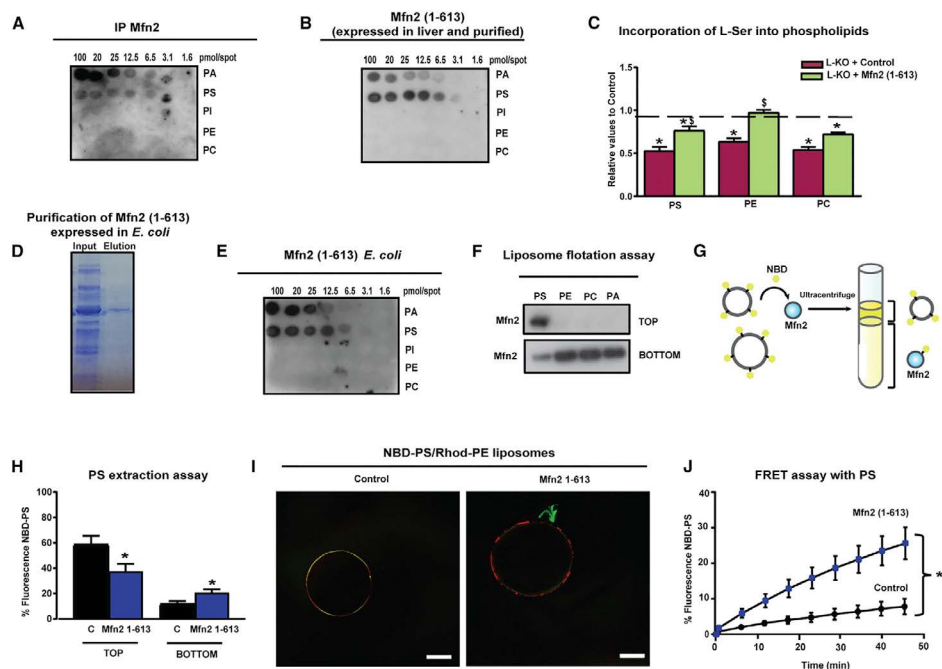


Figure 5. Mfn2 Binds Phosphatidylserine and Generates Phosphatidylserine-Rich Domains in Membranes

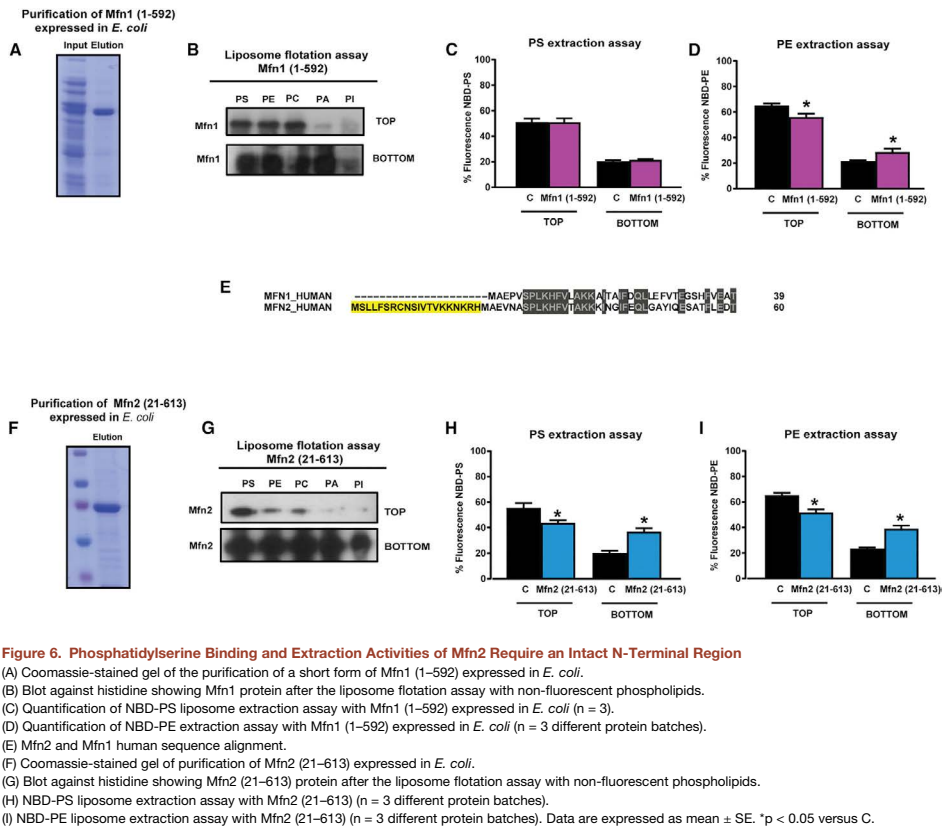
(A) Binding of Mfn2 protein isolated from liver to Membrane Lipid Strip.
 (B) Binding of a truncated form of Mfn2 (1–613) isolated from liver to Membrane Lipid Strip.
 (C) ^3H -L-serine incorporation into PS, PE, and PC ($n = 4$ mice). Data are expressed as values relative to the C+AdC group (shown as a discontinuous line).
 (D) Coomassie-stained gel of the purification of Mfn2 (1–613) expressed in *E. coli*.
 (E) Binding of Mfn2 (1–613) expressed in *E. coli* to Membrane Lipid Strip.
 (F) Blot against Mfn2 after the liposome flotation assay with fluorescent (NBD) phospholipids.
 (G) Scheme of the NBD-Phospholipid liposome extraction assay.
 (H) NBD-PS liposome extraction assay with Mfn2 (1–613) expressed in *E. coli* ($n = 6$ different protein batches).
 (I) Confocal microscopy images of liposomes showing the formation of the NBD-PS rigid domain with Mfn2 (1–613).
 (J) Kinetic FRET assay with NBD-PS and Rhod-PE ($n = 6$ different protein batches). Data are expressed as mean \pm SE. (H) * $p < 0.05$ versus C $^{\text{p}} < 0.05$ versus L-KO+AdC. (J) * $p < 0.0001$.

See also Figure S7 and Table S4.

Mfn1 (1–592) was re-cloned, expressed in *E. coli*, and purified under identical conditions as Mfn2 (1–613) (Figure 6A). We first determined whether Mfn1 (1–592) had phospholipid-binding activity. Liposome flotation assays revealed that, in contrast to Mfn2 (1–613), Mfn1 bound PC, PE, and PS to a similar extent (Figure 6B). In a second analysis, lipid extraction assays revealed that Mfn1 (1–592) failed to extract NBD-PS from liposomes (Figure 6C), but it did extract NBD-PE (Figure 6D), pointing to distinct functions for Mfn1 and Mfn2.

To better understand the basis for the differential capacity of Mfn1 and Mfn2 to bind and extract phospholipids, we examined the amino acid sequences of the two proteins (Figure 6E). Align-

ment analysis revealed that the N-terminal (20 aa residues) sequence of Mfn2 was absent in Mfn1. A mutant form of Mfn2 lacking this fragment (referred to as Mfn2 21–613) was re-cloned and overexpressed in *E. coli* and then purified under identical conditions as Mfn2 (1–613) (Figure 6F). After liposome flotation assays, results showed that Mfn2 (21–613) bound to PS, PE, and PC (Figure 6G). Notably, lipid extraction assays revealed that purified Mfn2 (21–613) extracted both NBD-PS and NBD-PE from liposomes (Figures 6H and 6I). Thus, the Mfn2 (21–613) mutant combines the properties of both Mfn1 and Mfn2, suggesting that the N-terminal fragment is key to confer selectivity to extract PS.



Re-expression of Mfn2 in Mice on MCD Diet Alleviates Liver Disease

After establishing the unique action of Mfn2 on phospholipid partition and metabolism, we next examined the consequences in liver under conditions of reduced Mfn2 expression during NASH. Specifically, we assessed whether the reduced Mfn2 levels in mice on MCD diet was linked to impaired PS transfer and it was key to the pathological alterations. We also investigated the possible role of ER stress in this scenario. Mice were placed on MCD or chow diet for 2 weeks and were then intravenously injected with a control or with adenoviruses encoding Mfn2 or BIP, and livers were studied 1 week later. Mfn2 expression was normalized in MCD mice upon injection of Mfn2 adenoviruses (Figures S7G, and S7I), whereas BIP failed to recover Mfn2 levels (Figures S7H and S7I). Compared with the control diet, MCD induced an enhanced incorporation of radiolabeled L-Ser into PS, and a low synthesis of PE and PC

in MAMs (Figure 7A). Mfn2 re-expression normalized the incorporation of L-Ser into PE and PC, whereas BIP did not ameliorate as Mfn2 the low levels of phospholipid synthesis (Figure 7A).

Analysis of fibrosis in liver sections of MCD mice showed that Mfn2-re-expressing mice had less fibrosis than mice treated with control adenovirus (Figure 7B), whereas the expression of BIP only partially diminished fibrosis (Figure 7B). Similarly, TAG accumulation in liver was decreased upon Mfn2 re-expression as assessed by H&E staining (Figure 7B) and by quantification (Figure 7C). By contrast, BIP expression failed to normalize hepatic TAG in MCD mice (Figures 7B and 7C). As expected, the expression of inflammatory and fibrosis markers was markedly decreased by Mfn2 re-expression but not by BIP overexpression (Figure 7D). Finally, both BIP and Mfn2 treatments normalized all UPR markers upregulated in MCD mice (Figure S7J). Overall, our data strongly suggest that Mfn2 repression

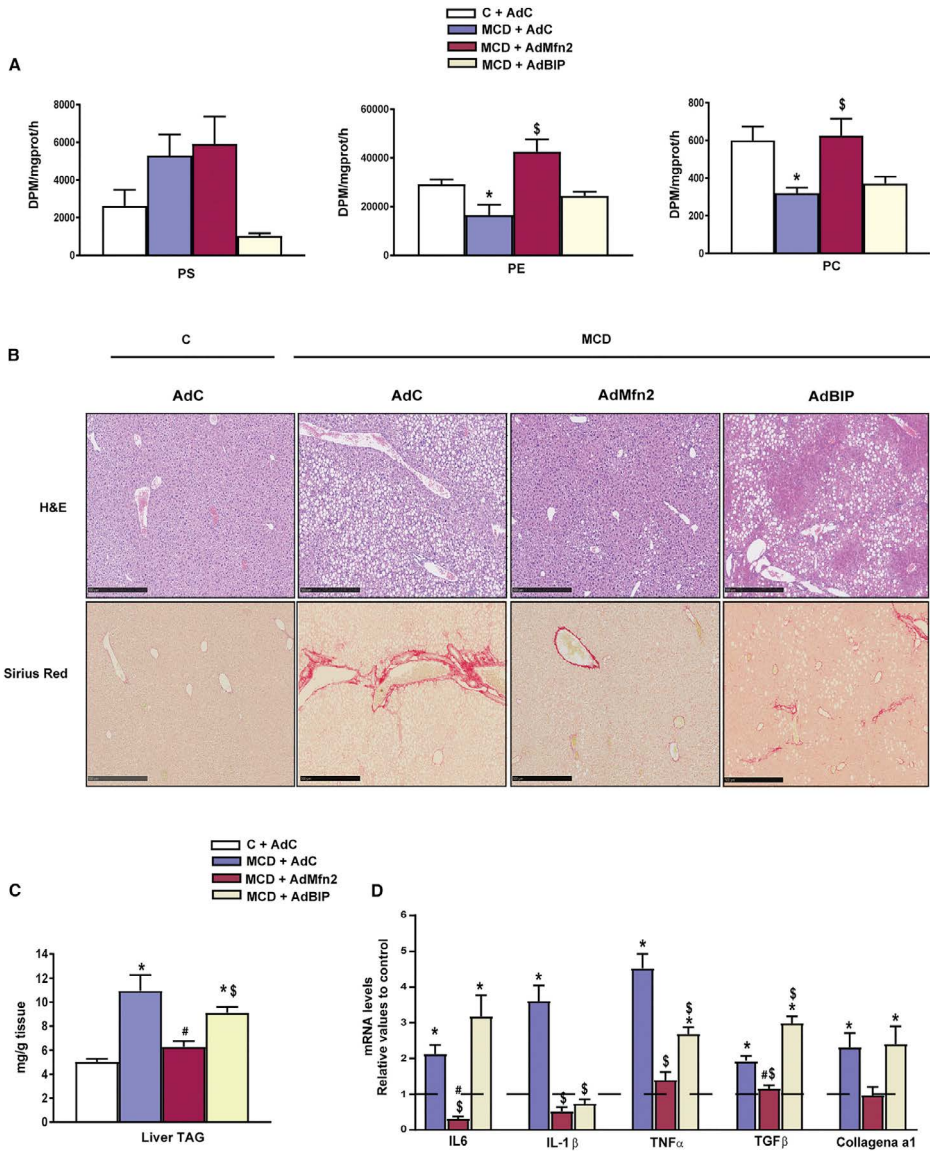


Figure 7. Mfn2 Re-expression Improves the NASH Phenotype in Mice

(A) ³H-L-serine incorporation into PS, PE, and PC (n = 4 mice).

(B) H&E and Sirius Red staining images in liver sections (scale bar, 200 μm).

(legend continued on next page)

plays a key role in the development of steatosis, inflammation, and fibrosis in a mouse model of NASH.

DISCUSSION

We report that Mfn2 deficiency markedly impairs phospholipid metabolism and this lies upstream of the UPR. Our results also indicate that loss of hepatic Mfn2 changes phospholipid metabolism by: (1) reducing the transfer of PS from the ER to mitochondria, and (2) inhibiting PS synthesis as a consequence of a compensatory reduced expression of PSS1 and PSS2.

Importantly, we describe a new molecular function of Mfn2 in the maintenance of phospholipid metabolism. Mfn2 binds PS *in vitro*, and causes partitions of PS into rigid membrane domains. These activities are specific for PS and are not found with other phospholipids such as PE or PC. In addition, our observations provide molecular insights into the steps involved in the transfer of PS from ER to mitochondria. We propose that Mfn2 participates in the generation of PS-enriched domains at the ER-mitochondria contact sites and they favor the activity of potential PS transport proteins such as the oxysterol-binding protein (OSBP)-related proteins or VAT-1. ORP5/8 binds PS *in vitro* (Maeda et al., 2013) and mediates PI4P/PS counter transport between the ER and the plasma membrane (Chung et al., 2015). These proteins have also been identified in MAMs (Galmes et al., 2016) and therefore may participate in the transfer of PS between ER and mitochondria.

The observation of a link between Mfn2 and phospholipids is highly relevant because of their influence on membrane-dependent cellular functions, antioxidant, anti-inflammatory, anti-fibrotic properties, and cellular signaling (Gundermann et al., 2011; Chakravarthy et al., 2009). Thus, obesity has been reported to increase the hepatic PC/PE ratio that inhibits SERCA activity. In addition, genetic inhibition of PEMT, which catalyzes the conversion of PE to PC, relieves ER stress and improves systemic glucose homeostasis in obesity (Fu et al., 2011; Jacobs et al., 2010). Mfn2 levels are increased in MAMs in obese mice (Arruda et al., 2014) under conditions in which enhanced PC production has been reported. Furthermore, low levels of phospholipids in bile due to the disruption of membrane transporters are linked to liver disease (Tanaka et al., 2012). Another important feature of our work is the observation that hepatic Mfn2 ablation provokes MAMs remodeling similar to that detected in HFD or genetic obesity. This is also relevant because remodeling of MAMs interactions in liver in obesity has been shown to result in undesirable side effects such as TAG accumulation and insulin resistance. Specifically, hepatic MAMs shows an enhanced abundance of protein markers such as PACS2, IP3R1, and IP3R2 during obesity (Arruda et al., 2014), which is consistent with the pattern of changes detected in Mfn2-deficient livers. Accordingly, we propose that alterations in Mfn2 expression have an impact on MAM reorganization, perhaps through changes in the phospholipid composition in ER-mitochondrial

contact sites. These observations also reveal that changes to Mfn2 levels may alter the composition of tethers at ER-mitochondrial contact sites, and this may be dependent on the cell context. In addition, those data complement the observations that disruption of individual MAM components seem to be sufficient to alter phospholipid synthesis in disorders such as Alzheimer disease and Lenz-Majewski syndrome (Area-Gomez and Schon, 2014).

In contrast to the function of Mfn2, Mfn1 shows a broader phospholipid binding activity but it does not generate PE- or PC-rich domains. The N-terminal region (20 amino acid residues) of Mfn2 (not present in Mfn1) is key for PS specificity, because elimination of this region generates a mutant form of Mfn2 incorporating the capacities of Mfn1 and Mfn2, indicating a hybrid behavior. Further studies will be needed to understand the molecular basis for the PS binding and extraction activities of Mfn2.

In conclusion, our data support the view that Mfn2 sustains PS transfer to the mitochondria for conversion to PE. The effects on phospholipid metabolism may explain the role of Mfn2 in the maintenance of MAMs and proper lipid metabolism and ER homeostasis. We did not discriminate whether the reduction in Mfn2 expression was different according to sex due to insufficient statistical power, it will be relevant to analyze whether the downregulation of Mfn2 in NASH is similar in men and women. Thus, we propose Mfn2 as a potential therapeutic target for counteracting the development of liver disease related to NASH and liver cancer.

STAR★METHODS

Detailed methods are provided in the online version of this paper and include the following:

- KEY RESOURCES TABLE
- CONTACT FOR REAGENT AND RESOURCE SHARING
- EXPERIMENTAL MODEL AND SUBJECT DETAILS
 - Animal care, generation of animal models, and diet treatments
 - Human liver biopsies
 - Isolation of primary hepatocytes
 - E. coli strain used for protein purification
- METHOD DETAILS
 - DEN treatment
 - Plasma measurements
 - Liver subcellular fractionation and MAM purification
 - Adenoviral transduction
 - Oleate β -oxidation in isolated hepatocytes
 - Oleate incorporation into lipids in isolated hepatocytes
 - Histological sample preparation and analysis
 - Western blotting and immunoprecipitation assays
 - RNA extraction and real-time PCR
 - Hepatic triglyceride measurements
 - Lipidomic analysis from liver

(C) TAG levels (n = 4 mice).

(D) Hepatic pro-inflammatory factors and genes involved in collagen synthesis (n = 4 mice). Data are expressed as the mean \pm SE. *p < 0.05 versus C+AdC, \$p < 0.05 versus MCD+AdC and #p < 0.05 versus MCD+AdBIP.

See also Figure S7.

- QTOF-based untargeted lipidomics of liver subcellular fractionation
- ³H- L-serine incorporation into phospholipids in subcellular fractions
- Mfn2 immunoprecipitation for phospholipid binding assays
- Purification of a short Mfn2 (1-613) for phospholipid binding assays
- Cloning, Expression and Purification of Mfn2 (1-613), Mfn1 (1-592) and Mfn2 (21-613) from *E. coli*
- Binding to Lipid Strip assays
- Lipid binding by liposome flotation assays
- Lipid extraction assay
- *In vitro* phospholipid FRET assays
- Liposome imaging

- **QUANTIFICATION AND STATISTICAL ANALYSIS**
- **DATA AND SOFTWARE AVAILABILITY**

SUPPLEMENTAL INFORMATION

Supplemental Information can be found online at <https://doi.org/10.1016/j.cell.2019.04.010>.

ACKNOWLEDGMENTS

We thank Jennifer Rieusset for the BIP adenovirus, Estela Area-Gomez for the protocol of phospholipid synthesis, Helena Cortez-Pinto (Hospital Santa Maria, Lisbon) for liver biopsies, Mar Garcia-Rochá for discussion, Jorge Manuel Seco and Laura Alcaide for technological assistance, Neus Prats and the Histopathology Core Facility (IRB Barcelona), and Raquel Garcia-Castellanos and the Protein Expression Core Facility (IRB Barcelona) for cloning and production of Mfn2 and Mfn1 constructs in *E. coli*. We also thank the Mouse Mutant, Mass Spectrometry & Proteomics, Advanced Digital Microscopy (ADM), and the Biostatistics/Bioinformatics Core Facilities (IRB Barcelona); the Lipidomics Unit of IRB Lleida; the Unit of Electron Cryo-Microscopy (UB); and Iris Joval for the artwork. M.I.H.-A. was recipient of a pre-doctoral fellowship from the CONACYT, Mexico and of a “Juan de la Cierva-Incorporación” fellowship from MICINN Spain. P.K. is recipient of a pre-doctoral fellowship from “Coordenção de Aperfeiçoamento do Pessoal de Nível Superior (CAPES).” M.J. is a Serra Hünter Fellow. This study was supported by the MINECO (SAF2016-75246R), the Generalitat de Catalunya (2014SGR48, 2017SGR696, ICREA Acadèmia), INFLAMES (PIE-14/00045, ISCIII), CIBERDEM, ISCIII, INTERREG IV-B-SUDOE-FEDER (DIOMED, SOE1/P1/E178), and “la Caixa” Foundation. S.F.-V. acknowledges support from the Miguel Servet tenure-track program (CP10/00438 and CP116/00008) from the Fondo de Investigación Sanitaria, co-financed by the ERD. We gratefully acknowledge institutional funding from the MINECO through the Centres of Excellence Severo Ochoa Award and from the CERCA Programme of the Generalitat de Catalunya.

AUTHOR CONTRIBUTIONS

M.I.H.-A. conceived, designed the study and the strategy, performed experiments, discussed the results, and wrote the manuscript. D. Sebastián, S.V., P.B., P.K., N.P., S.R.V., V.H., N.V., G.P., A.A., M.J., R.P., I.G.-A., E.C., N.C., R.C., A.K., M.B., D. Sala, T.H., J.F., E.E.-M., and C.M.P.R. performed experiments. S.I. conceived and performed experiments. J.J., M. Oresic, M. Orozco, C.C., M.P., S.F.-V., and J.V. revised experimental data and contributed to the discussion. A.Z. designed the study and the strategy, discussed the results, and wrote the manuscript.

DECLARATION OF INTERESTS

The authors declare no conflict of interest. C.C. and M.B. are employees of the Nestlé Institute of Health Sciences S.A.

Received: December 25, 2017

Revised: December 19, 2018

Accepted: April 3, 2019

Published: May 2, 2019

REFERENCES

- Apellániz, B., and Nieva, J.L. (2015). Fusion-competent state induced by a C-terminal HIV-1 fusion peptide in cholesterol-rich membranes. *Biochim. Biophys. Acta* 1848, 1014–1022.
- Aravalli, R.N., Steer, C.J., and Cressman, E.N. (2008). Molecular mechanisms of hepatocellular carcinoma. *Hepatology* 48, 2047–2063.
- Area-Gomez, E. (2014). Assessing the Function of Mitochondria-Associated ER Membranes. *Methods Enzymol.* 547, 181–197.
- Area-Gomez, E., and Schon, E.A. (2014). Mitochondrial genetics and disease. *J. Child Neurol.* 29, 1208–1215.
- Arruda, A.P., Pers, B.M., Parlačkú, G., Güney, E., Inouye, K., and Hotamisligil, G.S. (2014). Chronic enrichment of hepatic endoplasmic reticulum-mitochondria contact leads to mitochondrial dysfunction in obesity. *Nat. Med.* 20, 1427–1435.
- Bach, D., Pich, S., Soriano, F.X., Vega, N., Baumgartner, B., Oriola, J., Daaugard, J.R., Loberas, J., Camps, M., Zierath, J.R., et al. (2003). Mitofusin-2 determines mitochondrial network architecture and mitochondrial metabolism. A novel regulatory mechanism altered in obesity. *J. Biol. Chem.* 278, 17190–17197.
- Broadhurst, D., Goodacre, R., Reinke, S.N., Kuligowski, J., Wilson, I.D., Lewis, M.R., and Dunn, W.B. (2018). Guidelines and considerations for the use of system suitability and quality control samples in mass spectrometry assays applied in untargeted clinical metabolomics studies. *Metabolomics* 14, 72.
- Chakravarthy, M.V., Lodhi, I.J., Yin, L., Malapaka, R.R., Xu, H.E., Turk, J., and Semenkovich, C.F. (2009). Identification of a physiologically relevant endogenous ligand for PPARalpha in liver. *Cell* 138, 476–488.
- Chalasanani, N., Younossi, Z., Lavine, J.E., Diehl, A.M., Brunt, E.M., Cusi, K., Charlton, M., and Sanyal, A.J. (2012). The diagnosis and management of non-alcoholic fatty liver disease: practice Guideline by the American Association for the Study of Liver Diseases, American College of Gastroenterology, and the American Gastroenterological Association. *Hepatology* 55, 2005–2023.
- Chen, H., McCaffery, J.M., and Chan, D.C. (2007). Mitochondrial fusion protects against neurodegeneration in the cerebellum. *Cell* 130, 548–562.
- Cheng, X., Zhou, D., Wei, J., and Lin, J. (2013). Cell-cycle arrest at G2/M and proliferation inhibition by adenovirus-expressed mitofusin-2 gene in human colorectal cancer cell lines. *Neoplasia* 60, 620–626.
- Chong, J., and Xia, J. (2018). MetaboAnalystR: an R package for flexible and reproducible analysis of metabolomics data. *Bioinformatics* 34, 4313–4314.
- Chung, J., Torta, F., Masai, K., Lucast, L., Czaplá, H., Tanner, L.B., Narayanaswamy, P., Wenk, M.R., Nakatsu, F., and De Camilli, P. (2015). INTRACELLULAR TRANSPORT. PI4P/phosphatidylserine countertransport at ORP5- and ORP8-mediated ER-plasma membrane contacts. *Science* 349, 428–432.
- Connerth, M., Tatsuta, T., Haag, M., Klecker, T., Westermann, B., and Langer, T. (2012). Intramitochondrial transport of phosphatidic acid in yeast by a lipid transfer protein. *Science* 338, 815–818.
- de Brito, O.M., and Scorrano, L. (2008). Mitofusin 2 tethers endoplasmic reticulum to mitochondria. *Nature* 456, 605–610.
- DeZwaan-McCabe, D., Riordan, J.D., Arensdorf, A.M., Icardi, M.S., Dupuy, A.J., and Rutkowski, D.T. (2013). The stress-regulated transcription factor CHOP promotes hepatic inflammatory gene expression, fibrosis, and oncogenesis. *PLoS Genet.* 9, e1003937.
- Dunn, W.B., Broadhurst, D., Begley, P., Zelena, E., Francis-McIntyre, S., Anderson, N., Brown, M., Knowles, J.D., Halsall, A., Haselden, J.N., Nicholls, A.W., Wilson, I.D., Kell, D.B., and Goodacre, R. (2011). Procedures for large-scale metabolic profiling of serum and plasma using gas chromatography

- and liquid chromatography coupled to mass spectrometry. *Nat. Protoc.* 6, 1060–1083.
- Enrique-Tarancón, G., Castan, I., Morín, N., Martí, L., Abella, A., Camps, M., Casamitjana, R., Palacin, M., Testar, X., Degerman, E., et al. (2000). Substrates of semicarbazide-sensitive amine oxidase co-operate with vanadate to stimulate tyrosine phosphorylation of insulin-receptor-substrate proteins, phosphoinositide 3-kinase activity and GLUT4 translocation in adipose cells. *Biochem. J.* 350, 171–180.
- Fagone, P., and Jackowski, S. (2009). Membrane phospholipid synthesis and endoplasmic reticulum function. *J. Lipid Res.* 50 (Suppl.), S311–S316.
- Fahy, E., Cotter, D., Byrnes, R., Sud, M., Maer, A., Li, J., Nadeau, D., Zhou, Y., and Subramaniam, S. (2007). Bioinformatics for lipidomics. *Methods Enzymol* 432, 247–273.
- Ferreira, D.M.S., Castro, R.E., Machado, M.V., Evangelista, T., Silvestre, A., Costa, A., Coutinho, J., Carepa, F., Cortez-Pinto, H., and Rodrigues, C.M.P. (2011). Apoptosis and insulin resistance in liver and peripheral tissues of morbidly obese patients is associated with different stages of non-alcoholic fatty liver disease. *Diabetologia* 54, 1788–1798.
- Flis, V.V., and Daum, G. (2013). Lipid transport between the endoplasmic reticulum and mitochondria. *Cold Spring Harb. Perspect. Biol.* 5, a013235.
- Fu, S., Yang, L., Li, P., Hofmann, O., Dicker, L., Hide, W., Lin, X., Watkins, S.M., Ivanov, A.R., and Hotamisligil, G.S. (2011). Aberrant lipid metabolism disrupts calcium homeostasis causing liver endoplasmic reticulum stress in obesity. *Nature* 473, 528–531.
- Gabor, F. (2011). Characterization of Nanoparticles Intended for Drug Delivery. *Sci. Pharm.* 79, 701–702.
- Gaemers, I.C., Stallen, J.M., Kunne, C., Wallner, C., van Werven, J., Nederveen, A., and Lamers, W.H. (2011). Lipotoxicity and steatohepatitis in an overfed mouse model for non-alcoholic fatty liver disease. *Biochim. Biophys. Acta* 1812, 447–458.
- Galmes, R., Houcine, A., van Vliet, A.R., Agostinis, P., Jackson, C.L., and Giordano, F. (2016). ORP5/ORP8 localize to endoplasmic reticulum-mitochondria contacts and are involved in mitochondrial function. *EMBO Rep.* 17, 800–810.
- Gundermann, K.J., Kuenker, A., Kuntz, E., and Drożdżik, M. (2011). Activity of essential phospholipids (EPL) from soybean in liver diseases. *Pharmacol. Rep.* 63, 643–659.
- Herranz, D., Muñoz-Martin, M., Cañamero, M., Mulero, F., Martínez-Pastor, B., Hernandez-Capetillo, O., and Serrano, M. (2010). Sirt1 improves healthy ageing and protects from metabolic syndrome-associated cancer. *Nat. Commun.* 1, 3.
- Jacobs, R.L., Zhao, Y., Koonen, D.P., Sletten, T., Su, B., Lingrell, S., Cao, G., Peake, D.A., Kuo, M.S., Proctor, S.D., et al. (2010). Impaired de novo choline synthesis explains why phosphatidylethanolamine N-methyltransferase-deficient mice are protected from diet-induced obesity. *J. Biol. Chem.* 285, 22403–22413.
- Katajamaa, M., Miettinen, J., and Orešić, M. (2006). MZmine: toolbox for processing and visualization of mass spectrometry based molecular profile data. *Bioinformatics* 22, 634–636.
- Kawano, S., Tamura, Y., Kojima, R., Bala, S., Asai, E., Michel, A.H., Kommann, B., Riezman, I., Riezman, H., Sakae, Y., et al. (2018). Structure-function insights into direct lipid transfer between membranes by Mmm1-Mdm12 of ERMES. *J. Cell Biol.* 217, 959–974.
- Kleiner, D.E., Brunt, E.M., Van Natta, M., Behling, C., Contos, M.J., Cummings, O.W., Ferrell, L.D., Liu, Y.-C., Torbenson, M.S., Unalp-Arida, A., et al.; Nonalcoholic Steatohepatitis Clinical Research Network (2005). Design and validation of a histological scoring system for nonalcoholic fatty liver disease. *Hepatology* 41, 1313–1321.
- Kotroten, A., Seppänen-Laakso, T., Westerbacka, J., Kiviluoto, T., Arola, J., Ruskeepää, A.-L., Yki-Järvinen, H., and Orešić, M. (2010). Comparison of lipid and fatty acid composition of the liver, subcutaneous and intra-abdominal adipose tissue, and serum. *Obesity (Silver Spring)* 18, 937–944.
- Krick, R., Busse, R.A., Scacioc, A., Stephan, M., Janshoff, A., Thumm, M., and Kühnel, K. (2012). Structural and functional characterization of the two phosphoinositide binding sites of PROPPINs, a β -propeller protein family. *Proc. Natl. Acad. Sci. USA* 109, E2042–E2049.
- Leal, N.S., Schreiner, B., Pinho, C.M., Filadi, R., Wiegner, B., Karlström, H., Pizzo, P., and Ankarcróna, M. (2016). Mitofusin-2 knockdown increases ER-mitochondria contact and decreases amyloid β -peptide production. *J. Cell. Mol. Med.* 20, 1686–1695.
- Lee, A.S. (2001). The glucose-regulated proteins: stress induction and clinical applications. *Trends Biochem. Sci.* 26, 504–510.
- Maeda, K., Anand, K., Chiapparino, A., Kumar, A., Poletto, M., Kaksonen, M., and Gavin, A.C. (2013). Interactome map uncovers phosphorylation transport by oxysterol-binding proteins. *Nature* 507, 257–261.
- Malhi, H., Guicciardi, M.E., and Gores, G.J. (2010). Hepatocyte death: a clear and present danger. *Physiol. Rev.* 90, 1165–1194.
- Mantovani, A., Allavena, P., Sica, A., and Balkwill, F. (2008). Cancer-related inflammation. *Nature* 454, 436–444.
- Massagué, J., and Guinovart, J.J. (1977). Insulin control of rat hepatocyte glycogen synthase and phosphorylase in the absence of glucose. *FEBS Lett.* 82, 317–320.
- Matsumoto, M., Hada, N., Sakamaki, Y., Uno, A., Shiga, T., Tanaka, C., Ito, T., Katsume, A., and Sudoh, M. (2013). An improved mouse model that rapidly develops fibrosis in non-alcoholic steatohepatitis. *Int. J. Exp. Pathol.* 94, 93–103.
- Muñoz, J.P., Ivanova, S., Sánchez-Wandelmer, J., Martínez-Cristóbal, P., Noguera, E., Sancho, A., Díaz-Ramos, A., Hernández-Alvarez, M.I., Sebastián, D., Mauvezin, C., et al. (2013). Mfn2 modulates the UPR and mitochondrial function via repression of PERK. *EMBO J.* 32, 2348–2361.
- Neuschwander-Tetri, B.A., and Caldwell, S.H. (2003). Nonalcoholic steatohepatitis: summary of an AASLD Single Topic Conference. *Hepatology* 37, 1202–1219.
- Nygren, H., Seppänen-Laakso, T., Castillo, S., Hyötyläinen, T., and Orešić, M. (2011). Liquid Chromatography-Mass Spectrometry (LC-MS)-Based Lipidomics for Studies of Body Fluids and Tissues. In *Metabolic Profiling*, T.O. Metz, ed. (Humana Press).
- Osman, C., Voelker, D.R., and Langer, T. (2011). Making heads or tails of phospholipids in mitochondria. *J. Cell Biol.* 192, 7–16.
- Pich, S., Bach, D., Briones, P., Liesa, M., Camps, M., Testar, X., Palacin, M., and Zorzano, A. (2005). The Charcot-Marie-Tooth type 2A gene product, Mfn2, up-regulates fuel oxidation through expression of OXPHOS system. *Hum. Mol. Genet.* 14, 1405–1415.
- Pluskal, T., Castillo, S., Villar-Briones, A., and Orešić, M. (2010). MZmine 2: modular framework for processing, visualizing, and analyzing mass spectrometry-based molecular profile data. *BMC Bioinformatics* 11, 395.
- Potting, C., Tatsuta, T., König, T., Haag, M., Wai, T., Aaltonen, M.J., and Langer, T. (2013). TRIAP1/PREL complexes prevent apoptosis by mediating intramitochondrial transport of phosphatidic acid. *Cell Metab.* 78, 287–295.
- Rehman, J., Zhang, H.J., Toth, P.T., Zhang, Y., Marsboom, G., Hong, Z., Salgia, R., Husain, A.N., Wietholt, C., and Archer, S.L. (2012). Inhibition of mitochondrial fission prevents cell cycle progression in lung cancer. *FASEB J.* 26, 2175–2186.
- Ruozzi, B., Belletti, D., Tombesi, A., Tosi, G., Bondioli, L., Forni, F., and Vandelli, M.A. (2011). AFM, ESEM, TEM, and CLSM in liposomal characterization: a comparative study. *Int. J. Nanomedicine* 6, 557–563.
- Schenkel, L.C., and Bakovic, M. (2014). Formation and regulation of mitochondrial membranes. *Int. J. Cell Biol.* 2014, 709828.
- Schneeberger, M., Dietrich, M.O., Sebastián, D., Imbernon, M., Castaño, C., García, A., Esteban, Y., Gonzalez-Franquesa, A., Rodriguez, I.C., Bortolozzi, A., et al. (2013). Mitofusin 2 in POMC neurons connects ER stress with leptin resistance and energy imbalance. *Cell* 155, 172–187.
- Sebastián, D., Herrero, L., Serra, D., Asins, G., and Hegardt, F.G. (2007). CPT I overexpression protects L6E9 muscle cells from fatty acid-induced insulin resistance. *Am. J. Physiol. Endocrinol. Metab.* 292, E677–E686.
- Sebastián, D., Hernández-Alvarez, M.I., Segalés, J., Soriano, E., Muñoz, J.P., Sala, D., Waget, A., Liesa, M., Paz, J.C., Gopalacharyulu, P., et al.

- (2012). Mitofusin 2 (Mfn2) links mitochondrial and endoplasmic reticulum function with insulin signaling and is essential for normal glucose homeostasis. *Proc. Natl. Acad. Sci. USA* 109, 5523–5528.
- Segalés, J., Paz, J.C., Hernández-Alvarez, M.I., Sala, D., Muñoz, J.P., Noguera, E., Pich, S., Palacin, M., Enríquez, J.A., and Zorzano, A. (2013). A form of mitofusin 2 (Mfn2) lacking the transmembrane domains and the COOH-terminal end stimulates metabolism in muscle and liver cells. *Am. J. Physiol. Endocrinol. Metab.* 305, E1208–E1221.
- Steenbergen, R., Nanowski, T.S., Nelson, R., Young, S.G., and Vance, J.E. (2006). Phospholipid homeostasis in phosphatidylserine synthase-2-deficient mice. *Biochim. Biophys. Acta* 1767, 313–323.
- Stone, S.J., and Vance, J.E. (1999). Cloning and expression of murine liver phosphatidylserine synthase (PSS)-2: differential regulation of phospholipid metabolism by PSS1 and PSS2. *Biochem. J.* 342, 57–64.
- Stone, S.J., and Vance, J.E. (2000). Phosphatidylserine synthase-1 and -2 are localized to mitochondria-associated membranes. *J. Biol. Chem.* 275, 34534–34540.
- Sun, B., and Karin, M. (2012). Obesity, inflammation, and liver cancer. *J. Hepatol.* 56, 704–713.
- Takeda, D., Nitta, H., Takahara, T., Hasegawa, Y., Itou, N., and Wakabayashi, G. (2013). Effect of preoperative chemotherapy on postoperative liver regeneration following hepatic resection as estimated by liver volume. *World J. Surg. Oncol.* 11, 65.
- Tanaka, N., Matsubara, T., Krausz, K.W., Patterson, A.D., and Gonzalez, F.J. (2012). Disruption of phospholipid and bile acid homeostasis in mice with nonalcoholic steatohepatitis. *Hepatology* 56, 118–129.
- Tilg, H., and Hotamisligil, G.S. (2006). Nonalcoholic fatty liver disease: Cytokine-adipokine interplay and regulation of insulin resistance. *Gastroenterology* 131, 934–945.
- Tubbs, E., Theurey, P., Vial, G., Bendridi, N., Bravard, A., Chauvin, M.A., Ji-Cao, J., Zoulim, F., Bartosch, B., Ovize, M., Vidal, H., and Rieusset, J. (2014). Mitochondria-associated endoplasmic reticulum membrane (MAM) integrity is required for insulin signaling and is implicated in hepatic insulin resistance. *Diabetes* 63, 3279–3294.
- Vance, J.E., and Vance, D.E. (2004). Phospholipid biosynthesis in mammalian cells. *Biochem. Cell Biol.* 82, 113–128.
- Wang, W., Lu, J., Zhu, F., Wei, J., Jia, C., Zhang, Y., Zhou, L., Xie, H., and Zheng, S. (2012). Pro-apoptotic and anti-proliferative effects of mitofusin-2 via Bax signaling in hepatocellular carcinoma cells. *Med. Oncol.* 29, 70–76.
- Wieckowski, M.R., Giorgi, C., Lebiedzinska, M., Duszynski, J., and Pinton, P. (2009). Isolation of mitochondria-associated membranes and mitochondria from animal tissues and cells. *Nat. Protoc.* 4, 1582–1590.
- Wu, Y., Wang, Y.Y., Nakamoto, Y., Li, Y.Y., Baba, T., Kaneko, S., Fujii, C., and Mukaida, N. (2010). Accelerated hepatocellular carcinoma development in mice expressing the Pim-3 transgene selectively in the liver. *Oncogene* 29, 2228–2237.
- Wu, Y., Zhou, D., Xu, X., Zhao, X., Huang, P., Zhou, X., Song, W., Guo, H., Wang, W., and Zheng, S. (2016). Clinical significance of mitofusin-2 and its signaling pathways in hepatocellular carcinoma. *World J. Surg. Oncol.* 14, 179.
- Xia, J., and Wishart, D.S. (2016). Using MetaboAnalyst 3.0 for Comprehensive Metabolomics Data Analysis. *Curr. Protoc. Bioinformatics* 55, 14.10.1–14.10.91.
- Yeh, M.M., and Brunt, E.M. (2014). Pathological features of fatty liver disease. *Gastroenterology* 147, 754–764.
- Zhou, X., Zhang, L., Zheng, B., Yan, Y., Zhang, Y., Xie, H., Zhou, L., Zheng, S., and Wang, W. (2016). MicroRNA-761 is upregulated in hepatocellular carcinoma and regulates tumorigenesis by targeting Mitofusin-2. *Cancer Sci.* 107, 424–432.

STAR★METHODS

KEY RESOURCES TABLE

REAGENT or RESOURCE	SOURCE	IDENTIFIER
Antibodies		
Mouse monoclonal anti-Mitofusin 2	Abcam	Cat#ab56889; RRID:AB_2142629
Mouse monoclonal anti-Mitofusin 1	Abcam	Cat#ab57602 RRID:AB_2142624
Rabbit anti cleaved Caspase-3	Cell Signaling	Cat#9661 RRID:AB_2341188
Rabbit monoclonal anti-PARP	Cell Signaling	Cat#9532 RRID:AB_10695538
Mouse monoclonal anti- β -actin	Sigma-Aldrich	Cat#A1978 RRID:AB_476692
Rabbit monoclonal BIP (C50B12)	Cell Signaling	Cat# 3177, RRID:AB_2119845
Rabbit monoclonal Phospho-PERK (Thr980) (16F8)	Cell Signaling	Cat# 3179, RRID:AB_2095853
Rabbit Anti-PERK (C-terminal)	Sigma-Aldrich	Cat# P0074, RRID:AB_1841092
Rabbit anti-phospho-eIF2 α (Ser51)	Cell Signaling	Cat# 9721, RRID:AB_330951
Rabbit anti-eIF2 alpha	Cell Signaling	Cat# 9722, RRID:AB_2230924
Rabbit anti-GADD 153 (F-168)	Santa Cruz Biotechnology	Cat# sc-575, RRID:AB_631365
Rabbit anti-IRE1 (phospho S724)	Abcam	Cat# ab48187, RRID:AB_873899
Rabbit monoclonal anti-IRE1 α -alpha (14C10)	Cell Signaling	Cat# 3294, RRID:AB_823545
Mouse monoclonal ATF6 (Full-length and Active/Cleaved Forms) (Clone 70B1413.1)	IMGENEX	Cat# IMG-273, RRID:AB_316610
Rabbit PTDSS1 (phosphatidyserine synthase 1)	Aviva Systems Biology	Cat# ARP47068_P050, RRID:AB_2047657
Rabbit PTDSS2 antibody - N-terminal region	Aviva Systems Biology	Cat# ARP49960_P050, RRID:AB_10713472
Rabbit PEMT antibody	Biorbyt	Cat# orb28133, RRID:AB_10933957
Rabbit Anti-PACS2	Sigma-Aldrich	Cat# HPA001423, RRID:AB_2156757
Rabbit OPRS1 (SIGMA1R)	Abcam	Cat# ab53852, RRID:AB_881796
Rabbit Calnexin (H-70)	Santa Cruz Biotechnology	Cat# sc-11397, RRID:AB_2243890
Rabbit monoclonal anti-FACL4 antibody [EPR8640]	Abcam	Cat# ab155282, RRID:AB_2714020
Mouse monoclonal Phospho-SAPK/JNK (Thr183/Tyr185) (G9)	Cell Signaling	Cat# 9255, RRID:AB_2307321
Rabbit SAPK/JNK	Cell Signaling	Cat# 9252, RRID:AB_2250373
Mouse monoclonal 6X His tag antibody [HIS.H8]	Abcam	Cat# ab18184, RRID:AB_444306
Rabbit anti-Histone H2a.x (H2AFX)	Acris Antibodies GmbH	Cat# AP02761PU-N, RRID:AB_1617150
Mouse monoclonal anti Ki67	GeneTex	Cat# GTX10913, RRID:AB_367707
Rabbit Rabbit Anti-PDI (H-160)	Santa Cruz Biotechnology	Cat# sc-20132, RRID:AB_653974
Rabbit ATP2A2/SERCA2	Cell Signaling	Cat# 4388, RRID:AB_2227684
Mouse Anti-Tim44 Monoclonal Antibody, Unconjugated, Clone 24	BD Biosciences	Cat# 612582, RRID:AB_399869
Mouse monoclonal RFP antibody	ChromoTek	Cat# 3f5-100, RRID:AB_2336063
Bacterial and Virus Strains		
Ad-m-PTDSS1-shRNA	Vector BioLabs	shADV-269726
Ad-m-PTDSS1	Vector BioLabs	ADV-269726
Ad-m-PTDSS2-shRNA	Vector BioLabs	shADV-269727
Ad-Control RFP	Arruda et al., 2014	N/A
Ad-Linker	Arruda et al., 2014	N/A
Ad-Mfn2	Schneeberger et al., 2013	N/A
Ad-BIP	Laboratory of Jennifer Rieusset	N/A
Ad-Mfn2 (1-613)	Segalés et al., 2013	N/A

(Continued on next page)

Continued

REAGENT or RESOURCE	SOURCE	IDENTIFIER
Ad-LacZ	Unitat de Vectors Virals	UPV-871
Ad-null	Unitat de Vectors Virals	UPV-929
Rosetta (DE3) pLysS <i>E. coli</i> cells	Novagen	Cat# 70956
Biological Samples		
Human liver biopsies	Hospital Sant Joan de Reus	project code: INFLAMED/15-04-30/4prog7
Human liver biopsies	Ferreira et al., 2011	N/A
Chemicals, Peptides, and Recombinant Proteins		
N-diethylnitrosamina	SIGMA ALDRICH	Cat# 73861
Nycodenz	Progen Biotechnik GmbH	Cat# 1002424
Ni-NTA Agarose	Quimigen S.L.	Cat# 50930230
Dulbecco's Modified Eagle's Medium (DMEM)	Life Technologies	Cat# 21969035
Fetal Bovine Serum (FBS)	Life Technologies	Cat# 26400-036
Insulin	Sigma	Cat# I1882-100MG
D-[U]- ¹⁴ C-Oleate	Amersham Biosciences	Cat# CFA243
collagen solution	SIGMA ALDRICH	Cat# C8919-20MG
dexamethasone	SIGMA ALDRICH	Cat# D2915-100MG
Power Broth	Molecular Dimensions	Cat# MD12-106-1
Collagenase Type I	Worthington Biochemical	Cat#46K286
Hanks' Balanced Salt solution	SIGMA ALDRICH	Cat#H6648
Medium 199	SIGMA ALDRICH	Cat#M2154
Bovine Serum Albumin	SIGMA ALDRICH	Cat#A8806
Critical Commercial Assays		
Triglycerides (GLYCEROL PHOSPHATE OXIDASE/PEROXIDASE)	BioSystems	Cat# 11528
Ultra Sensitive Mouse Insulin ELISA Kit	Crystal Chem	Cat# 90080
Cholesterol	BioSystems	Cat# 11805
EnzyChrom Free Fatty Acid Assay Kit	BioAssay Systems	Cat# EFFA-100
Tnf (Mouse) ELISA Kit	Abnova	Cat# KA0257
Ketone Body Assay Kit	Scharlab	Cat# 700190
Glucagon EIA	Cosmo Bio	Cat# YII-YK090-EX
Mouse IL-1 β ELISA Kit	Merck	Cat# RAB0275
Mouse IL-6 ELISA Kit	Merck	Cat# RAB0308
Membrane Lipid Strips	Echelon Biosciences	Cat# P-6001
Pierce™ BCA Protein Assay kit	Thermo scientific	Cat# 23225
Membrane Lipid Arrays	Echelon Biosciences	Cat# P-6003
RNeasy Mini Kit	QIAGEN	Cat# 74104
SuperScript RTIII kit	ThermoFisher	Cat# 18080093
Deposited Data		
Lipidomics data	This paper	https://www.ebi.ac.uk/metabolights/securedirect;jsessionid=E96393BE180562C60B5A3FDB0A1823A5?url=MTBLS845
Experimental Models: Cell Lines		
Male primary cultured hepatocytes	This paper	N/A
Experimental Models: Organisms/Strains		
STOCK Mfn2 ^{tm3Dcc} /Mmucd	MMRRC	029902-UCD, RRID:MMRRC_029902-UCD
C57BL/6JRj	Mouse Mutant Core Facility IRB Barcelona	Derived from Janvier
ALB-Cre mice	Laboratory of Carme Caelles	Derived from Jackson Laboratory

(Continued on next page)

Continued		
REAGENT or RESOURCE	SOURCE	IDENTIFIER
Oligonucleotides		
Table S5	N/A	N/A
Recombinant DNA		
pUC19hMfn1	Sino Biological Inc	Cat# HG19341-U
pCDNA3hMfn2	Laboratory of Antonio Zorzano	N/A
pOPINI vector	Oxford Protein Production Facility, UK	N/A
Software and Algorithms		
GraphPad Prism	GraphPad Software, San Diego USA	Version 7
ImageJ	NIH	https://fiji.sc/
MZmine software	Katajamaa et al., 2006 ; Pluskal et al., 2010	version 6.0
MassHunter Suite Software	Agilent Technologies	N/A
LipidBlast software	N/A	N/A
LipidMatch software	N/A	N/A
MZmine software	Katajamaa et al., 2006 ; Pluskal et al., 2010	version 6.0
LAS AF software	Leica	N/A
Other		
TopFluor PC	SIGMA ALDRICH	810281 (LIPID)
TopFluor PE	SIGMA ALDRICH	810282 (LIPID)
TopFluor PS	SIGMA ALDRICH	810283 (LIPID)
16:0 Liss Rhod PE	SIGMA ALDRICH	810158
16:0-16 Doxyl PC	SIGMA ALDRICH	810604 (LIPID)
16:0-12:0 NBD PS	Avanti Polar Lipids	810193 (LIPID)
16:0 PC-d62	INSTRUCHEMIE	860355
16:0 1,2-dipalmitoyl-sn-glycero-3-phosphoethanolamine	SIGMA ALDRICH	850705
16:0 PS 1,2 dipalmitoyl-sn-glycero-3phospho-L-serine	SIGMA ALDRICH	840037
16:0-12:0 NBD PE	Avanti Polar Lipids	810154 (LIPID)
16:0-12:0 NBD PC	INSTRUCHEMIE	810131
E.COLI TOTAL LIPID EXTRACT	INSTRUCHEMIE	100500

CONTACT FOR REAGENT AND RESOURCE SHARING

Further information and requests for resources and reagents should be directed to and will be fulfilled by the Lead Contact, Antonio Zorzano (antonio.zorzano@irbbarcelona.org).

EXPERIMENTAL MODEL AND SUBJECT DETAILS

Animal care, generation of animal models, and diet treatments

All animal work was approved and conducted according to guidelines established. This project has been assessed favorably by the Institutional Animal Care and Use Committee from Parc Científic de Barcelona (IACUC-PCB) and the IACUC considers that the above-mentioned project complies with standard ethical regulations and meets the requirements of current applicable legislation (RD 53/2013 Council Directive; 2010/63/UE; Order 214/1997/GC). C57BL/6 mice were purchased from Harlan Europe. Mfn2^{loxp/loxp} mice were provided by Dr. David C. Chan ([Chen et al., 2007](#)) through the Mutant Mouse Regional Resource Center. To generate L-KO mice, ALB-Cre mice were crossed with Mfn2^{loxp/loxp} mice. Colonies were maintained by breeding ALB-cre; loxp/loxp mice with loxp/loxp mice. Control and L-KO mice were littermates. Male mice of 8 weeks old were used unless is stated. Mice were kept under

a 12 h dark-light period and provided a standard chow-diet and water *ad libitum*. Eight-week-old C57Bl6/J males were fed a standard or a high-fat diet for 3 weeks (60% calories from fat, D12451 and D12492 from Research Diets, New Brunswick, USA). To MCD experiments: Eight-week-old C57Bl6/J males were fed a standard of methionine choline deficient diet combined with high fat diet (A06071305 MCD with 45% HFD from Research Diets) and supplemented with 0.1% L-methionine on drinking water during 3 weeks. At the times indicated in the figure legends, mice were anesthetized using isoflurane and sacrificed by cervical dislocation.

Human liver biopsies

Liver biopsies were obtained from NAFLD patients undergoing bariatric surgery; liver biopsies from normal individuals were not collected due to ethical issues. Biopsies were processed conventionally for diagnostic purposes, histological grading, and staging, as described previously (Ferreira et al., 2011). Exclusion criteria were the presence of other causes of liver disease, including alcohol ingestion superior to 20 g/day, chronic infection with hepatitis B and/or C virus, α -1 anti-trypsin deficiency, primary biliary cirrhosis, haemochromatosis, auto-immune hepatitis and Wilson's disease, as well as the use of anti-obesity, glucose-lowering and/or lipid-lowering pharmacological treatments. In the second cohort, all liver specimens were evaluated by an experienced pathologist, blinded to clinical data, and following the NAFLD histology scoring system. The severity of steatosis was graded from 0 to 3, inflammation from 0 to 3, hepatocellular ballooning from none to many, and fibrosis from 0 to 4. Each liver specimen was assessed for the presence or absence of NASH by pattern recognition, and for NAFLD activity score (NAS score), defined as the sum of steatosis, inflammation and hepatocyte ballooning. Patients with a NAS score of ≥ 5 were considered as likely to have NASH (Kleiner et al., 2005; Neuschwander-Tetri and Caldwell, 2003). Stratification analysis was not performed.

All patients gave written informed consent. The study protocols conformed to the Ethical Guidelines of the 1975 Declaration of Helsinki, revised in 2000, as reflected in *a priori* approval by the Hospital de Santa Maria (Lisbon, Portugal), by the Hospital Sant Joan de Reus (Institutional Review Board, project code: INFLAMED/15-04-30/4prog7) and Human Ethics Committee. For the cohort of patients with morbid obesity (OME), the inclusion criteria are those recommended by the Guidelines for Clinical Application of Laparoscopic Bariatric Surgery and Guidelines from the National Institute for Health and Clinical Excellence. Exclusion criteria included lack of informed consent, insufficient collaboration (irregularity in follow-up appointments), liver disease of non-metabolic etiology, infectious or chronic inflammatory diseases, and cancer. The medical or surgical complications that appear during the follow-up are excluding factors if they are resolved in a short time. In addition, patients in whom reliable data on important variables cannot be obtained were also excluded.

We did not discriminate whether the reduction in Mfn2 expression was different in women and in men due to insufficient statistical power.

Isolation of primary hepatocytes

Collagenase perfusion was used to isolate primary cultured hepatocytes from control and liver-specific Mfn2 knockout male mice (25–28 g), as described (Massagué and Guinovart, 1977). The phenotype of the liver isolated hepatocytes were authenticated by western blot against Mfn2. To isolation: liver perfusion was initiated with Hank's Cap-free buffer (pH 7.4, 38.5°C) containing 5 mM glucose, at 40 ml/min. After perfusion with 250 mL buffer, collagenase was added to a final concentration of 0.4 mg/ml (Worthington Biochemical, Type I, Lots CLS 46K283P and CLS 46K286) and bovine serum albumin (Fraction V) (Sigma Chemical) was added to a final concentration of 15 mg/ml. The recirculating perfusion with the enzyme was carried out at 60 ml/min for 12–15 min. The liver was then removed and gently teased apart in Hank's Ca²⁺-free buffer. The resulting cell suspension was washed three times and cells were suspended in Dulbecco's Modified Eagle's Medium (DMEM), supplemented with 10 mM glucose, 10% (v/v) fetal bovine serum (FBS), 100 nM insulin (Sigma), and 100 nM dexamethasone (Sigma), and then seeded at a final density of 4×10^6 cells/cm² onto 60-mm diameter plastic plates treated with 0.001% (w/v) collagen solution (Sigma). Media were replaced with fresh M199 media-free serum, 1% BSA, and cells were incubated for 12–14 h.

E. coli strain used for protein purification

The strain for protein expression and purification was *Escherichia coli* (*E. coli*) Rosetta (DE3) pLysS (Novagen), and all constructs were fully sequenced prior to use. For the protein expression, Rosetta (DE3) pLysS *E. coli* cells (Novagen) were transformed with the expression vectors and selected overnight at 37°C on Luria Bertani (LB)-agar plates supplemented with 1% w/v glucose, 35 μ g/mL chloramphenicol and 50 μ g/mL carbenicillin. Single colonies were picked and grown overnight in 5 mL Power Broth (PB-Molecular Dimensions, UK) supplemented with 1% w/v glucose, 35 μ g/mL chloramphenicol and 50 μ g/mL carbenicillin at 37°C with shaking. The pre-cultures were then diluted 1:50 in PB with 1% w/v glucose, 35 μ g/mL chloramphenicol and 50 μ g/mL carbenicillin, and grown as multiple 5 mL cultures in 24 deep-well plates for 3h at 37°C with shaking. The culture temperature was then lowered to 20°C and after 30 minutes IPTG was added to a final concentration of 0.5mM. Cultures were grown for a further 20h at 20°C and then collected in 2ml aliquots at 5,000 g for 10 min at 25°C.

METHOD DETAILS

DEN treatment

To further characterize the protector effect of Mfn2 in liver, we assessed an acute treatment with a high dose of the carcinogen Diethylnitrosamine (DEN). Then, we treated 16 week-old control and L-KO mice for 48h with a single injection of DEN at 50 mg/kg. Liver

sections from DEN-treated or untreated mice were stained with anti-Ki67 and anti- γ H2AX as well as Hematoxylin and Eosin staining. DNA damage and compensatory proliferation were assessed by microscopy on paraffin-embedded sections (Herranz et al., 2010). In addition, to corroborate the susceptibility of Mfn2 ablation to develop liver cancer we used DEN combined with high fat diet (HFD) to induce liver cancer in mice (Wu et al., 2010; Herranz et al., 2010). To this end, 5 days-old mice were injected with a single dose of DEN (5 mg/kg) and put on HFD immediately after weaning. After 7 month of treatment the mice were sacrificed and tumors in each liver lobule were counted and measured with a caliper.

Plasma measurements

Plasma concentrations measured by commercial kits: insulin (crystal chem), (NEFA BioAssay systems), glucagon (Cosmo bio co., LTD), ketone bodies (Scharlab), triglycerides (BioSystems), cholesterol (BioSystems), IL6 (Merck), TNF α (Abnova) and IL-1 β (Merck) were measured following the manufacturer's instructions.

Liver subcellular fractionation and MAM purification

Liver fractions were purified as previously described (Wieckowski et al., 2009; Tubbs et al., 2014). Briefly, after homogenization of about 1 g of liver with a Teflon potter in Isolation Buffer (225 mM mannitol, 75 mM sucrose, 0.5% BSA, 0.5 mM EGTA and 30 mM Tris-HCl, pH7.4), cellular debris and nucleus were removed with two centrifugations at 740 x g for 5 min. A small volume of supernatant was taken, this was called the homogenate fraction. Crude mitochondria were collected by centrifugation at 9,000 x g for 10 min, and the pellet was resuspended in Mitochondria Buffer (MB) (250 mM mannitol, 5 mM HEPES and 0.5 mM EGTA, pH 7.4). The supernatant was conserved for ER purification. Pure mitochondria and MAM fractions were obtained from the crude mitochondria fraction with a Percoll medium centrifugation at 95,000x g for 30 min in a SW40 rotor (Beckman). Pure mitochondria (pM) at the bottom of the tube were collected, washed twice by centrifugation at 6,300 x g for 10 min, and resuspended in RIPA buffer. MAMs were collected from a white band in the middle of the tube. They were then diluted in MB and centrifuged at 6,300 x g for 10 min to remove mitochondrial contamination, pelleted with a 1-h centrifugation at 100,000 x g in a 70Ti rotor (Beckman), and finally resuspended in MB. The ER was purified by two centrifugations at 20,000 x g and 100,000 x g for 30 min and 1 h respectively. Finally, the ER pellet was washed once in MB with a 10 min centrifugation at 9,000 x g and resuspended in RIPA buffer. In order to estimate the amount of each fraction within the liver, proteins were determined using the Pierce™ BCA Protein Assay kit (Thermo scientific). Purification yield was expressed as mg of protein/g of liver and the amount of MAM was then normalized by the amount of pure mitochondrial (pM) protein.

Adenoviral transduction

The following adenoviruses were used in this study: Ad-LacZ, Ad-Mfn2 Δ -Histidine (encoding for a truncated form of Mfn2 = Mfn2 (1-613)) (Pich et al., 2005; Segalés et al., 2013). Ad-Mfn2 was cloned by recombination into the pAdeno-CMV-V5 adenoviral vector (Invitrogen) using the Gateway system. Adenoviruses were generated by transfection of the adenoviral expression vectors in human embryonic kidney cell line (HEK293). The adenoviruses generated were then amplified at the *Unitat de Producció de Vectors Virals-CBATEG* (Universitat Autònoma de Barcelona). Ad-Ptdss1, Ad-Ptdss2 shRNAs and Ad. Ptdss1 (Vector Biolabs), AdControl and AdLinker (a gift from Dr. Gokan Hotamisligil, Harvard University), and Ad-BIP (a gift from Dr. Jennifer Rieusset, INSERM Lyon) were also used.

Cells

Isolated hepatocytes were grown in DMEM 10% FBS. On the day of the experiment, they were infected at a multiplicity of infection (moi) of 50 pfu/cell, and all the experiments were performed 48 h after infection. After infection, cells were incubated for a further 16 h in infection medium before performing the experiment.

Animals

Adenovirus transductions of mice were performed between 8 and 10 weeks of age, and 1×10^9 IFU/mouse were injected via the tail vein. Mice were randomly assigned to the different adenoviral treatments. Livers were isolated after 5 days of adenovirus infection.

Oleate β -oxidation in isolated hepatocytes

Isolated hepatocytes were pre-incubated for 30 min at 37°C in 2 mL of *Krebs-Ringer bicarbonate HEPES* buffer containing 2% bovine serum albumin (fatty acid free-BSA; Sigma, St Louis, MO, USA) and 5 mmol/l glucose (incubation medium). The medium was gassed continuously with 95% O₂, 5% CO₂. The medium was then removed and replaced by 2 mL of fresh incubation medium, containing 1 μ Ci/ml D-[U]-¹⁴C-Oleate (Amersham Biosciences). The hepatocytes were incubated for 180 min at 37°C. The test plates were hermetically sealed with parafilm with a center well that contained a piece of filter paper saturated with 200 μ L of 1M KOH (Sebastián et al., 2007). At the end of the incubation, the medium was acidified with 0.3 mL of 0.5N H₂SO₄ and gaseous ¹⁴CO₂ released after the acidification was trapped in the filter paper. The vials were incubated at 37°C for 60 min, and the filter papers were removed and transferred to vials for liquid scintillation counting (Sebastián et al., 2007).

Oleate incorporation into lipids in isolated hepatocytes

Isolated hepatocytes were pre-incubated for 30 min at 37°C in 2 mL of *Krebs-Ringer bicarbonate HEPES* buffer containing 2% bovine serum albumin (fatty acid free-BSA; Sigma, St Louis, MO, USA) and 5 mmol/l glucose (incubation medium). The medium was gassed

continuously with 95% O₂, 5% CO₂. The medium was then removed and replaced by 2 mL of fresh incubation medium, containing 1 μ Ci/ml D-[U]-¹⁴C-Oleate (Amersham Biosciences). The hepatocytes were incubated for 16 h at 37°C (95% O₂, 5% CO₂). At the end of the incubation, the medium was removed and plates were washed 3 times PBS 1X. The lipids were extracted using the Folch Method, dried by N₂, and run in a TLC. Total lipids that were dissolved in 30 μ L of chloroform were separated by thin-layer chromatography to measure the incorporation of labeled fatty acid into phospholipids, diacylglycerol (DAG), triacylglycerides, nonesterified labeled palmitate (NE palm), and cholesterol esters (CEs). Phosphatidyl-serine, dipalmitoyl-glycerol, glyceryl tripalmitate, cholesteryl palmitate, and labeled control palmitate were used as migration references. Plates were developed with hexane:diethylether:acetic acid (70:30:1, vol/vol/vol) and quantified with a Storm 840 Laser scanning system (Molecular Dynamics; Amersham Pharmacia Biotech) (Sebastián et al., 2007).

Histological sample preparation and analysis

For light microscopy, sections were stained with hematoxylin and eosin. For neutral lipids, liver slices were stained with Oil Red O following Roy Ellis (Woodville, South Australia). For the preparation of livers for electron microscopy, samples were sectioned in small fragments with a razor blade to 1 mm and then fixed in 2.5% glutaraldehyde 2% paraformaldehyde solution 0.1 M at 4°C for 2 h. The samples were washed three times with 0.1 M phosphate buffer. Following post-fixation in 1% osmium tetroxide in 0.1 M phosphate buffer at 4°C for 2 h, they were then washed with highly pure water and kept overnight in 0.1 M phosphate buffer. Samples were dehydrated at 4°C under shaking in graded solutions of acetone (50%, 70% and 90%) in highly pure water. They were then gradually infiltrated with Eponate 12 Resin (TED PELLA 18010), and polymerization of the resin was processed for 48 h at 60°C. Thin sections (50-nm) were cut using a Leica EM UC6 (Leica, Vienna) and mounted on bare 200-mesh copper grids. Sections were stained with uranyl acetate 2% for 30 min, then washed with highly pure water and finally incubated for 5 min with lead citrate and air-dried. Soleus samples were prepared at equal lengths along the long axis of the muscle. Sample sections were viewed on an FEI CM-12 transmission electron microscope.

Western blotting and immunoprecipitation assays

Homogenates for western blot analyses were obtained from either cell cultures or tissues. Cells were collected in ice-cold PBS 1X and homogenized with a douncer in lysis buffer (50 mM Tris pH 7.5, 150 mM NaCl, 1% Triton X-100, 2 mM EDTA, 2 mM sodium or-tovanadate, 50 mM NaF, 20 mM sodium pyrophosphate and protease inhibitors cocktail tablet, Roche) and centrifuged at 700 x g for 10 min to remove nuclei, cell debris, and floating cells. Tissues samples were homogenized in 10 volumes of lysis buffer using a polytron. Homogenates were rotated for 1 h at 4°C in an orbital shaker and centrifuged at 13,000 rpm for 15 min at 4°C. Proteins from total homogenates were resolved in 10% or 15% acrylamide gels for SDS-PAGE and transferred to Immobilon membranes (Millipore). The following antibodies were used: Mfn2, p-IRE1 and IRE1(1/1000, Abcam), p-eIF2 α , eIF2 α , BiP, p-PERK, PERK, pJNK, JNK (1/1000, Cell Signaling), CHOP, PSS1 and PSS2 (1/1000, Santa Cruz), ATF6 (1/1000, Imgenex), β -actin (1/10000, Sigma), α -tubulin (1/8000, Sigma), and porin (1/5000, Calbiochem). Proteins were detected by the ECL method (Enrique-Tarancón et al., 2000) and quantified by scanning densitometry.

RNA extraction and real-time PCR

Mice were killed by cervical dislocation, and tissues were immediately frozen for RNA isolation. RNA from liver tissues was extracted using a protocol combining TRIzol reagent (Invitrogen, Carlsbad Ca, USA) and RNeasy® minikit columns (QIAGEN, Alameda, CA, USA), following the manufacturer's instructions. RNA was reverse-transcribed with the SuperScript RTIII kit (Invitrogen, Carlsbad Ca, USA). PCRs were performed using the ABI Prism 7900 HT real-time PCR machine (Applied Biosystems, USA) and the SYBR® Green PCR Master Mix or the Taqman Probes 20X (Applied Biosystems, USA). All measurements were normalized to β -actin and ARP.

Hepatic triglyceride measurements

Levels of mouse liver triglycerides were quantified using the Triglyceride Determination Kit TRO100 with appropriate standards (Sigma-Aldrich, St. Louis, MO). Frozen liver samples were weighed, put into 2 mL of a chloroform:methanol mixture (2:1, v/v), and incubated for 2 h at room temperature with occasional shaking. Following the addition of 0.2 volumes of water, vortexing, and centrifuging at 2,500 x g, the lower phase containing the lipids was collected and dried under vacuum in a rotary evaporator for 5–6 h. The dried pellets were resuspended in the reaction buffer provided in the kit. Results were expressed as mg/g tissue.

Lipidomic analysis from liver

Lipidomic analysis was done as described previously (Nygren et al., 2011; Kotronen et al., 2010). Briefly, liver samples were cryo-homogenized (Covaris, CryoPrep CP02, MA) and weighed (5 mg). An aliquot (20 μ L) of an internal standard mixture containing PC(17:0/0:0), PC(17:0/17:0), PE(17:0/17:0), PG(17:0/17:0)[rac], Cer(d18:1/17:0), PS(17:0/17:0), PA(17:0/17:0) (Avanti Polar Lipids, Alabaster, AL), MAG(17:0/0:0/0:0)[rac], DAG(17:0/17:0/0:0)[rac] and TAG(17:0/17:0/17:0) was added to the sample, and the lipids were extracted using a mixture of HPLC-grade chloroform and methanol (2:1; 400 μ L). 50 μ L of 0.9% NaCl was added, and the lower phase (200 μ L) was collected and 20 μ L of an internal standard mixture containing labeled PC (16:1/0:0-D₂), PC(16:1/16:1-D₆) and TAG(16:0/16:0/16:0-¹³C₃) was added.

Lipid extracts were analyzed on a Waters Q-ToF Premier mass spectrometer combined with an Acquity Ultra Performance LCTM (UPLC). The column (at 50°C) was an Acquity UPLC BEH C18 1 × 50 mm with 1.7- μ m particles. The solvent system included A. ultrapure water (1% 1 M NH₄Ac, 0.1% HCOOH) and B. LC/MS grade acetonitrile/isopropanol (5:2, 1% 1 M NH₄Ac, 0.1% HCOOH). The gradient started from 65% A / 35% B, reached 100% B in 6 min and remained there for the next 7 min. The flow rate was 0.2 ml/min and the injected amount was 1.0 μ L (Acquity Sample Organizer). Reserpine was used as the lock spray reference compound. The lipid profiling was carried out using ESI+ mode, and the data were collected at mass range of m/z 300–1200 with a scan duration of 0.2 s. The data were processed using MZmine software version 6.0 (Katajamaa et al., 2006; Pluskal et al., 2010) and normalized using lipid class-specific internal standards. Lipid species identification was done using an internal spectral library or tandem mass spectrometry.

QTOF-based untargeted lipidomics of liver subcellular fractionation

For protein precipitation three volumes of acetone were added to each sample (containing 100 μ g of protein). After acetone addition the samples were vortexed for 10 s, incubated at 4°C for 30 min and centrifuged at 100 g, at 4°C for 10 minutes. Then, the supernatant was recovered and evaporated using a Speed Vac (Thermo Fisher Scientific, Barcelona, Spain).

After supernatant evaporation, 250 μ l of methanol were added and vortexed for 10 s. Then, 500 μ l of chloroform (containing internal standard) were added and vortexed for 10 s. Finally, 200 μ l of KCl 0.7% were added and vortexed for 10 s and samples centrifuged at 1000 g at 4°C for 15 min. The chloroform phase (lower) was recovered in a glass tube and aliquoted in chromatographic vials.

For LC-Q-TOF-based lipid molecular species analyses, lipid extracts were subjected to liquid chromatography-mass-spectrometry using a HPLC 1290 series coupled to ESI-Q-TOF MS/MS 6520 (Agilent Technologies, Barcelona, Spain) as previously described (Sandra et al.). Four microliters of lipid extract were injected onto an XBridge BEH C18 shield column (100 mmL × 2.1 mm ID × 1.7 μ m; Waters, Milford, MA, USA) kept at 80°C. The mobile phases, delivered at 0.5 ml/min, consisted of ammonium formate (20 mM at pH 5) (A) and methanol (B). The gradient started at 50% B and reached 70% B in 14 min and was followed by a slow gradient of 70%–90% B over 50 min and an isocratic separation at 90% B for 15 min. The mobile phase B subsequently reached 100% over 5 min and was maintained for an additional 5 min. Data were collected in positive electrospray ionization-TOF operated in full-scan mode at 100–3000 m/z in an extended dynamic range (2 GHz) (MassHunter Data Acquisition Software, Agilent Technologies, Barcelona, Spain), using N₂ as nebulizer gas (5 L/min, 300°C). The capillary voltage was 3500 V with a scan rate of 1 scan/s.

MassHunter Qualitative Analysis Software (Agilent Technologies, Barcelona, Spain) to obtain the molecular features of the samples, representing different, co-migrating ionic species of a given molecular entity using the Molecular Feature Extractor (MFE) algorithm (Agilent Technologies, Barcelona, Spain). MassHunter Mass Profiler Professional Software (Agilent Technologies, Barcelona, Spain) and Metaboanalyst Software (Xia and Wishart, 2016; Chong and Xia, 2018) was used to perform a non-targeted lipidomic analysis over the extracted features. Only those features with a minimum abundance of 5000 counts and 2 ions as a minimum were selected. After that, the molecular characteristics in the samples were aligned using a retention time window of 0,1% \pm 0,25 min and 20,0 ppm \pm 2,0 mDa. Quality control-based correction was performed in order to correct the sample intensities according to injection order. A LOESS regression was performed for each QC metabolite, using polynomials of second degree and with an optimum smoothing parameter each time. Sample values were predicted and the relation between real values and predicted values was obtained, based on (Broadhurst et al., 2018; Dunn et al., 2011). To avoid background, only common features (found in at least 70% of the samples of the QC) were taken into account to correct for individual bias. Multivariate statistics (Partial Least-squares Discriminant Analysis (PLS-DA) and Hierarchical Analyses) were done using Metaboanalyst software (Chong and Xia, 2018; Xia and Wishart, 2016). Variable importance in projection (VIP) score was calculated using Metaboanalyst software (Chong and Xia, 2018; Xia and Wishart, 2016). The masses with an important weight defining PLS-DA model and Hierarchical analyses as well as those masses representing significant differences by Student T-Test ($p < 0.05$), defined by exact mass and retention time, were searched against the LIPID MAPS database (accuracy < 20 ppm) (Fahy et al., 2007). The identities obtained were compared to retention time of the authentic standards added. Finally, identities were confirmed by MS/MS by checking the MS/MS spectrums using LipidBlast software and LipidMatch, a R-based tool for lipid identification.

³H- L-serine incorporation into phospholipids in subcellular fractions

Liver was homogenized (use Teflon-glass homogenizer) in Isolation Buffer (225mM Mannitol, 25mM HEPES-KOH, 1mM EGTA, pH7.4 add protease inhibitors trypsin and chymotrypsins) at a ratio of 4 mL of IB for every gram of tissue. The homogenate was pelleted for 10 min at 1,500 × g at 4°C. SPN was transferred to a new tube and pelleted again under the same conditions. SPN was transferred again to a new tube and pelleted at 13,000 × g for 20 min at 4°C. This new pellet contained the crude mitochondrial fraction and was used to measure lipid transfer because it contains mitochondria and ER-MAM. The SPN contained the ER fraction, which was pelleted at 100,000 × g for 1 h at 4°C. This pellet was used as a control in the assay. 1 mg of the fraction was pelleted again and resuspended in 200 μ L of Ptdser assay buffer (25 mM HEPES-KOH, 10 mM CaCl₂ adding 0.4 mM of ³Hser (20–30 μ ci/ μ mol) pH 7.4). The mixture was incubated for 45 min at 37°C and the reaction was stopped by adding 3 volumes of chloroform: MeOH (2:1). The lipids were extracted using the Folch Method, dried by N₂, and run in a TLC. The dried lipids were resuspended in a small volume of chloroform:methanol (2:1, v/v) and spotted on a 20 × 20 thin layer chromatography (TLC) silica plate (60 Å adsorption) with appropriate standards for all the PLs under analysis. To analyze PS, PE and PC, the chromatography is run in two phases. First, the TLC plates are placed in a chamber containing a mix of petroleum ether:diethyl ether:acetic acid (84:16:1, v/v/v) and then in a second

chamber containing chloroform:methanol:water:acetic acid (60:40:4:1, v/v/v/v). Note: as these solvents are toxic, the preparation of the solvents, and the TLC step itself, should be performed in a well-ventilated chemical hood. Once the plates are run, the lipidic species can be visualized as spots on the TLC plates by staining with iodine vapor in a third TLC chamber. Iodine binds to unsaturated bonds in lipids, so saturated lipids will not be visualized on the TLC plate. Spots corresponding to PS, PE and PC are cut carefully from the plate and quantified in a scintillation counter. Data are represented as counts per minute of 1h per unit of total protein (Area-Gomez, 2014).

Mfn2 immunoprecipitation for phospholipid binding assays

Liver from control mice was homogenized in 50 mM Tris-HCl (pH 7.4), 150 mM NaCl, 1 mM EDTA, 1% Triton X-100, 2 mM sodium orthovanadate, 50 mM NaF, 20 mM sodium pyrophosphate and 1% SDS, pH 7.4. Protease inhibitors: Pepstatin A 2 uM, Leupeptin 2 uM, PMSF 1 mM or one tablet from Roche per 10 mL of fresh buffer added. These conditions cause dissociation of Mfn2 from other potential binding partners including lipid species.

The lysate was centrifuged for 10 min at 10,000 x g at 4°C. The supernatant was warmed at 95°C for 5 min. Supernatant was diluted 10 times with homogenization buffer without SDS and placed onto 50% Protein G-Agarose beads (30ul). 10 ul of Mfn2 ab or IgG was added and the mixture was incubated O/N at 4°C on the roller. Next day, washes were done with 300–500 ul washing buffer (5 times). Then protein was extracted using glycine buffer elution (0.2 M glycine pH 2.0–3.0) and neutralized with Tris, pH 8.0. Protein concentration was determined by the BCA Pierce assay, and the protein was used in fresh to assay the lipid strips. A small aliquot of protein was used for western blotting.

Purification of a short Mfn2 (1-613) for phospholipid binding assays

Liver Mfn2 KO mice were injected with 1×10^9 pfu/bodyweight Ad-Mfn2 Δ -Histidine through the tail vein; the adenovirus was used as previously reported (Segalés et al., 2013). Injected mice were left in *ad libitum* conditions for adenoviral expression. After 5 days mice were sacrificed and liver was extracted and immediately frozen in liquid nitrogen and stored at –80°C until the assay was performed. Liver was homogenized in lysis buffer (25 mM Imidazol, 300 mM NaCl, 1% Triton X-100, 100 mM NaPO₄, 1 mM Na₃VO₄, 50 nM calyculin A and EDTA-free complete pH 7.5 and 1% SDS) and put to rotate for 1 h at 4°C. The lysate was centrifuged at 10,000 x g for 10 min at 4°C. Then the supernatant was warmed to 95°C for 5 min. The supernatant was then diluted ten times with lysis buffer and incubated with Ni-NTA beads (previously equilibrated with lysis buffer without SDS). The mixture was incubated O/N at 4°C under rotation. Next day, the beads were washed 5 times with washing buffer (50 mM Imidazol, 500 mM NaCl and 1 mM Na₃VO₄, pH 7.5). At the end elution buffer (250 mM Imidazol, 300 mM NaCl, pH 7.5) was added and the mixture was put into the thermomixer for 15 min at 25°C and 1150 rpm. Protein concentration was determined by the BCA Pierce assay, and the protein was used in fresh to assay the lipid strips. A small aliquot of protein was used for western blotting.

Cloning, Expression and Purification of Mfn2 (1-613), Mfn1 (1-592) and Mfn2 (21-613) from E.coli

All three constructs were amplified with KOD polymerase (Novagen) according to the manufacturer's instructions, using the plasmids pUC19hMfn1 (Sino Biological) and pCDNA3hMfn2 from A. Zorzano as templates for Mfn1 and Mfn2 respectively and the following primer pairs to add the extensions necessary for cloning:

Mfn2 (1-613) Fwd 5'- ATCATCACAGCAGCGGCatgtccctgctctctc-3'

Mfn2 (1-613) Rev 5'- ATGGTCTAGAAAGCTTTAcctggatgtcaaggaggccag-3'

Mfn2 (20-613) Fwd 5'- ATCATCACAGCAGCGGCatgtgctgaggtgaatgcatccccacttaag-3' (the reverse primer for the 1-613 construct is re-used here).

Mfn1 (1-594) Fwd 5'- ATCATCACAGCAGCGGCatggcagaacctgttctccactg-3'

Mfn1 (1-594) Rev 5'- ATGGTCTAGAAAGCTTTAtctagatgtaacggacccaatcctg-3'.

The amplified fragments were purified from the PCR reactions using Ampure (Beckman Coulter) and cloned into the pOPINI vector (Oxford Protein Production Facility, UK) previously cut with KpnI and HindIII (New England Biolabs), using the In-Fusion cloning method (Clontech). This yielded the plasmids for expression of these proteins in *Escherichia coli* (*E. coli*) Rosetta (DE3) pLysS (Novagen), with N-terminal hexa-histidine affinity tags (MAHHHHHHSSG-POI [protein of interest]), all constructs were fully sequenced prior to use. For the protein expression, Rosetta (DE3) pLysS *E. coli* cells (Novagen) were transformed as explained in Experimental model and subject details section. Protein purification: each pellet of 2 mL of culture was resuspended in 200 μ l of Lysis Buffer (25mM Imidazole, 300mM NaCl, 1mM NaVO₄, 1% SDS), and incubated 1h at room temperature on a roller. At the same time than cell lysis Ni-NTA beads (QIAGEN) were washed with lysis buffer without SDS. After the incubation the homogenate was centrifuged 3 min at 7000 g at 4°C. The SN was diluted 10 times in lysis buffer without SDS and transferred to a new tube with 100 μ l of Ni-NTA beads and was incubated at 4°C overnight rotating. The next day the tubes were centrifuged 3 min at 7000 g and the SN was kept as flow through. Then 3 wash cycles (centrifuge 3 min at 7000 g and discard supernatant) were performed (Wash buffer: 500mM NaCl, 50mM Imidazole). Finally, 200 μ l of elution buffer (300mM NaCl, 250mM Imidazole) were added and thermomixed at 500 rpm 10' at room temperature. Then the mix was centrifuged 3 min x 7000 g and the supernatant was kept as elution 1. This step was repeated 3 times collecting 3 different elutions of each sample. Purified protein was conserved at –80°C.

Binding to Lipid Strip assays

Membrane lipid strips were obtained from Echelon Bioscience (P-6002 and P-6003). Lipid strips were assayed, following the manufacturer's instructions. Briefly, the membrane was blocked with 3% of fatty acid-free BSA in TBS-Tween 0.1% and gently agitate O/N at 4°C. After discarding the blocking solution, the membrane was incubated with 10 µg/ml of protein at room temperature for 1 h. The protein solution was discarded, and the membrane washed for about 8 min with TBS-Tween 0.1% (repeated this step 4–5 times). The membrane was then incubated with a 1:1,000 dilution of primary antibody in 3% of fatty acid-free BSA TBS-Tween 0.1%. Gently agitated for 1 h at RT. The antibody solution was discarded, and the membrane washed for about 8 min with TBS-Tween 0.1% (repeated this step 4–5 times). The membrane was incubated with a 1:25,000 dilution of secondary antibody in 3% of fatty acid-free BSA TBS-Tween 0.1%. Gently agitated for 1 h at RT. The secondary antibody solution was discarded, and the membrane washed for about 8 min with TBS-Tween 0.1% (repeated this step 4–5 times). The bound of protein to lipid was detected by Chemiluminescent or ECL.

Lipid binding by liposome flotation assays

Phospholipids and *E. coli* lipids were obtained from Avanti Polar Lipids, unless is stated. Lipids in stock solution in chloroform were prepared at 1 mM concentration (according to <https://bio-protocol.org/e2169> and [Apellániz and Nieva \[2015\]](#)): 80% of: *E. coli* (100500P) or PC (860355P) and 20% of: PC (860355P), PS (840037P), PA (830855P), PE (850705P) or PI (P2517-25MG). The lipid suspension was incubated at room temperature for 1 hour. Then, it was first sonicated during 4 cycles of 3 minutes each (Ultrasonic Cleaner; Branson 200) and then 5 freeze/thaw cycles in liquid nitrogen/warm water (26°C) were performed to break the lipid cake. Finally the liposome mix was extruded through 400 nm polycarbonate membrane filter using a mini-extruder for large unilamellar vesicles (LUVs) formation.

Five µl of protein ($\approx 1.5\mu\text{M}$) were incubated with 45 µl of *E. coli* or PC liposomes containing either PA, PE, PC, PS or PI in TBS 1X during 1 hour at room temperature as reported. After the incubation, the mixture was subjected to liposome flotation. Briefly, the 50 µL of liposome/protein mixture was put into 800 µL of an ultracentrifuge tube (Beckman Coulter, ref: 343776) and mixed with 120 µL of TBS 1X containing 60% sucrose (Sigma). The mixture was subsequently overlaid by 200 µL of TBS 1X containing 27% sucrose and then by 150 µL of TBS 1X containing 17% sucrose. After centrifugation at 84000 rpm for 3h at 4°C, fractions were collected from top to bottom with a Hamilton syringe, and each fraction was analyzed by western blotting as reported ([Apellániz and Nieva, 2015](#)).

Lipid extraction assay

To monitor PS transfer extraction from liposomes we followed the protocol proposed by [Kawano et al. \(2018\)](#) ([Krick et al., 2012](#)). 200 µM liposomes: 80% of PC (860355P) and 20% of NBD-PS (810193P) or NBD-PE (810154P), were hydrated in TBS 1X (50 mM Tris-Cl, pH 7.5, 150 mM NaCl). The lipid suspension was incubated at room temperature for 1 hours. Then, it was first sonicated during 4 cycles of 3 minutes each (Ultrasonic Cleaner; Branson 200) and then 5 freeze/thaw cycles in liquid nitrogen/warm water (26°C) were performed to break the lipid cake. Finally the liposome mix was extruded through 400 nm polycarbonate membrane filter using a mini-extruder for large unilamellar vesicles (LUVs) formation. For lipid extraction, 10 µl of protein ($\approx 3\mu\text{M}$) of protein were mixed with 90 µl of liposomes in 100µl TBS 1X and incubated at room temperature for 3 hours. After the incubation, the mixture was subjected to liposome flotation. The mixture of liposome/protein in TBS 1X was put into 5 mL of an ultracentrifuge tube (Beckman Coulter, ref: 344057) and mixed with 1400 µL of buffer A (20mM Tris-HCl, pH 7.4, and 150mM NaCl) and 1500 µL of buffer A containing 80% Nycodenz AG (Axis-Shield). The mixture was subsequently overlaid by 1500 µL of buffer A containing 30% Nycodenz AG and then 900 µL of buffer A without Nycodenz AG (see [Figure 4A](#)). After centrifugation at 54000 rpm for 2h at 4°C, 2 different fractions, top and bottom, were collected and analyzed for fluorescence with Spectra fluorimeter (SYNERGY H1M Fluorescence plate reader) at excitation/emission 460-590nm and protein quantification by western blot.

In vitro phospholipid FRET assays

To monitor the kinetics of FRET reaction, we assessed a modified protocol reported by [Potting et al. \(2013\)](#) and [Connerth et al. \(2012\)](#). Briefly, Donor liposomes (12,5 µM): 90% *E. coli* (100500P), 2% Rhod PE (810158P), 8% NBD-PE (810154P) or NBD-PS (810193P) or NBD-PA (810174P) or NBD-PC (810131P) were resuspended in BLTS (10% sucrose in buffer BLT = 5mM Tris/HCl ph 7.4, 150mM NaCl), and acceptor liposomes (50µM): 90% *E. coli* (100500P) and 10% of PC (860355P) or PS (840037P) or PA (830855P) or PE (850705P) were resuspended in BLT buffer without sucrose. The lipid suspension was incubated at room temperature for 1 hour. Then, it was first sonicated during 4 cycles of 3 minutes each (Ultrasonic Cleaner; Branson 200) and then 5 freeze/thaw cycles in liquid nitrogen/warm water (26°C) were performed to break the lipid cake. Finally the liposome mix was extruded through 400 nm polycarbonate membrane filter using a mini-extruder for large unilamellar vesicles (LUVs) formation. The donor and acceptor liposomes were mix with 200nM of purified recombinant protein and fluorescence of NBD was monitored during 3 hours in TECAN SAFIRE II-BASIC at constant temperature of 25C.

To TOPFluor liposomes: 12,5 µM Donor liposomes contained: 90% *E. coli* (100500P), 2% Doxyl PC (810604P), 8% TopFluor PS (810283P), or TopFluor PE (810282P) were resuspended in BLTS and mixed with the same acceptor liposomes prepared for NBD liposomes. Next, exactly the same protocol above described for NBD to monitor kinetics was assessed.

Liposome imaging

Donor liposomes (12.5 μ M): 90% *E. coli* (100500P), 2% Rhod PE (810158P), 8% NBD-PC (810131P) or NBD-PS (810193P) resuspended in BLTS and acceptor liposomes (50 μ M): 90% *E. coli* (100500P) and 10% of PC (860355P) or PS (840037P) resuspended in BLT were incubated with 200nM of recombinant Mfn2 (1-613) protein in 300 μ L buffer TA (20 mM Tris/HCl pH 7.4, 150 mM NaCl, 1 mM EDTA) at 25°C. After incubation the mixture was placed on ice, mixed with 100 μ L buffer TA30 (30% sucrose in TA) and incubated for 10 min. The mix was placed on an ultracentrifuge tube and overlaid with 600 μ L buffer TA5 (5% sucrose in TA), 400 μ L ofTA2.5 (2.5% sucrose in TA) and 75 μ L buffer TA. Tubes were centrifuged at 217,000 xg for 2.5 h. Fractions fraction of 750 μ L from the top middle and bottom were collected to be analyzed (Connerth et al., 2012). Liposomes were identified by confocal following bibliographic examples of liposome imaging (Gabor, 2011; Ruozi et al., 2011). Confocal images were obtained with a spectral confocal microscope multiphoton (Leica, Mannheim, Germany) and a Leica confocal system equipped with a 3-channel multiband Leica scanner TCS SP5. To obtain confocal images a small drop of the extraction flotation assay sample (usually 5 μ l) was transferred to a coverslip (slide) and directly observed. Samples were scanned using a 63z Leitz objective (oil) to analyze the liposomes using LAS AF software from Leica. The NBD was excited with the 488 laser.

QUANTIFICATION AND STATISTICAL ANALYSIS

Phospholipid content measured by lipidomics was analyzed separately using a linear model in which type of sample (control or L-KO) and experimental batch were included as covariates. Values were previously Box-Cox transformed in order to fit the assumptions of the model. Adjusted mean groups and fold-changes were extracted from the models and presented in their original scale. Statistical significance was assessed using the corresponding F-test.

Data in the different experimental series including mice or cells showed a Gaussian distribution (D'Agostino-Pearson omnibus normality test, GraphPad Prism 7.0). Those data were analyzed with Student's t test or ANOVA followed by post hoc t tests. Data are presented as mean \pm SEM unless stated. Significance was established at $p \leq 0.05$. Statistical analysis were performed using the GraphPad Prism Version 7.0.

No statistical method was use to predetermine sample size, and replicates are shown in Figure legends. The investigators were not blinded to allocation during experiments and outcome assessment. Animals that did not induce correctly the protein overexpressed (Mfn2, BiP, etc) were excluded from the experimental group and they were not taken into account in the statistical analyses.

For clinical and anthropometrical variables, normal distributed data are expressed as mean value \pm SD, and for variables with no Gaussian distribution values are expressed as median (interquartile range). Differences were analyzed by the unpaired t test (normal distribution) or Mann-Whitney U test (data not-normally distributed).

DATA AND SOFTWARE AVAILABILITY

Lipidomics data on liver fractions have been deposited in the EMBL-EBI under accession code MTBLS600. Data will be accessible upon publication of the manuscript.

